

AD A068039

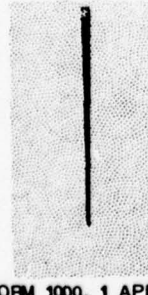


**U.S. ARMY  
MISSILE  
RESEARCH  
AND  
DEVELOPMENT  
COMMAND**

DDC FILE COPY



Redstone Arsenal, Alabama 35809



LEVEL ~~II~~

(6)

TECHNICAL REPORT T-79-35

**AERODYNAMIC ANALYSIS OF THE RIFLEMAN'S  
ASSAULT WEAPON**

Jimmie N. Derrick  
Systems Simulation Directorate  
Technology Laboratory



March 1979

Approved for public release; distribution unlimited.

**DISPOSITION INSTRUCTIONS**

**DESTROY THIS REPORT WHEN IT IS NO LONGER NEEDED. DO NOT  
RETURN IT TO THE ORIGINATOR.**

**DISCLAIMER**

**THE FINDINGS IN THIS REPORT ARE NOT TO BE CONSTRUED AS AN  
OFFICIAL DEPARTMENT OF THE ARMY POSITION UNLESS SO DESIG-  
NATED BY OTHER AUTHORIZED DOCUMENTS.**

**TRADE NAMES**

**USE OF TRADE NAMES OR MANUFACTURERS IN THIS REPORT DOES  
NOT CONSTITUTE AN OFFICIAL INDORSEMENT OR APPROVAL OF  
THE USE OF SUCH COMMERCIAL HARDWARE OR SOFTWARE.**

UNCLASSIFIED

SECURITY CLASSIFICATION OF THIS PAGE (When Data Entered)

REPORT DOCUMENTATION PAGE		READ INSTRUCTIONS BEFORE COMPLETING FORM
1. REPORT NUMBER T-79-35	2. GOVT ACCESSION NO.	3. RECIPIENT'S CATALOG NUMBER
4. TITLE (and Subtitle) <b>(6) AERODYNAMIC ANALYSIS OF THE RIFLEMAN'S ASSAULT WEAPON</b>		5. TYPE OF REPORT & PERIOD COVERED <b>(9) Technical Report</b>
7. AUTHOR(s) <b>(10) Jimmie N. Derrick</b>		6. PERFORMING ORG. REPORT NUMBER
9. PERFORMING ORGANIZATION NAME AND ADDRESS Commander US Army Missile Research and Development Command Attn: DRDMI-TDK Redstone Arsenal, Alabama 35809		10. PROGRAM ELEMENT, PROJECT, TASK AREA & WORK UNIT NUMBERS DA 9.03627 AMCMS 69100R.89710.21
11. CONTROLLING OFFICE NAME AND ADDRESS Commander US Army Missile Research and Development Command Attn: DRDMI-TI Redstone Arsenal, Alabama 35809		11. REPORT DATE <b>(11) March 1979</b>
14. MONITORING AGENCY NAME & ADDRESS (if different from Controlling Office) <b>(12) 173 P</b>		12. NUMBER OF PAGES <b>172</b>
16. DISTRIBUTION STATEMENT (of this Report) Approved for public release; distribution unlimited.		15. SECURITY CLASS. (of this report) Unclassified
17. DISTRIBUTION STATEMENT (of the abstract entered in Block 20, if different from Report) <b>(14) DRDMI-T-79-35</b>		
18. SUPPLEMENTARY NOTES		
19. KEY WORDS (Continue on reverse side if necessary and identify by block number) Wind tunnel test Shell configurations Aerodynamic forces		
20. ABSTRACT (Continue on reverse side if necessary and identify by block number) A wind tunnel was conducted for seven different shell configurations. The basic configuration was a spherical shell with modification to the base section. A spherical aft shell, a truncated aft shell, and various artificial boundary layer trip devices on the base section was used. The test was conducted for Mach numbers up to 0.3 to determine the aerodynamic forces at angles-of-attack from -2 to 15 deg and various spin rates. Force and moment data were obtained for these runs. <i>Over</i>		

ABSTRACT (Continued)

DD FORM 1 JAN 73 1473 EDITION OF 1 NOV 65 IS OBSOLETE

UNCLASSIFIED

SECURITY CLASSIFICATION OF THIS PAGE (When Data Entered)

393 427

SLT

UNCLASSIFIED

SECURITY CLASSIFICATION OF THIS PAGE(When Data Entered)

ABSTRACT (Concluded)

The magnus forces due to the velocity component normal to the spin axis were measured in terms of the side force coefficient CY.

ACCESSION for	
NTIS	White Section <input checked="" type="checkbox"/>
BDC	Buff Section <input type="checkbox"/>
UNANNOUNCED	<input type="checkbox"/>
JUSTIFICATION	
BY	
DESCRIPTION OF MAGNUS FORCES	
DI	SPECIAL
P1	

UNCLASSIFIED

SECURITY CLASSIFICATION OF THIS PAGE(When Data Entered)

## **CONTENTS**

	<b>Page</b>
I. INTRODUCTION . . . . .	5
II. TEST MODEL . . . . .	7
III. TEST DESCRIPTION . . . . .	9
IV. TEST RESULTS . . . . .	9
V. CONCLUSIONS AND RECOMMENDATIONS . . . . .	15
Appendix A. PLOTS OF AERODYNAMIC COEFFICIENTS VERSUS ALPHA . . .	21
Appendix B. DATA COLLATION SHEETS . . . . .	169

## NOMENCLATURE

$\alpha$	Angle-of-attack, deg
CA	Axial force coefficient, axial force/QSr
CN	Normal force coefficient, normal force/QSr
CY	Side force coefficient, side force/QSr
CM	Pitching moment coefficient, PM/QSr dia
CLN	Yawing moment coefficient, YM/QSr dia
CL	Coefficient of lift, lift/QSr
CD	Coefficient of drag, drag/QSr
Dia	Diameter of RAW, 0.13335 m, (5.25 in.)
Fv	Net vertical aerodynamic force
MDOT	Mass flow from exhaust simulator, lb/in. <sup>2</sup>
Mref	Moment reference is about geometric center of model
M	Mach number
Q	Dynamic pressure (0.5 $\rho V^2$ )
Sr	Maximum frontal area, 0.0139 m <sup>2</sup> , (0.15 ft <sup>2</sup> )
Re	Reynolds number
RPS	Revolutions per second (spin rate)
A	Speed of sound in air, 341.38 m/sec (1120 ft/sec)
Ah	Acceleration along horizontal flight path
Av	Vertical acceleration (nominally zero)
T	Thrust
$\phi$	Angle of inclination of thrust vector
m	Mass of the projectile

$g$  Acceleration due to gravity

$\rho$  Density of air,  $1.2 \text{ kg/m}^3$ , ( $0.00233 \text{ slug/ft}^3$ )

$\theta$  Angle between spin vector and forward velocity

## I. INTRODUCTION

The Rifleman's Assault Weapon (RAW) is being developed for infantryman support in urban warfare type conflicts. It is self-contained weapon responsive to the needs for a versatile assault weapon. The weapon is attached to the service rifle with an explosive filled warhead. When the service rifle is fired, the weapon is ignited and a desired spin rate about the thrust vector is obtained which produces stability about the thrust axis. Upon release from the service rifle, the constant spin rate and the regressive burning thrust-to-weight ratio motor will cause the weapon to maintain stability along a straight-line flight path.

An analysis of the RAW configuration was conducted by the Systems Planning Corporation in October, 1975<sup>1</sup>. The analysis points out the potential problem areas for all phases of the round. The problem areas that concerned the aerodynamic portion of the configuration was Magnus forces, crosswinds, and drag.

A Magnus force will act on the projectile since it employs a spinning motion at an angle-of-attack relative to the flight path. An additional Magnus force, resulting from crosswinds, will also act on the projectile; however, this will be very small since the crosswind velocity is low. The primary Magnus force will act perpendicular to the spin axis and cause the projectile to accelerate laterally and move along a horizontally curved flight path.

Crosswind errors are dependent on the drag, the frontal area, the projectile velocity, and crosswind velocity. Since the crosswind is essentially parallel to the ground, this error contributes only to lateral dispersions.

The drag coefficient is primarily a function of Reynolds number ( $Re$ ) and the geometry of the projectile. During a considerable portion of the RAW flight, the  $Re$  is between  $10^5$  and  $10^6$  ( $Re$  reaches a value of  $10^5$  at a range of approximately 15 m and a value of  $7 \times 10^5$  at a range of 200 m. In this region, transition from laminar to turbulent flow takes place and the coefficient of drag (CD) decreases from a laminar value of 0.5 to a turbulent flow value of 0.1 as shown in Figure 1. It is therefore important to determine when transition takes place so that appropriate values of CD can be used to predict errors.

---

<sup>1</sup>McDaniel, R. L., Meni, J., Lewis, E. W., Rifleman's Assault Weapon (RAW) Effectiveness Analysis, October 1975.

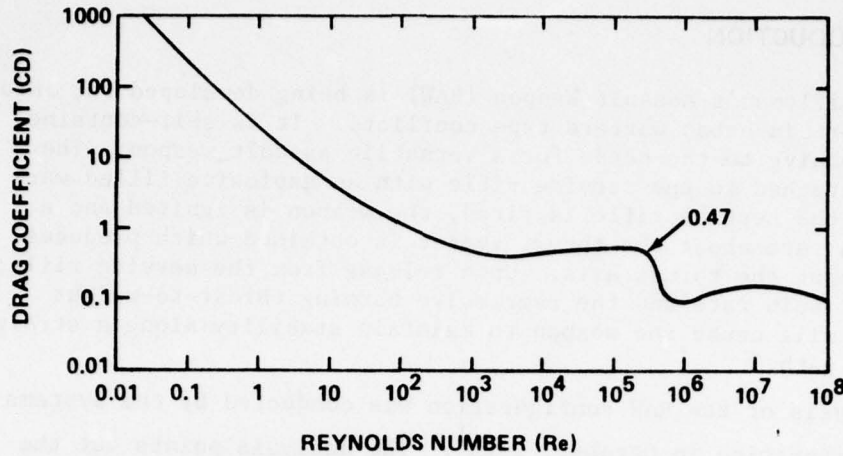


Figure 1. Experimental value of drag coefficient versus Reynolds number.

When the system is initiated, the rocket motor is ignited and the exhaust gases are directed through a turbine cup which causes the turbine and the projectile to spin. When the desired spin rate is achieved, the spinning projectile is released and propelled forward by the rocket motor. The straight-line flight path is attained by configuring the projectile to incorporate a regressive burning, constant thrust-to-weight ratio rocket motor; the thrust vector is inclined so that the vertical component of the thrust balances the gravitational effects. The spherical shape of the projectile provides an essentially aerodynamically neutral configuration which minimizes the effect of lift and moments. The spin stabilization about the thrust axis maintains the initial orientation of the thrust vector and minimizes trajectory deviations due to thrust vector misalignments, center-of-gravity offsets, and other asymmetries. The regressive burning motor maintains a constant thrust-to-weight ratio so that the vertical thrust component is equal to the weight throughout the powered flight. The force diagram of an idealized RAW projectile is shown in Figure 2. The two dimensional general equations of motion are as follows:

$$Ah = (T \cos \theta - D)/m$$

$$Av = (T \sin \theta - mg + F_v)/m ,$$

where  $Ah$  is the horizontal acceleration and  $Av$  is the vertical acceleration.

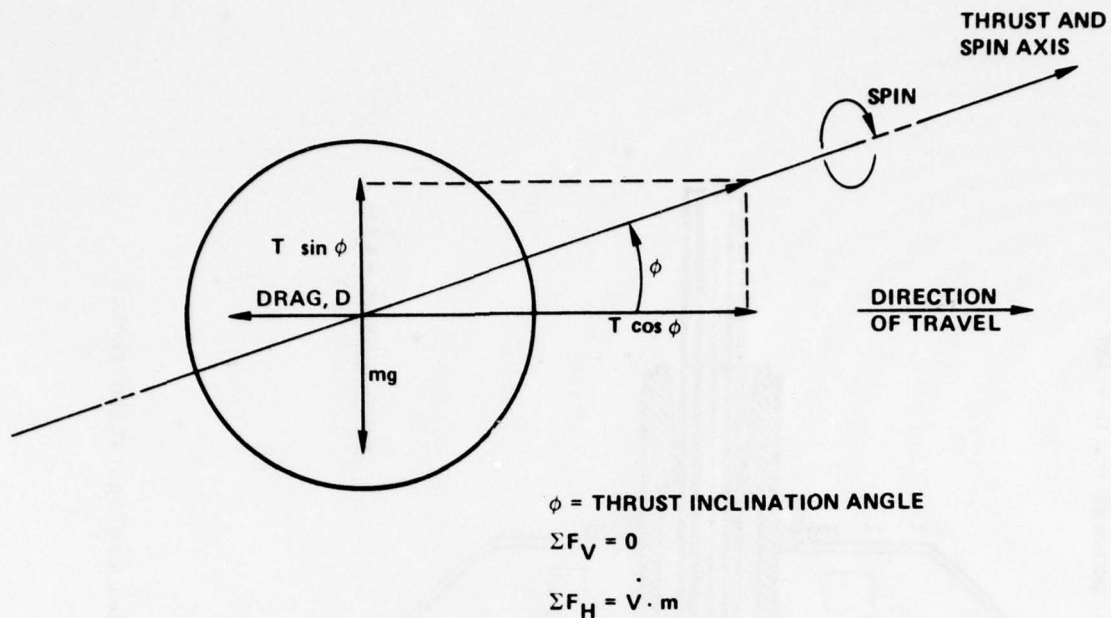


Figure 2. Raw projectile force diagram.

A wind tunnel test was conducted at the US Army Aviation Research and Technology Laboratory, Aviation Research and Development Command (AVRADCOM), Ames Research Center, Moffett Field, California. The primary purpose of the test was to determine a configuration that would meet the accuracy required for the weapon during its flight. For the configurations tested, the effects of the external shell configuration, spin rate, Mach number, angle-of-attack, and simulation of rocket exhaust were examined to produce data that would best describe the weapon in flight.

## II. TEST MODEL

The RAW full scale wind tunnel model is shown in Figure 3. The model has a principal radius of 2.625 in. and is truncated in length to 4.73 in. overall. The rocket nozzle (simulator) extends 1.23 in. out from the truncated aft end.

Seven configurations were used in the wind tunnel test.

- a) The primary configuration (Configuration 1) was a smooth spherical external shell including a spherical aft section and a standard rocket nozzle.

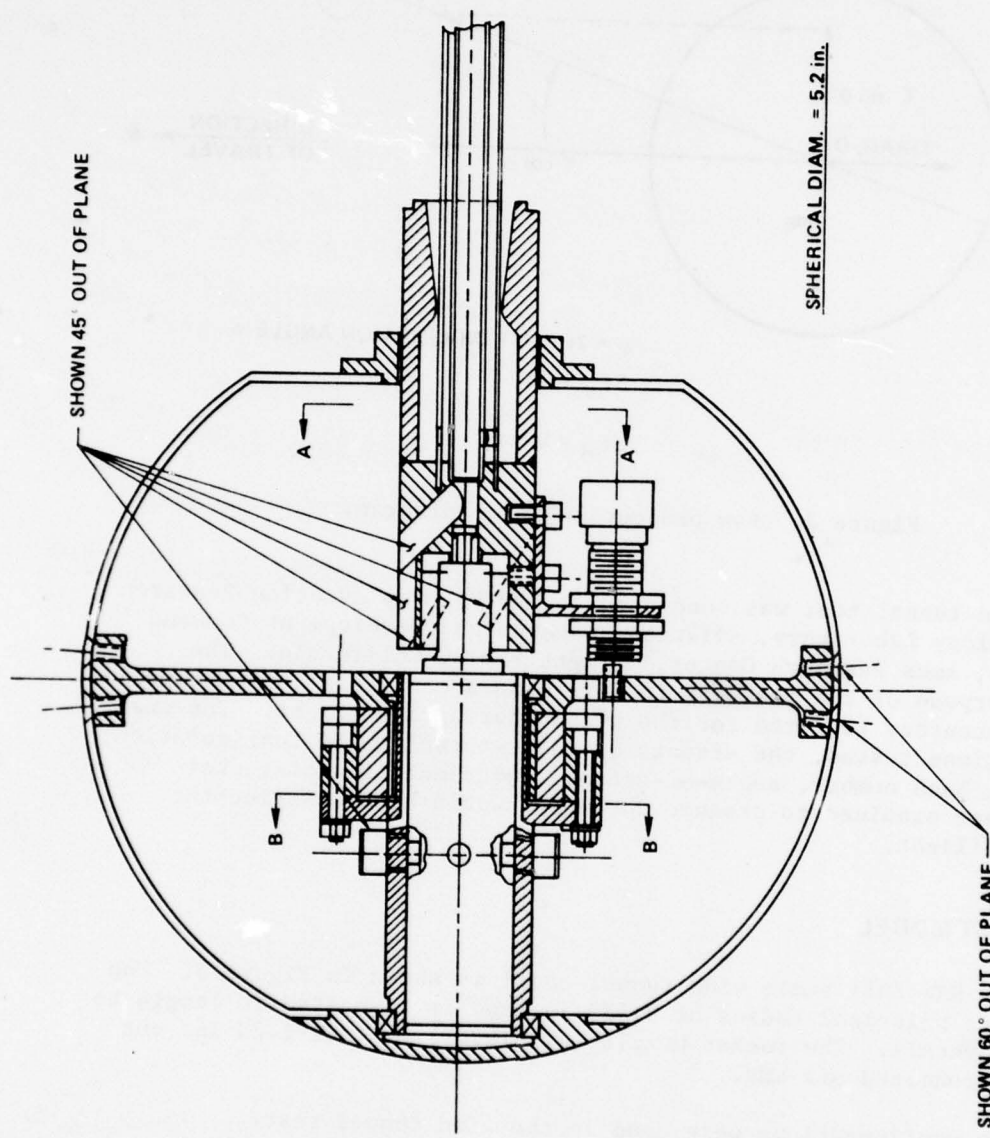


Figure 3. RAW full scale wind tunnel model configuration sketch.

- b) Configuration 2 was a smooth spherical external shell with a spherical truncated aft section and a standard rocket nozzle.
- c) Configuration 3 was the same as Configuration 2 except for a dimpled external shell.
- d) Configuration 4 was the same as Configuration 2 except for a highly polished surface.
- e) Configuration 5 was the same as Configuration 2 except for a large separation ring on the aft shell.
- f) Configuration 6 was the same as Configuration 2 except for a trip wire on the aft section.
- g) Configuration 7 was the same as Configuration 2 except for a small separation ring on the aft shell.

A photograph of the model in the tunnel is shown in Figure 4 and a sketch of all the configurations is shown in Figure 5.

### III. TEST DESCRIPTION

The test was conducted in the US Army's 7 × 10 ft wind tunnel at Mach numbers varying from 0 to 0.3 using a NASA internal strain gage balance that had a normal force of 20 lb and a side force of 10 lb.

Force and moment data were obtained for the model while varying Mach number, spin rate, mass flow from rocket nozzle simulator, and angle-of-attack.

Configurations 5, 6, and 7 were not tested as extensively as Configurations 1, 2, 3, and 4 since the Magnus force was not significantly affected by the rings and trip wires on the aft shell.

An air supply of 3000 psi was used to simulate the nozzle flow. Several mass flow rates from the nozzle were tested at different spin rates and Mach numbers by varying the pressure to the nozzle.

### IV. TEST RESULTS

The data obtained from the test can be reduced to coefficient form using the Buckingham Pi Theorem. The implicit form of this theorem for the parameters of tunnel condition and balance loads are as follows:

$$f(F_N, F_Y, F_L, F_D, V, D, \rho, \mu, A, \alpha, P, L) = 0.$$

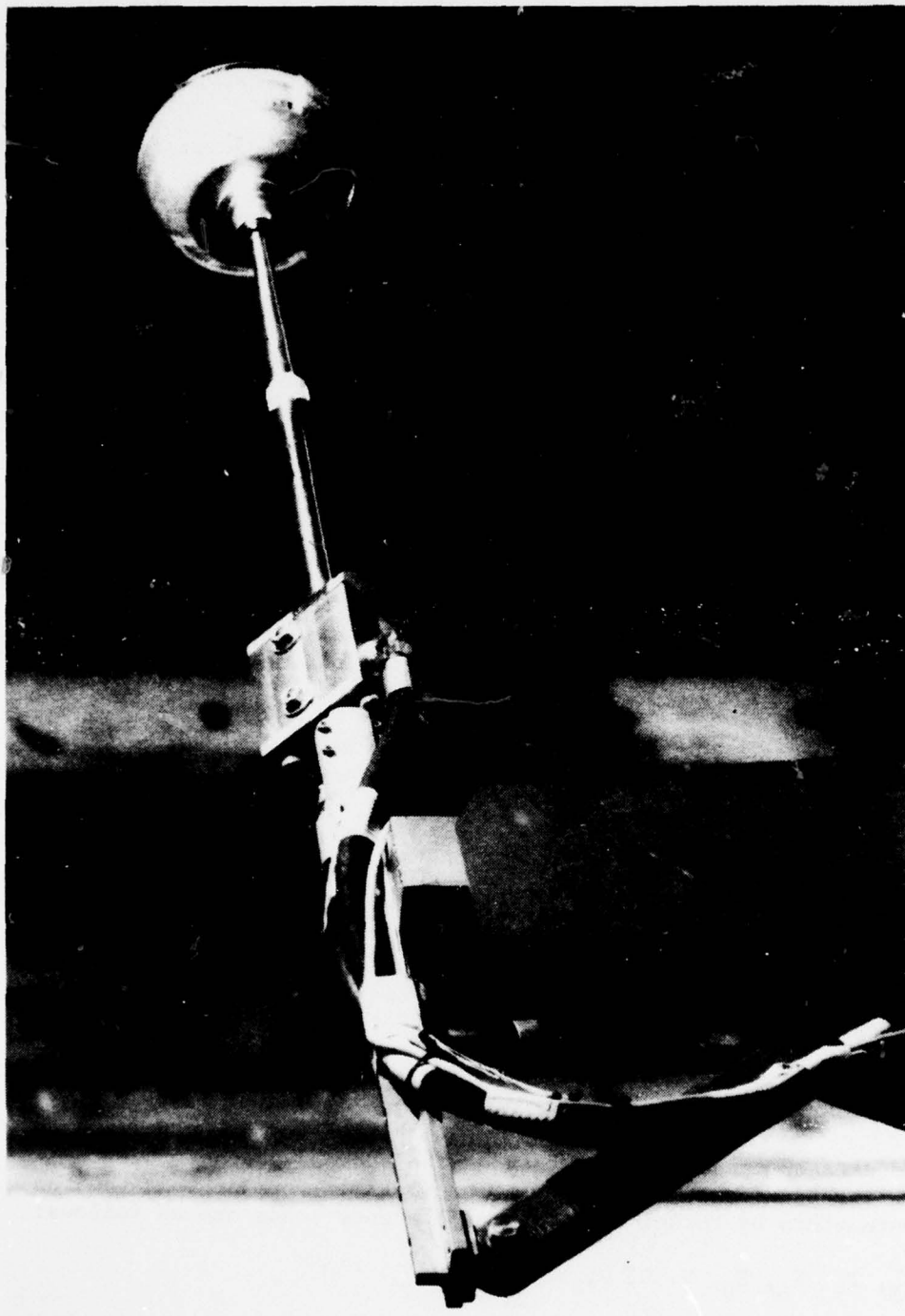


Figure 4. Photograph of the model in the wind tunnel.

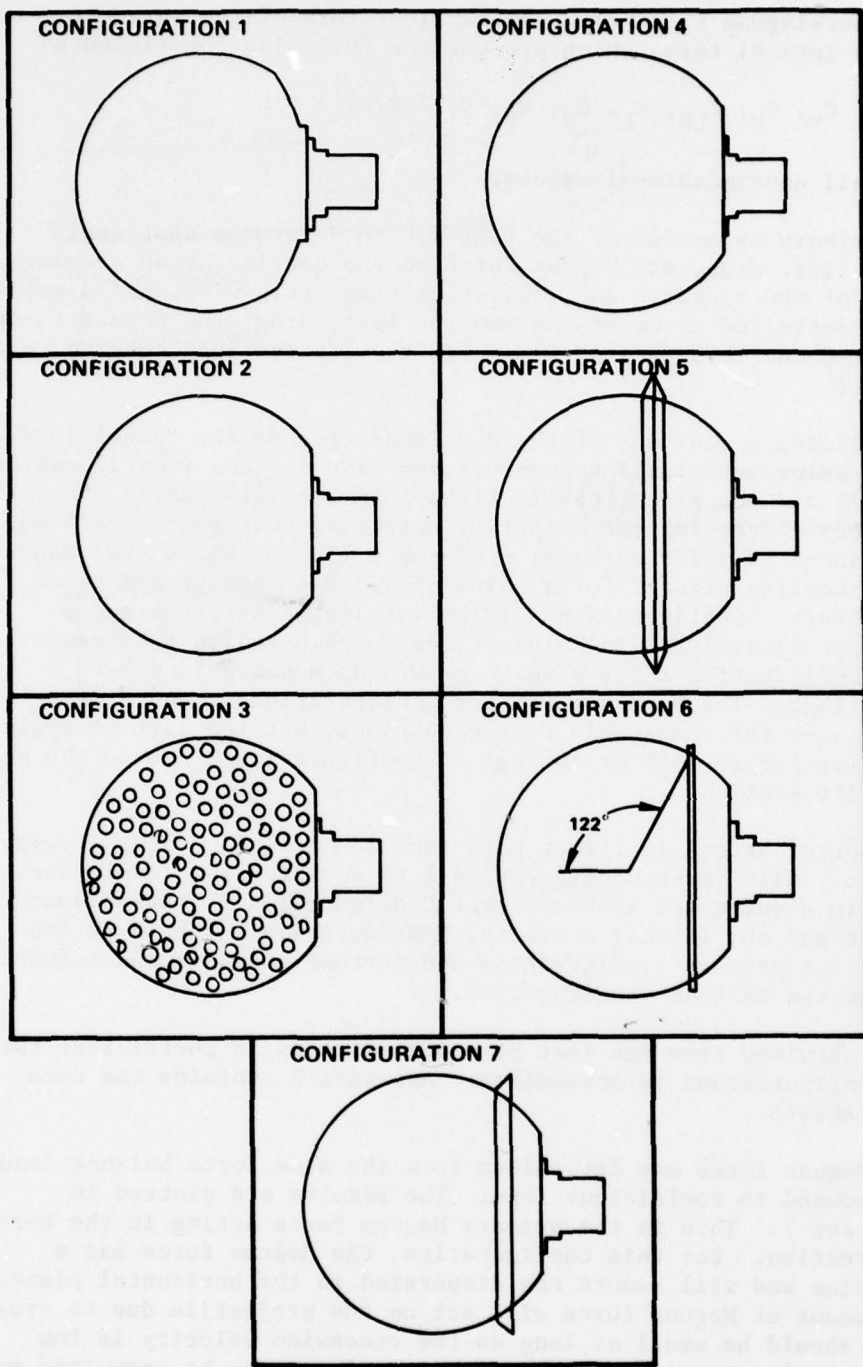


Figure 5. Sketch of all configurations.

Using the Buckingham Pi Theorem, an explicit form of the parameters can be arranged into Pi terms which produce the following coefficients:

$$f(C_N, C_Y, C_M, C_{LN}, C_L, C_D, R_E, M, 2\Delta P/\rho V^2) = 0$$

which are all nondimensional values.

The primary objective of the test was to determine what would affect the lift, drag, and Magnus force on the configuration causing a dispersion of the rounds. The separation ring, trip wire, and dimpled shell were installed to determine how the lift, drag, and Magnus force were affected due to separated flow over the aft section compared to a smooth shell.

A preliminary analysis of the data conducted at the tunnel indicated that using artificial boundary layer trip devices (Configurations 5, 6, and 7) did not significantly (less than 2 to 5%) change the results, thus decreasing the number of potential test configurations. Configuration 3 (dimpled surface) produced a (30 to 40%) higher Magnus force than Configuration 2 for a value of 0.3 Mach number and zero angle-of-attack. Configuration 4 (highly polished surface) had a decrease approximately 8% in Magnus force as compared to the Magnus force of Configuration 2 for a value of 0.3 Mach number and zero angle-of-attack. The Magnus force for Configurations 1 and 2 were almost the same for comparable test conditions, but the lift at angles-of-attack was larger (30% at 10 deg) on Configuration 1 due to the more spherical aft section.

Any perturbations in flight path because of wind, center-of-gravity shifts, etc., will cause Configuration 1 to deviate from level flight, resulting in a decreased accuracy over Configuration 2. Based upon this result and the initial criteria, Configuration 2 should be considered as the primary configuration and further analysis and comments will be limited to that configuration.

Data obtained from the test have been plotted in coefficient form for all configurations in Appendix A. Appendix B contains the data collation sheets.

The Magnus force was determined from the side force balance loads and was reduced to coefficient form. The results are plotted in Figures 6 and 7. This is the primary Magnus force acting in the horizontal direction. For this configuration, the Magnus force has a minimum value and will reduce the dispersion in the horizontal plane. A small amount of Magnus force will act on the projectile due to cross-winds but should be small as long as the crosswind velocity is low (12 ft/sec or less). An increase in Magnus force can be seen from an increase in angle-of-attack for the projectile. The increase is due to the shift of the crosswinds.

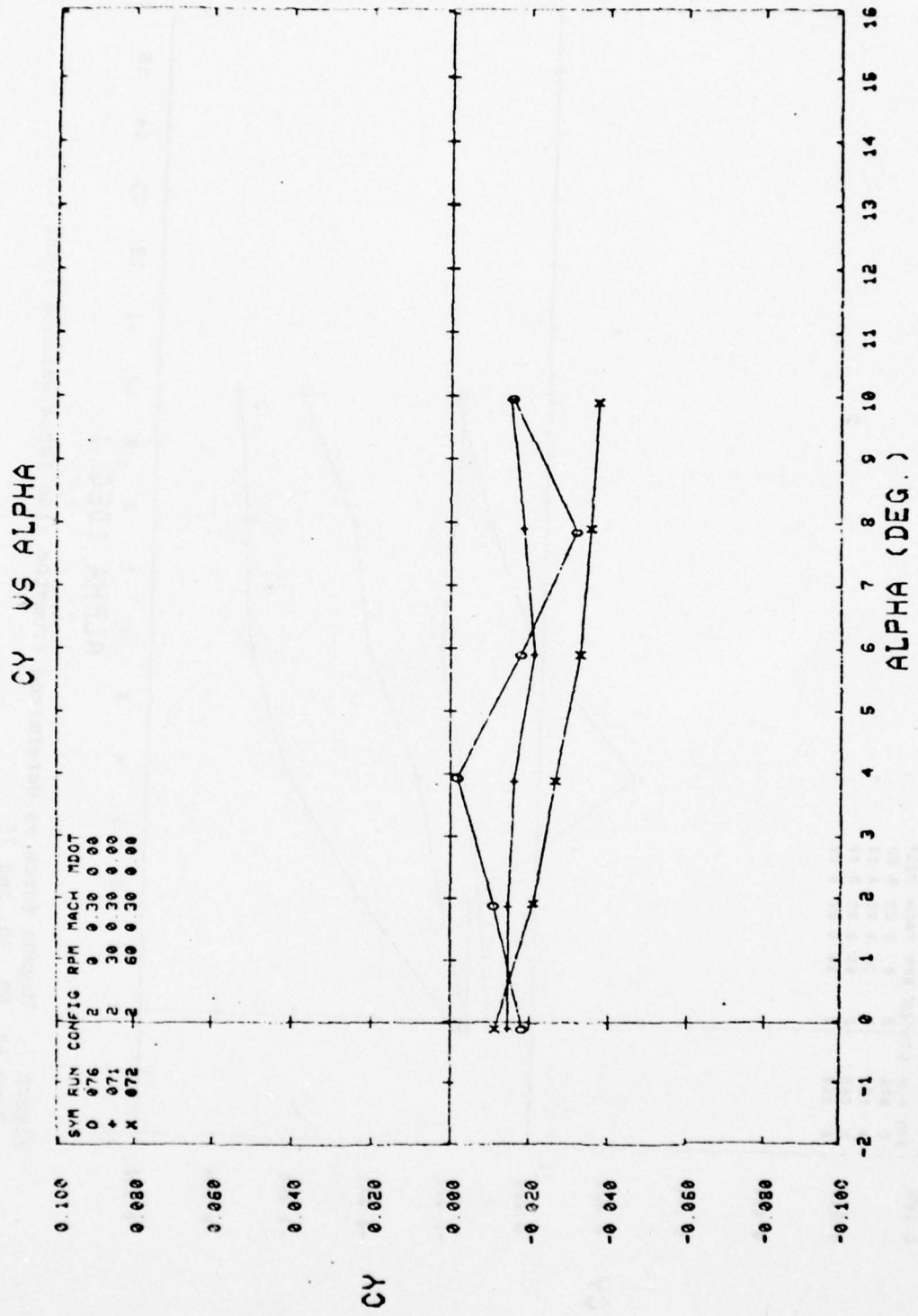


Figure 6. Magnus force as determined from the side force balance loads for Runs 71, 72, and 76.

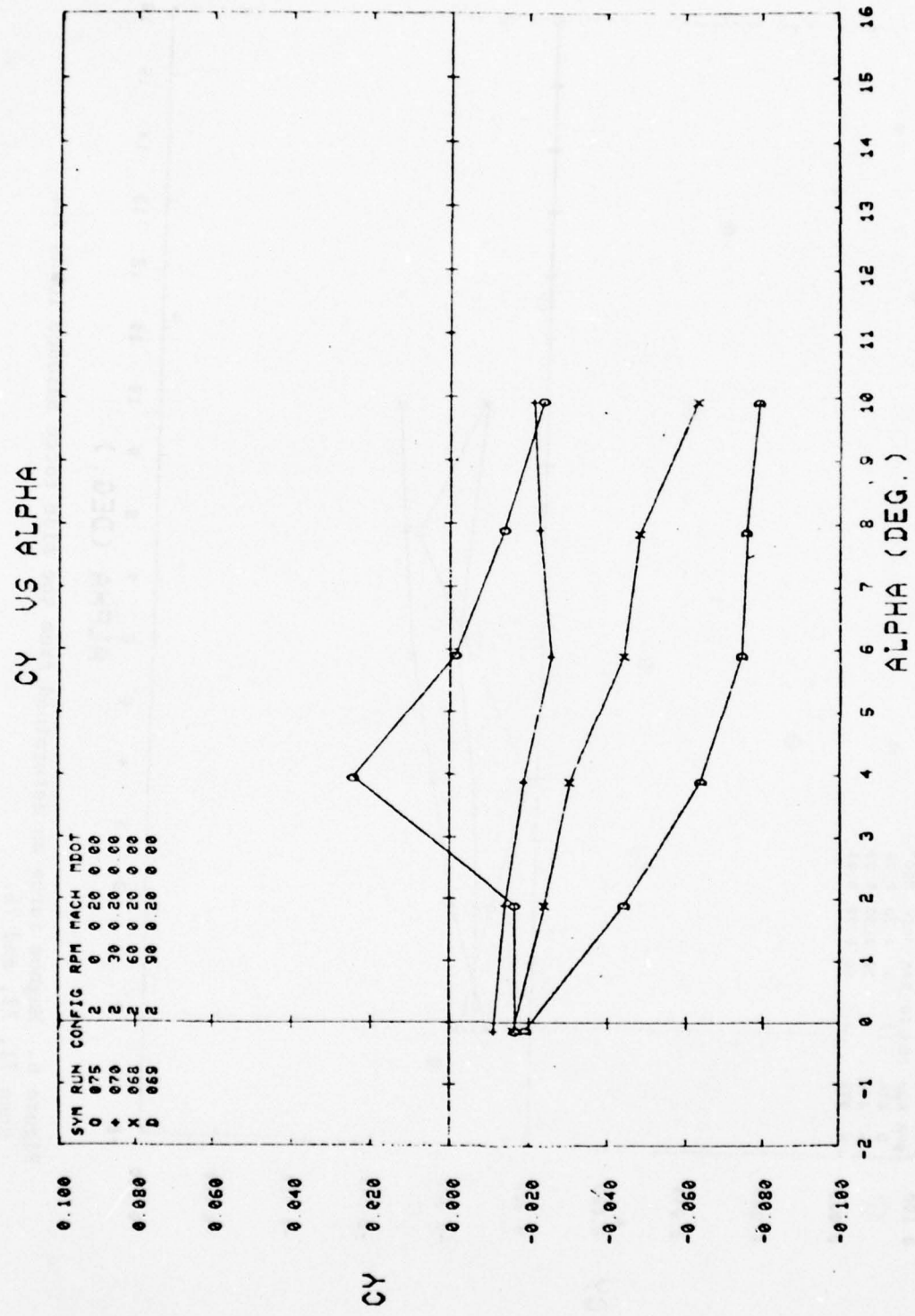


Figure 7. Magnus force as determined from the side force balance loads for Runs 68, 69, 70, and 75.

The lift coefficient was determined from the normal and axial force coefficient obtained from the balance loads. The data for this coefficient is plotted in Figures 8 and 9. The lift at angles-of-attack was minimized due to the truncated aft section, therefore reducing the dispersion for the round and increasing its accuracy.

The drag coefficient is plotted in Figures 10 and 11. The drag coefficient is primarily a function of the Reynolds number and the geometry of the round. The error due to crosswind is dependent on the drag coefficient, frontal area, the velocity of the round, and crosswind velocity. It is desirable for a transition from laminar to turbulent flow to take place as soon as possible during the flight; this transition decreases the drag which decreases the crosswind error. Figures 1 and 12 are plots of coefficient of drag versus Reynolds number using previously mentioned experimental data<sup>2</sup> for Figure 1 and wind tunnel data in Figure 12. The results for this configuration indicates that the transition takes place early in the flight between Mach numbers 0.09 and 0.14. The transition time from laminar to turbulent flow is decreased due to the spinning projectile. This transition minimizes the drag coefficient and improves the accuracy by reducing the crosswind error.

## V. CONCLUSIONS AND RECOMMENDATIONS

The potential problems that effected aerodynamic forces for the flight requirements were the primary objective of the test. The configurations tested produced data that gave a better understanding of the forces acting on the round. After completing the data analysis, it appears that Configuration 2 would have the most accurate line of flight due to the Magnus, lift, and drag force.

Analysis of the flight test data should be conducted and compared with the wind tunnel data to determine the best configuration and the most effective spin rate that would decrease the dispersion of the round. These tests should be conducted before a final configuration is selected.

---

<sup>2</sup>McDaniel, et al., loc. cit.

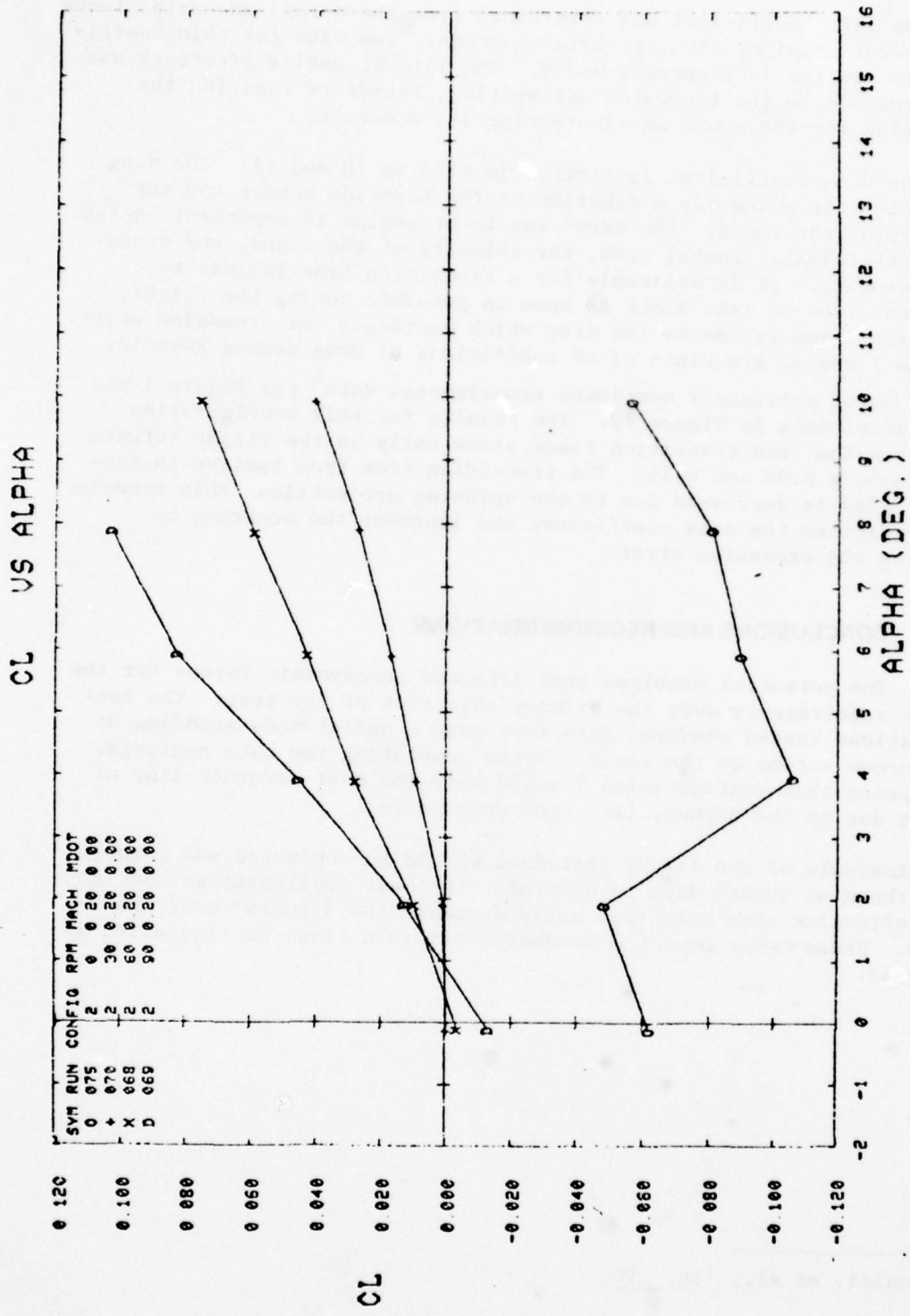


Figure 8. Lift coefficient as determined from the normal and axial force coefficient obtained from the balance loads for Runs 68, 69, 70, and 75.

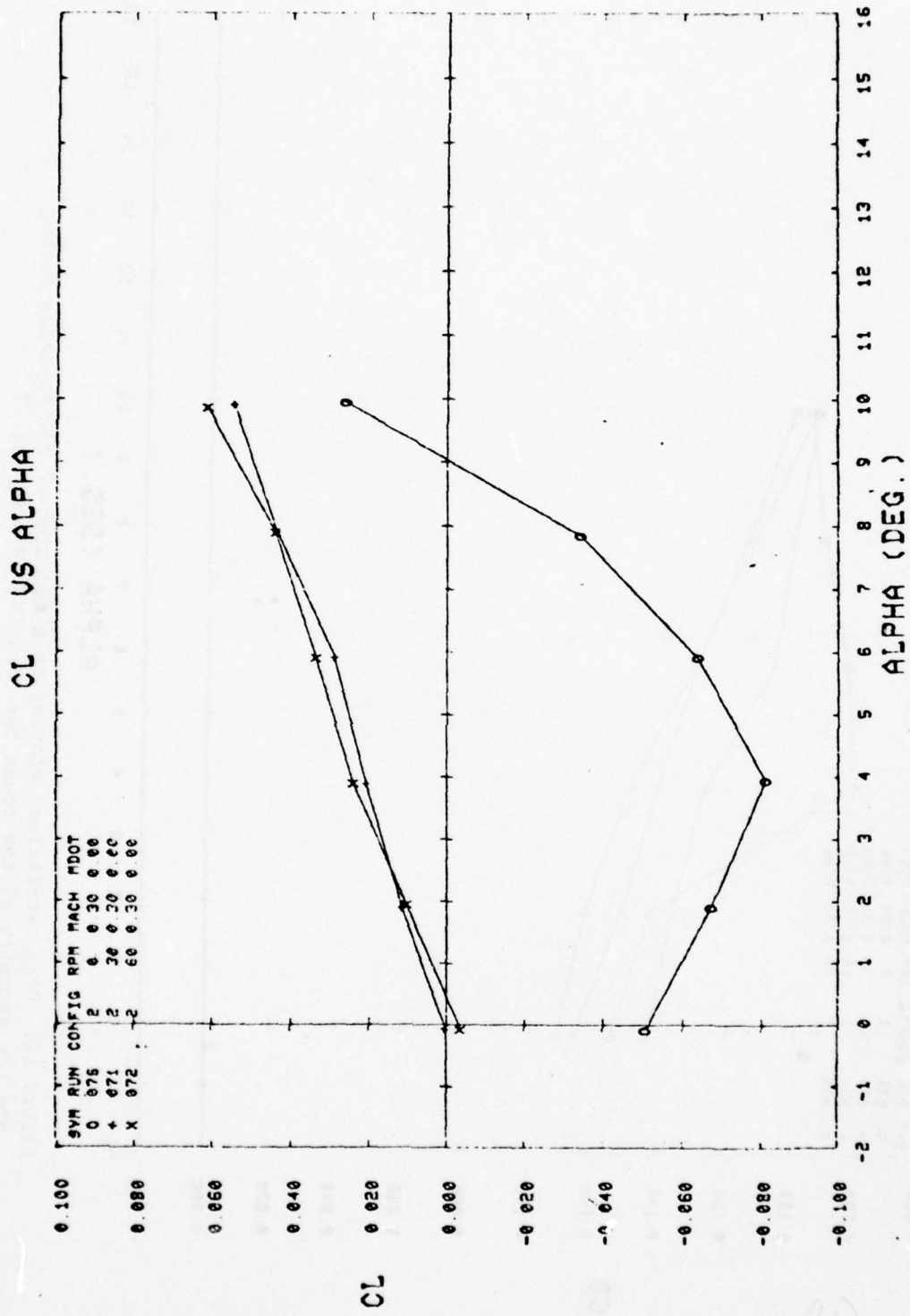


Figure 9. Lift coefficient as determined from the normal and axial force coefficient obtained from the balance loads for Runs 71, 72, and 76.

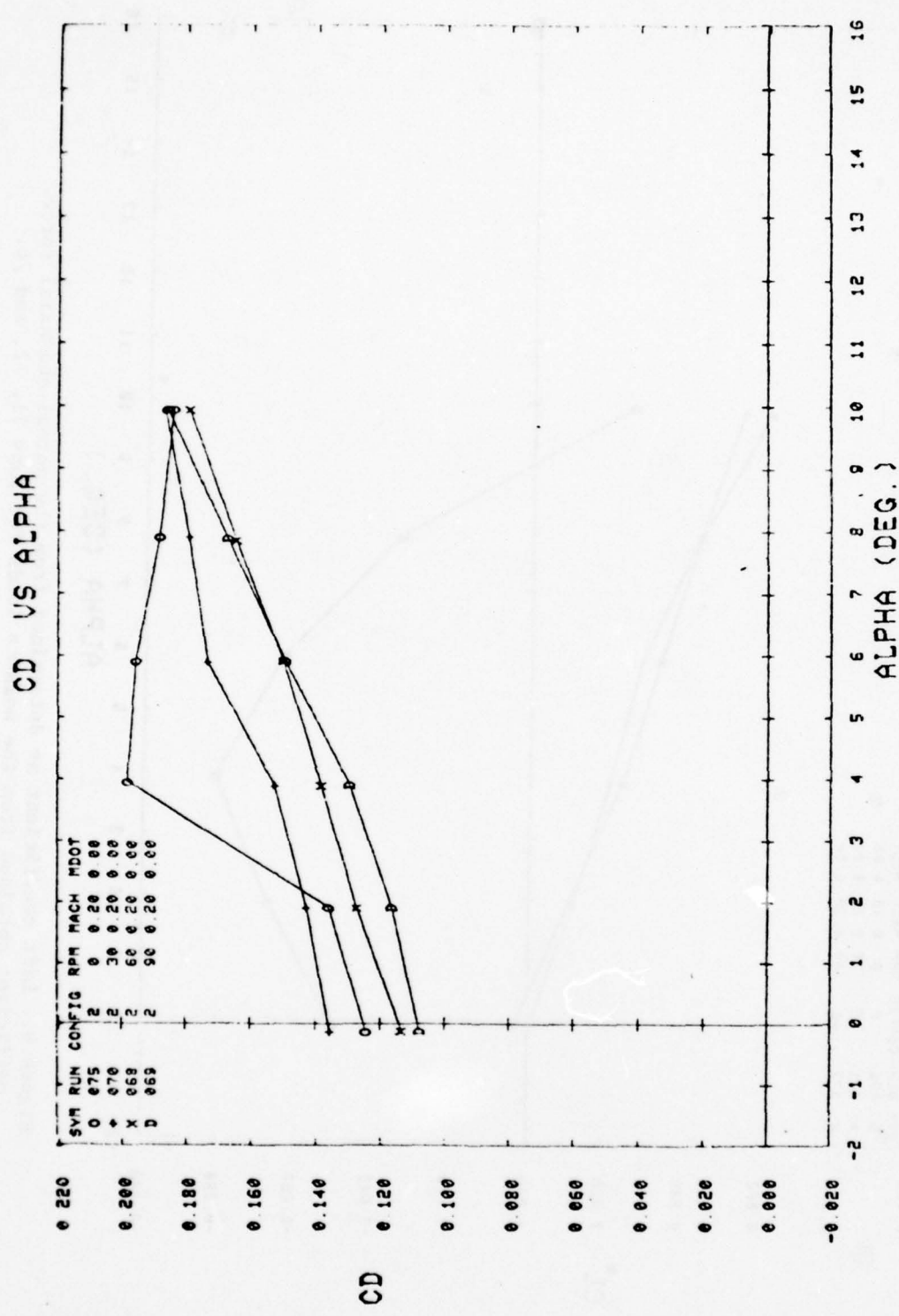


Figure 10. Drag coefficient plotted as a function of the Reynolds number and the geometry of the round for Runs 68, 69, 70, and 75.

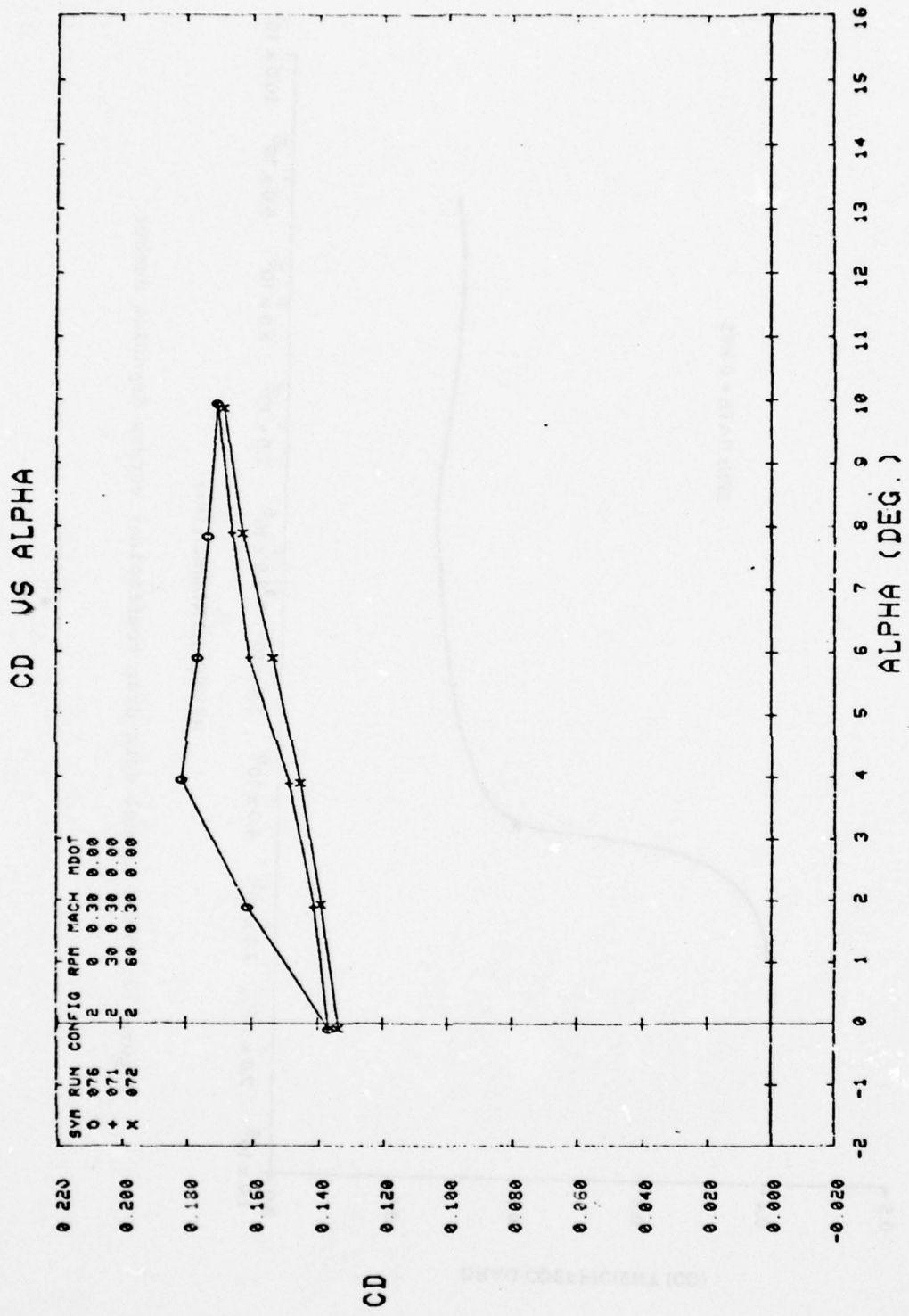


Figure 11. Drag coefficient plotted as a function of the Reynolds number and the geometry of the round for Runs 71, 72, and 76.

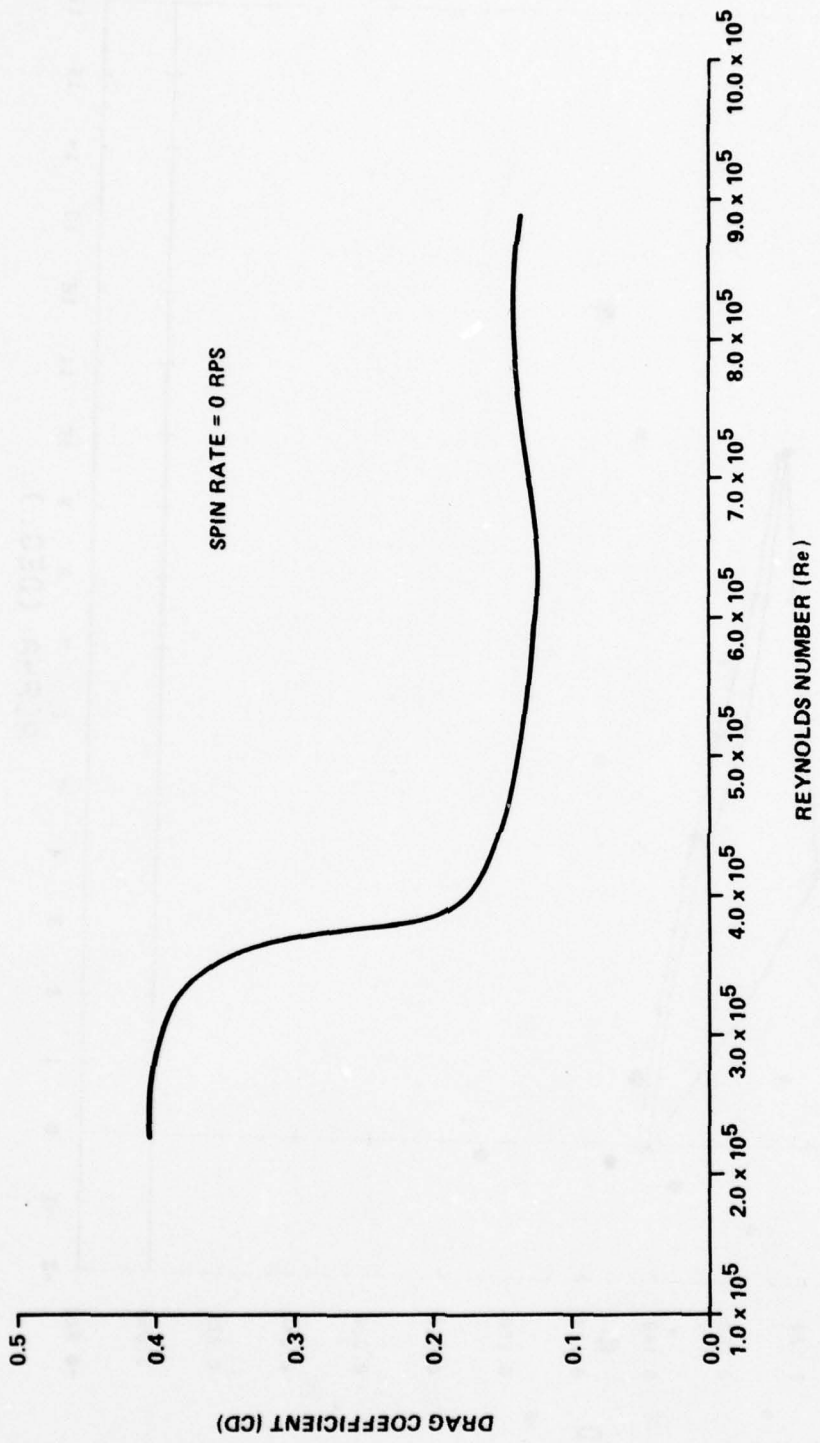


Figure 12. Wind tunnel data drag coefficient versus Reynolds number.

**Appendix A. PLOTS OF AERODYNAMIC COEFFICIENTS  
VERSUS ALPHA \***

---

**\*NOTE: RPM should be read RPS on all figures.**

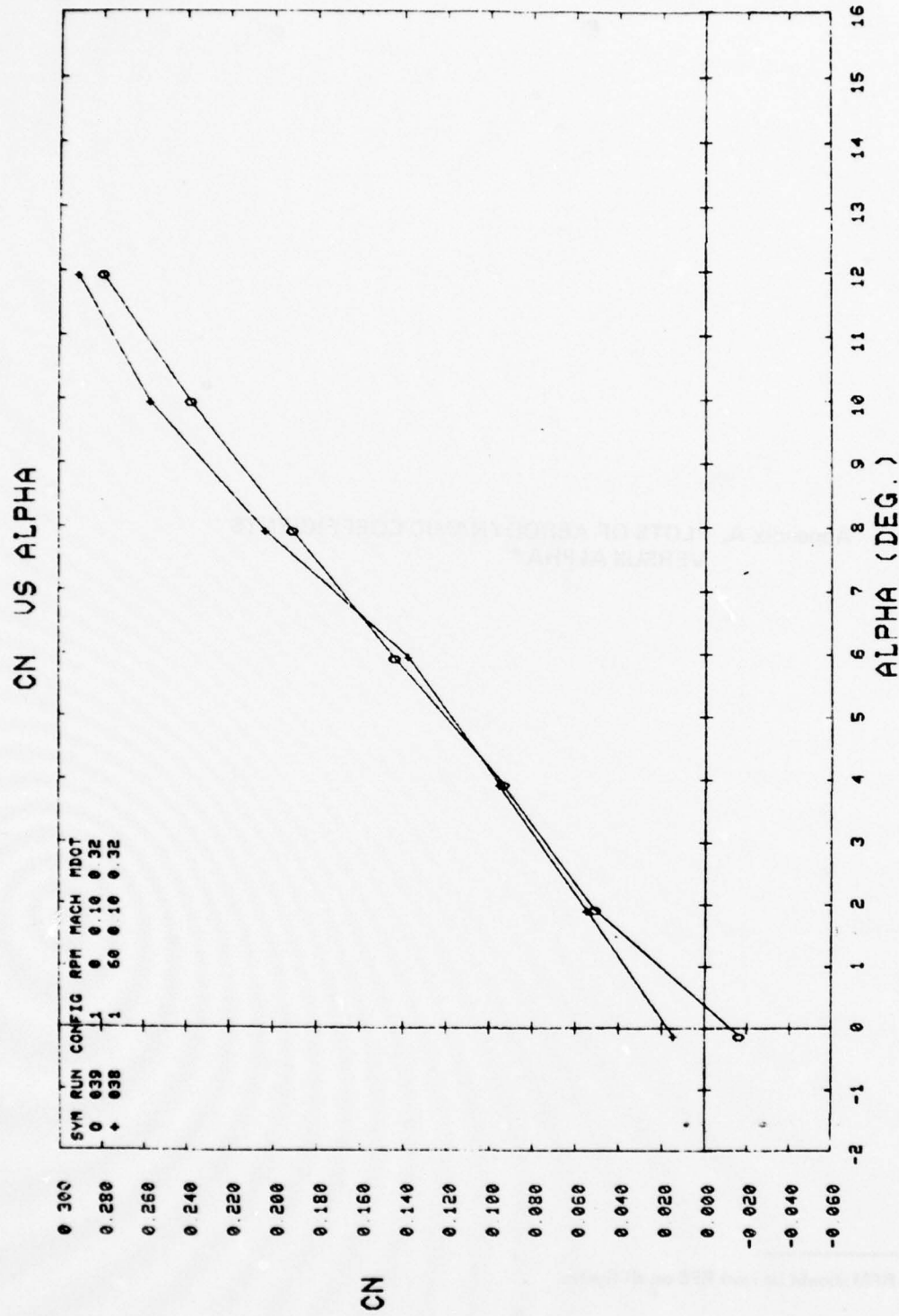


Figure A-1. Configuration 1 — aerodynamic coefficients versus alpha with varying spin rates.

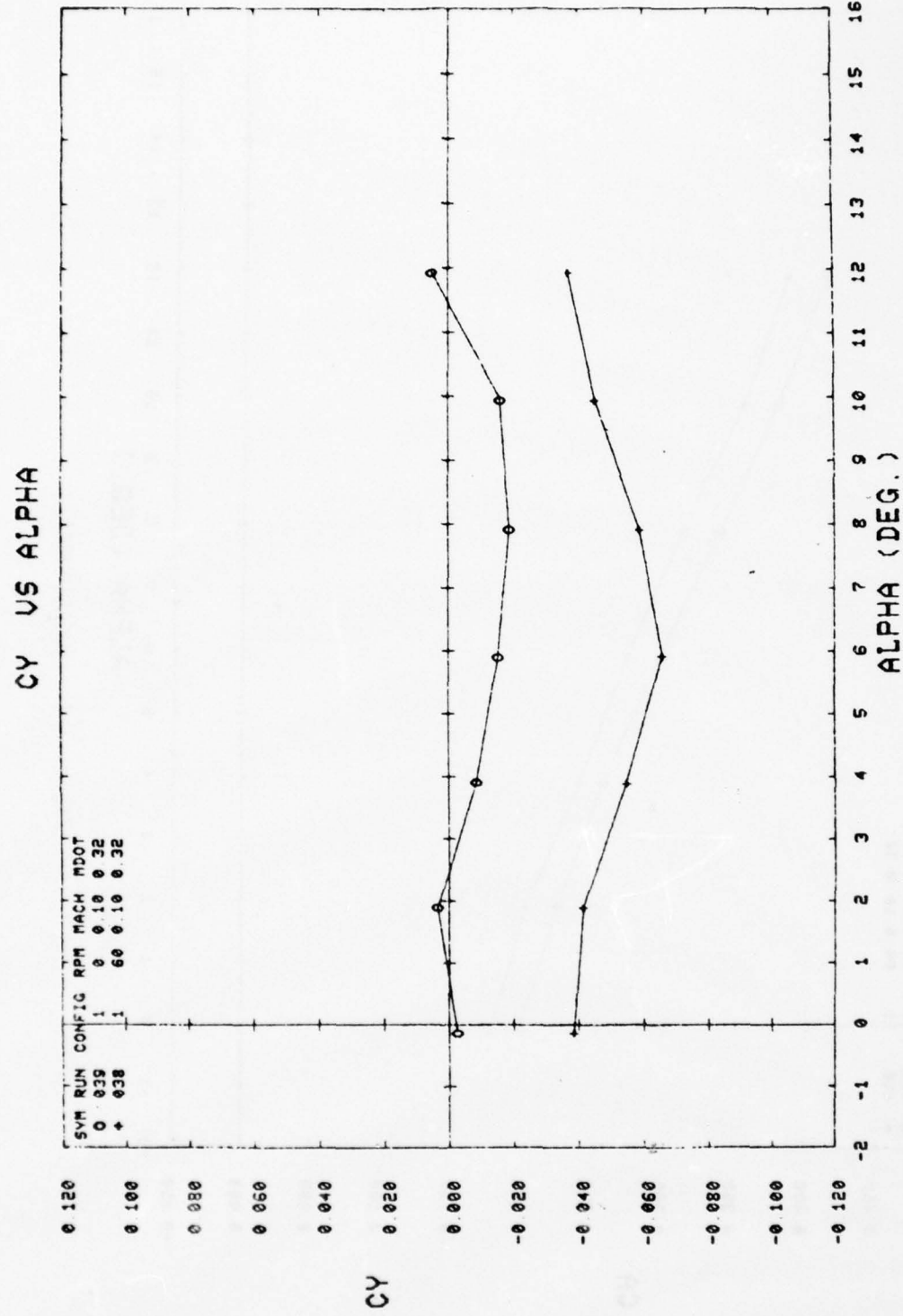


Figure A-1. (Continued).

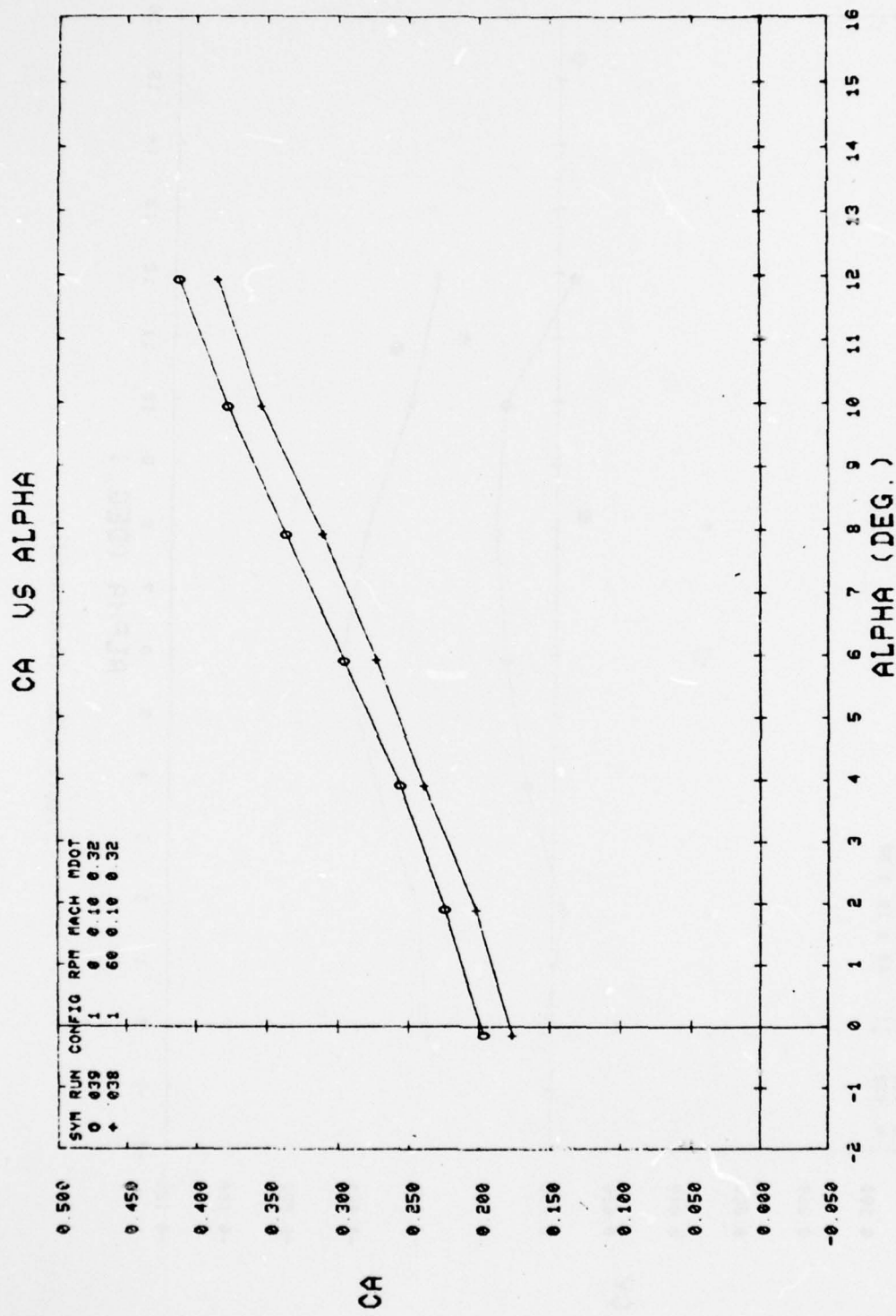


Figure A-1. (Continued).

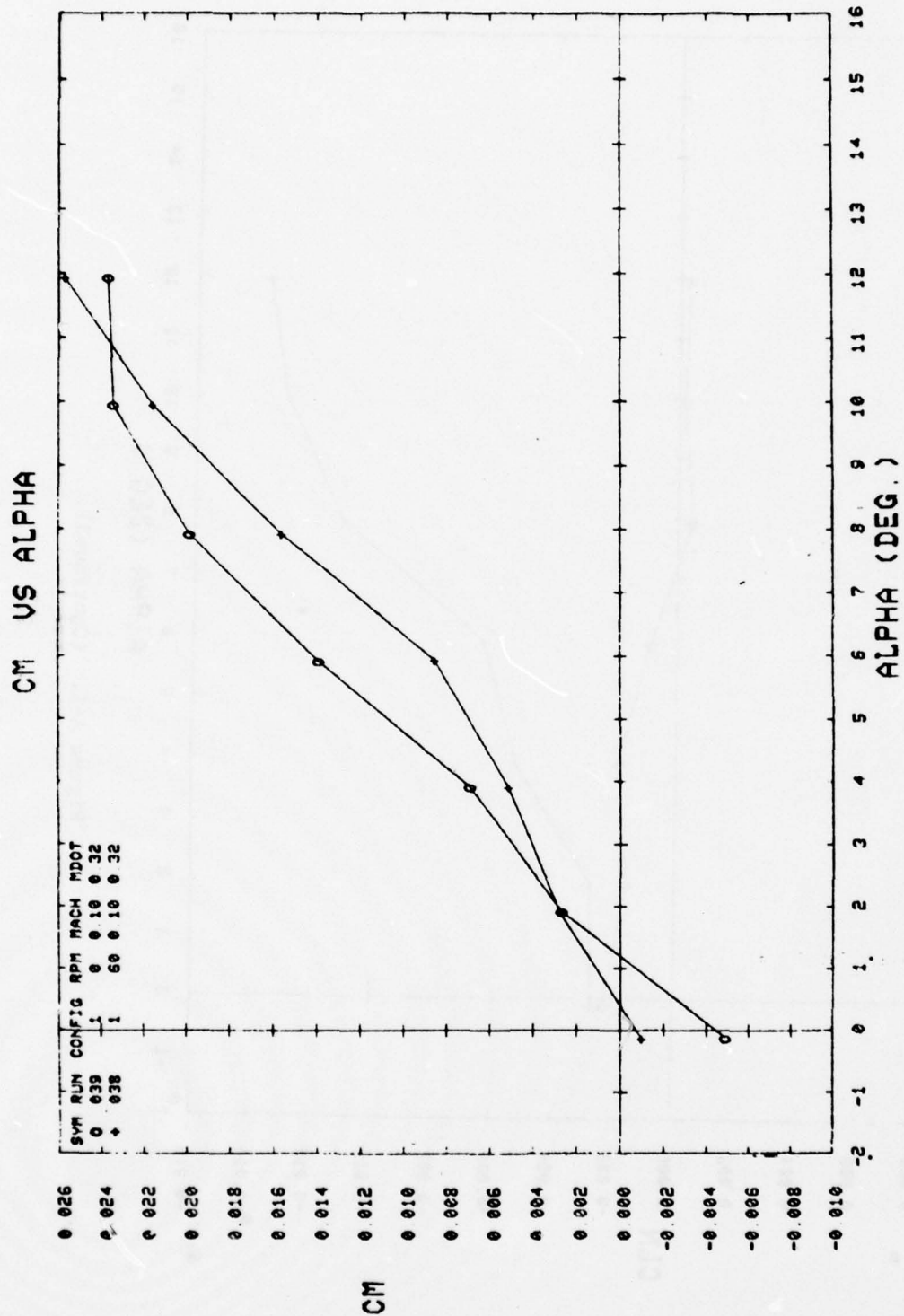


Figure A-1. (Continued).

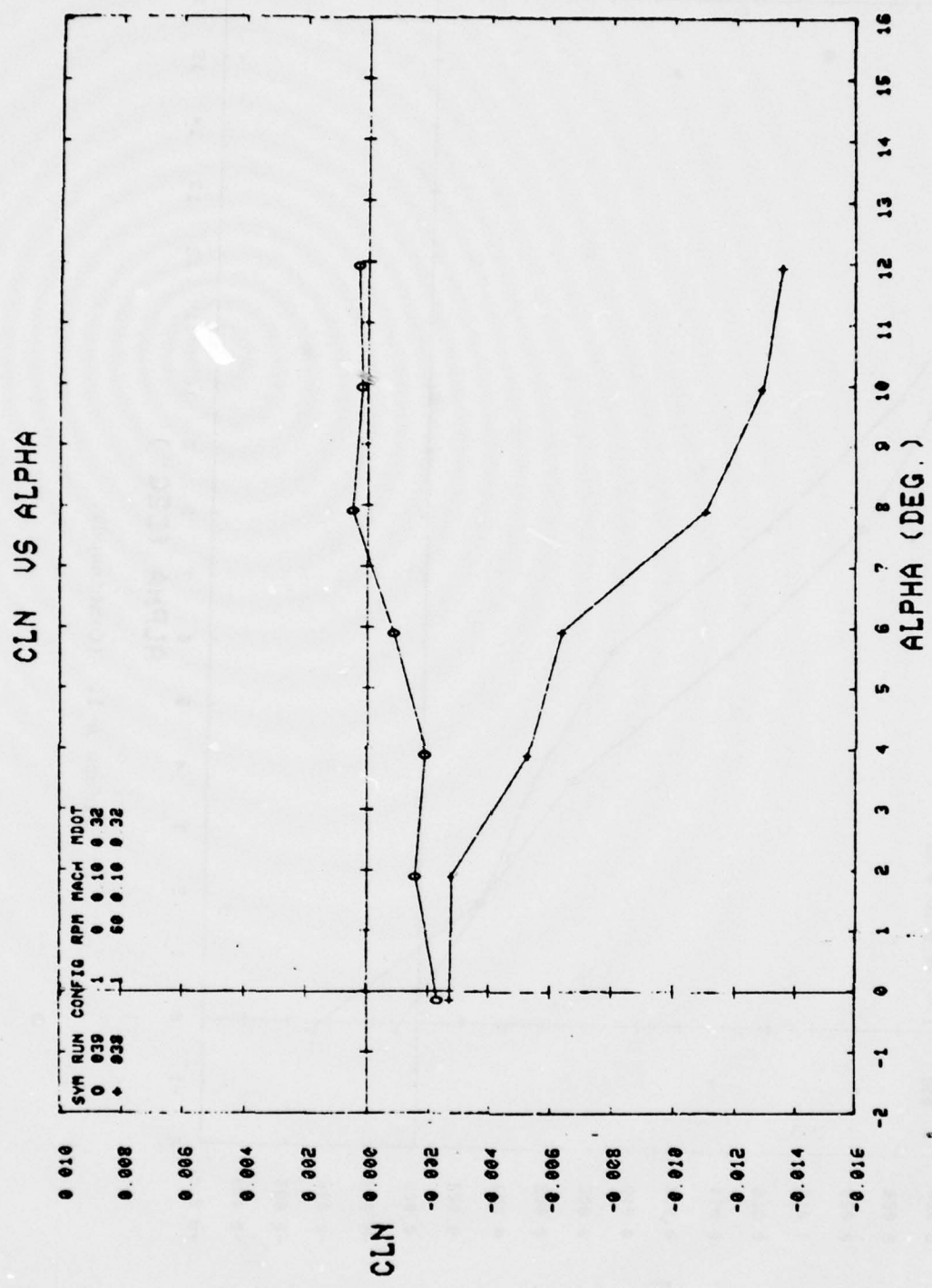


Figure A-1. (Continued).

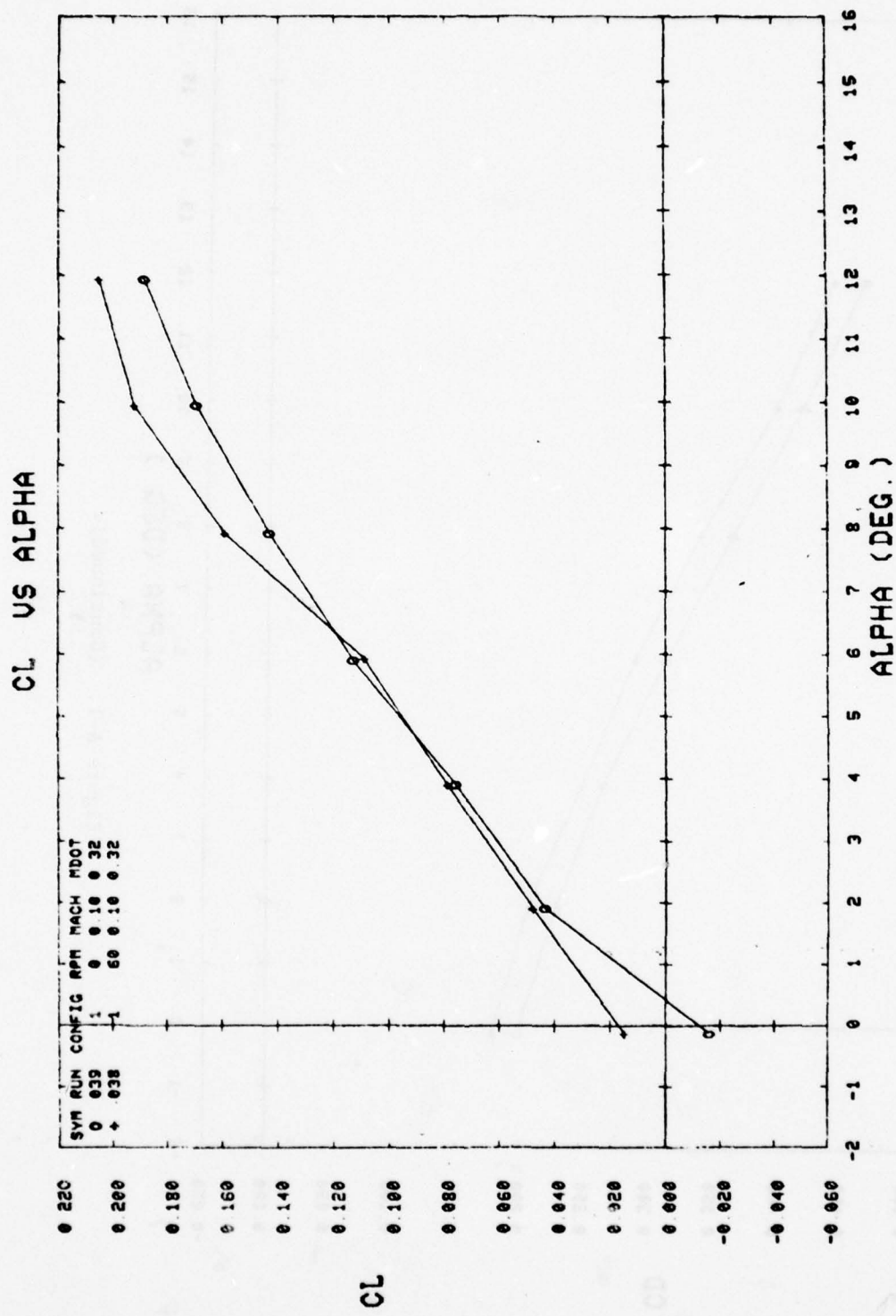


Figure A-1. (Continued).

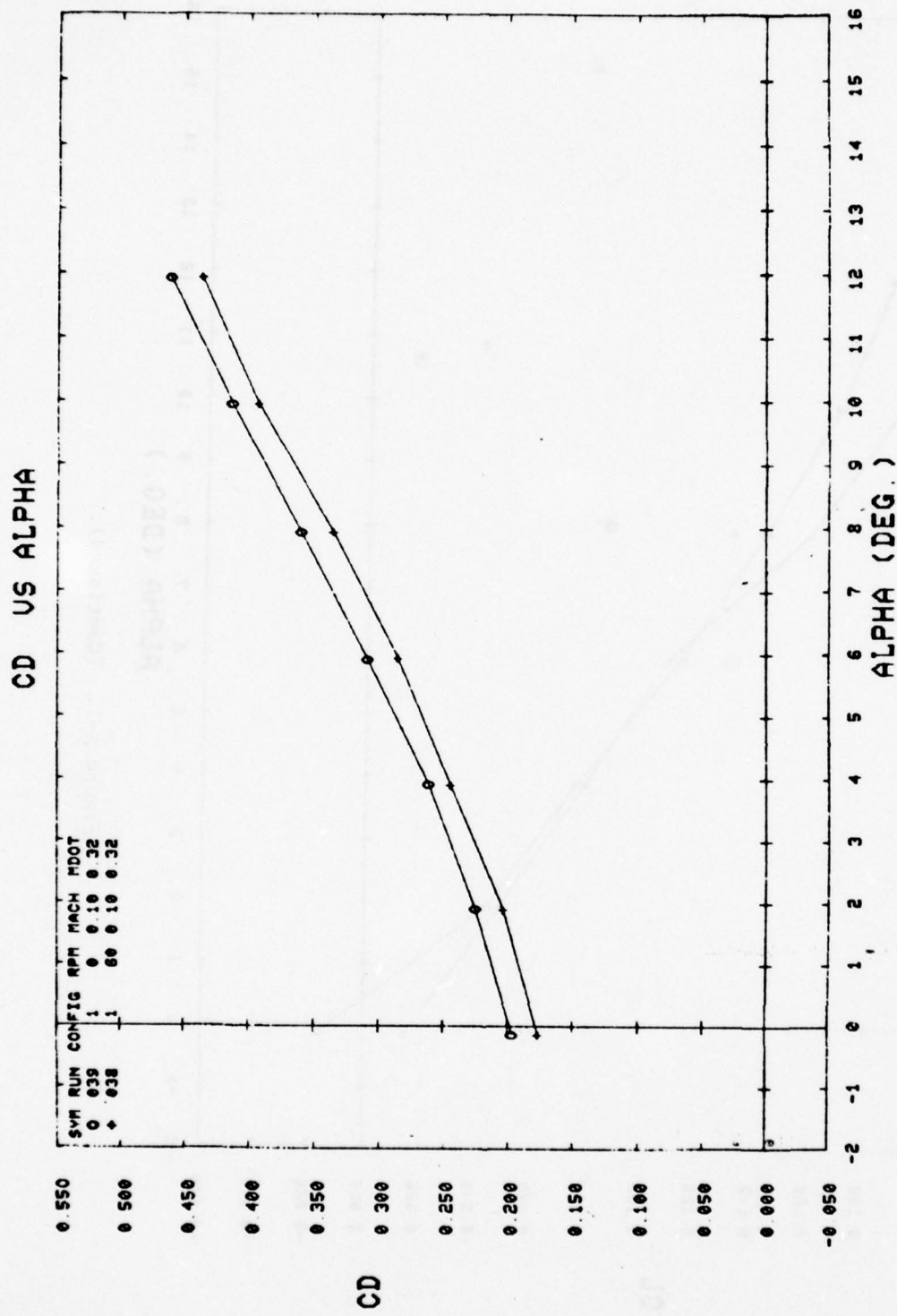


Figure A-1. (Continued).

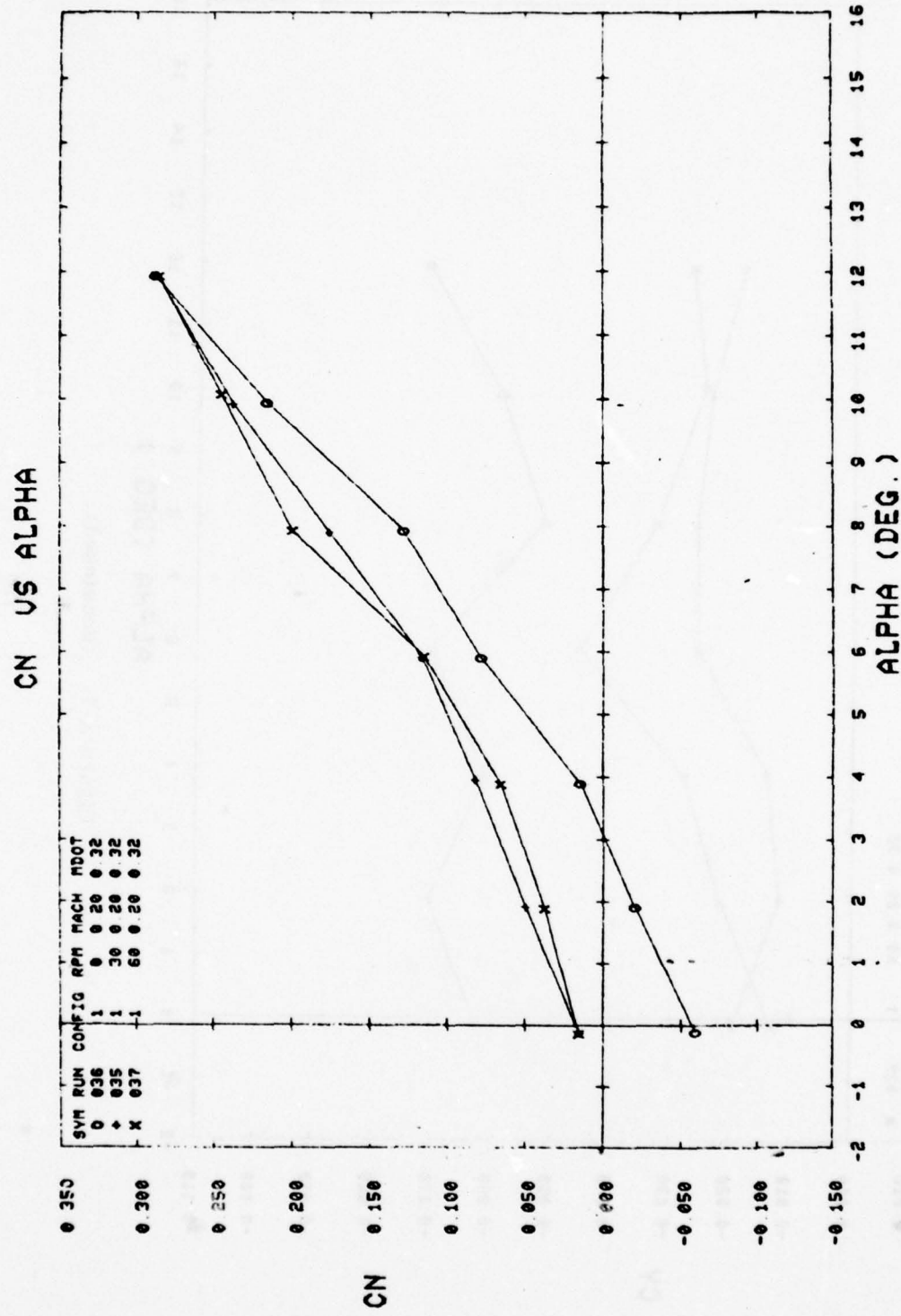


Figure A-1. (Continued).

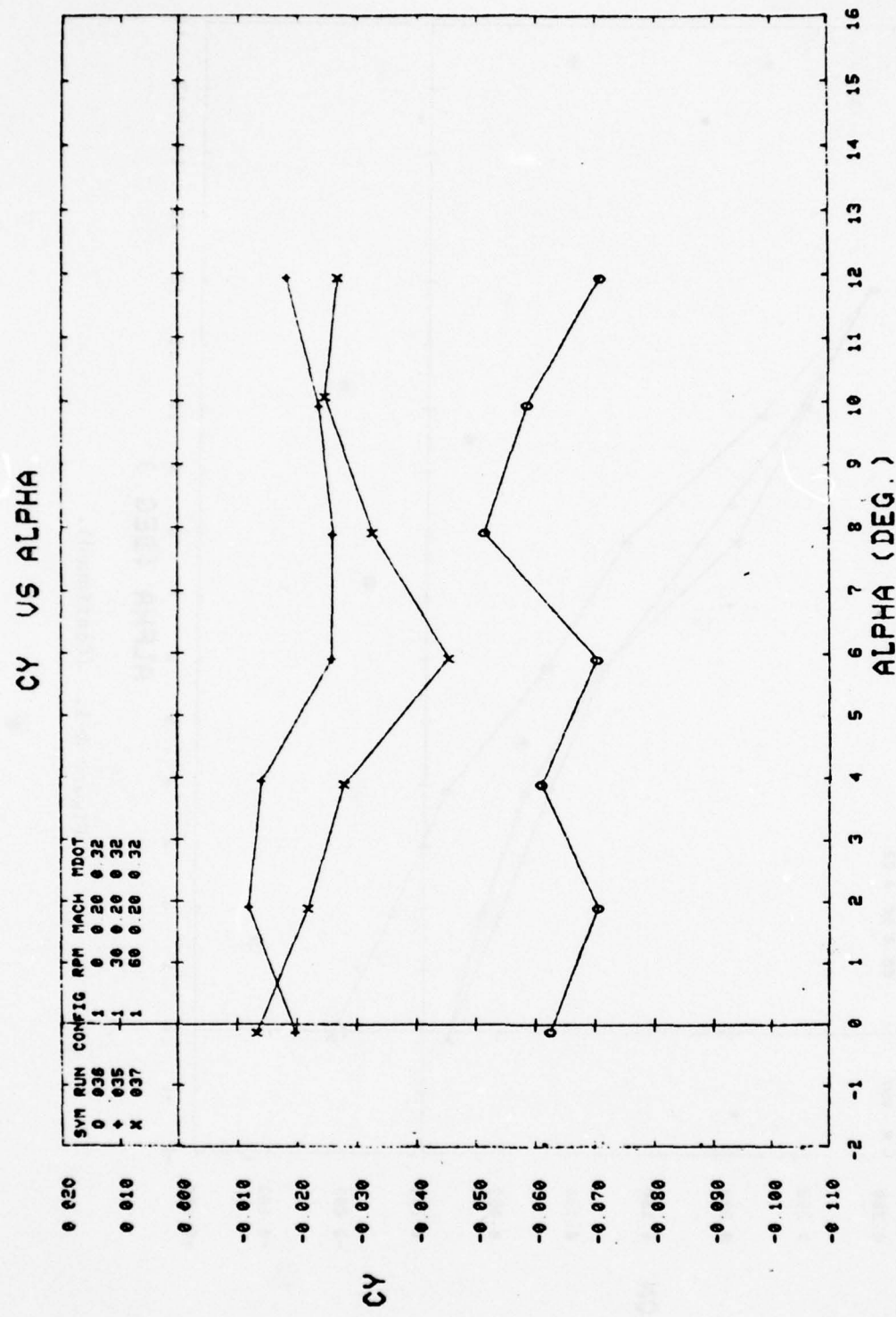


Figure A-1. (Continued).

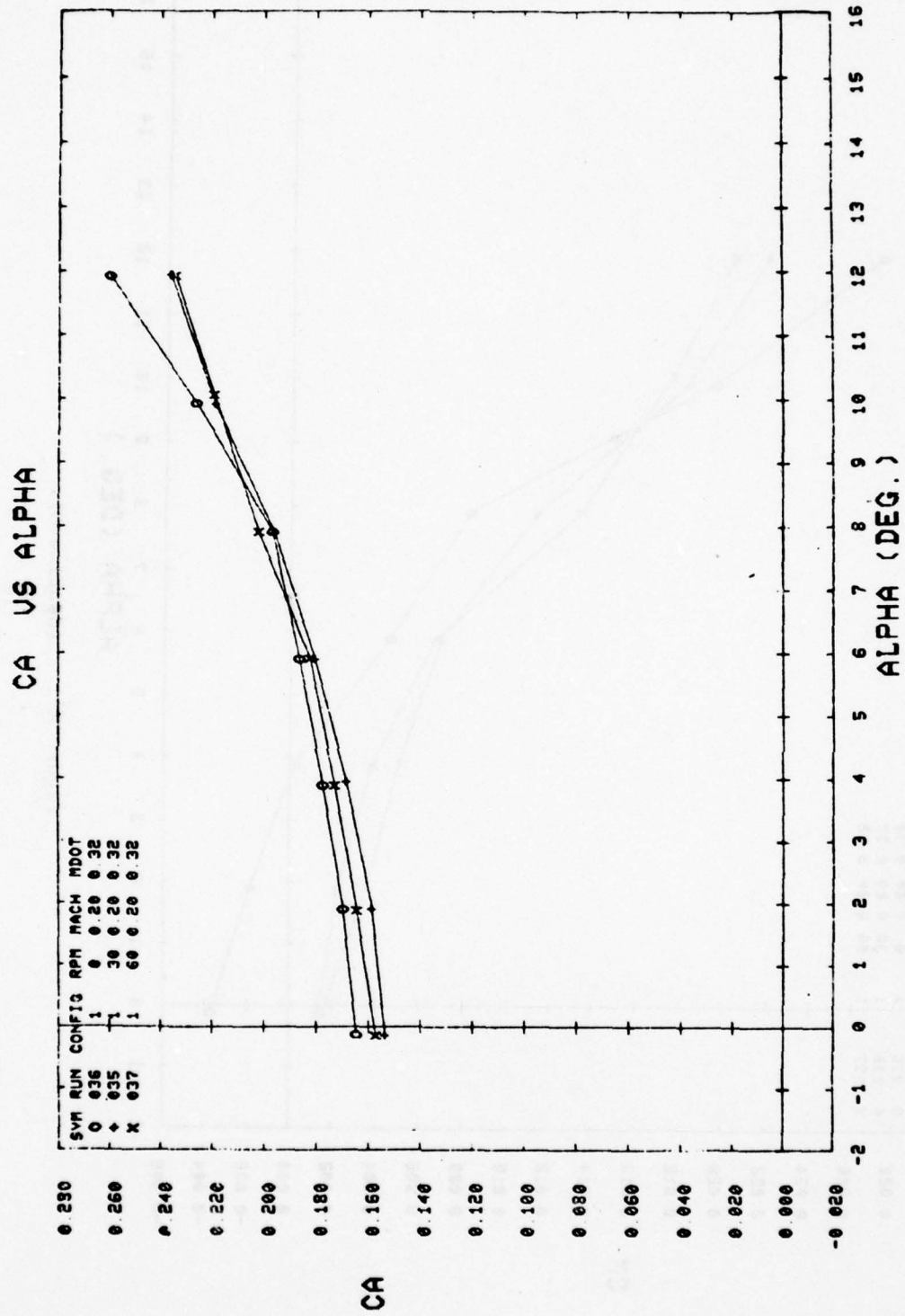


Figure A-1. (Continued).

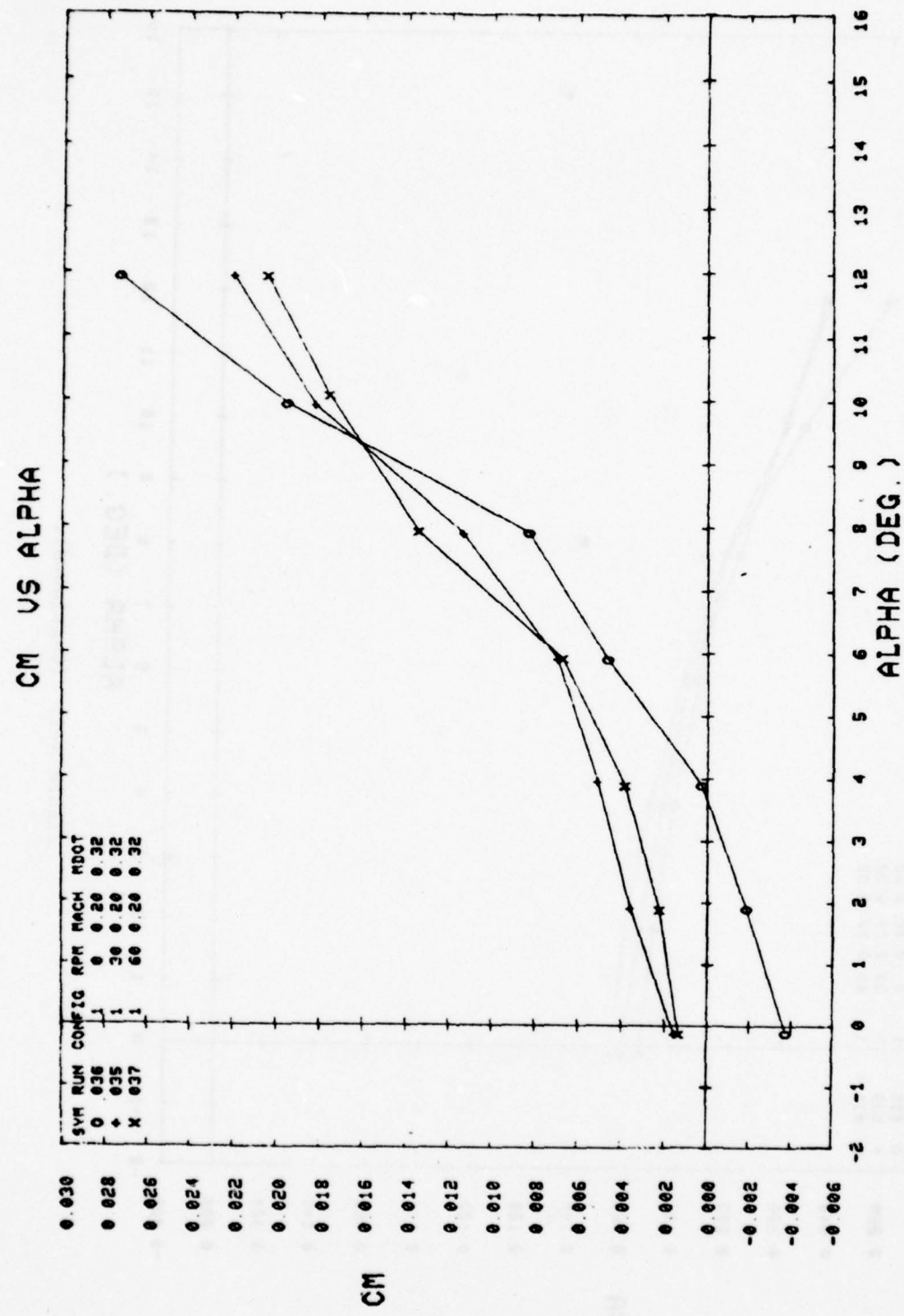


Figure A-1. (Continued).

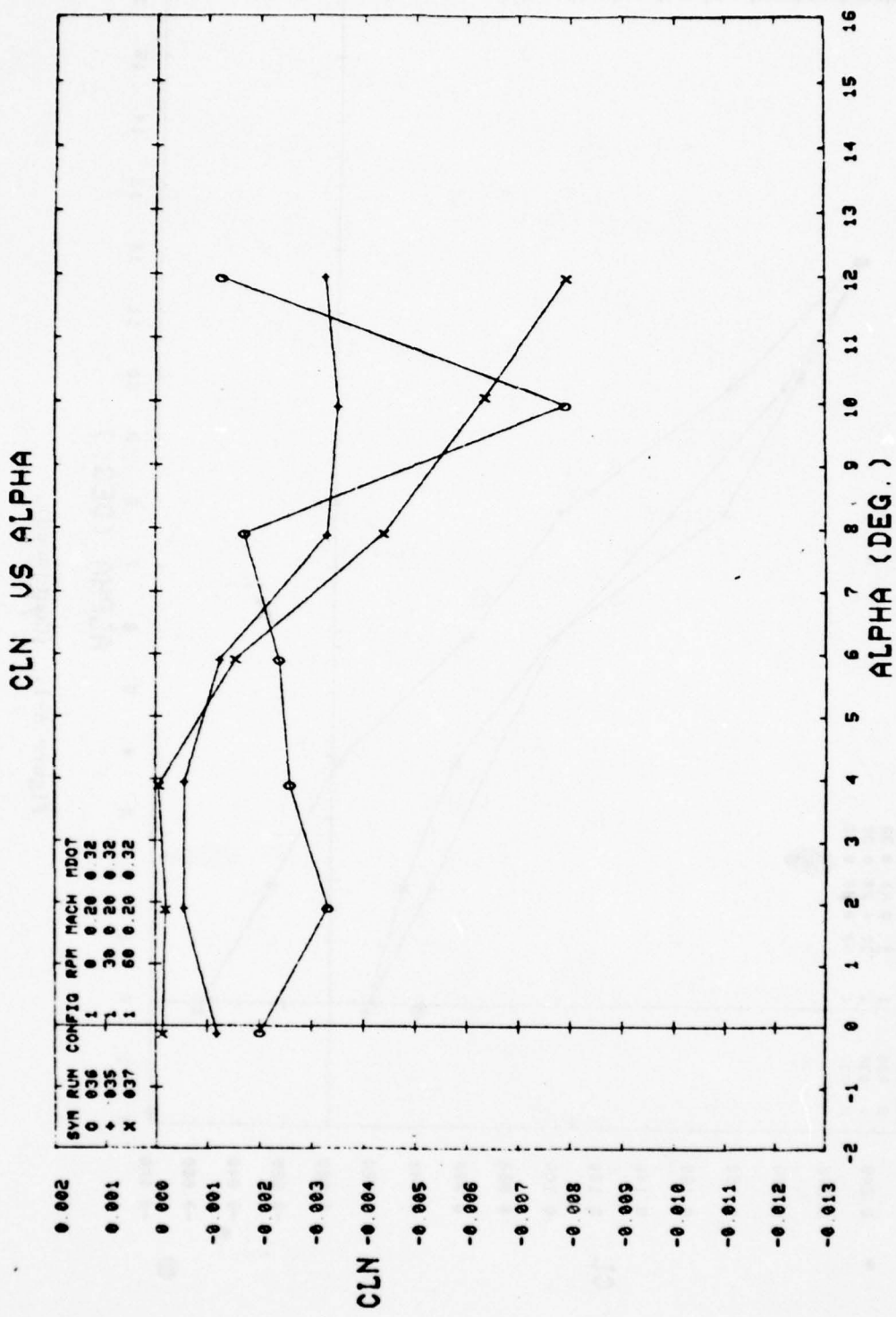


Figure A-1. (Continued).

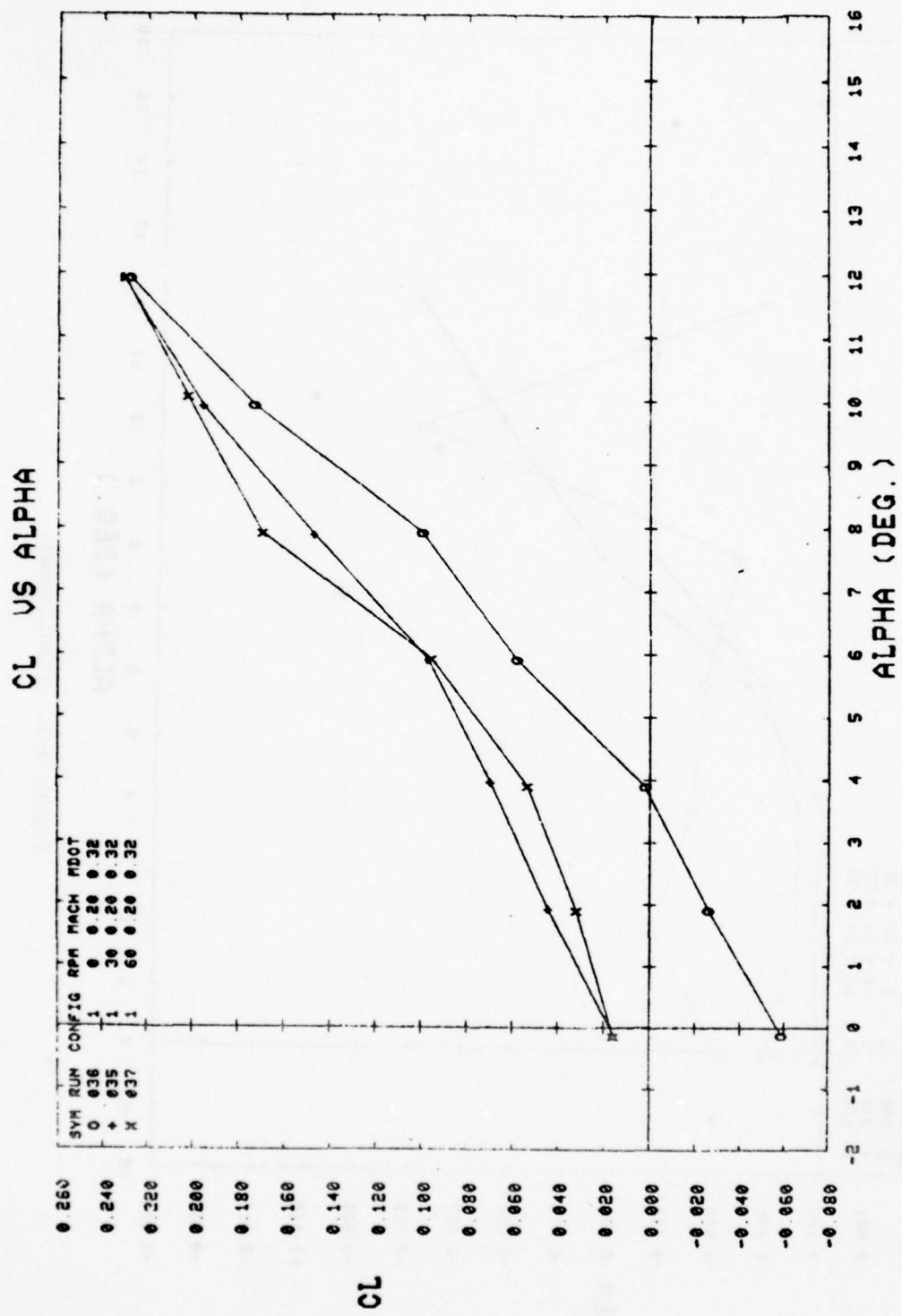


Figure A-1. (Continued).

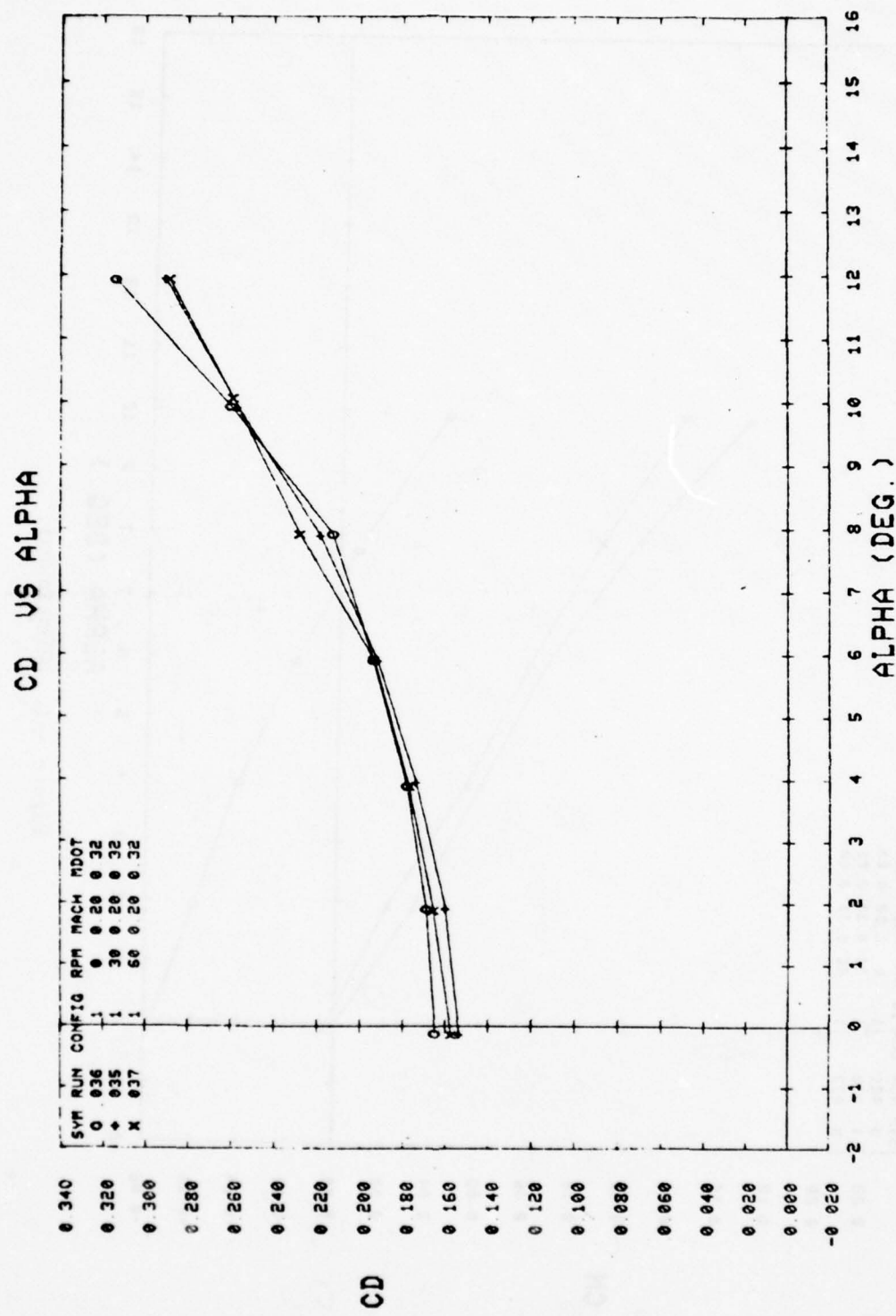


Figure A-1. (Continued).

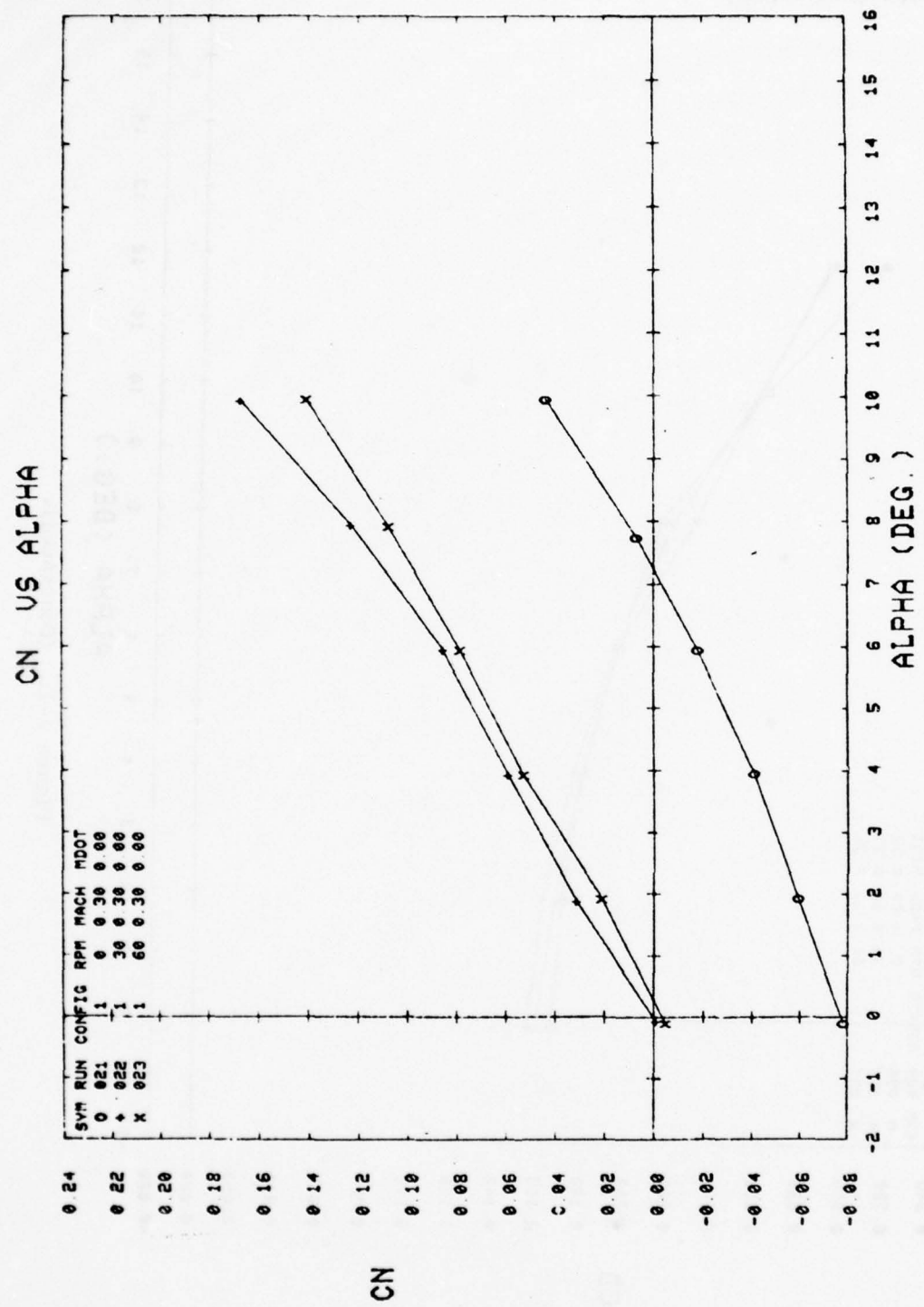


Figure A-1. (Continued).

CY VS ALPHA

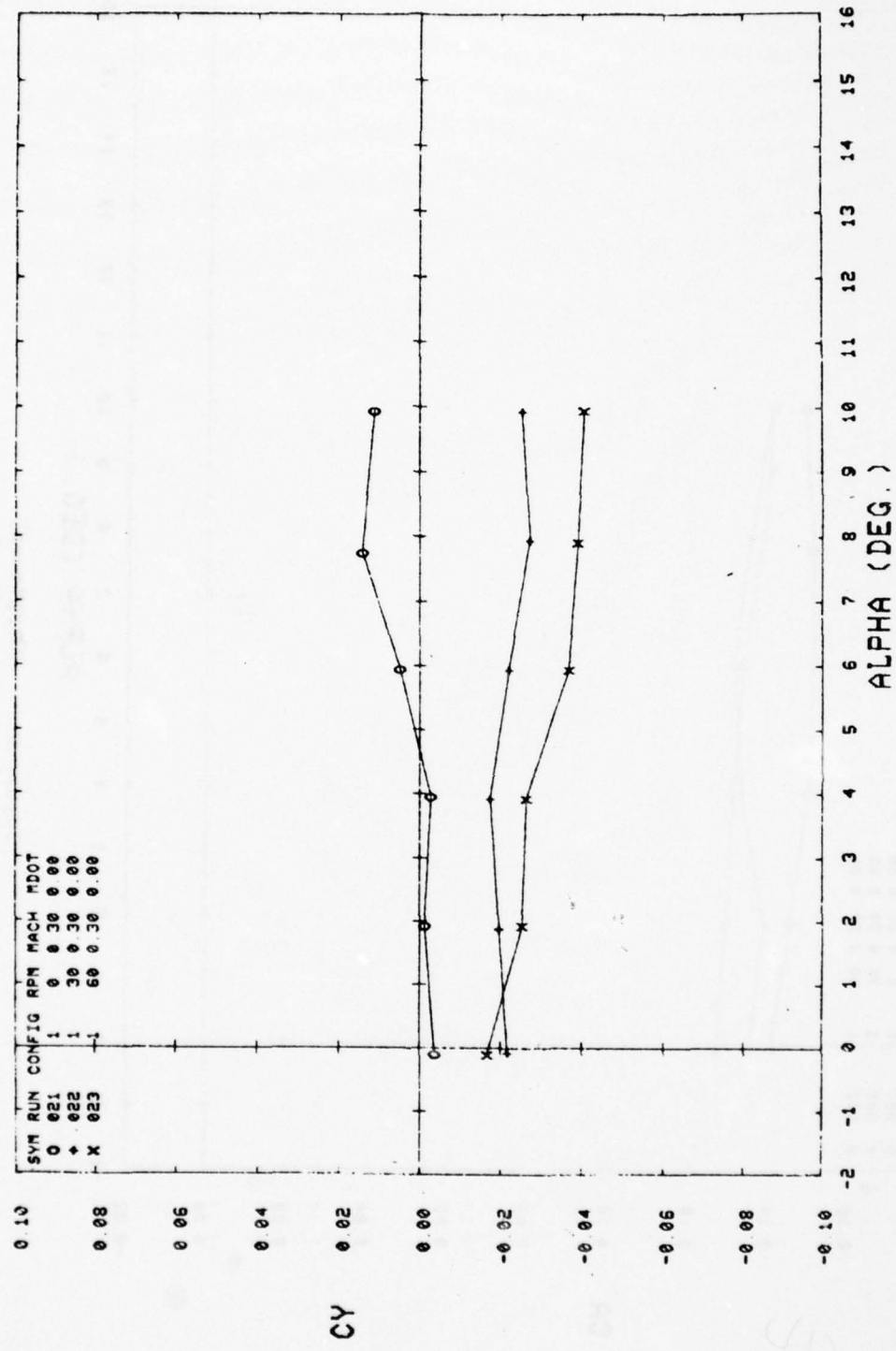


Figure A-1. (Continued).

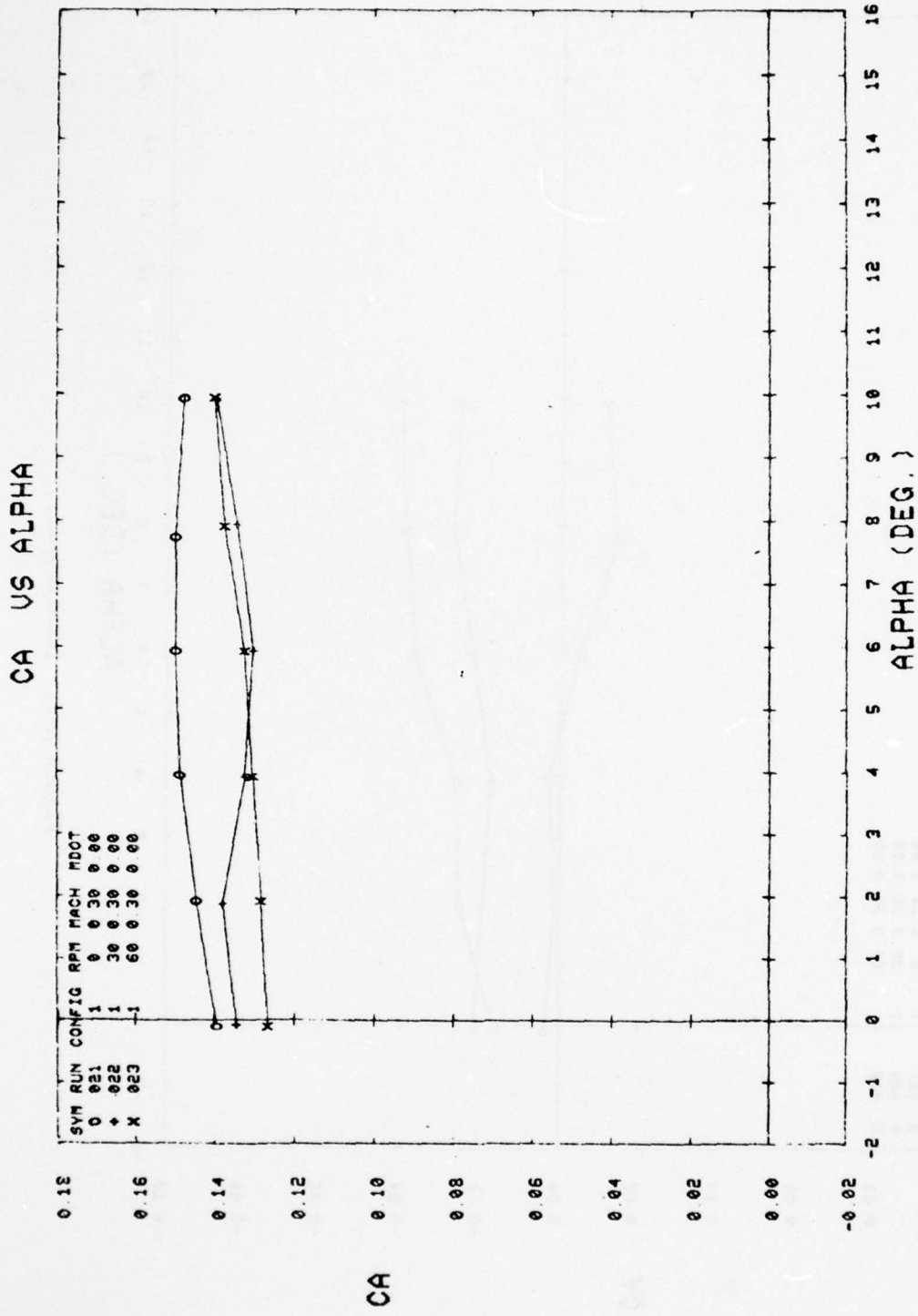


Figure A-1. (Continued).

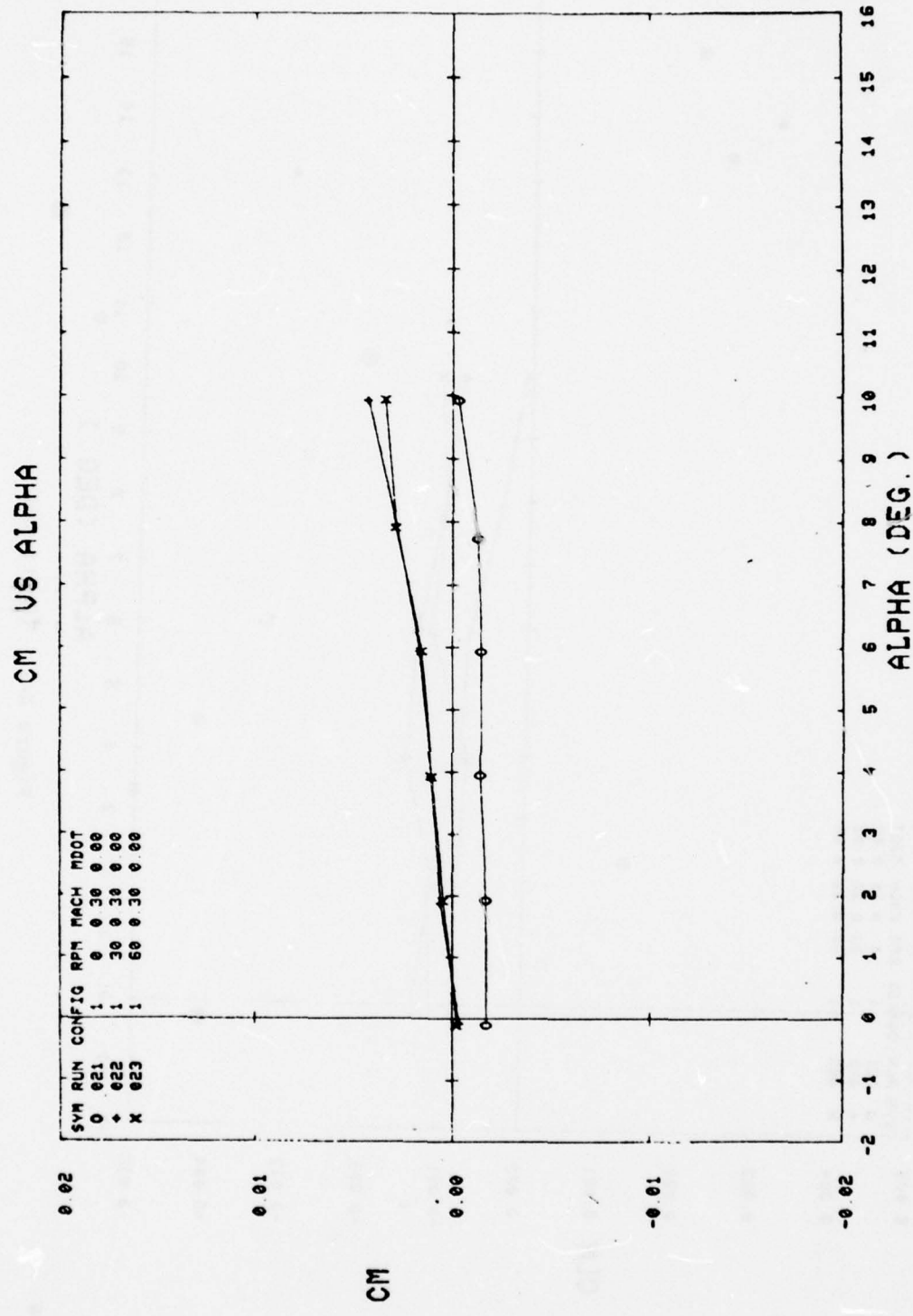


Figure A-1. (Continued).

CLN VS ALPHA

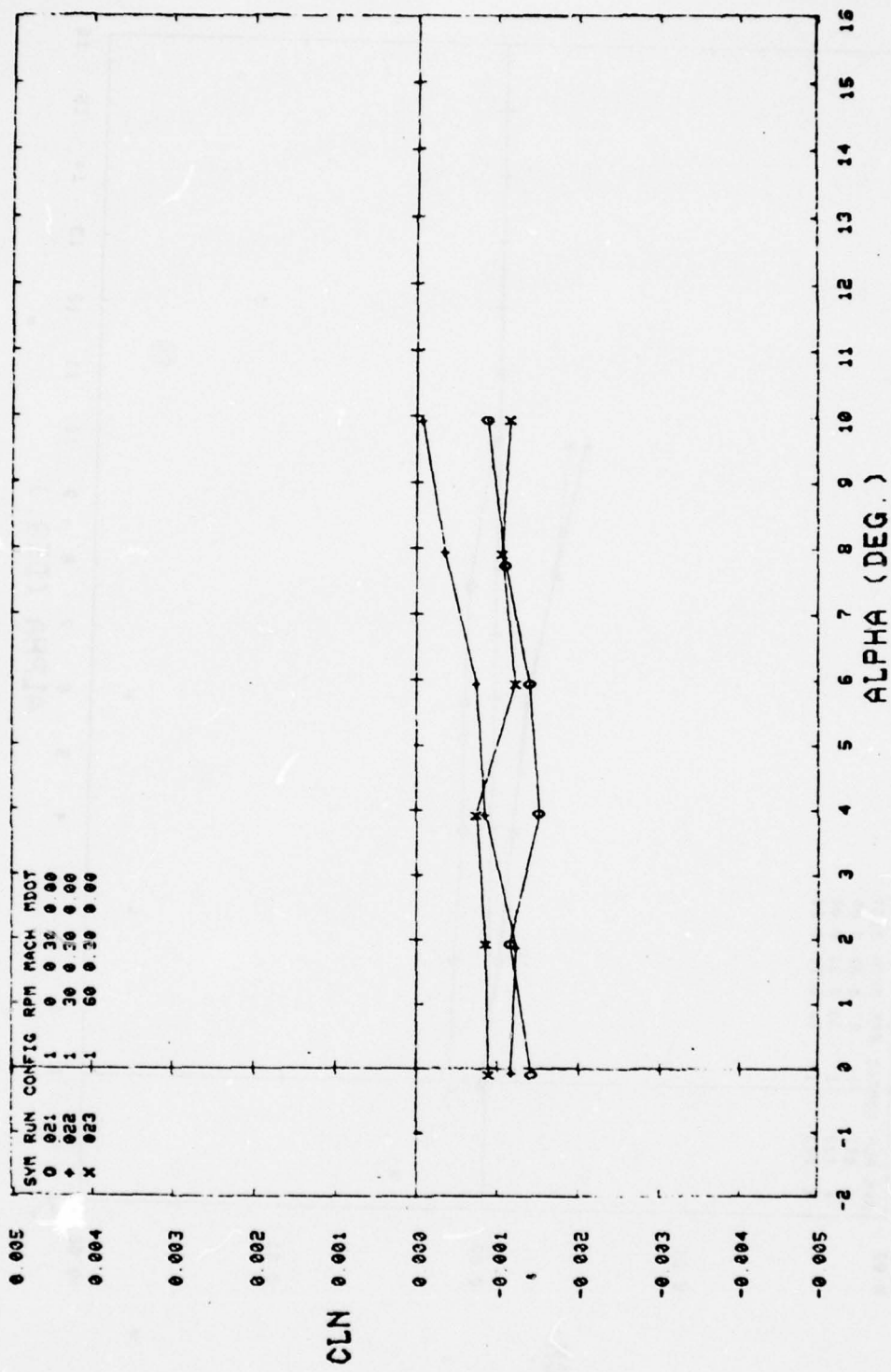


Figure A-1. (Continued).

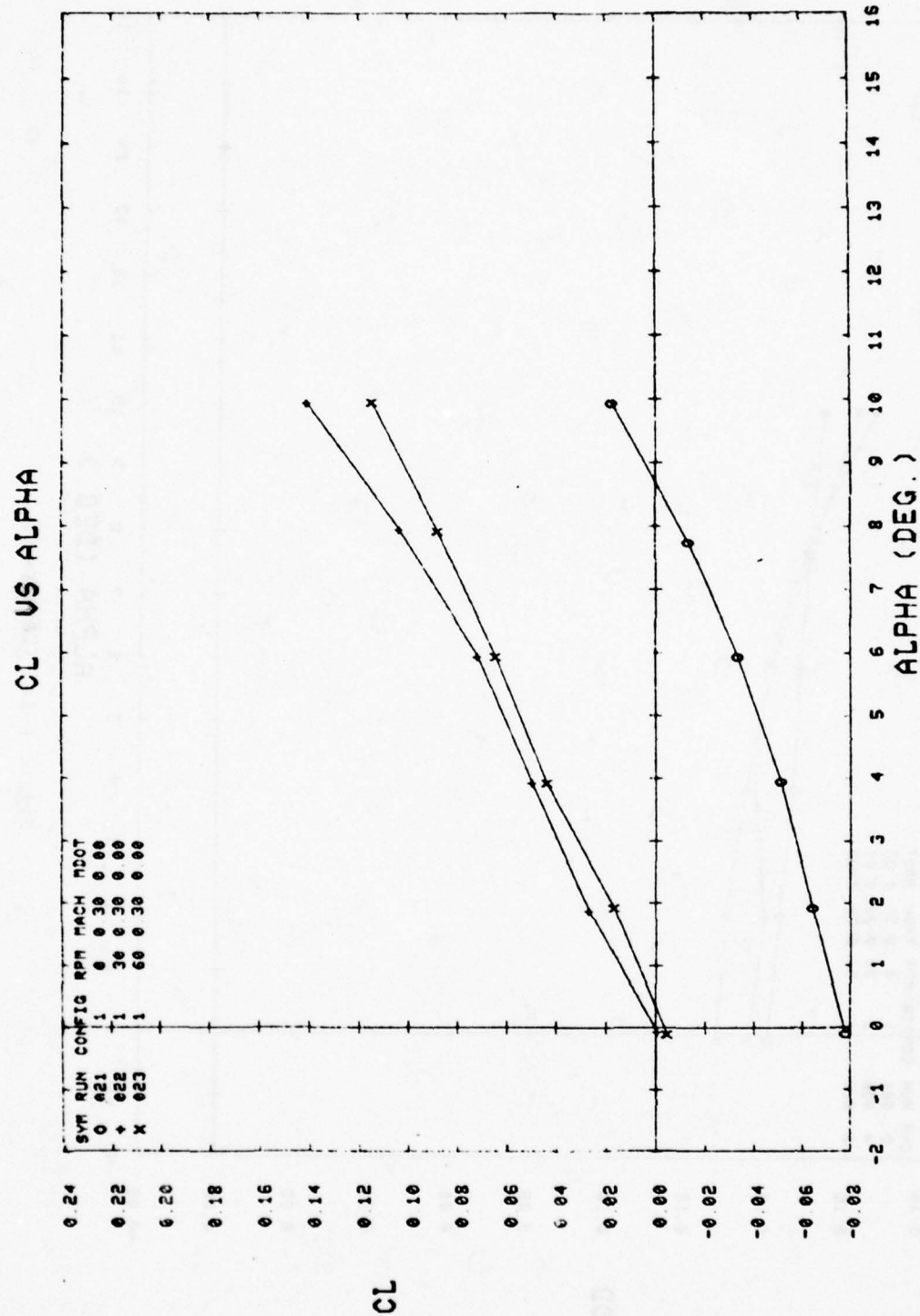


Figure A-1. (Continued).

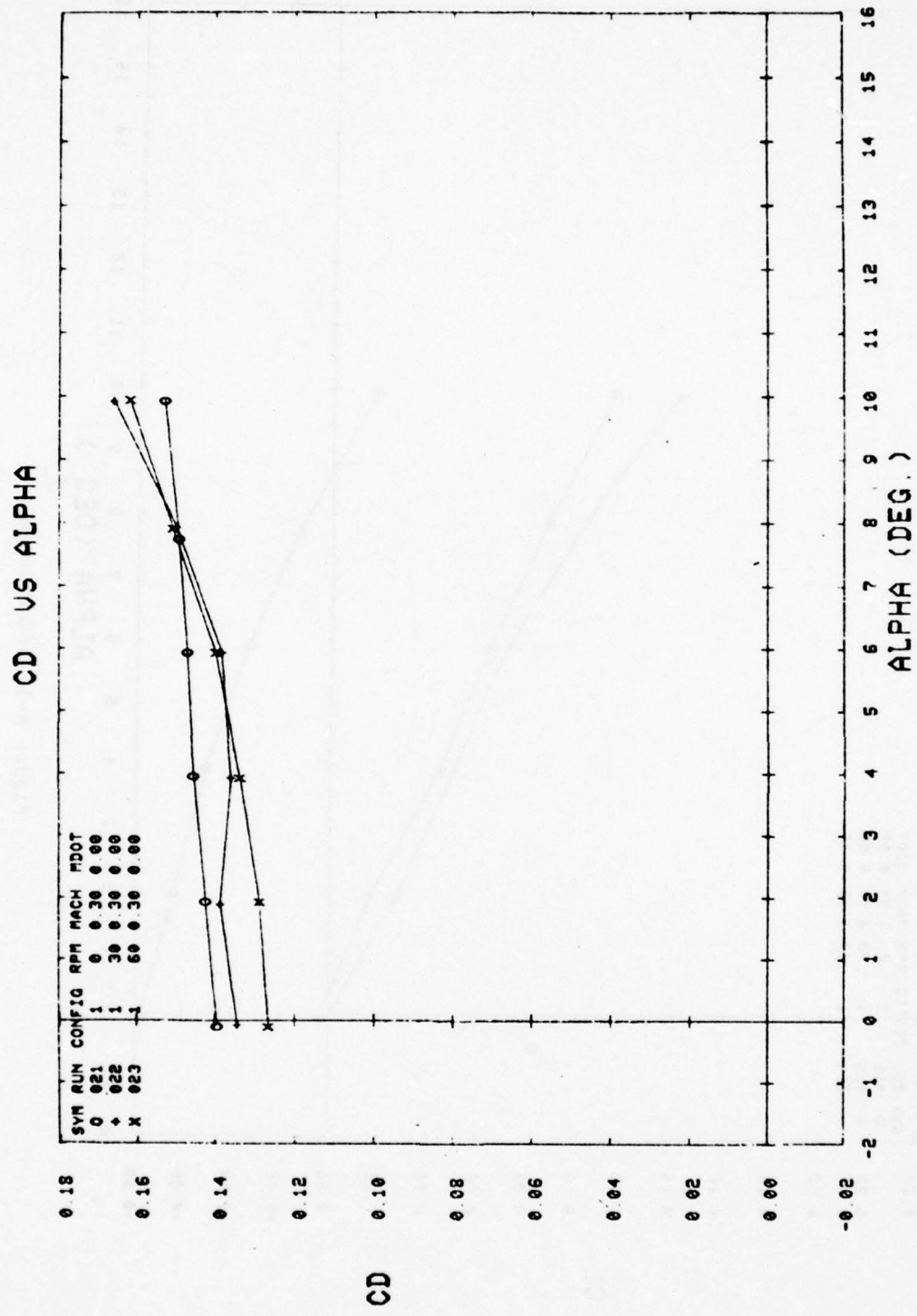


Figure A-1. (Continued).

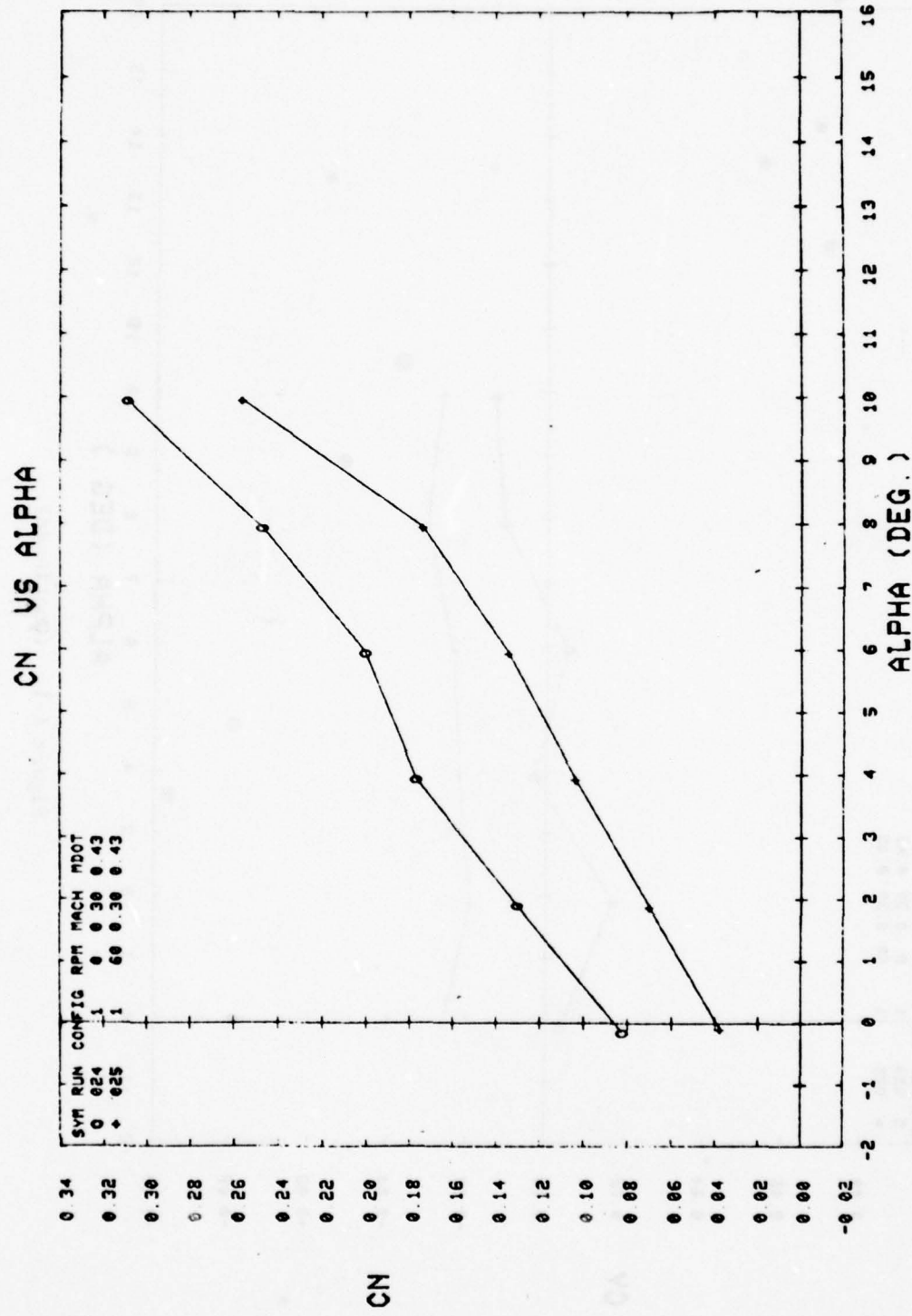


Figure A-1. (Continued).

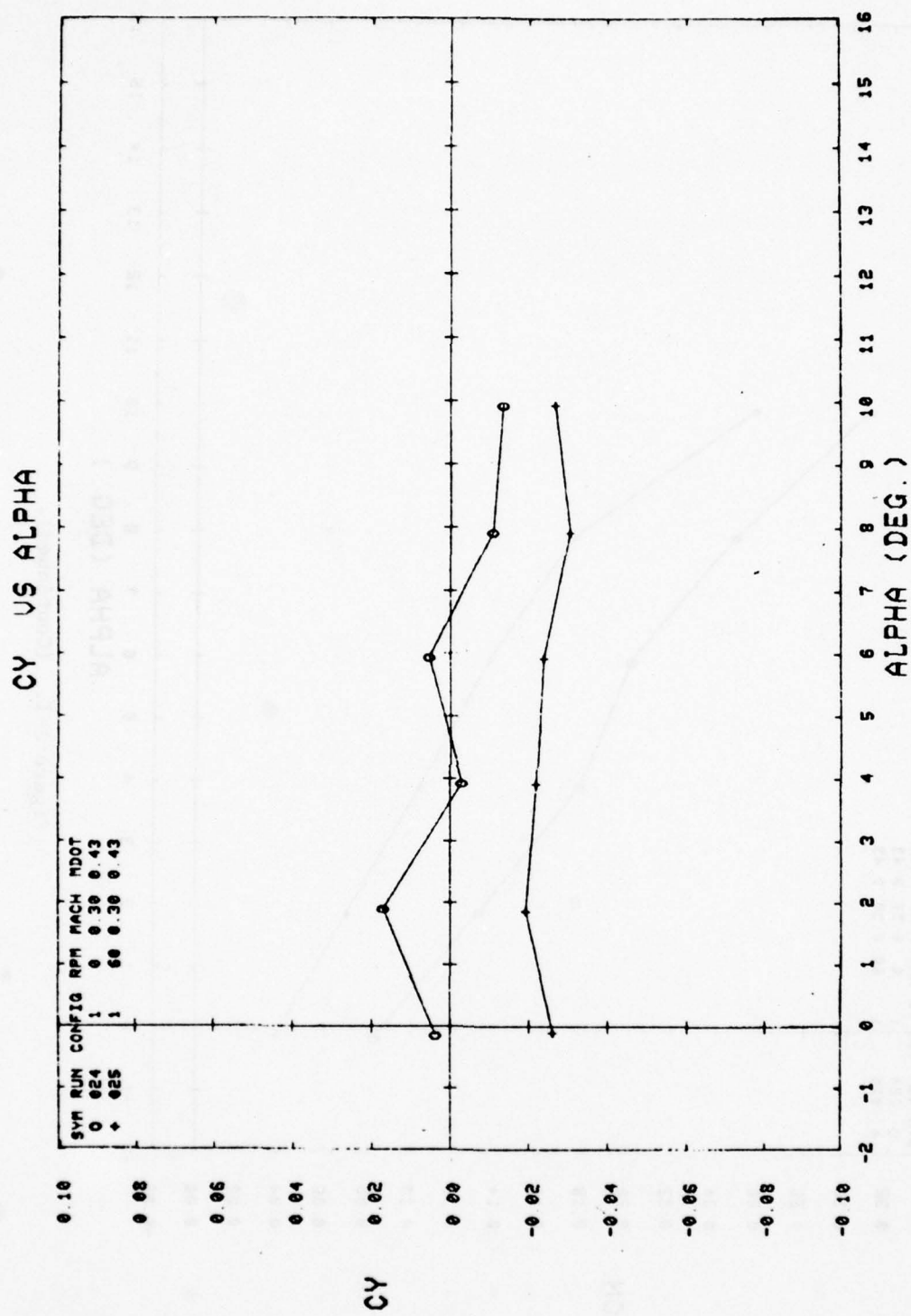


Figure A-1. (Continued).

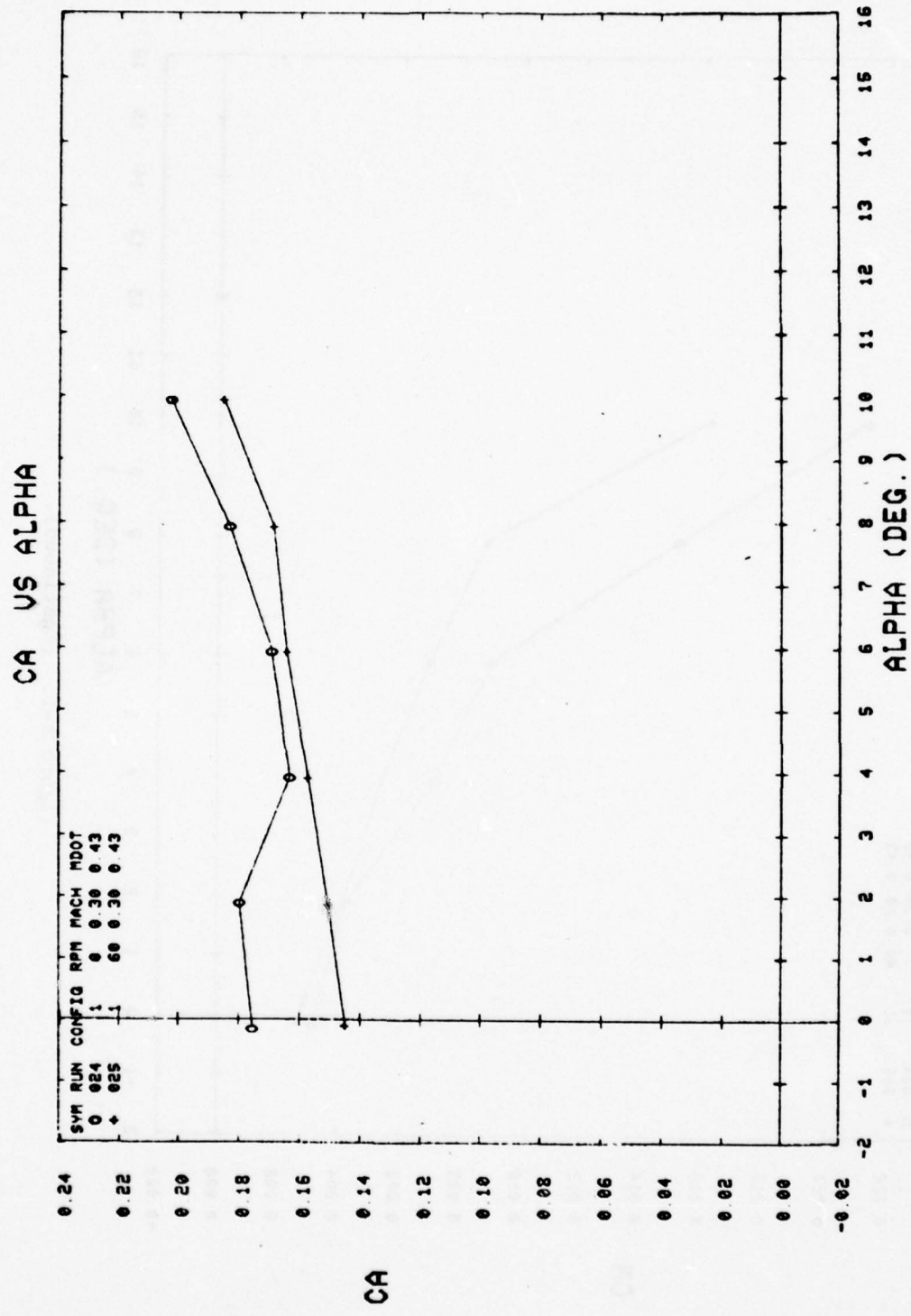


Figure A-1. (Continued).

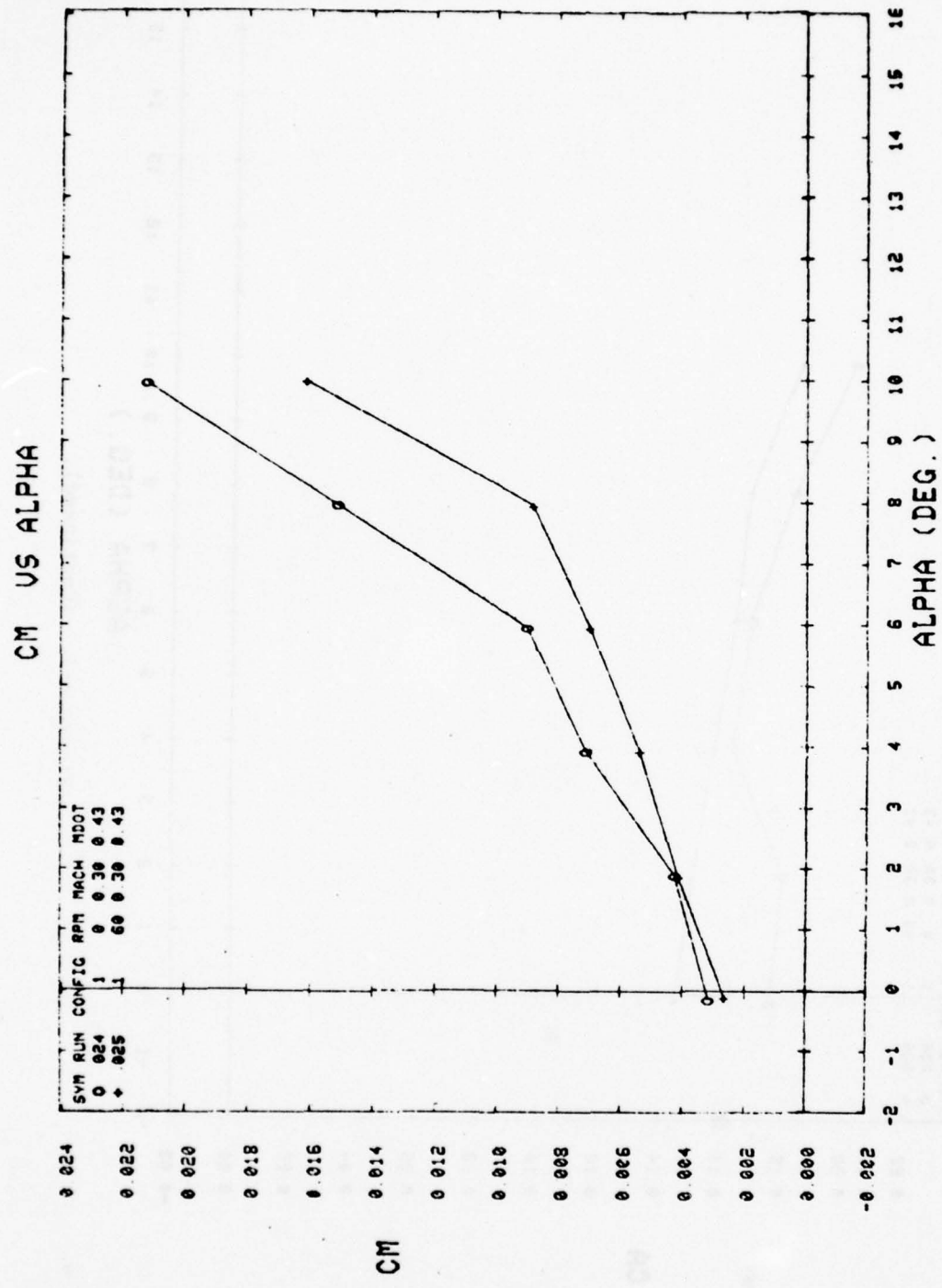


Figure A-1. (Continued).

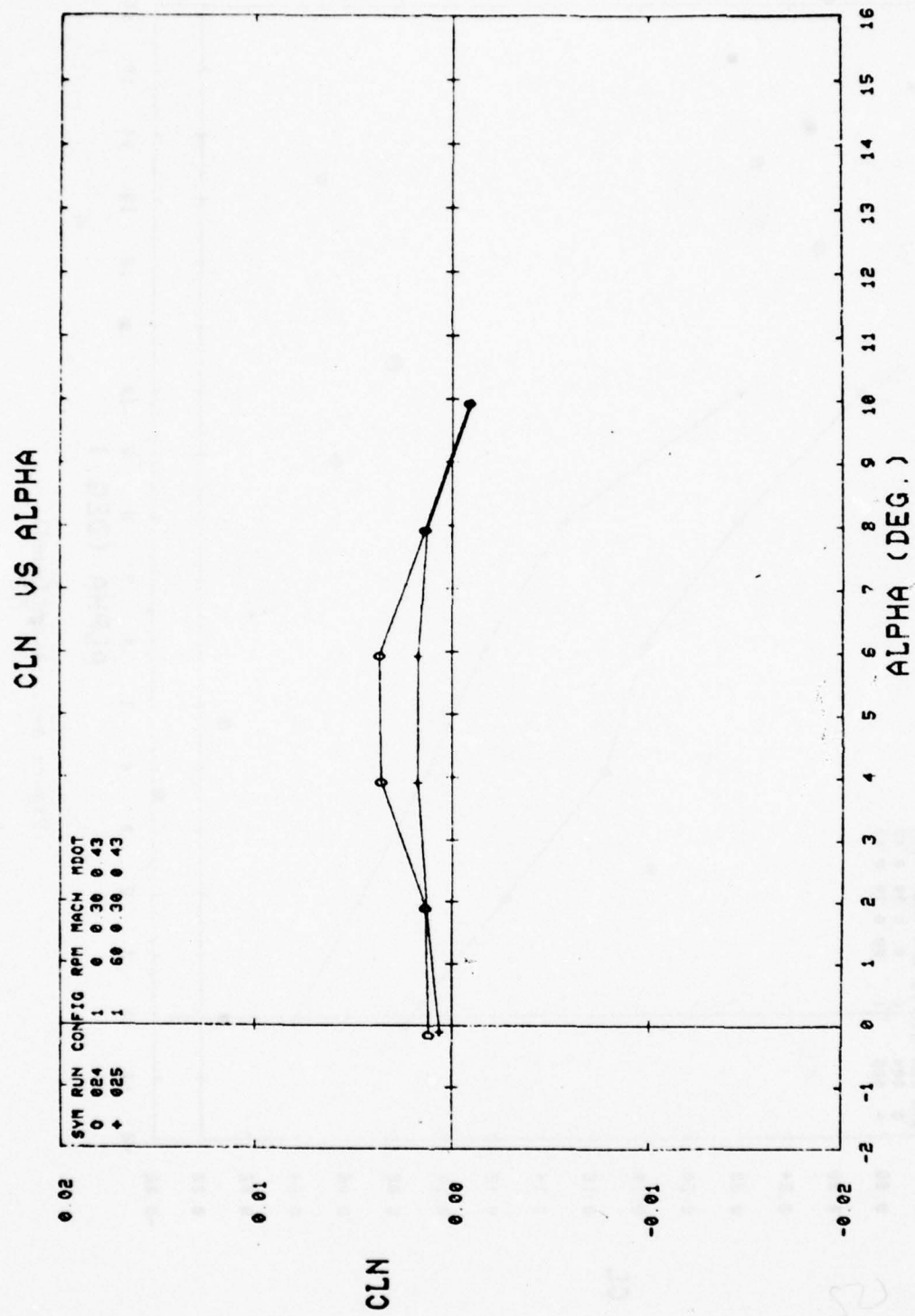


Figure A-1. (Continued).

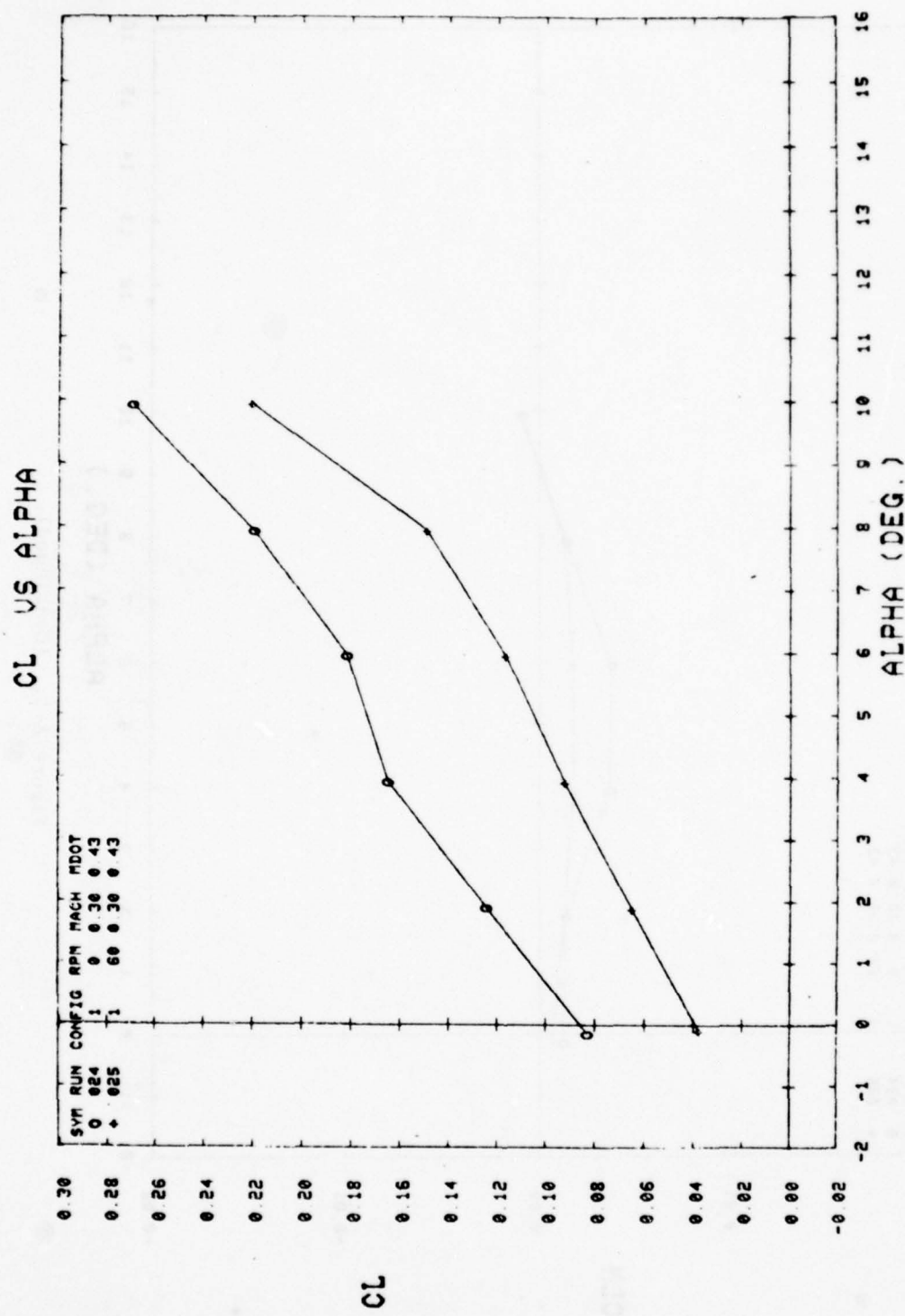


Figure A-1. (Continued).

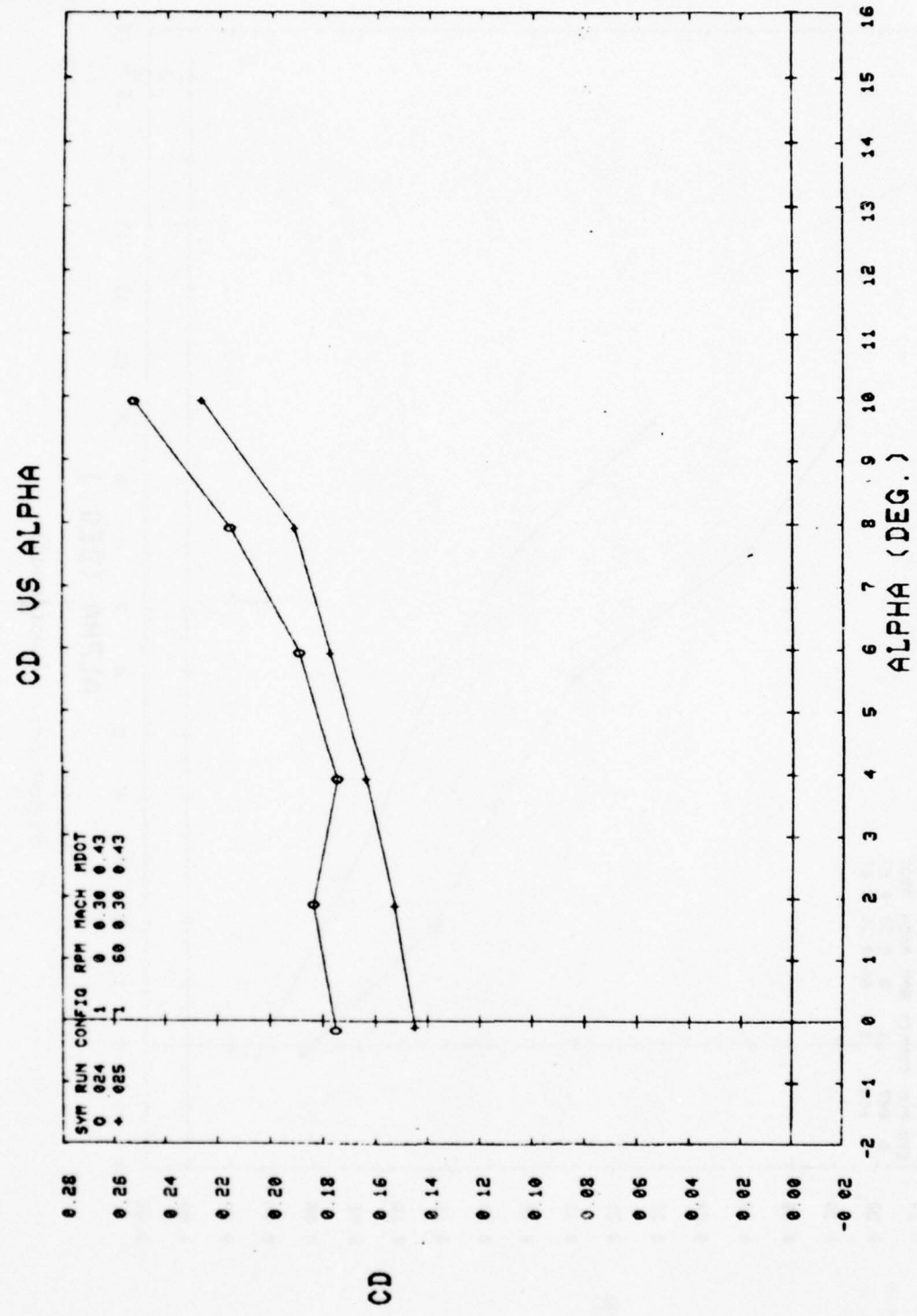


Figure A-1. (Continued).

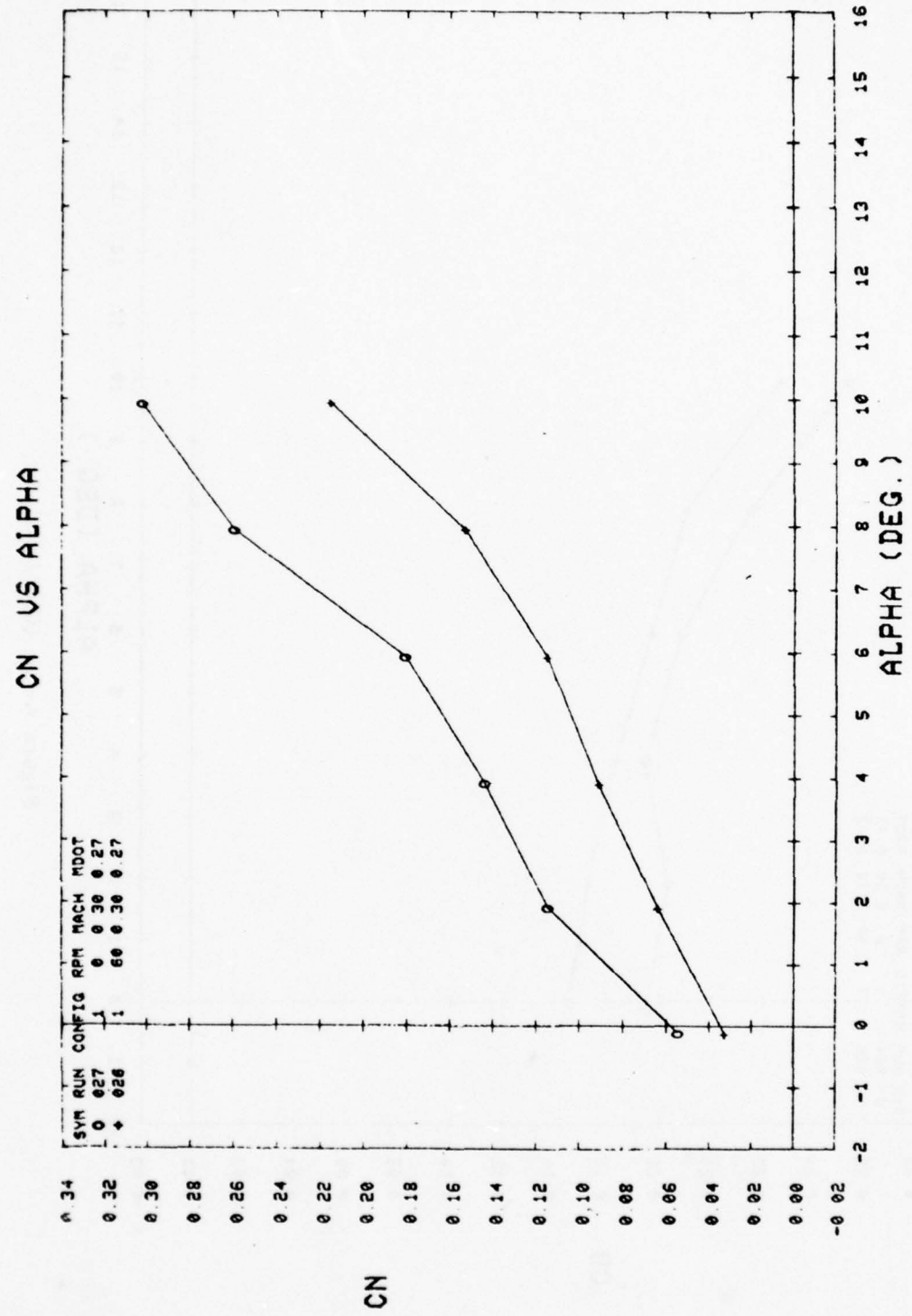


Figure A-1. (Continued).

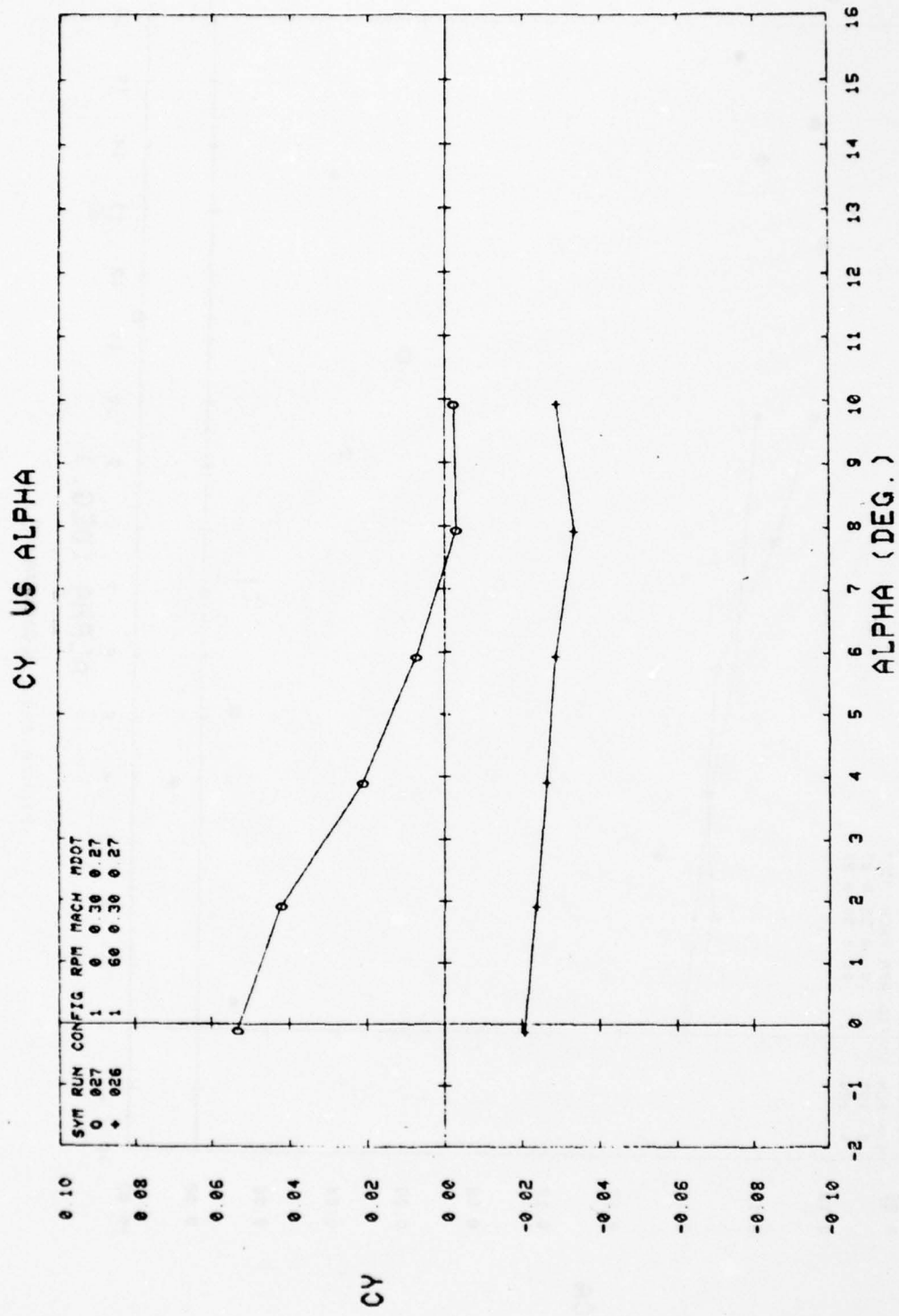


Figure A-1. (Continued).

CA VS ALPHA

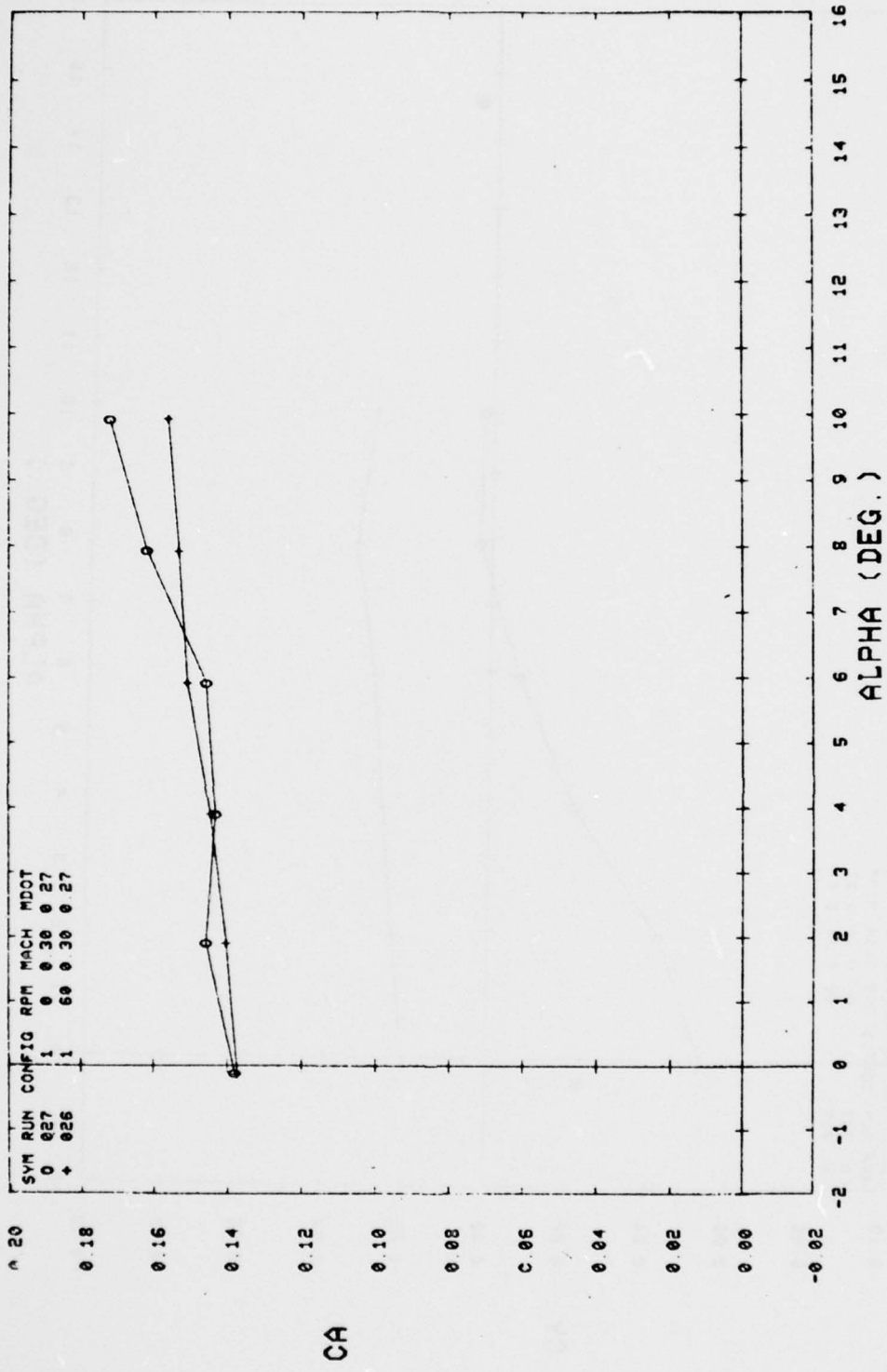


Figure A-1. (Continued).

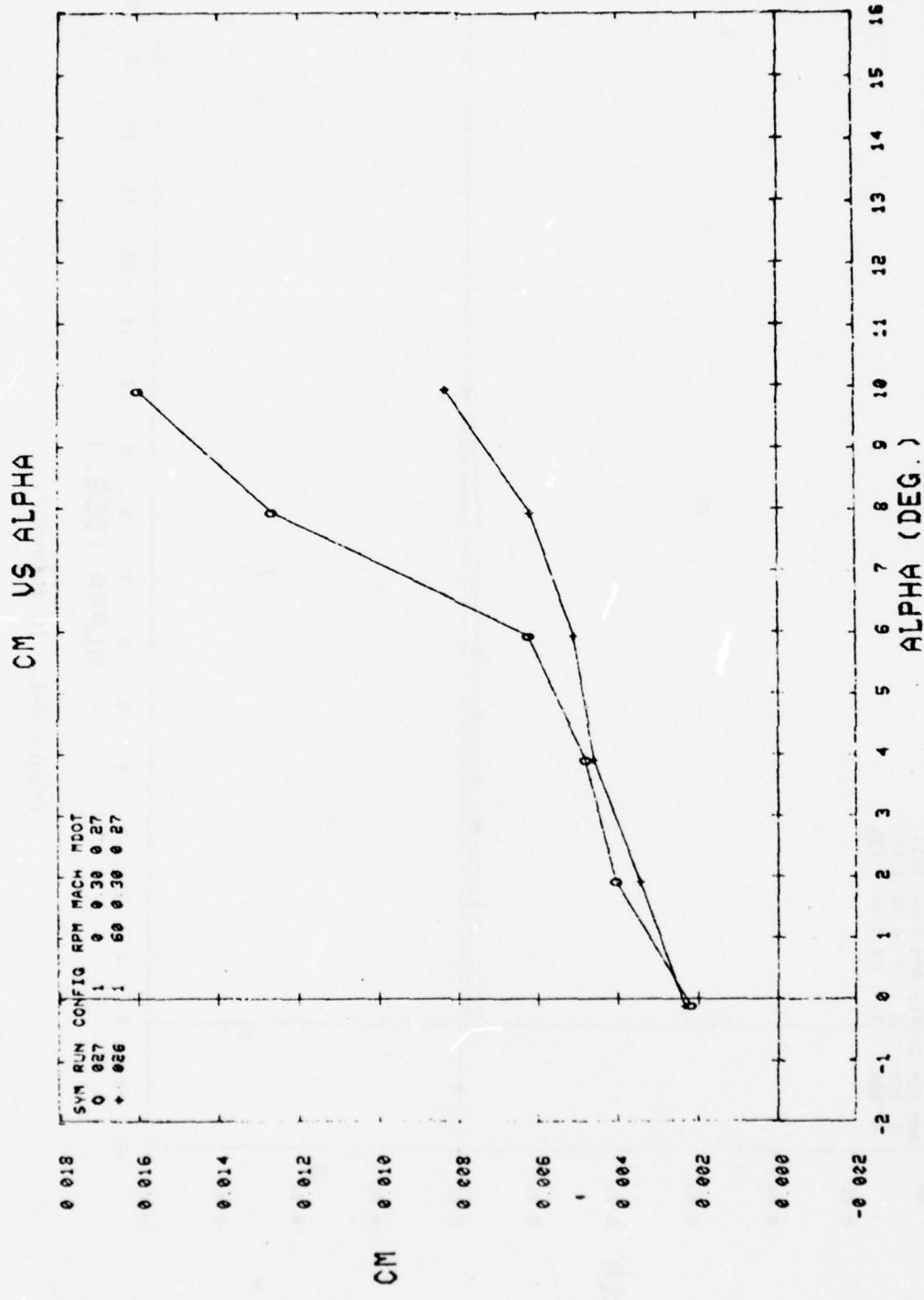


Figure A-1. (Continued).

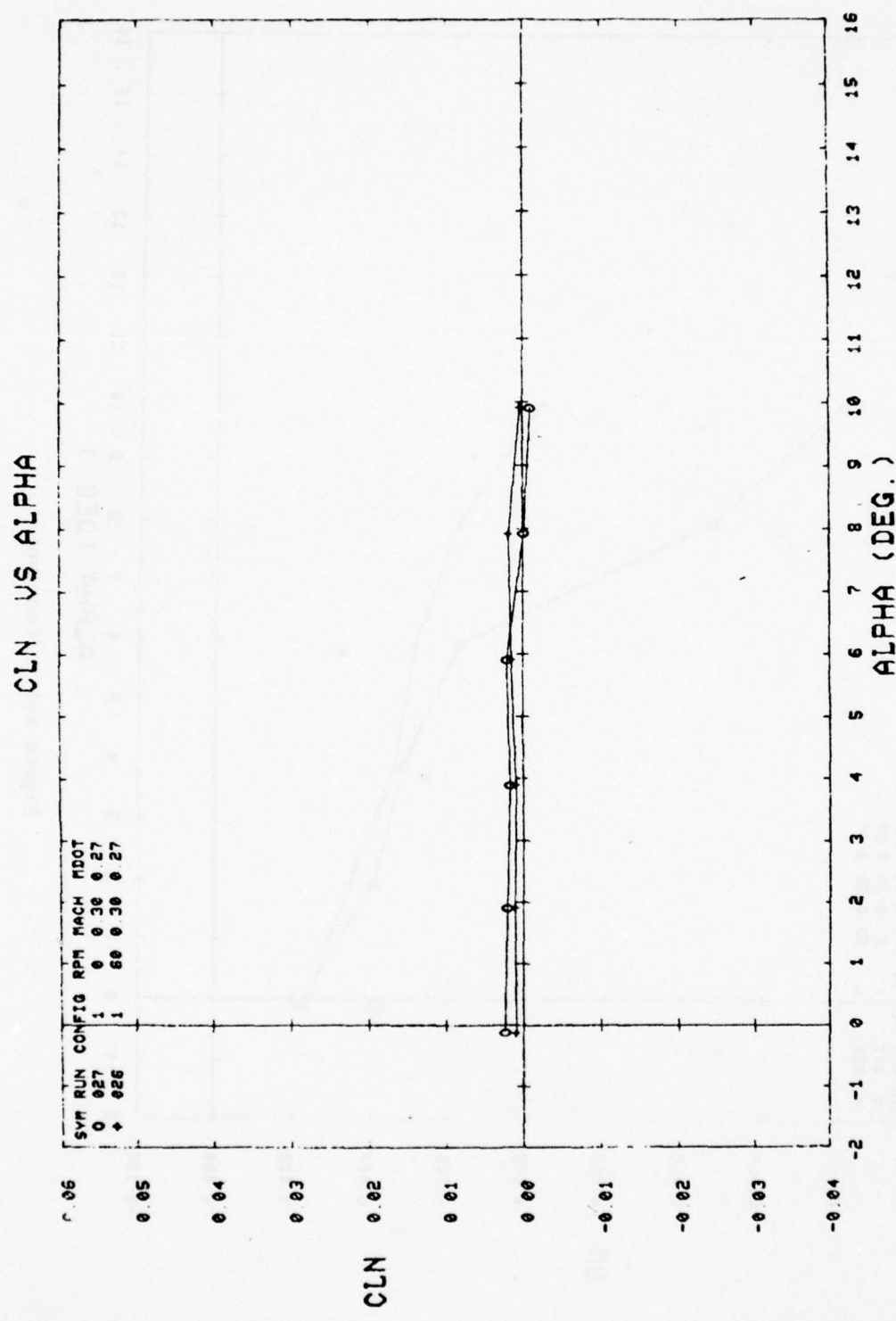


Figure A-1. (Continued).

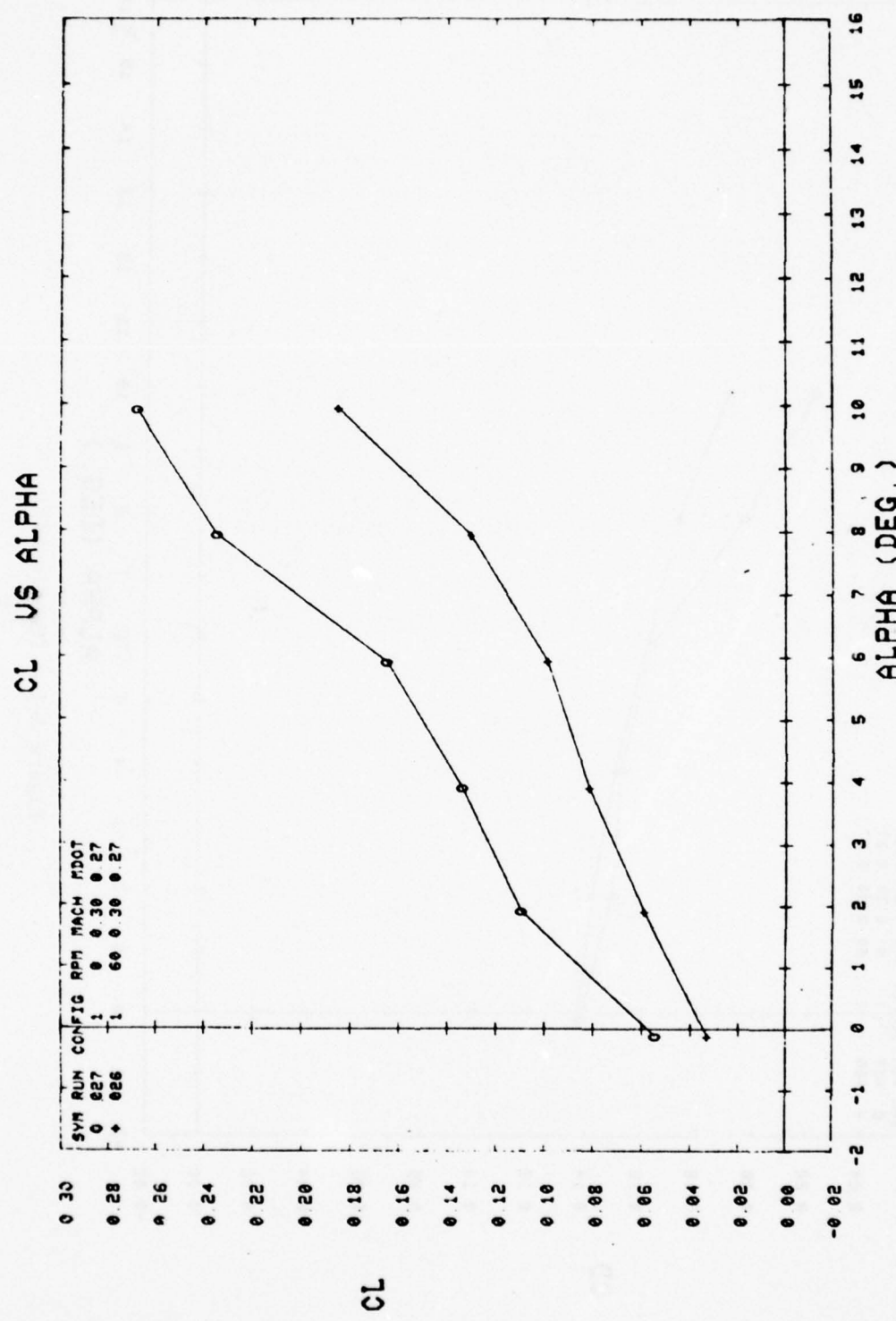


Figure A-1. (Continued).

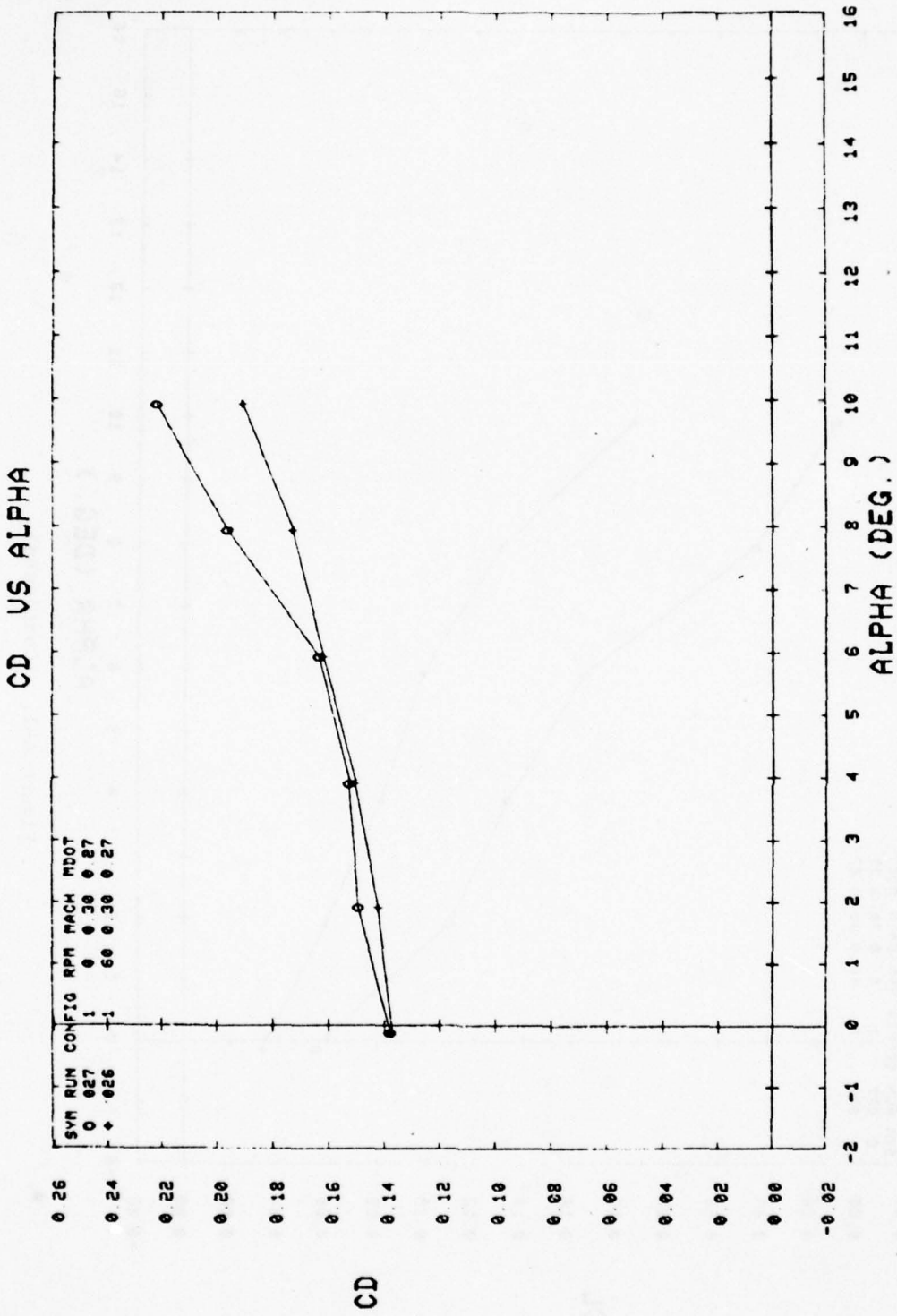


Figure A-1. (Continued).

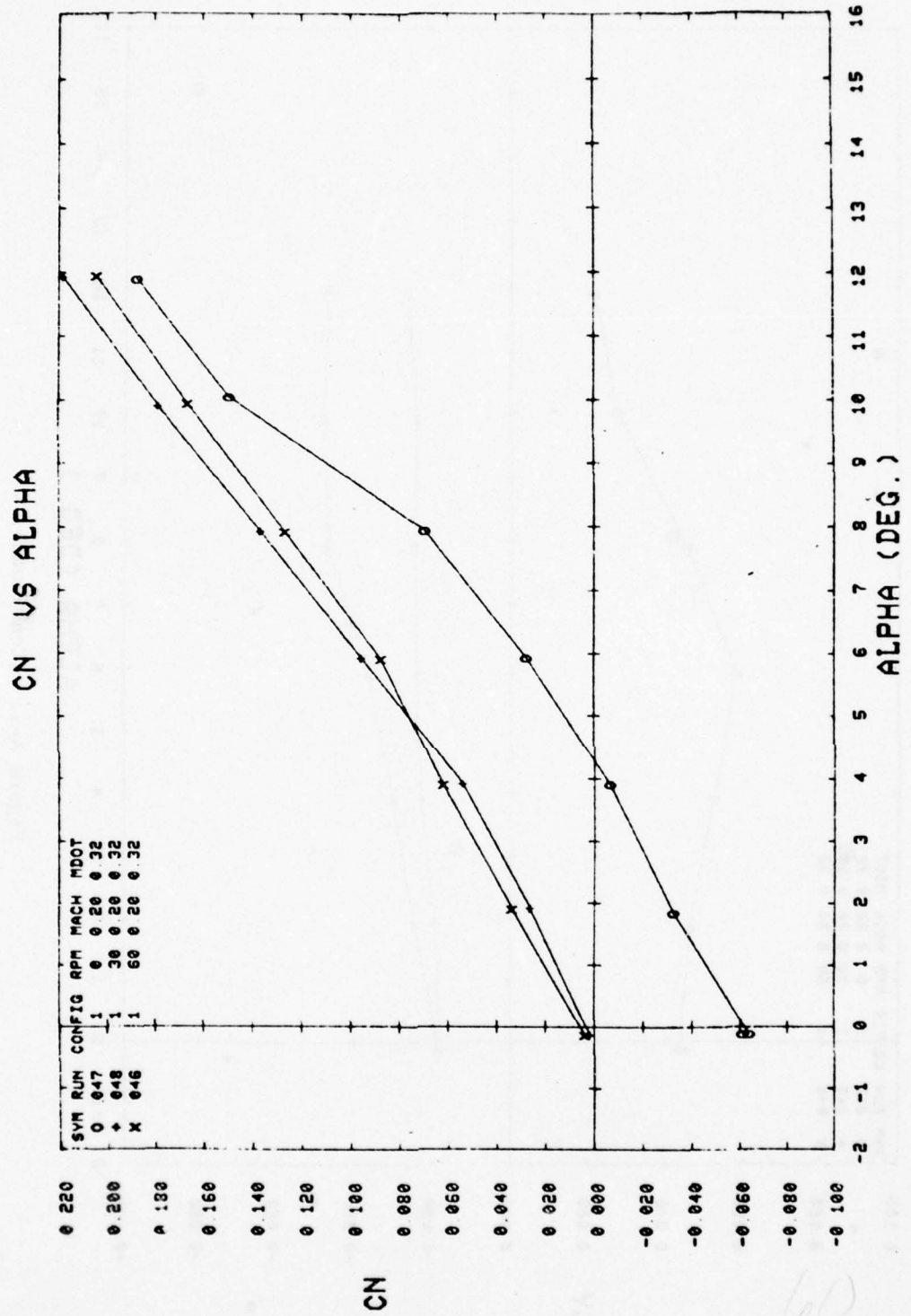


Figure A-1. (Continued).

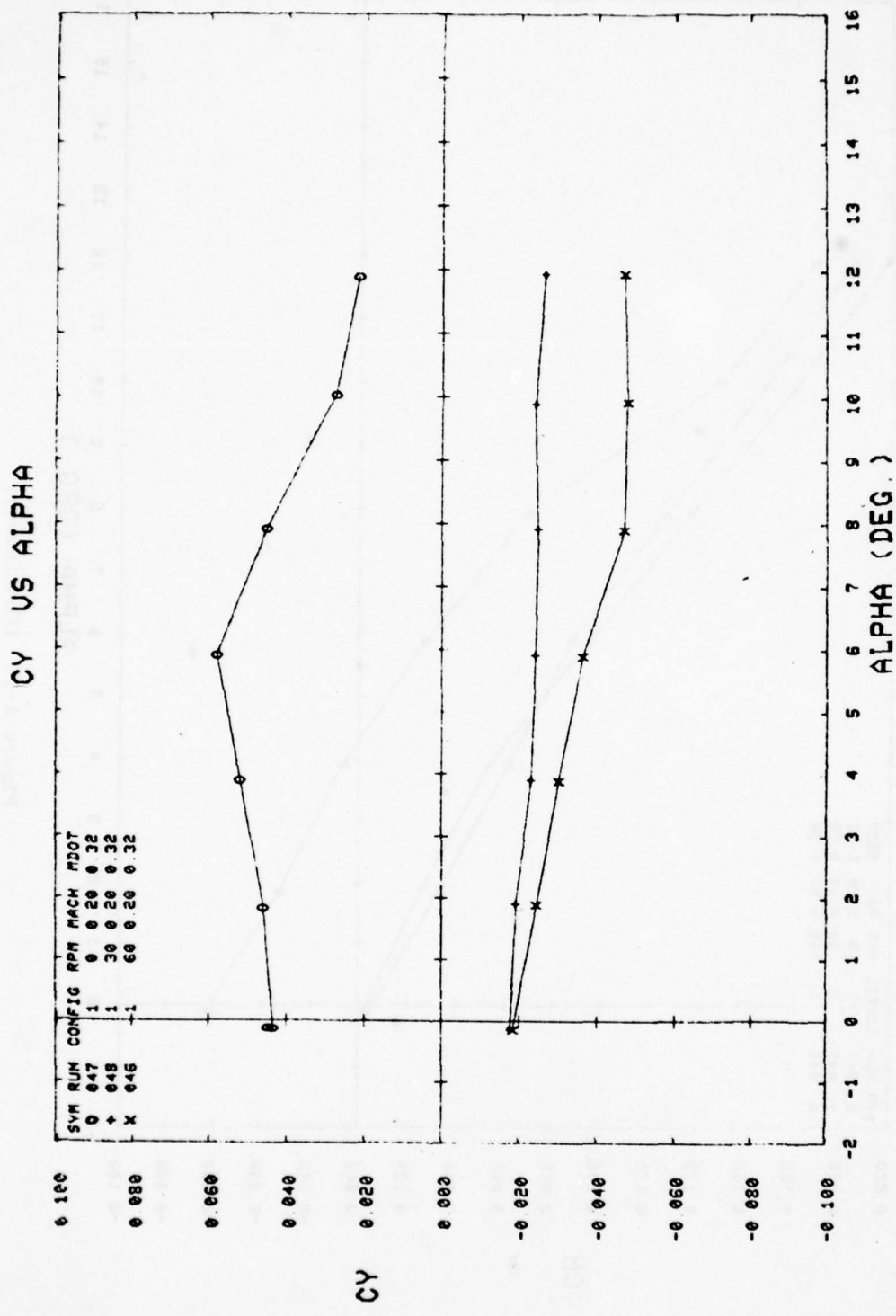


Figure A-1. (Continued).

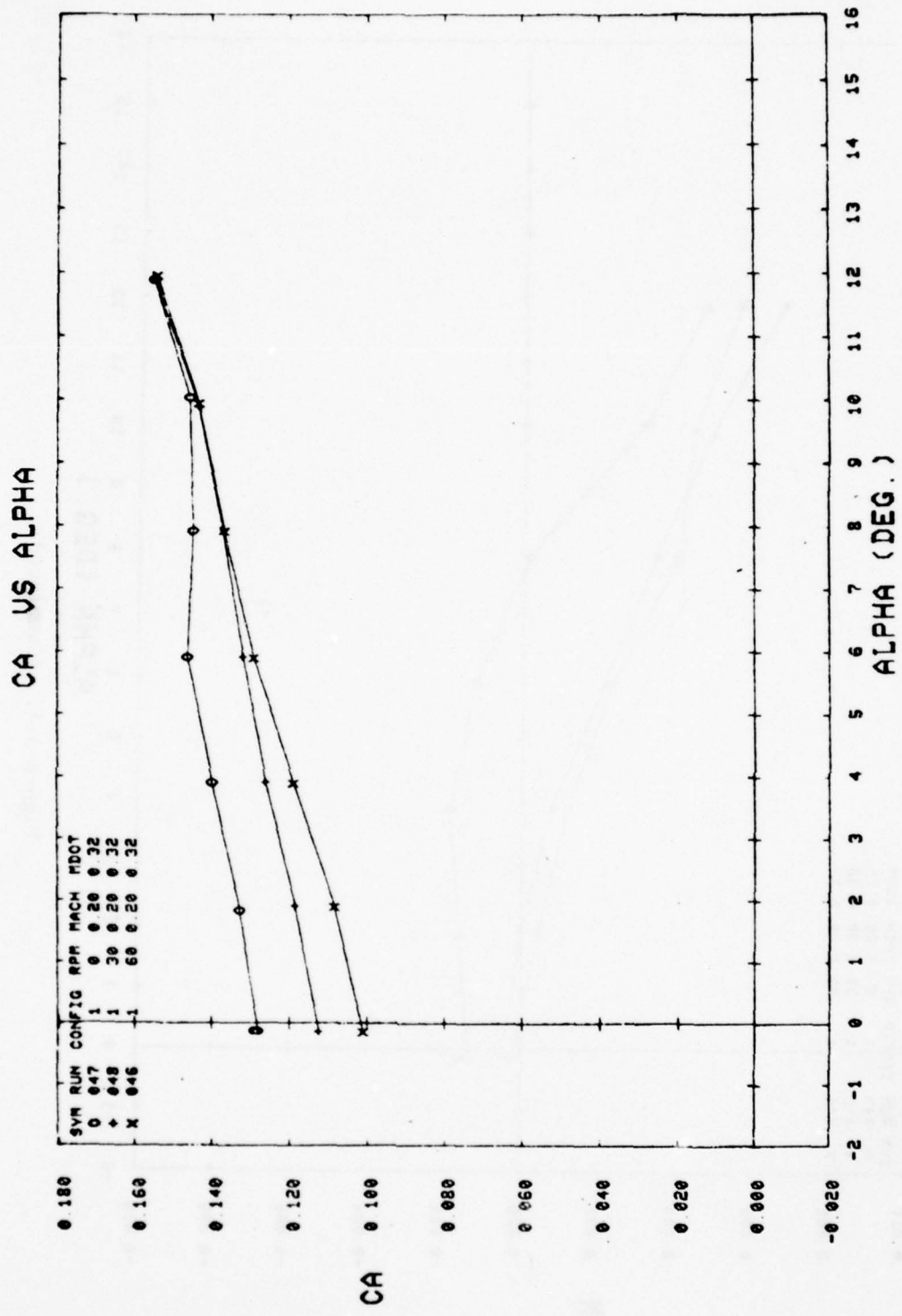


Figure A-1. (Continued).

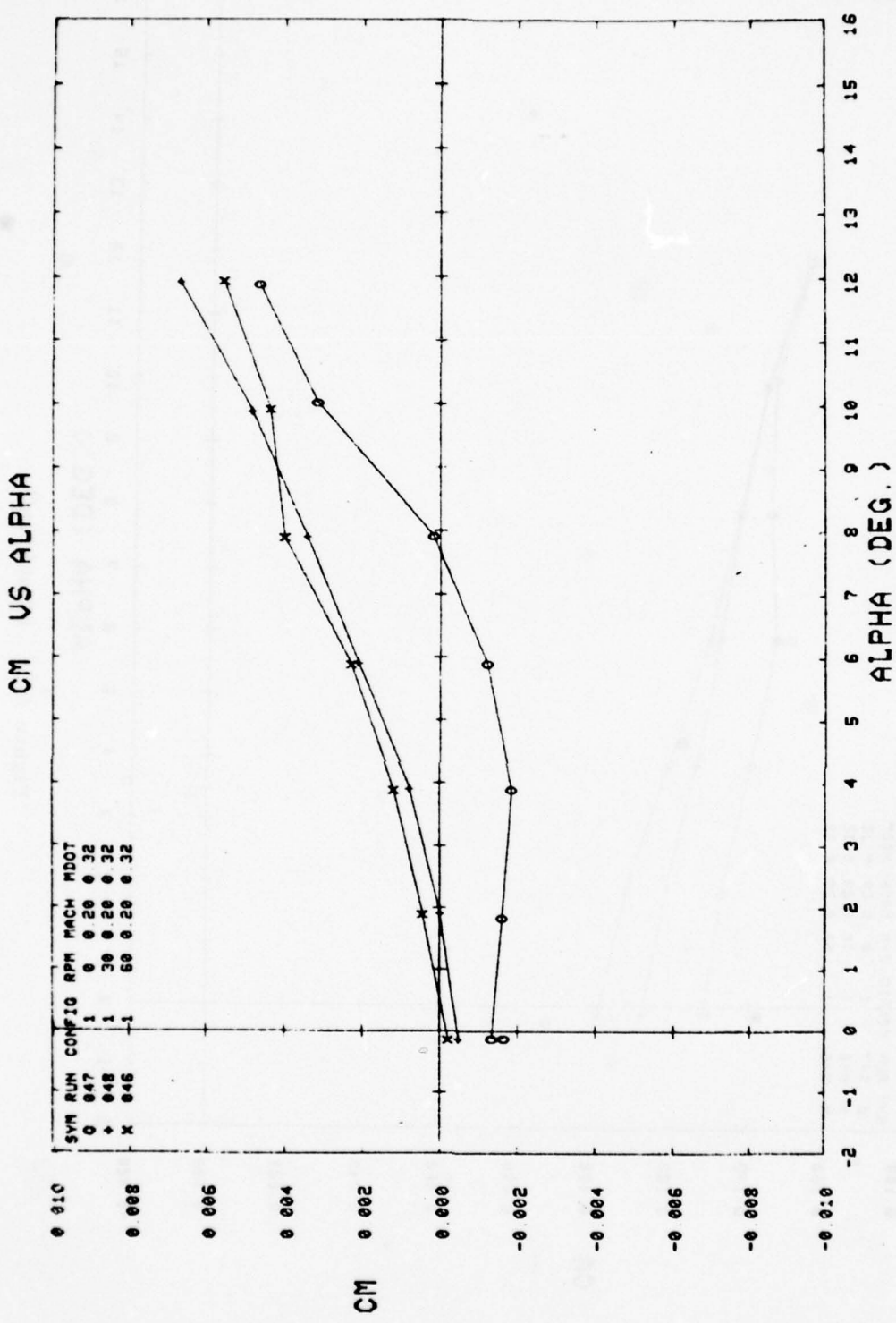


Figure A-1. (Continued).

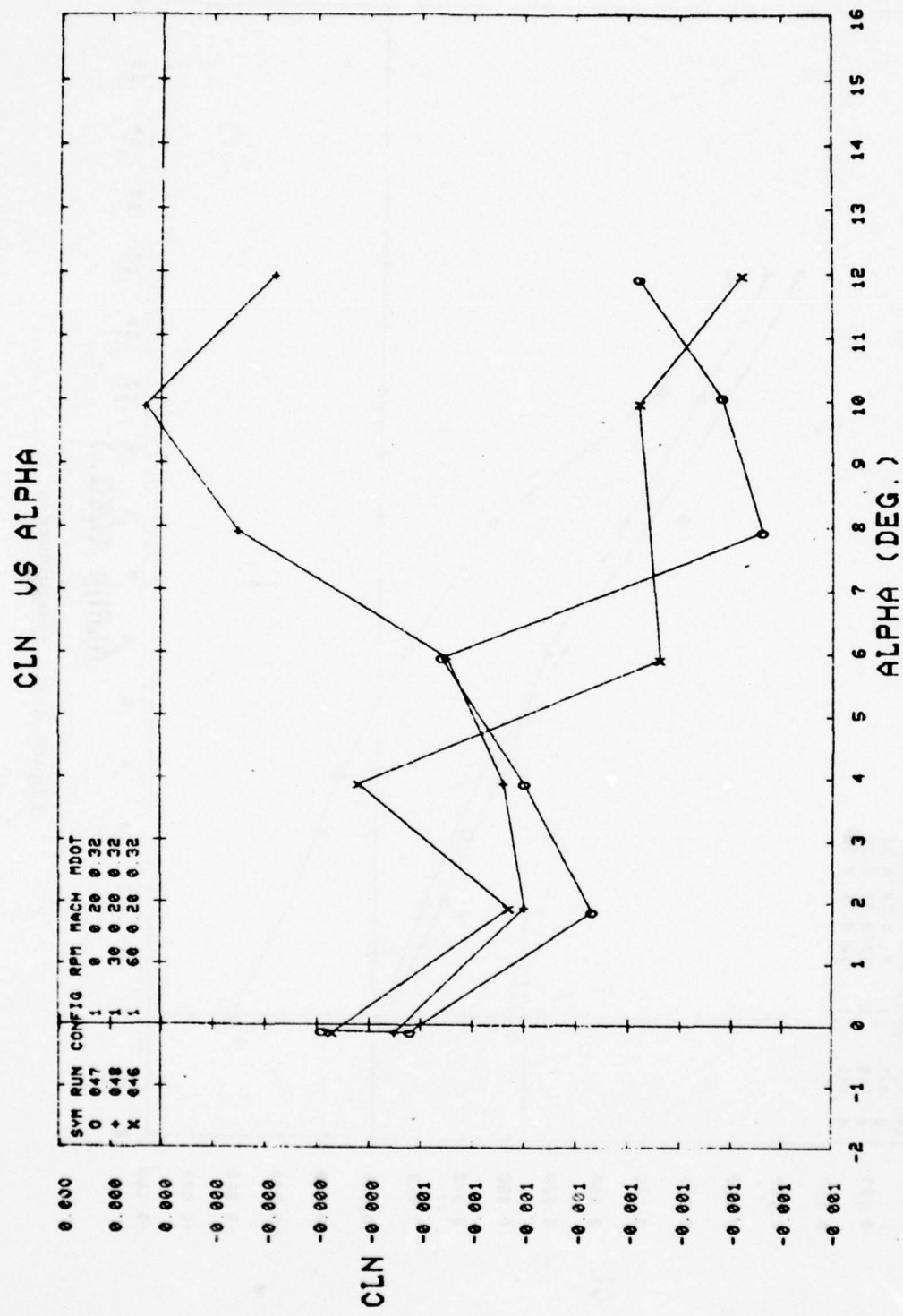


Figure A-1. (Continued).

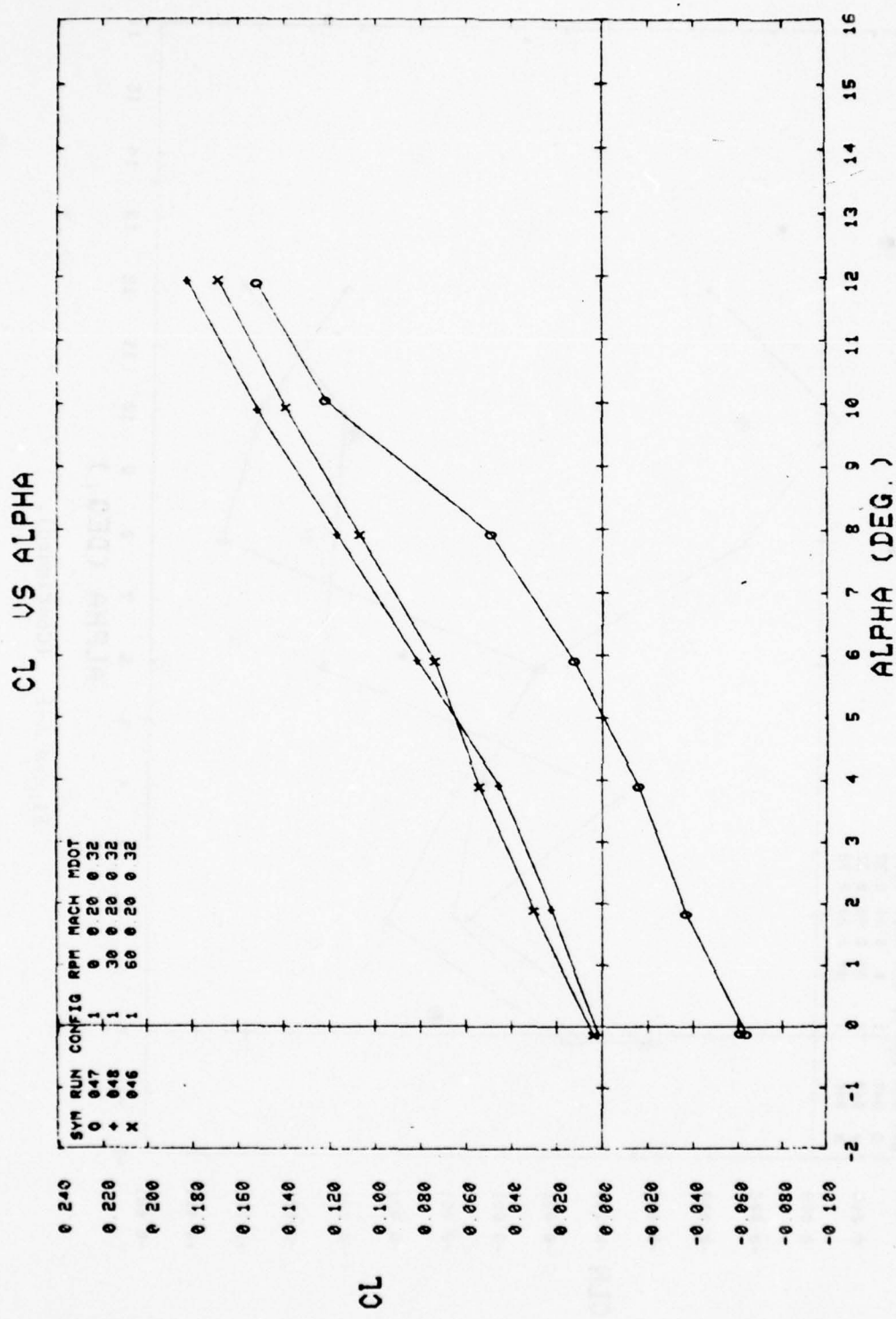


Figure A-1. (Continued).

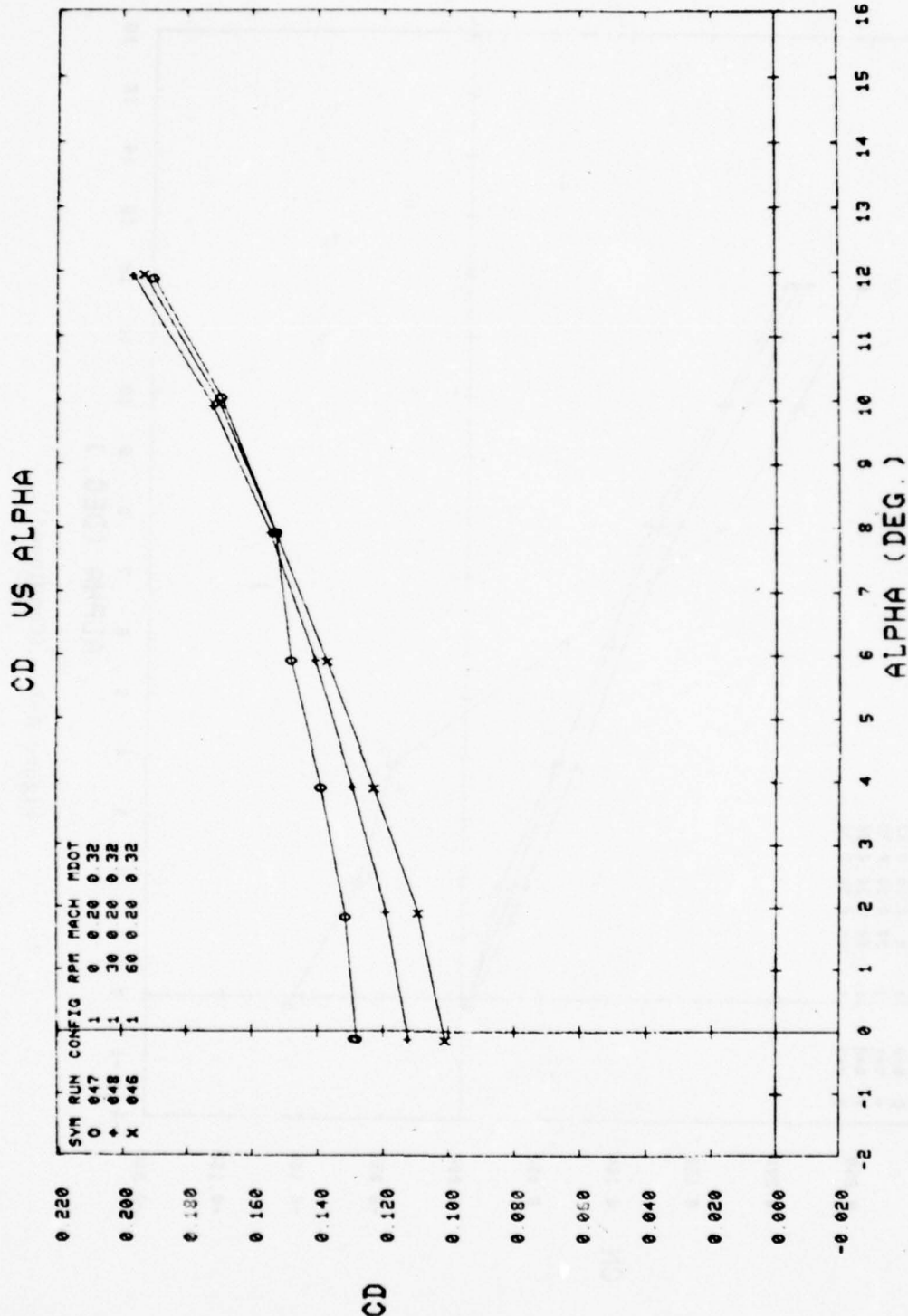


Figure A-1. (Continued).

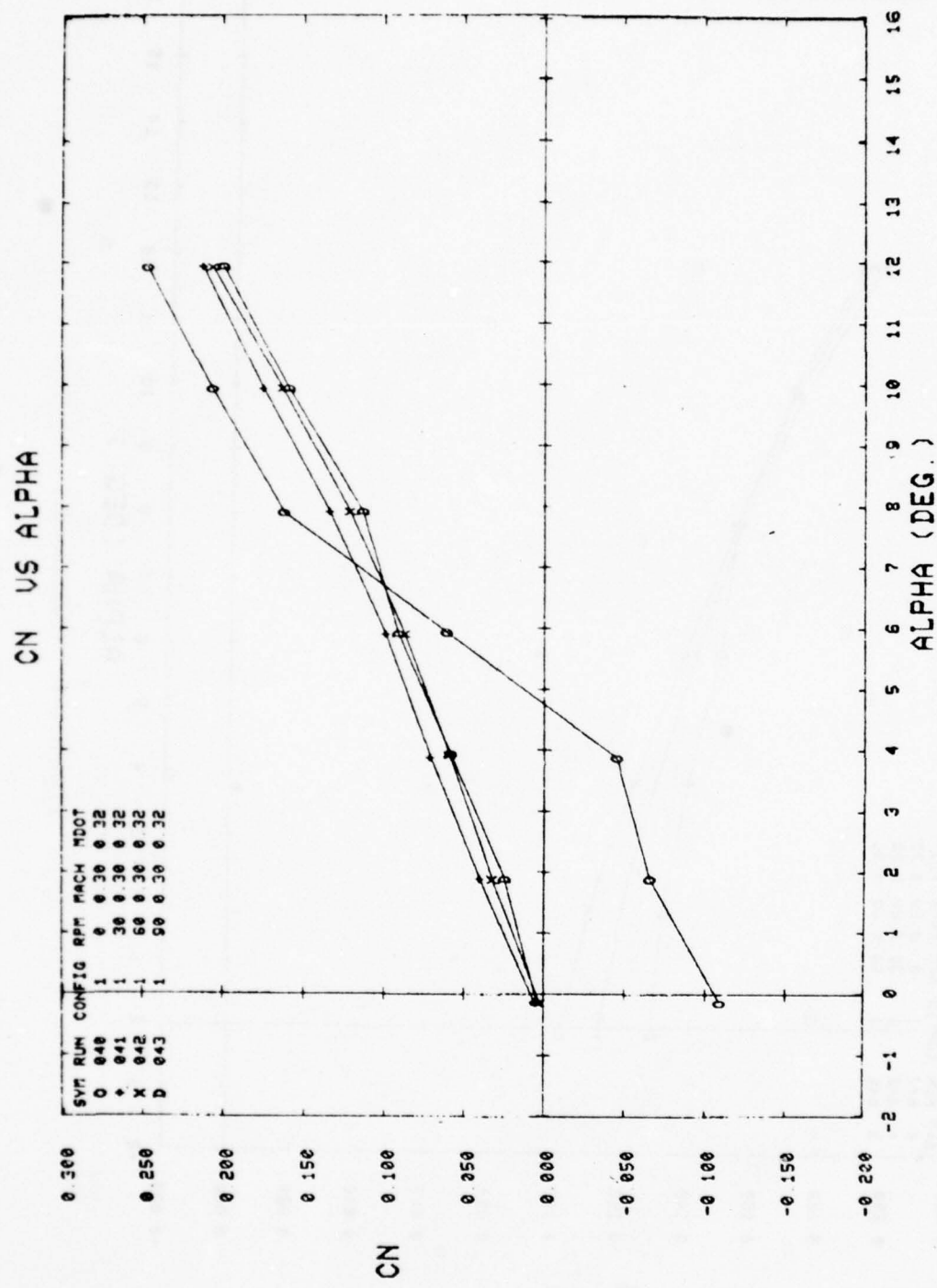


Figure A-1. (Continued).

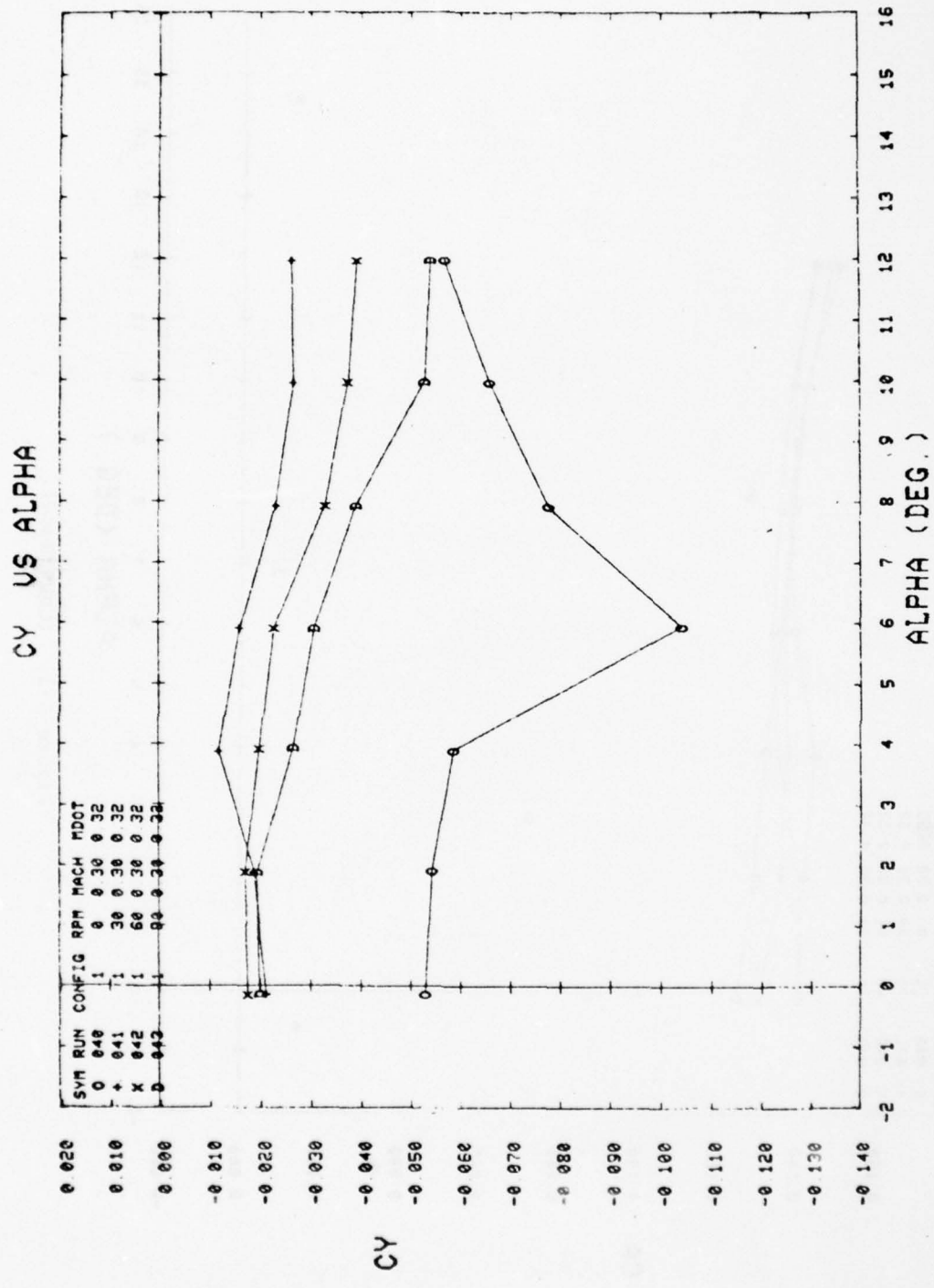


Figure A-1. (Continued).

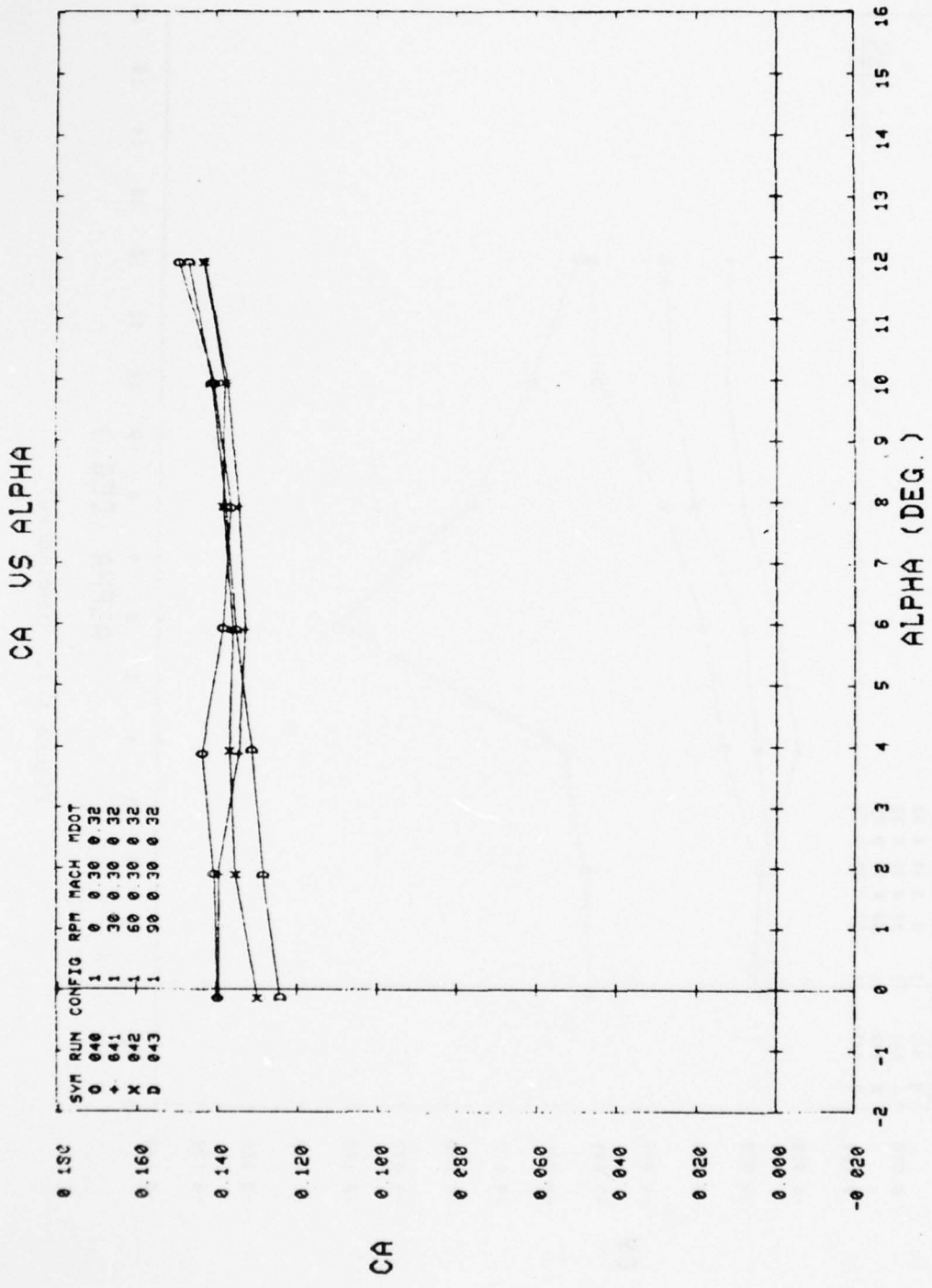


Figure A-1. (Continued).

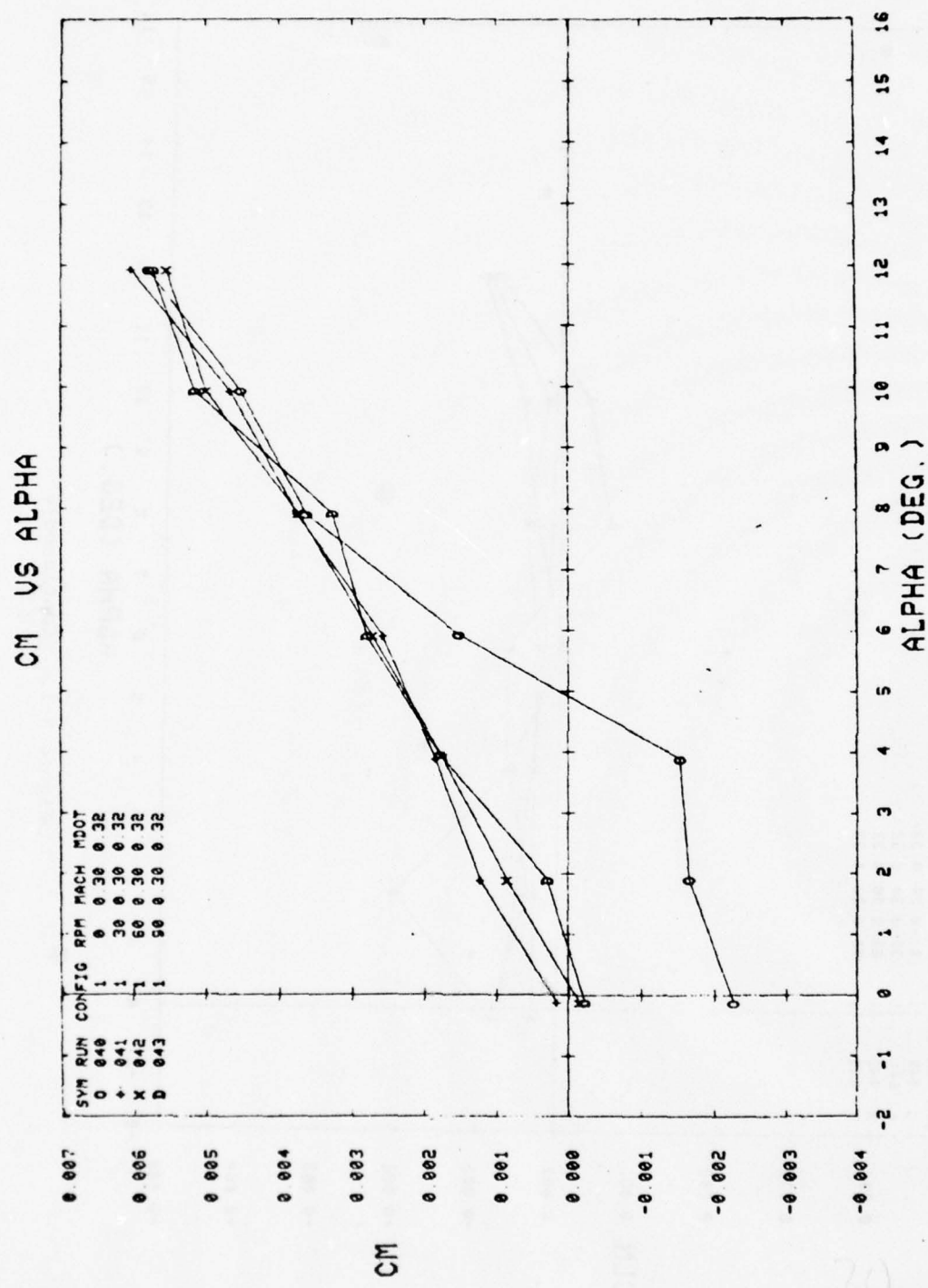


Figure A-1. (Continued).

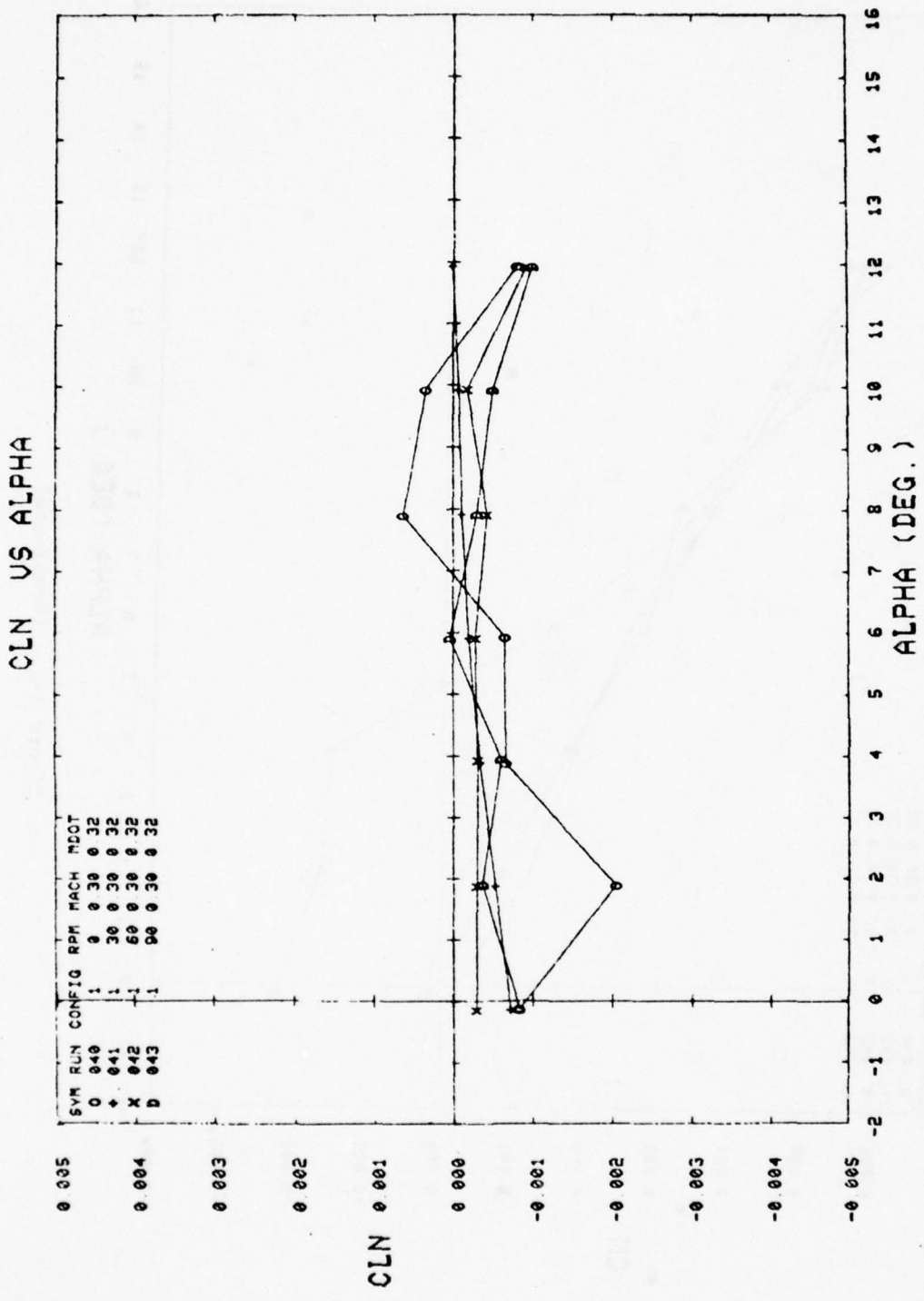


Figure A-1. (Continued).

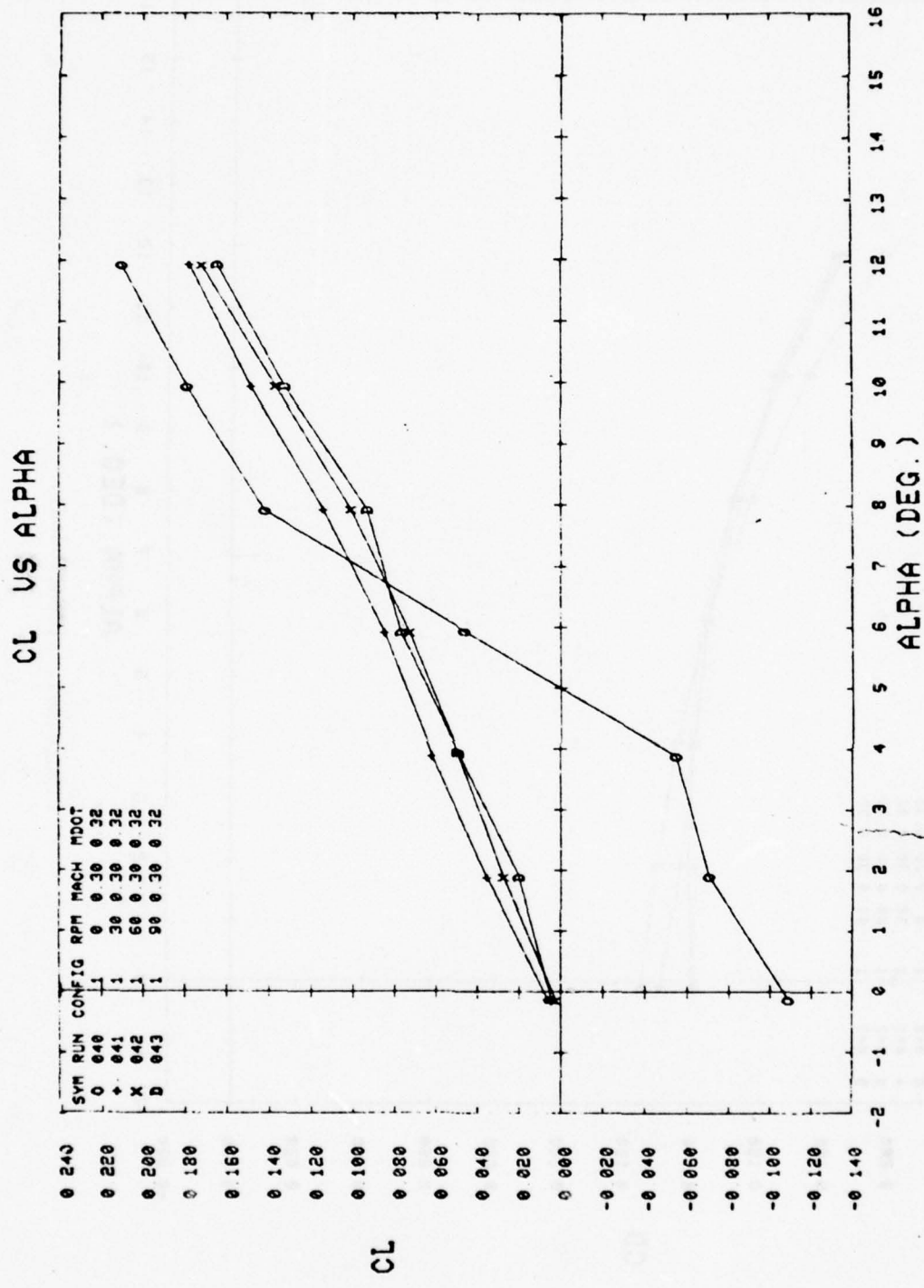


Figure A-1. (Continued).

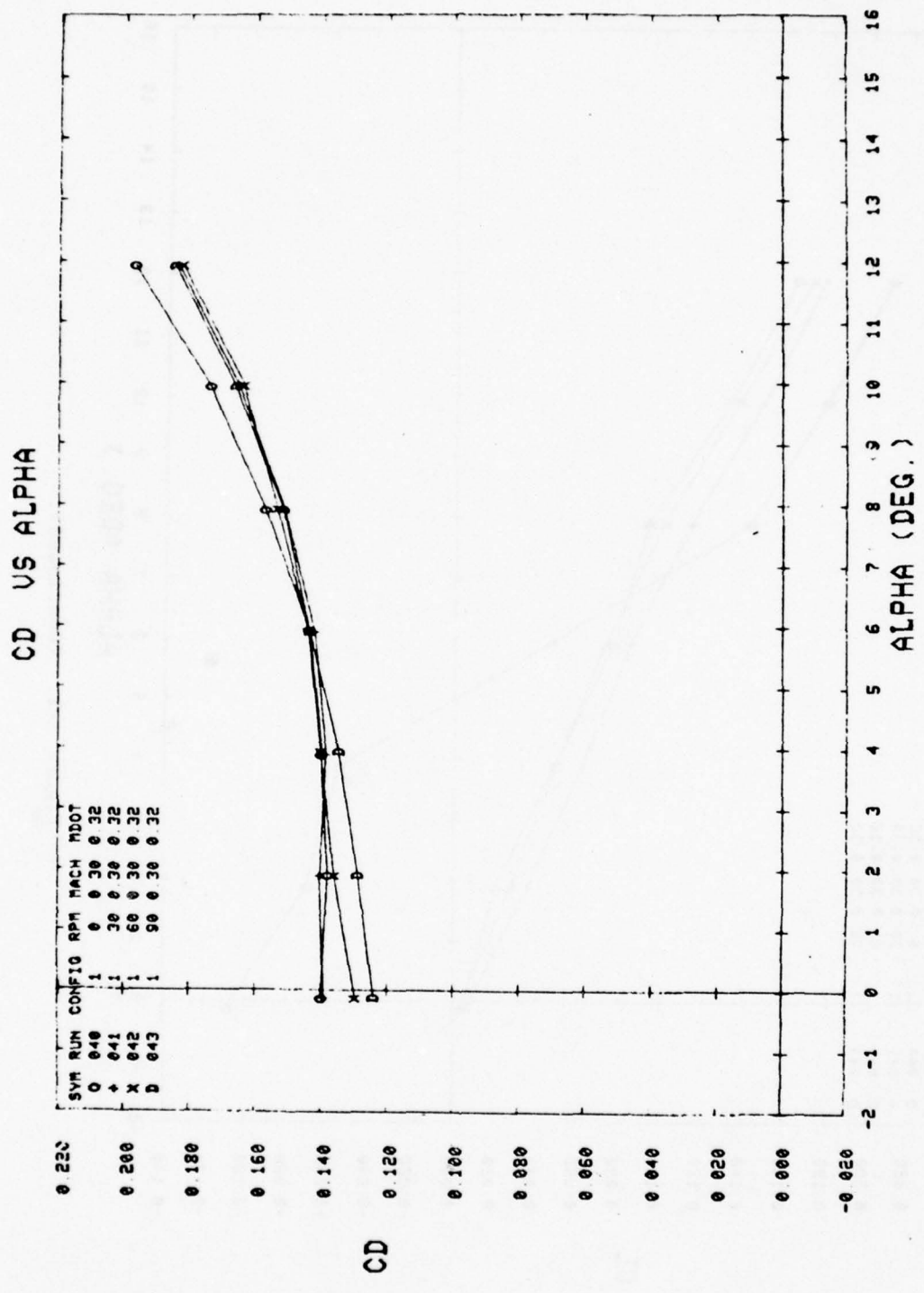


Figure A-1. (Concluded).

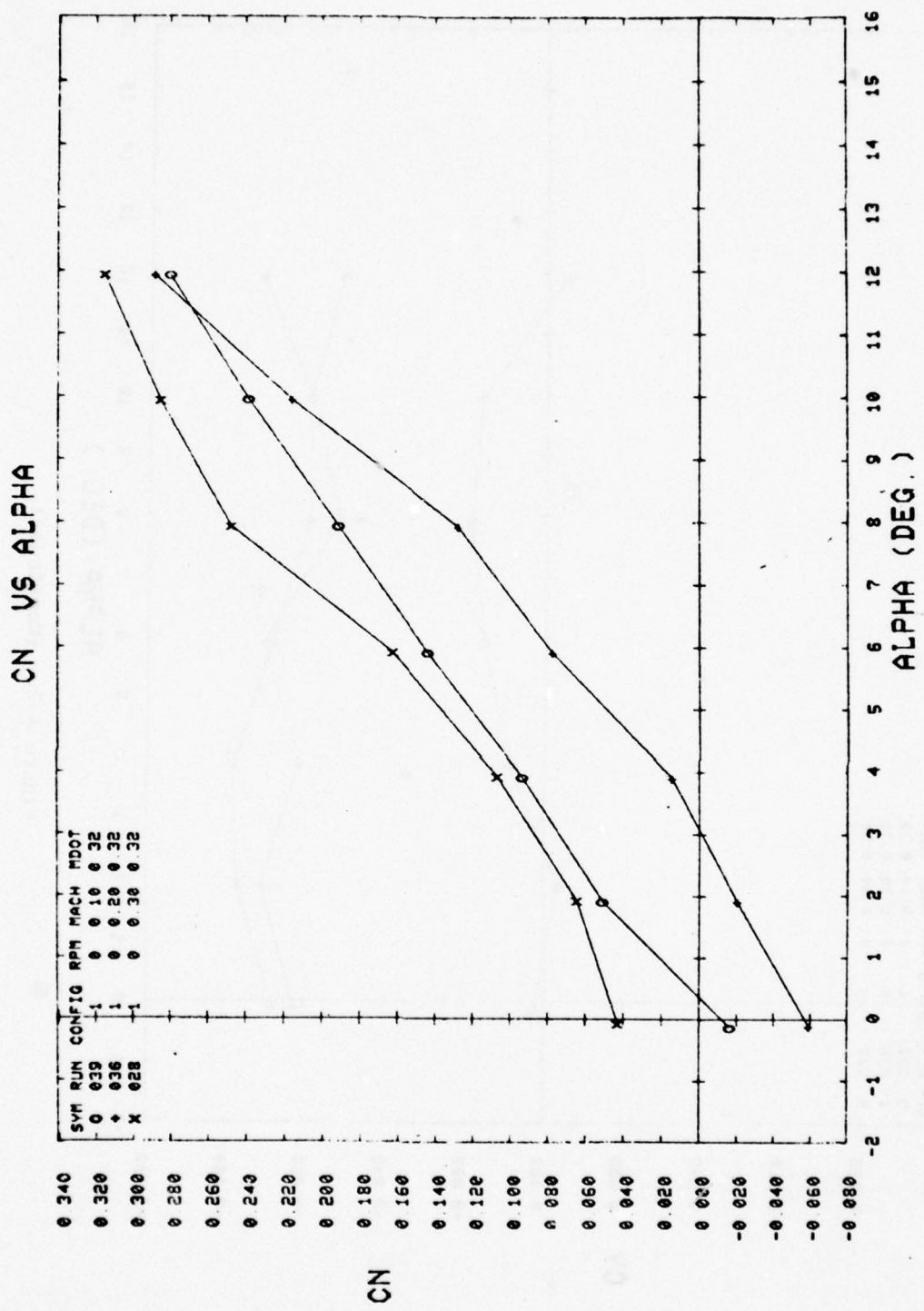


Figure A-2. Configuration 1 — aerodynamic coefficient versus alpha with varying Mach number.

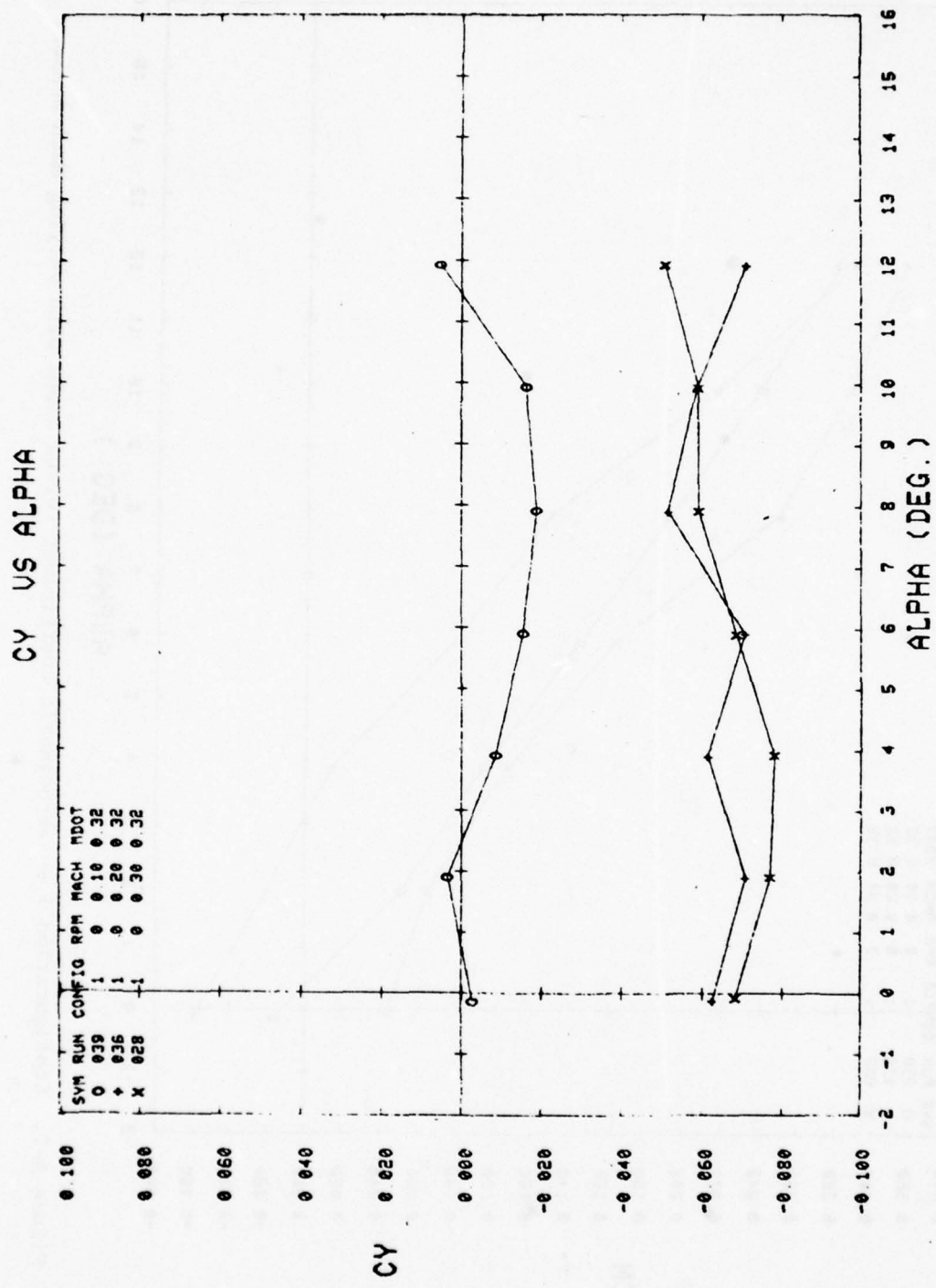


Figure A-2. (Continued).

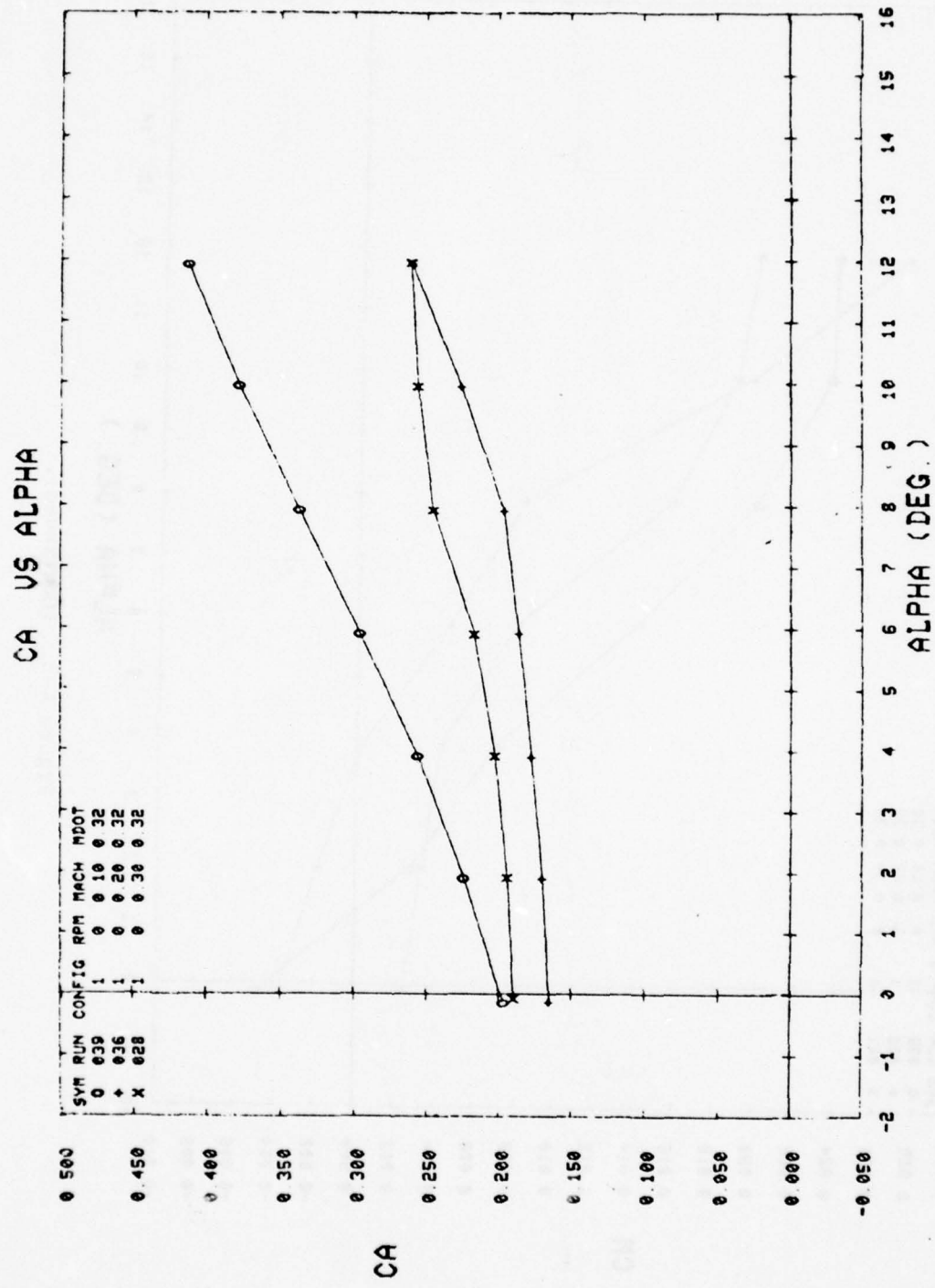


Figure A-2. (Continued).

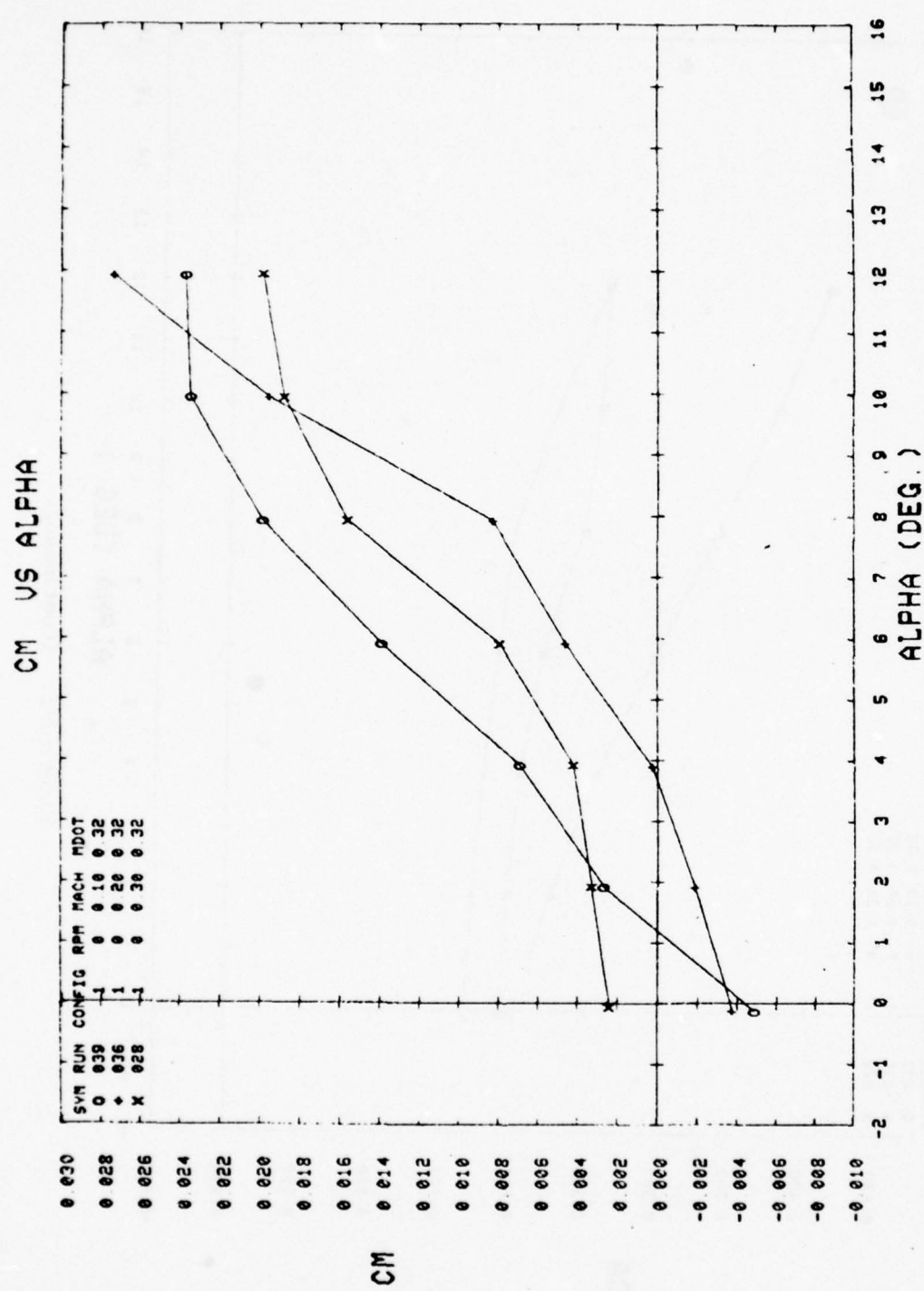


Figure A-2. (Continued).

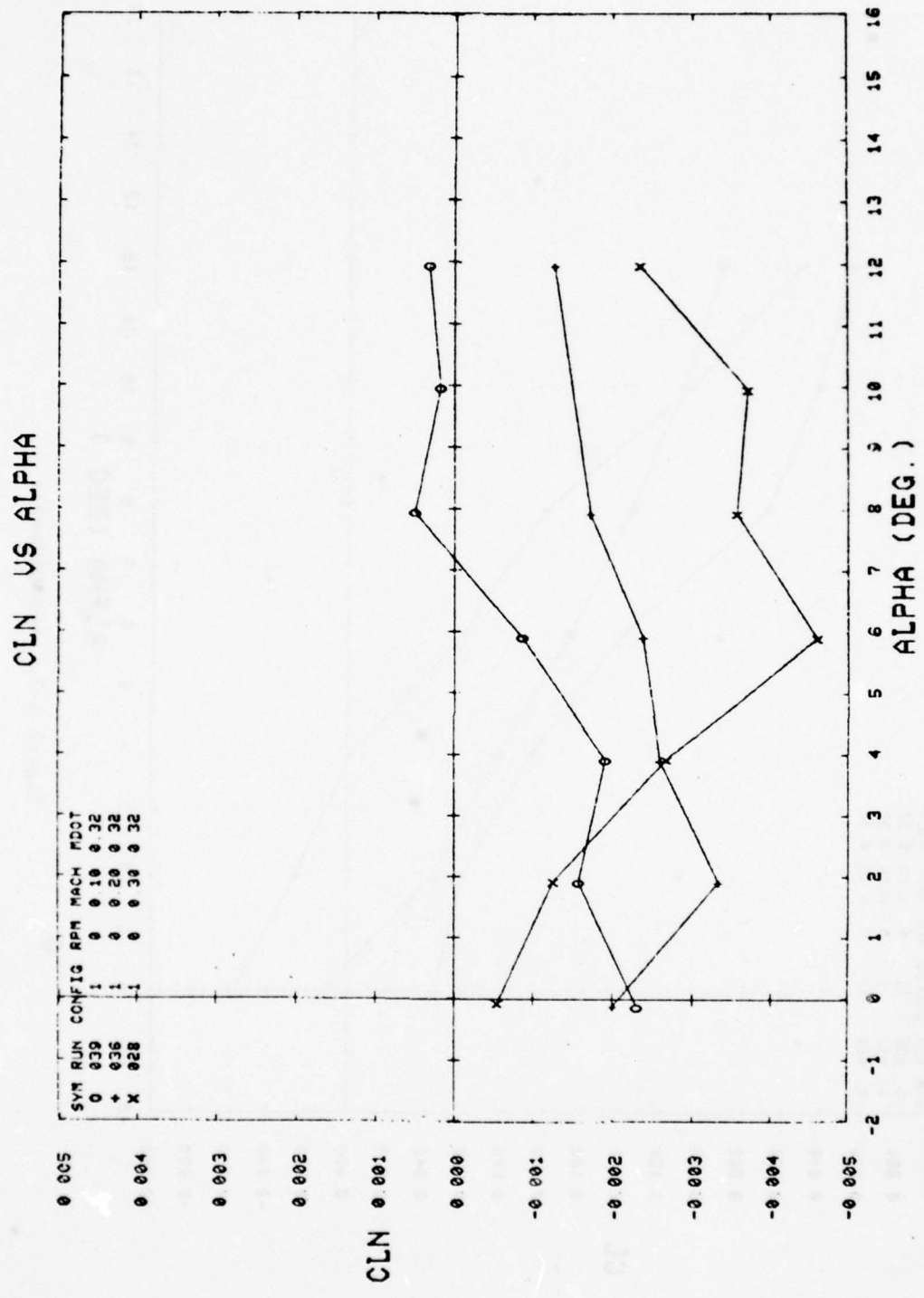


Figure A-2. (Continued).

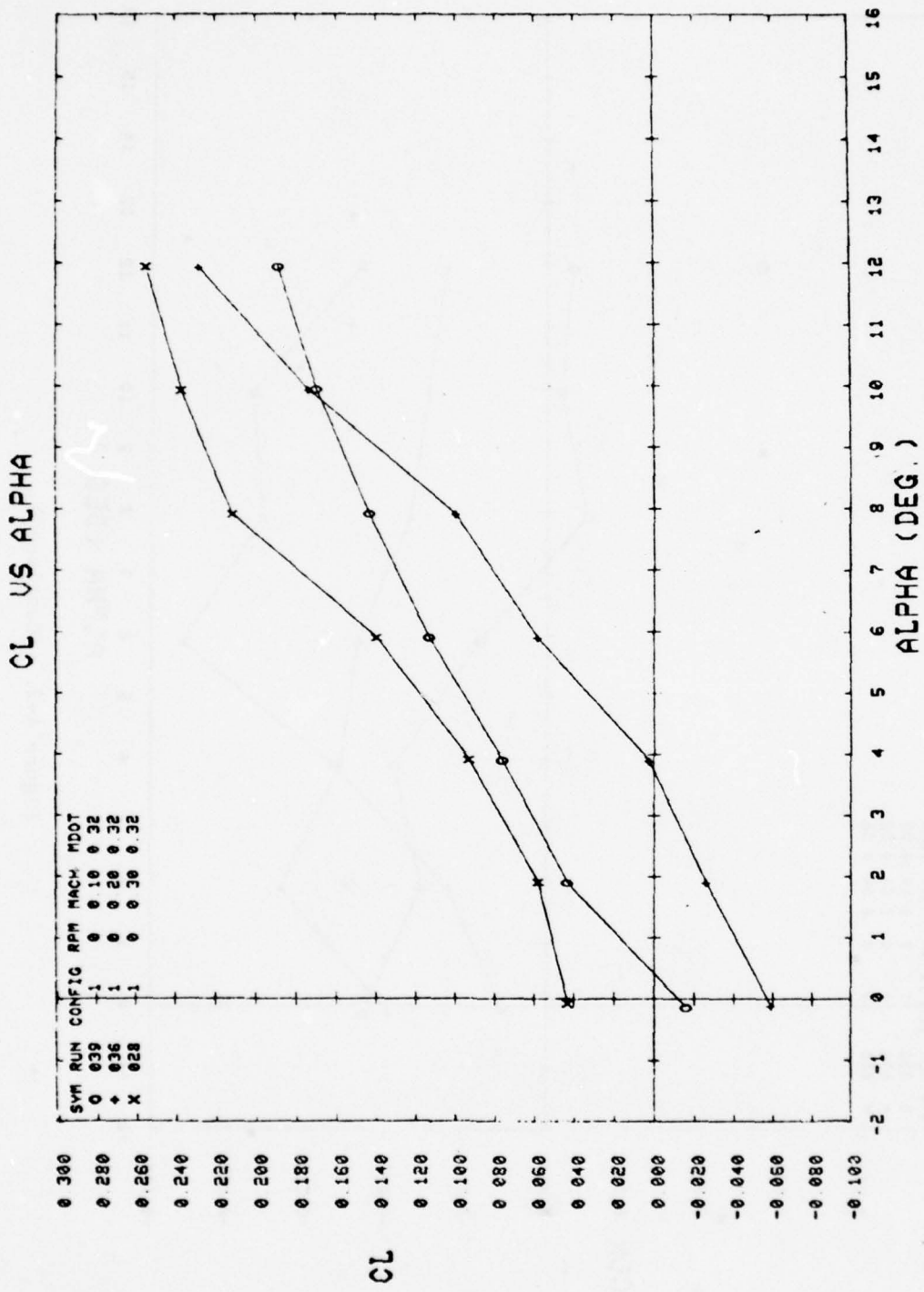


Figure A-2. (Continued).

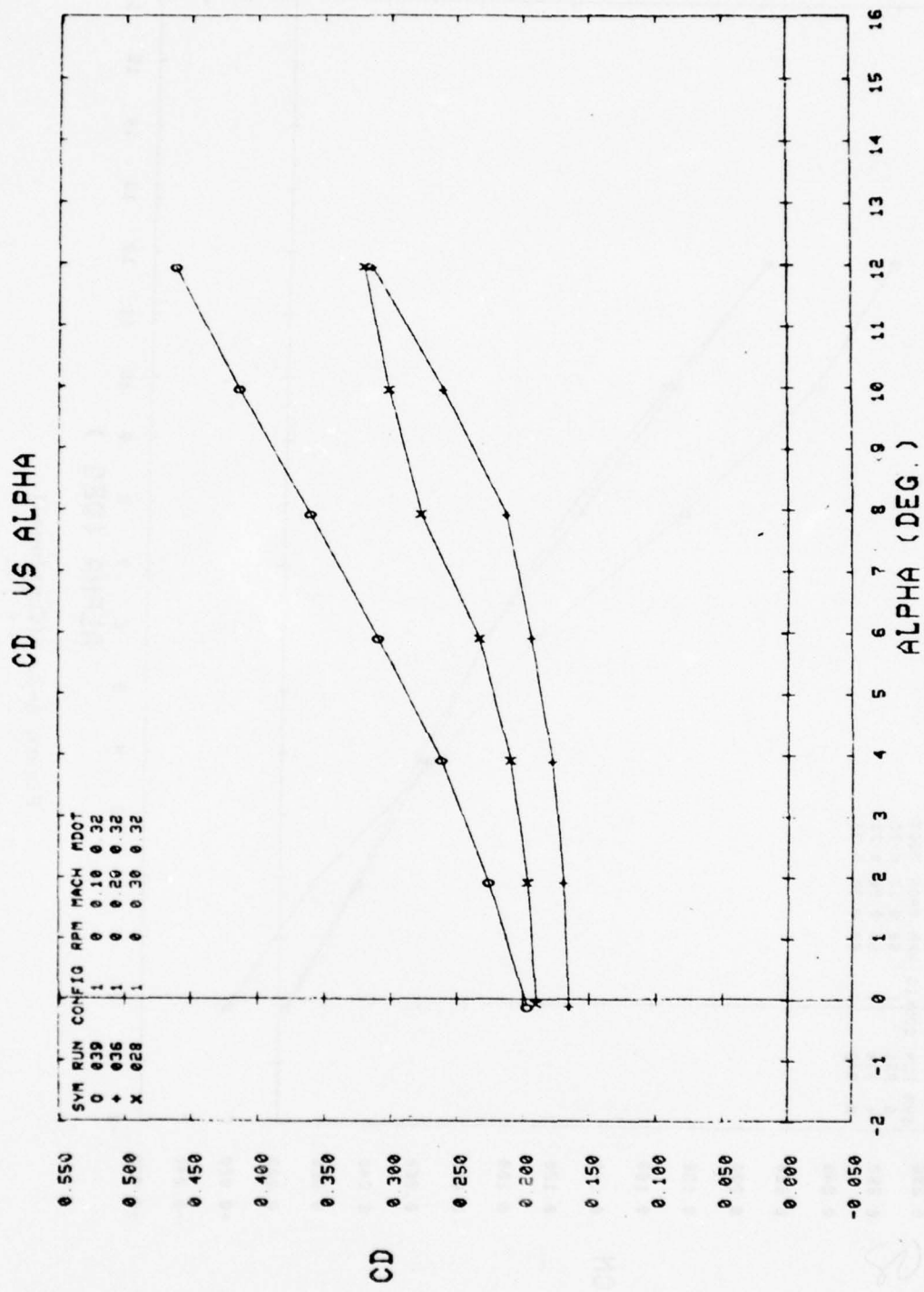


Figure A-2. (Continued).

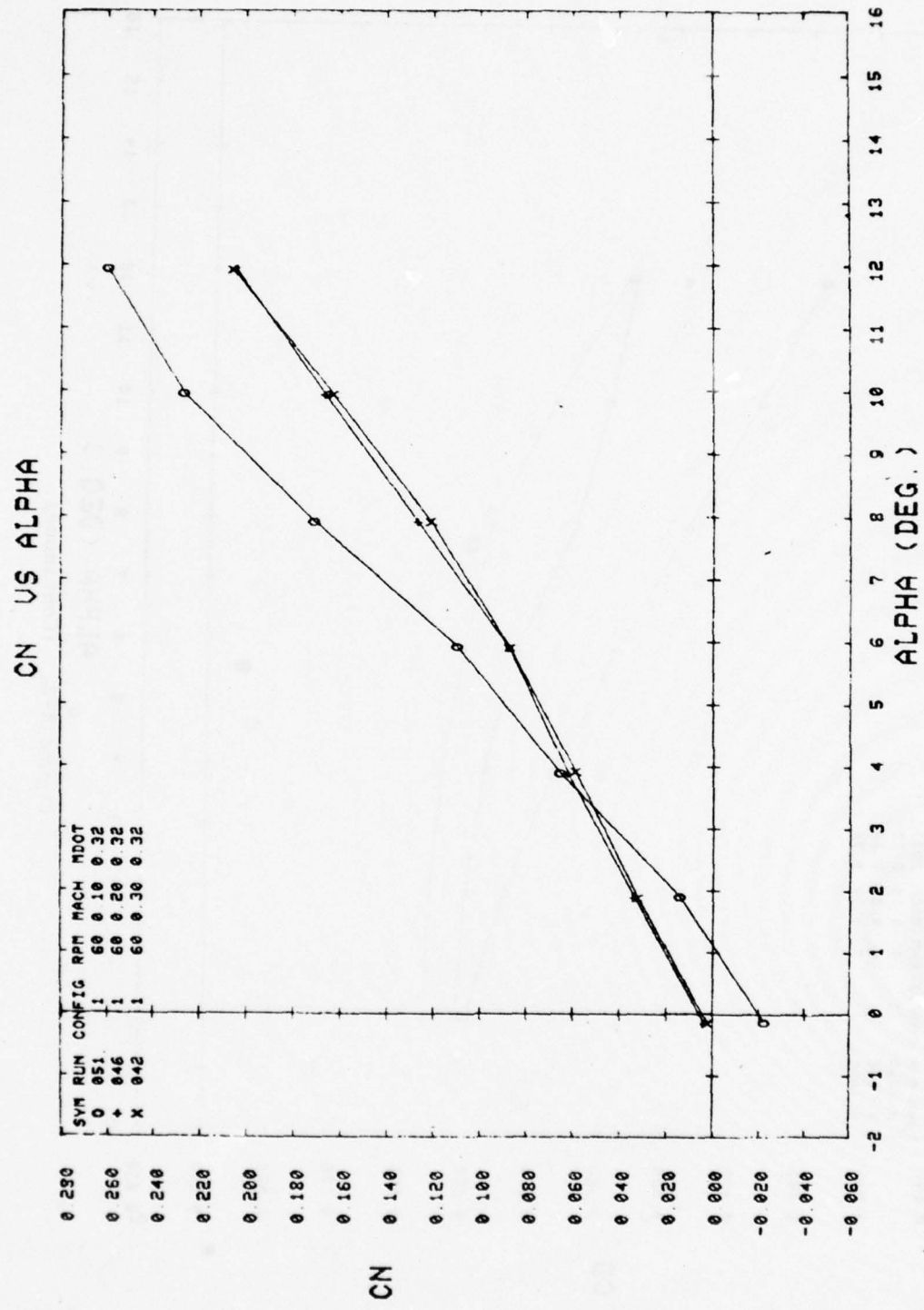


Figure A-2. (Continued).

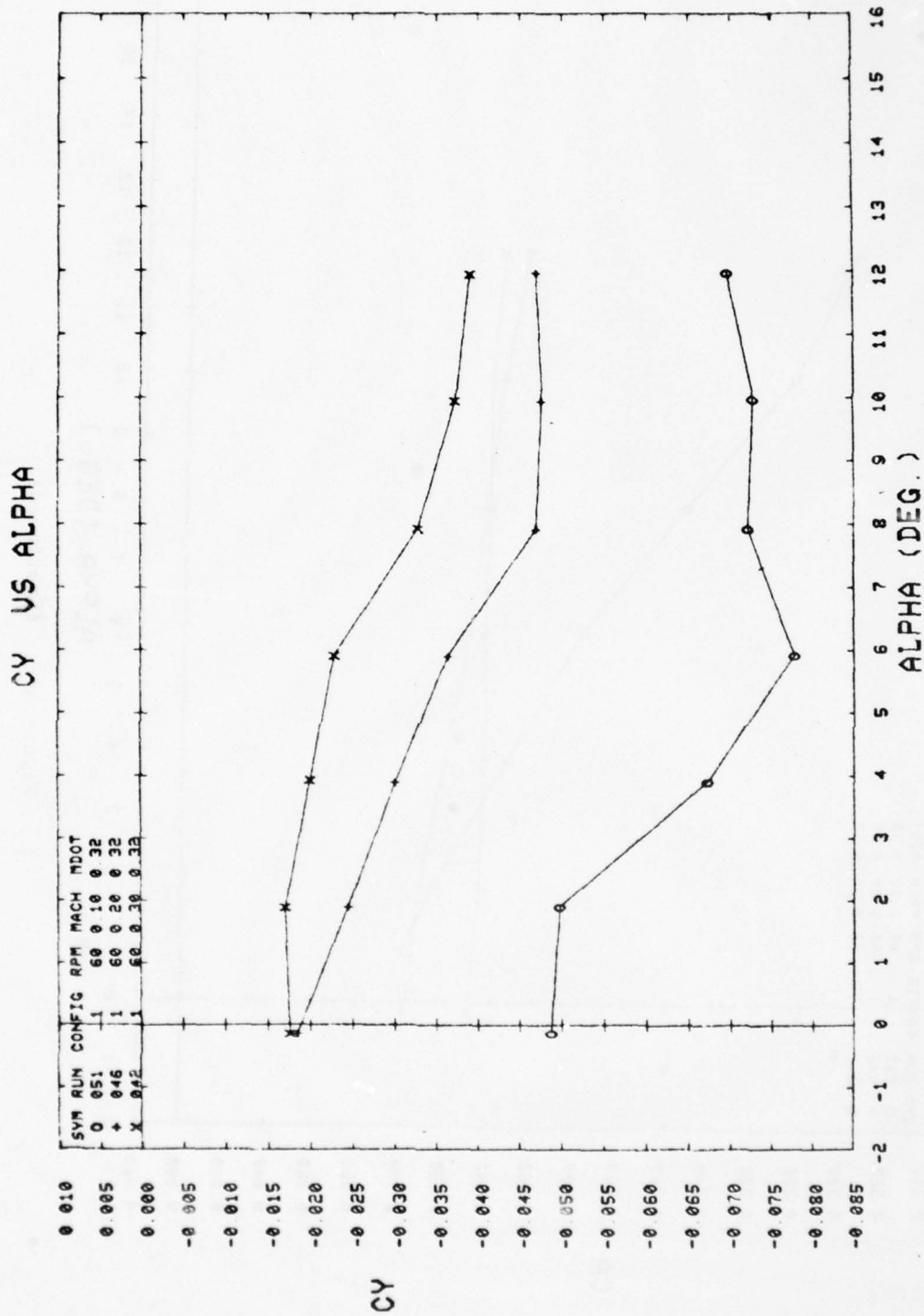


Figure A-2. (Continued).

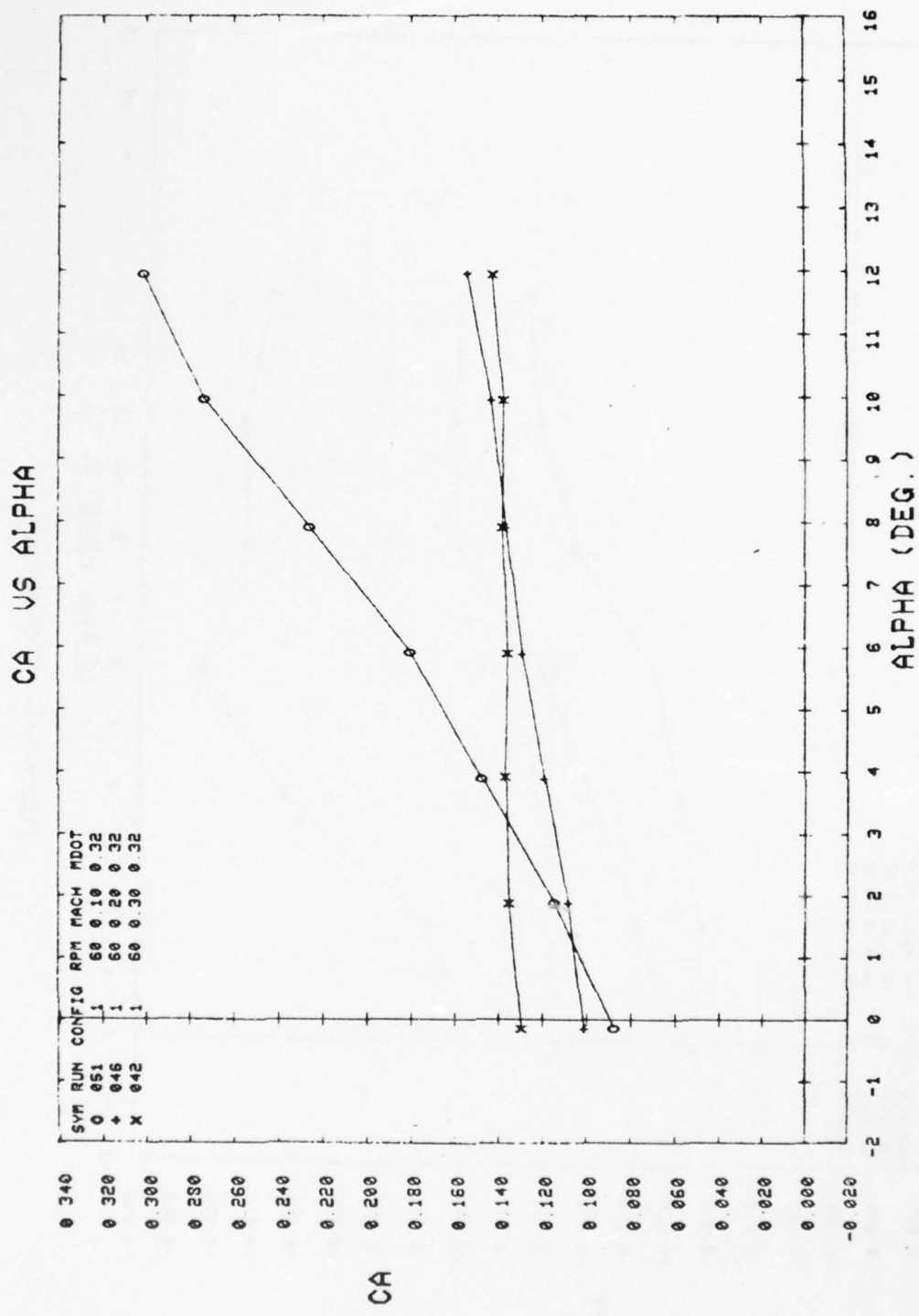


Figure A-2. (Continued).

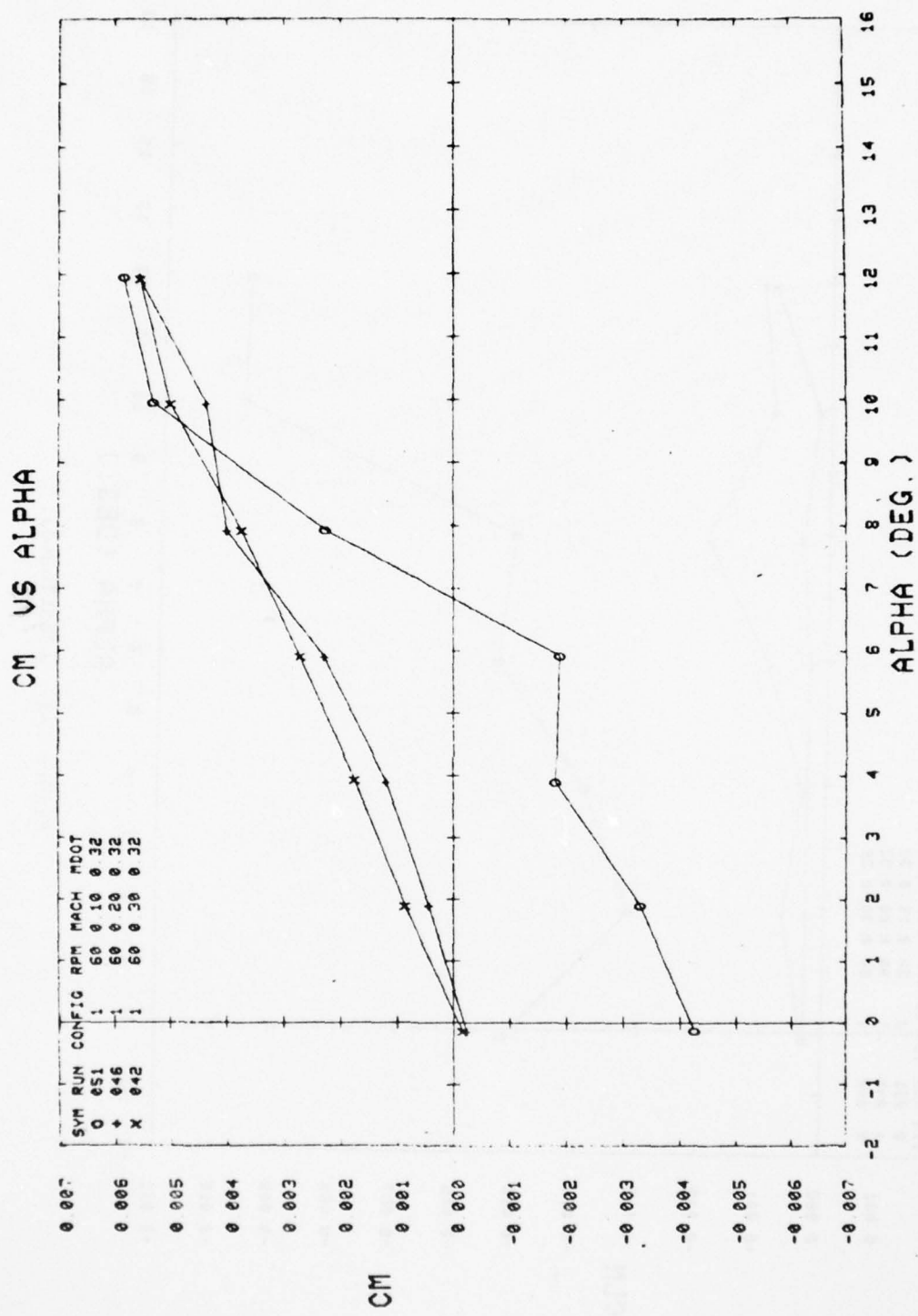


Figure A-2. (Continued).

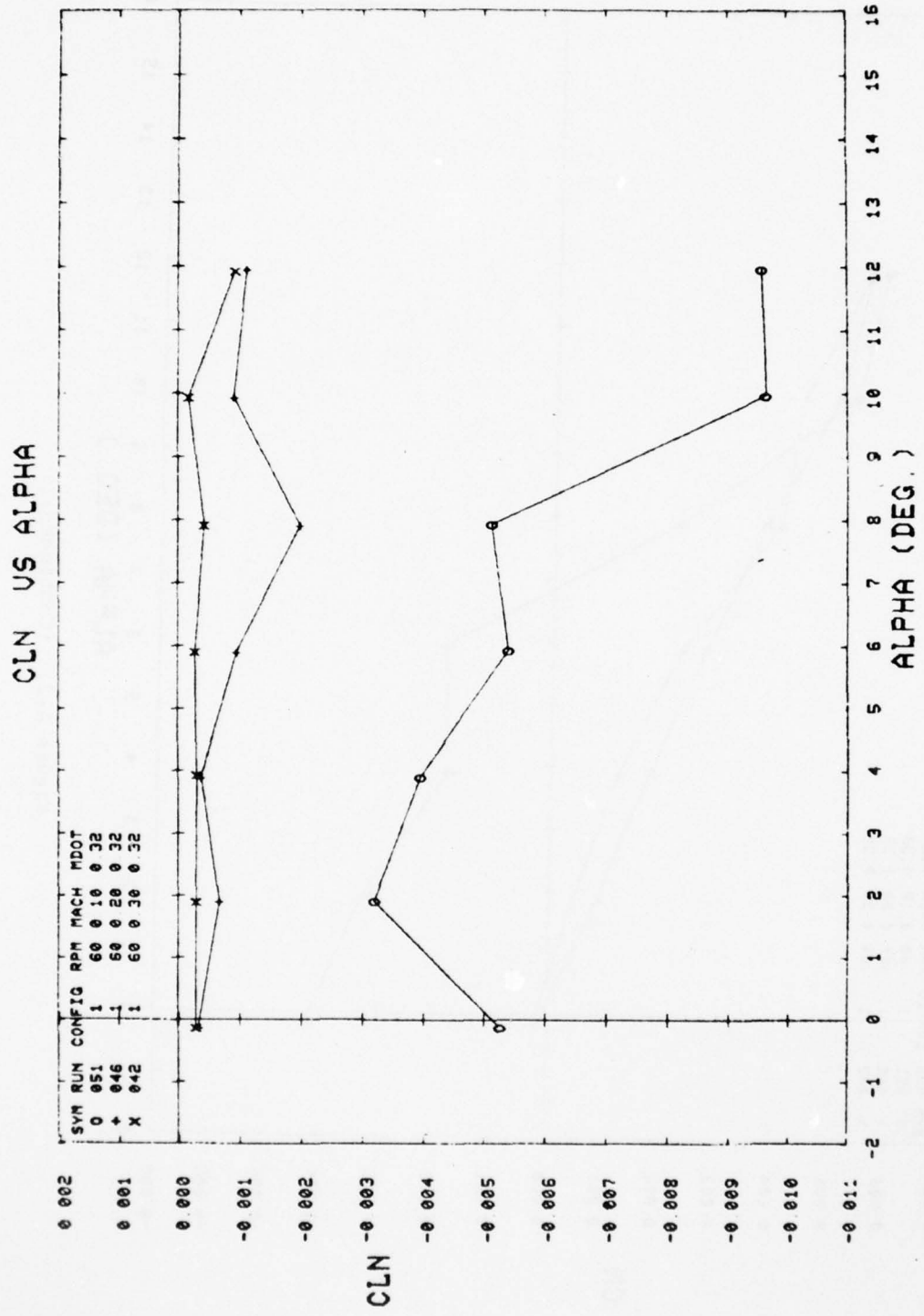


Figure A-2. (Continued).

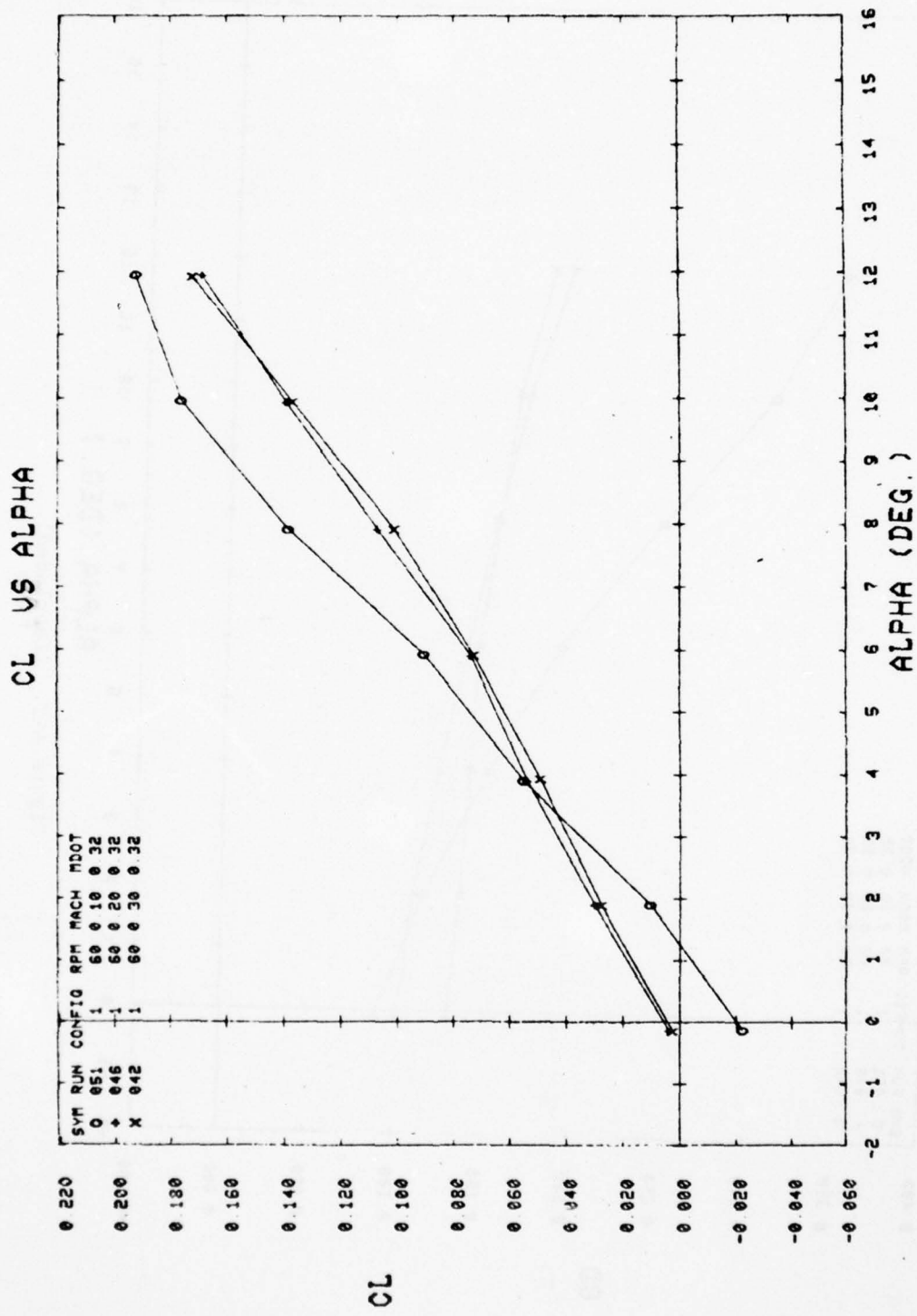


Figure A-2. (Continued).

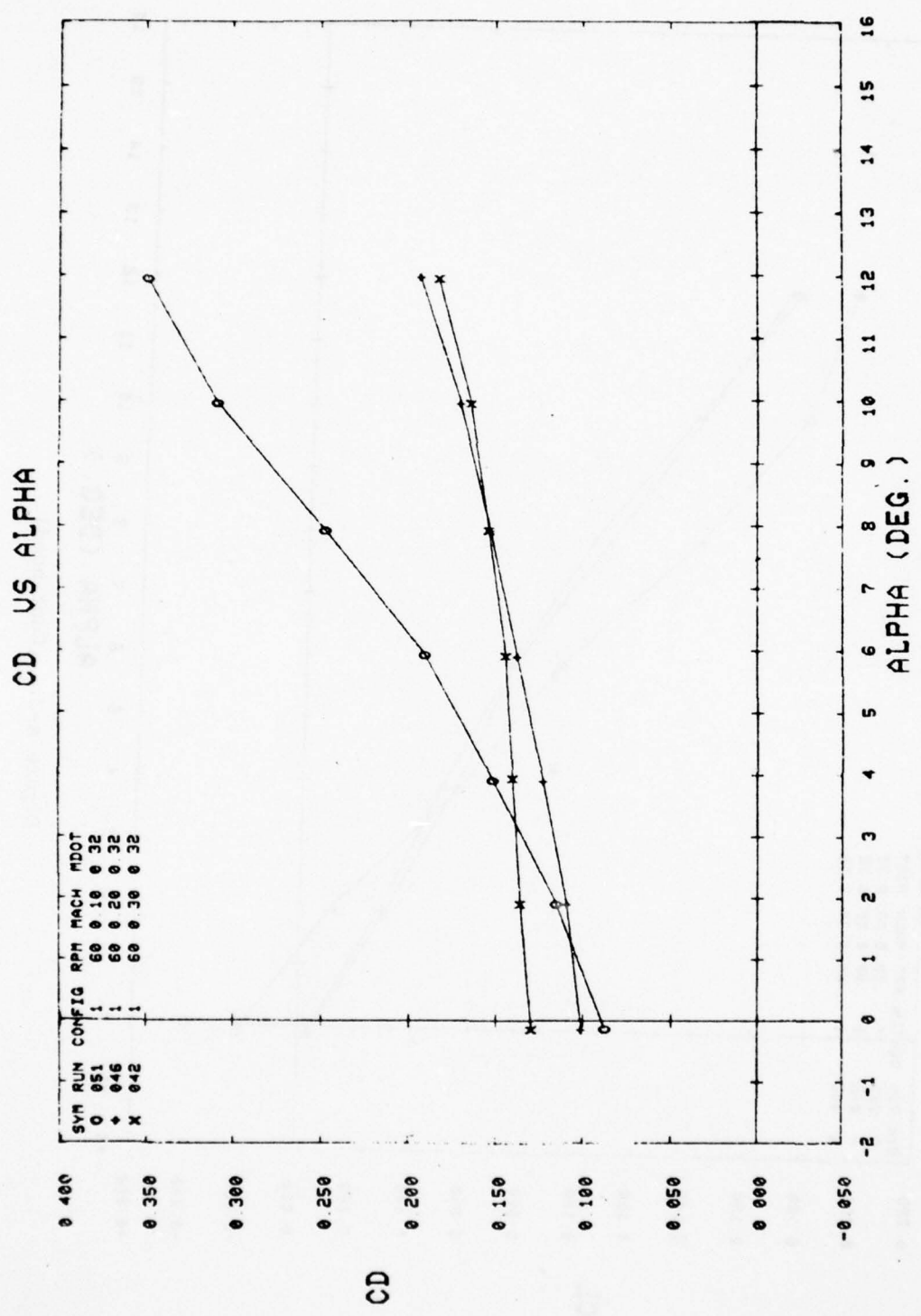


Figure A-2. (Concluded).

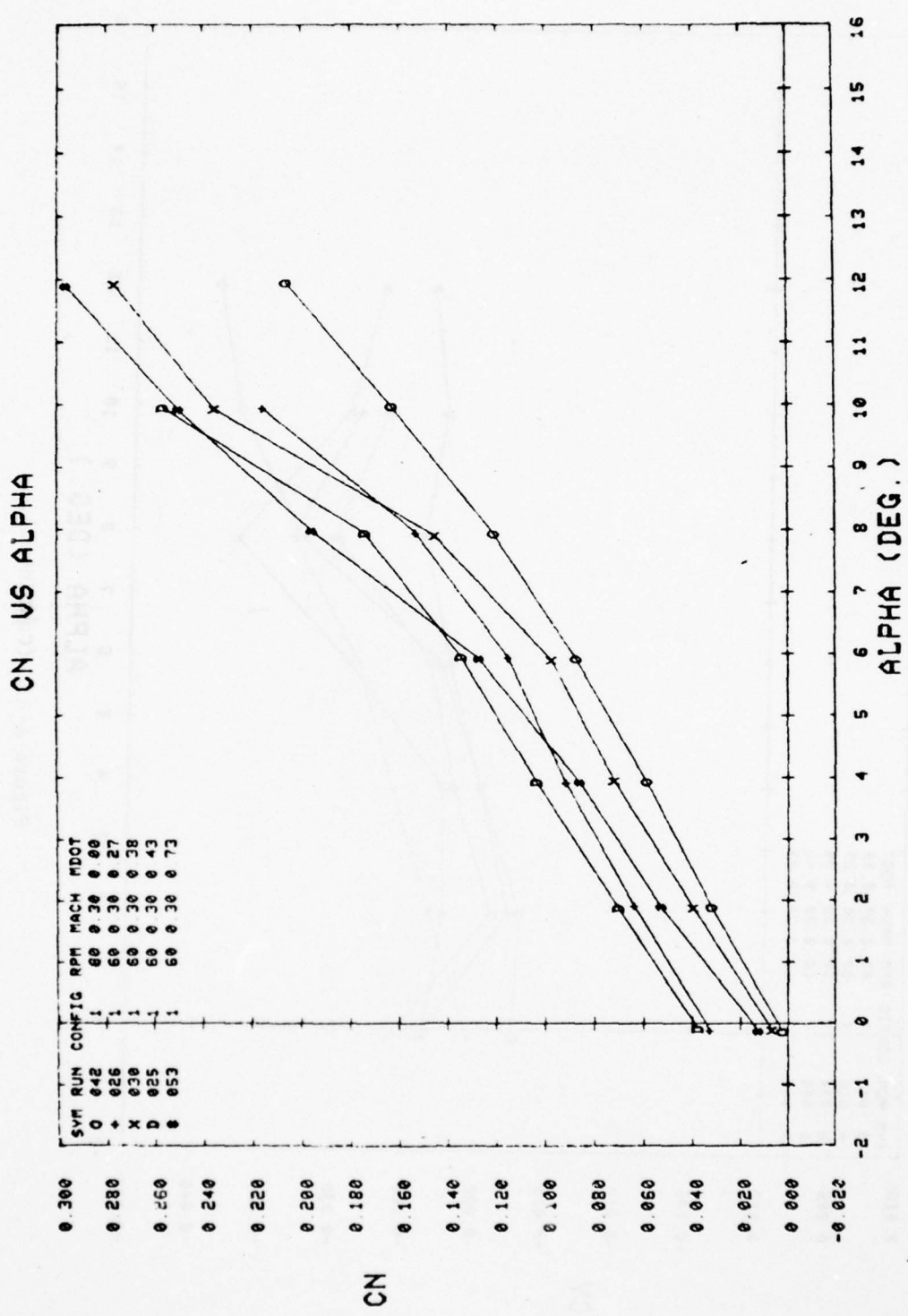


Figure A-3. Configuration 1 — aerodynamics coefficients versus alpha with varying mass flow from nozzle.

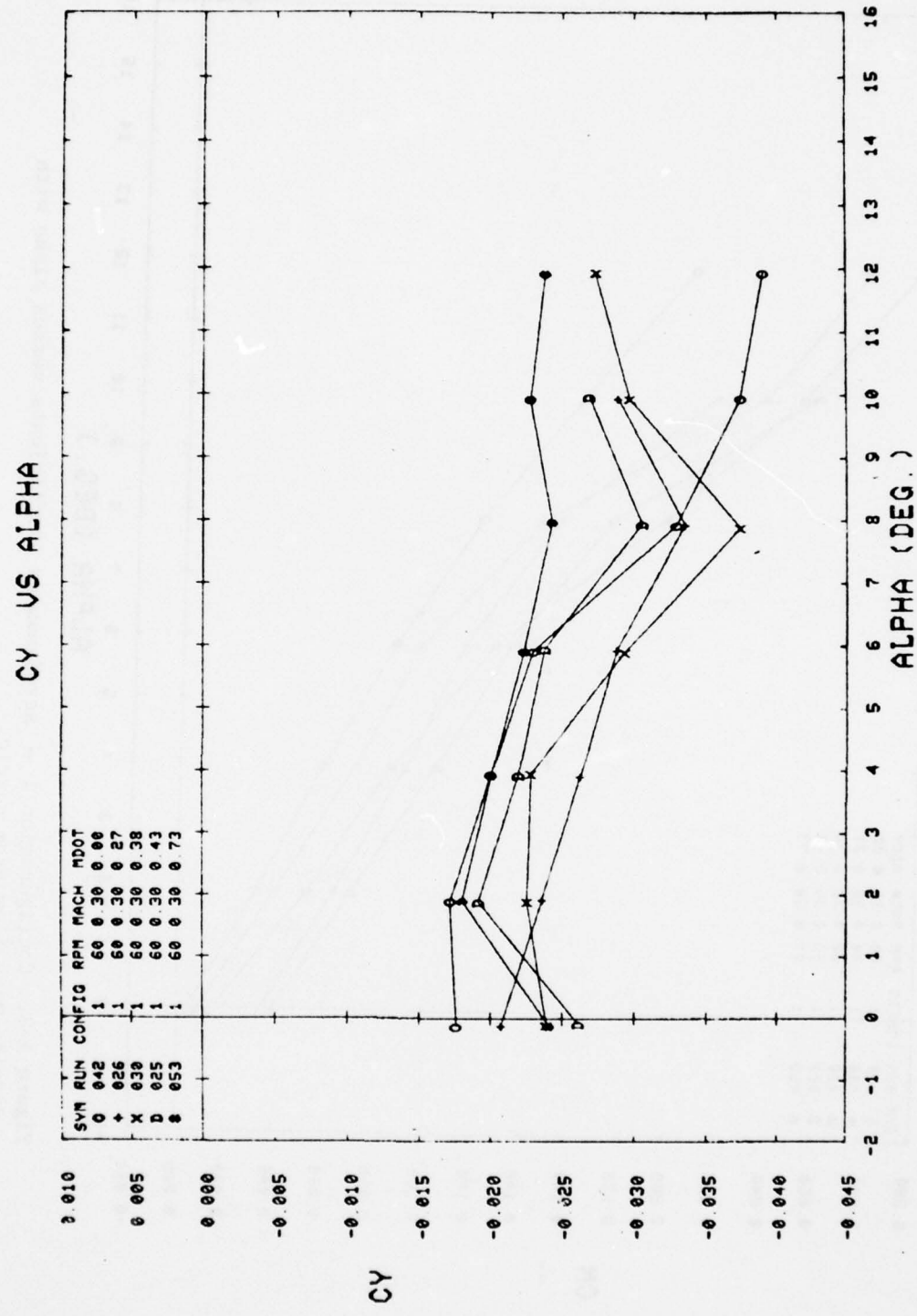


Figure A-3. (Continued).

CA VS ALPHA

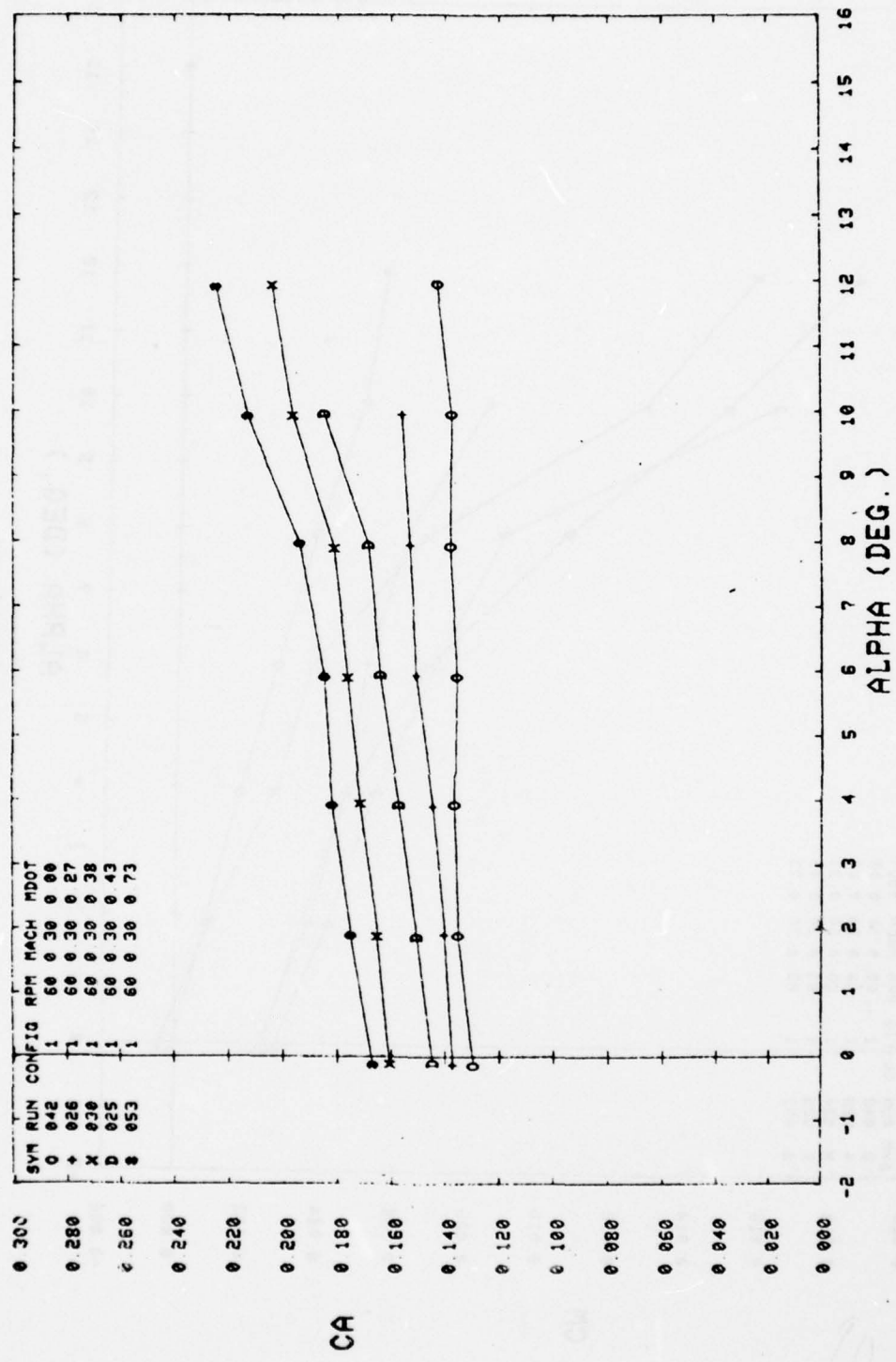


Figure A-3. (Continued).

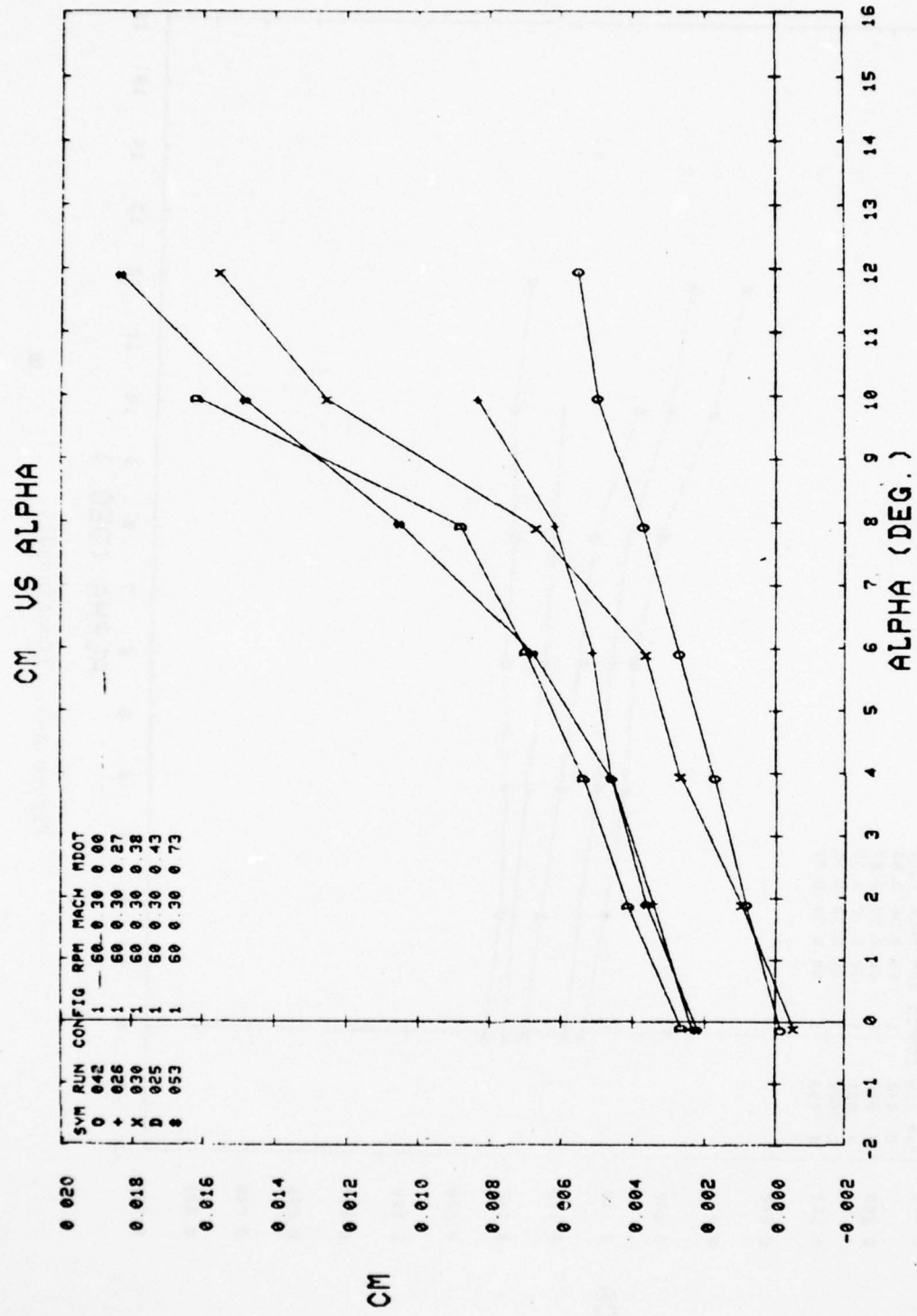


Figure A-3. (Continued).

CLN VS ALPHA

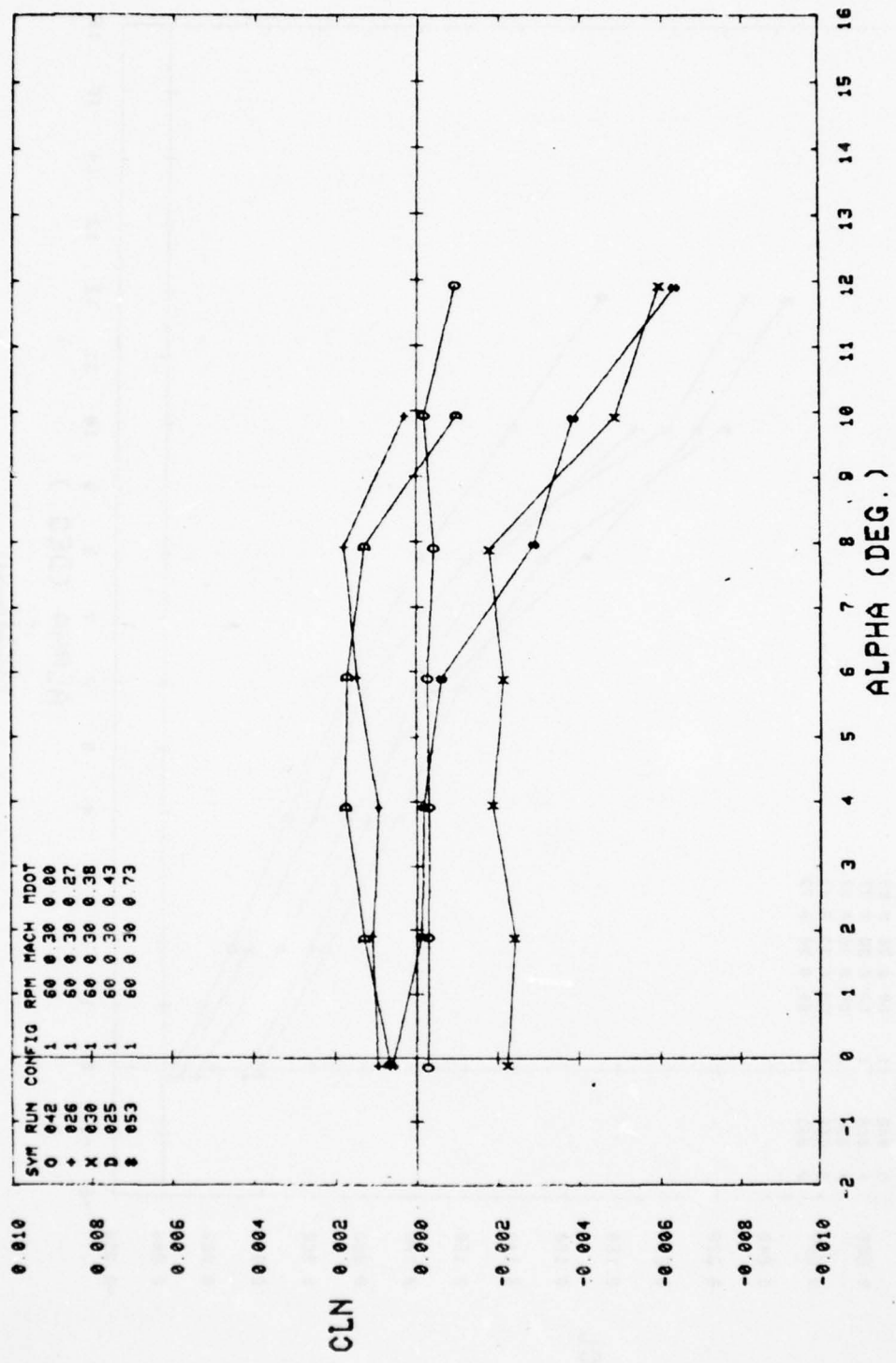


Figure A-3. (Continued).

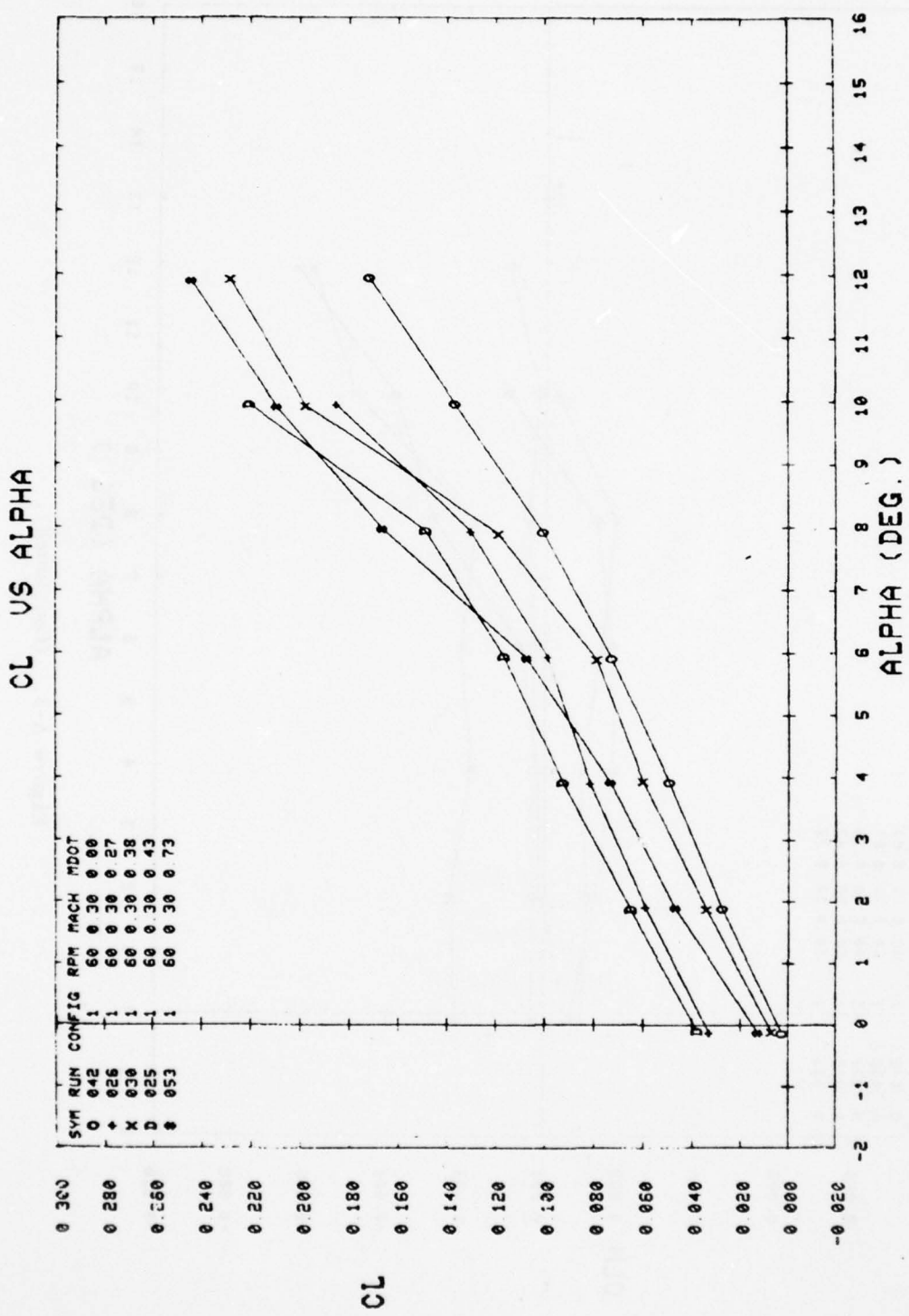


Figure A-3. (Continued).

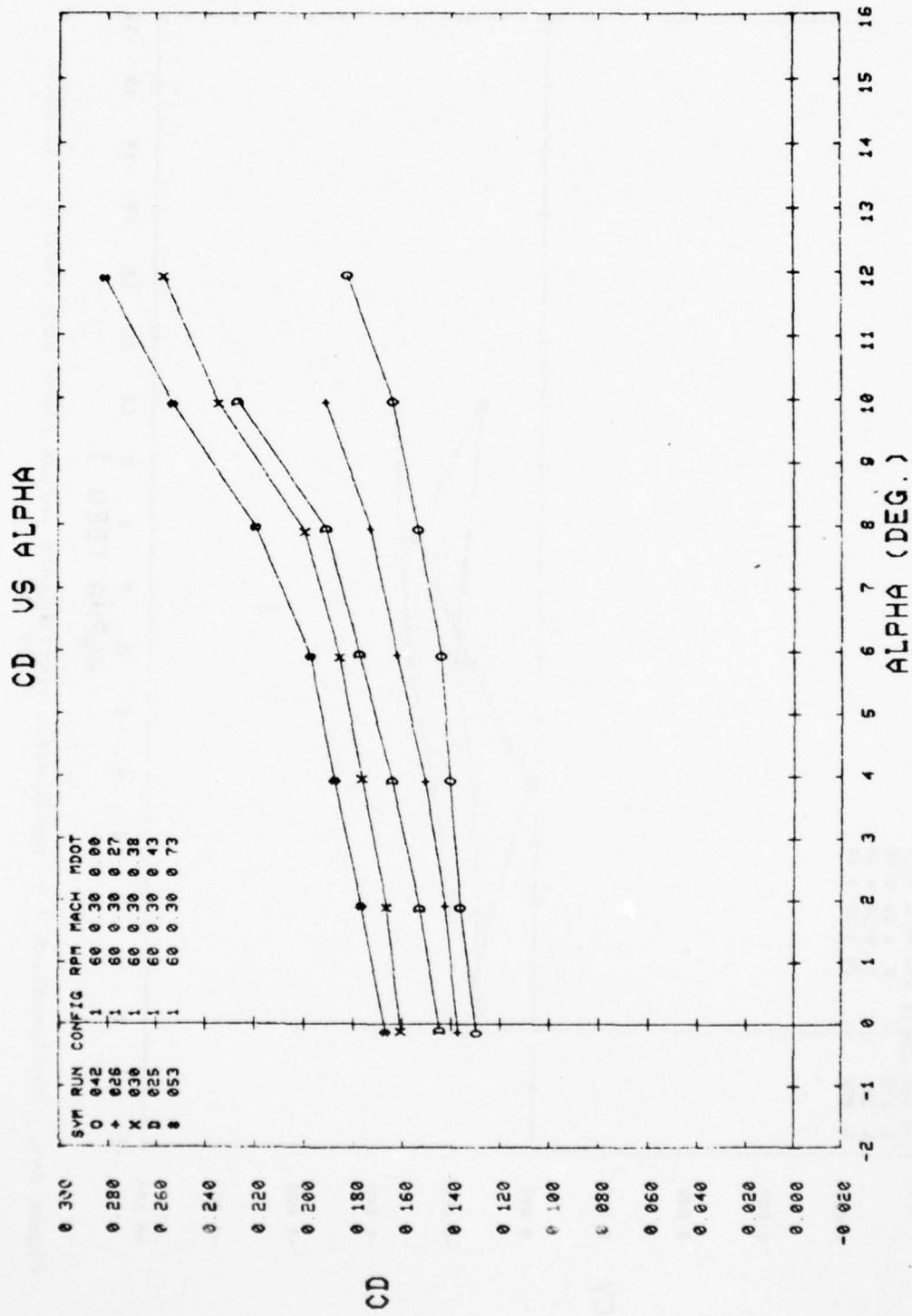


Figure A-3. (Concluded).

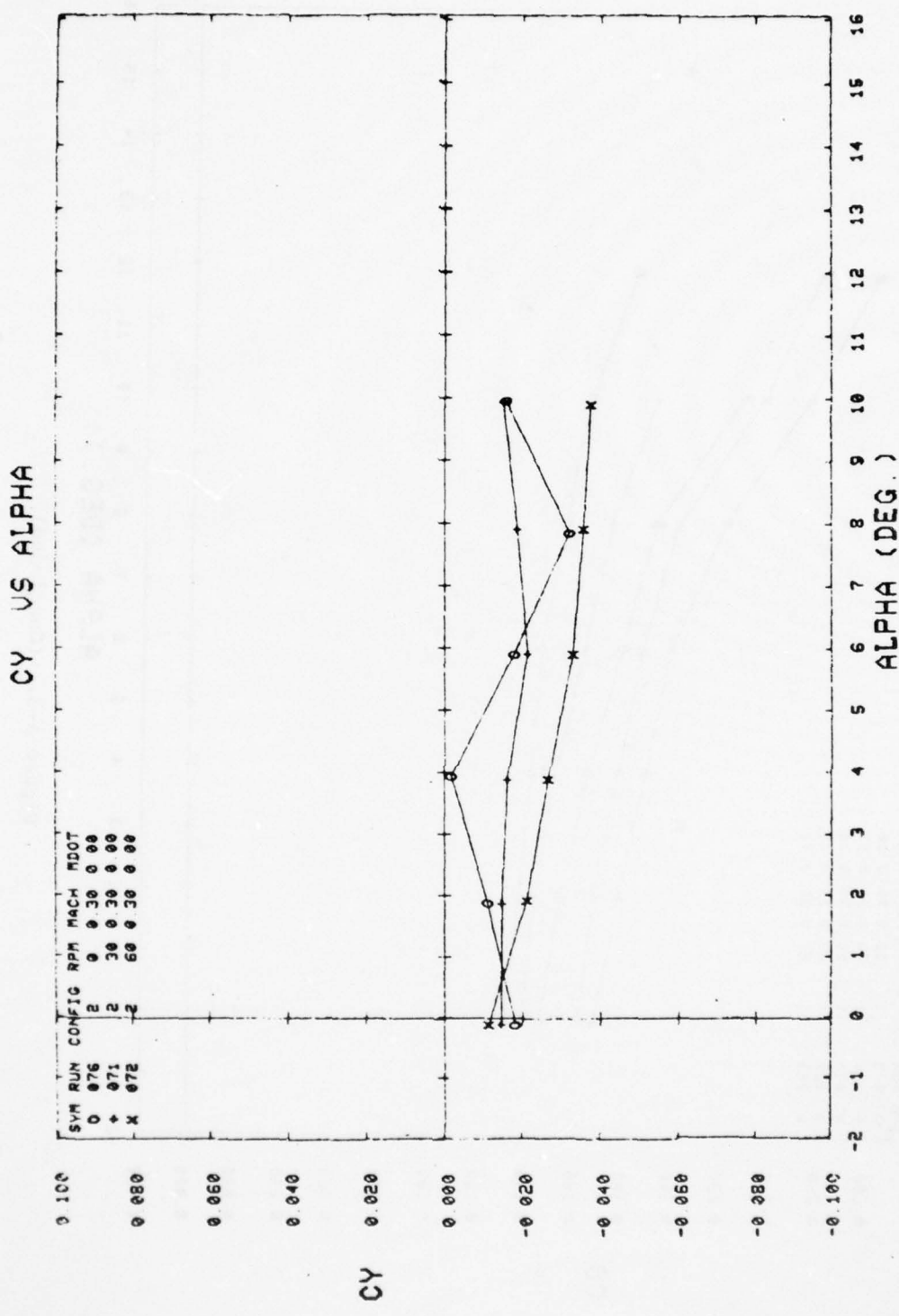


Figure A-4. Configuration 2 — aerodynamic coefficients versus alpha with varying spin rate.

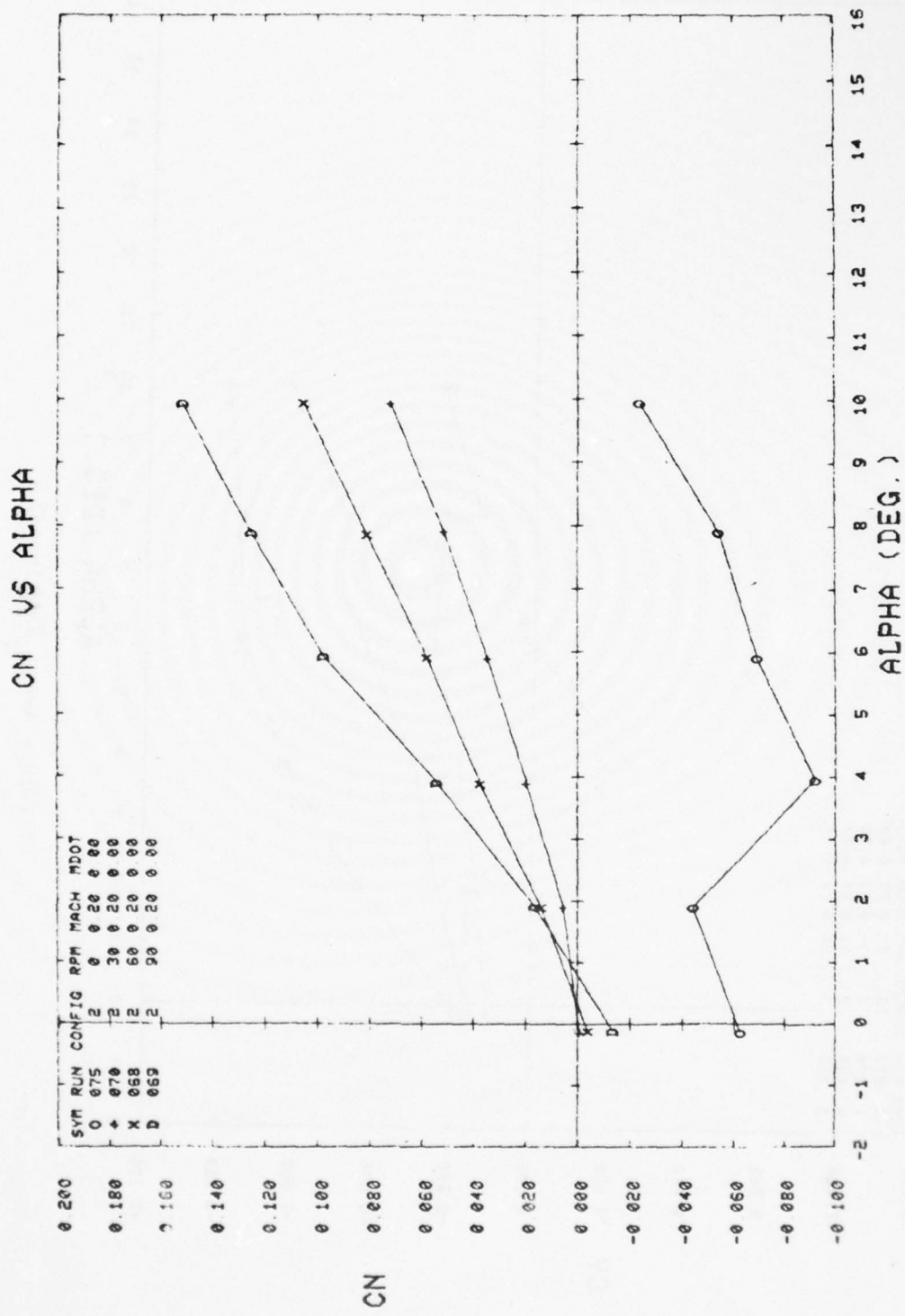


Figure A-4. (Continued).

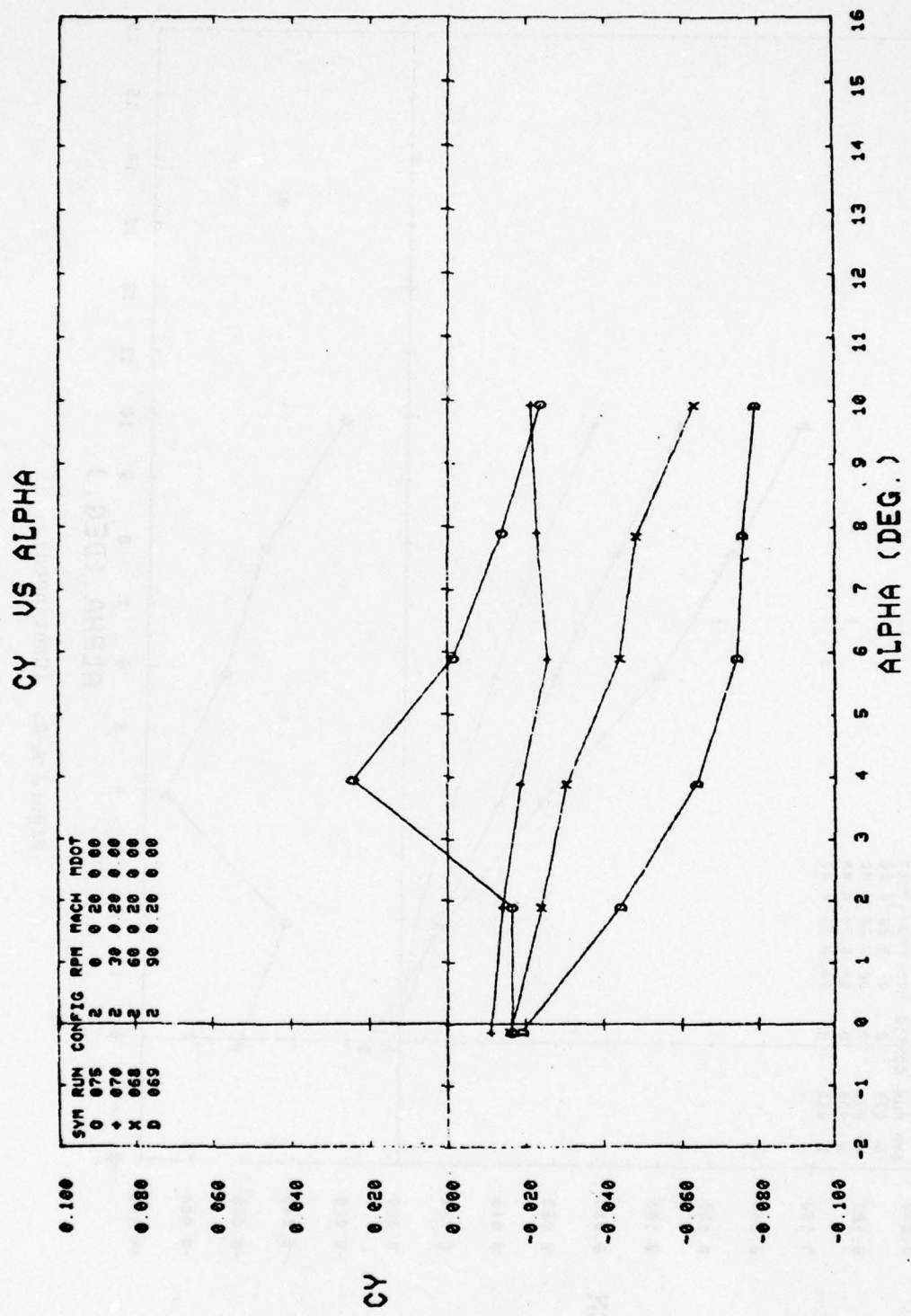


Figure A-4. (Continued).

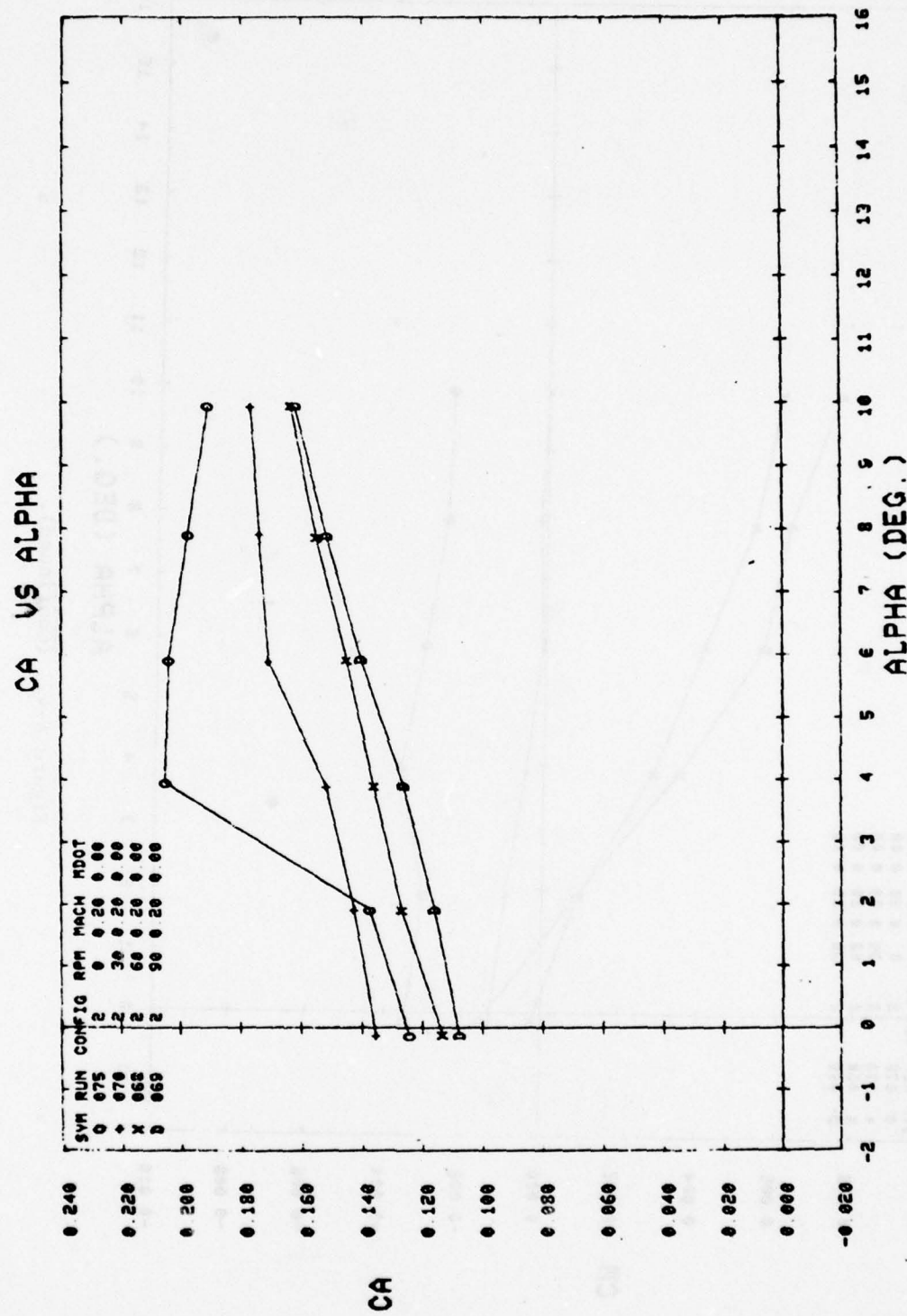


Figure A-4. (Continued).

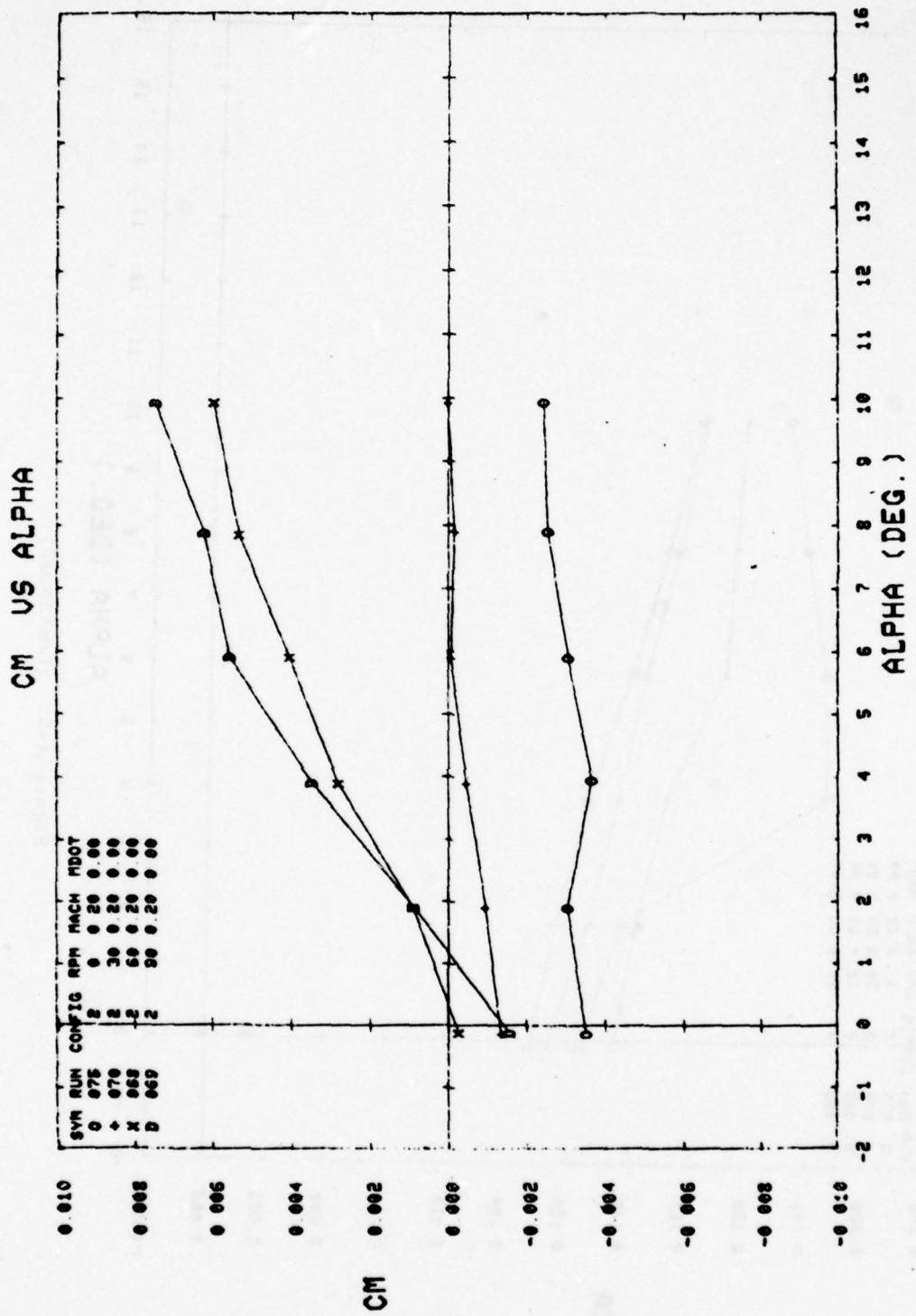


Figure A-4. (Continued).

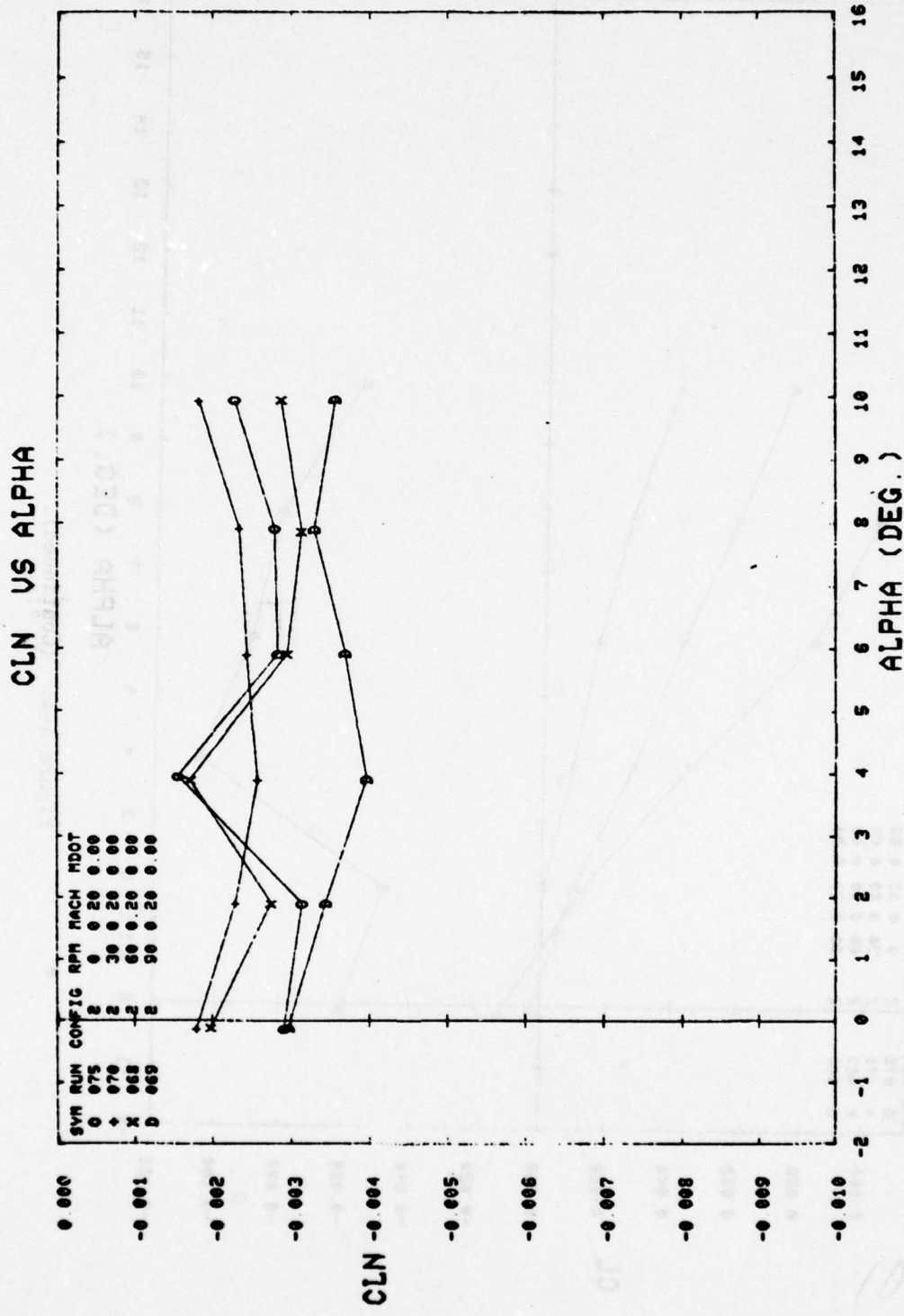


Figure A-4. (Continued).

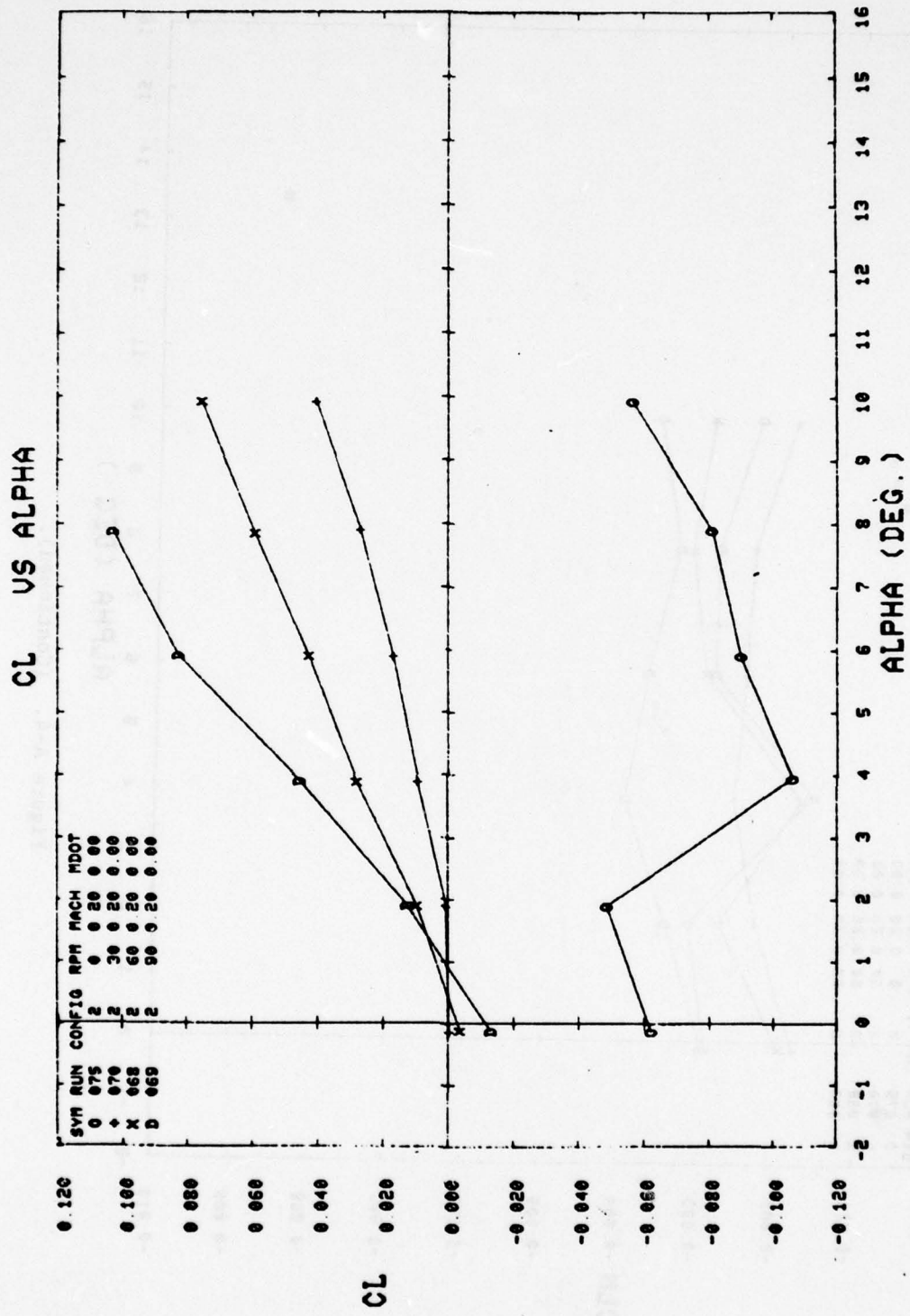


Figure A-4. (Continued).

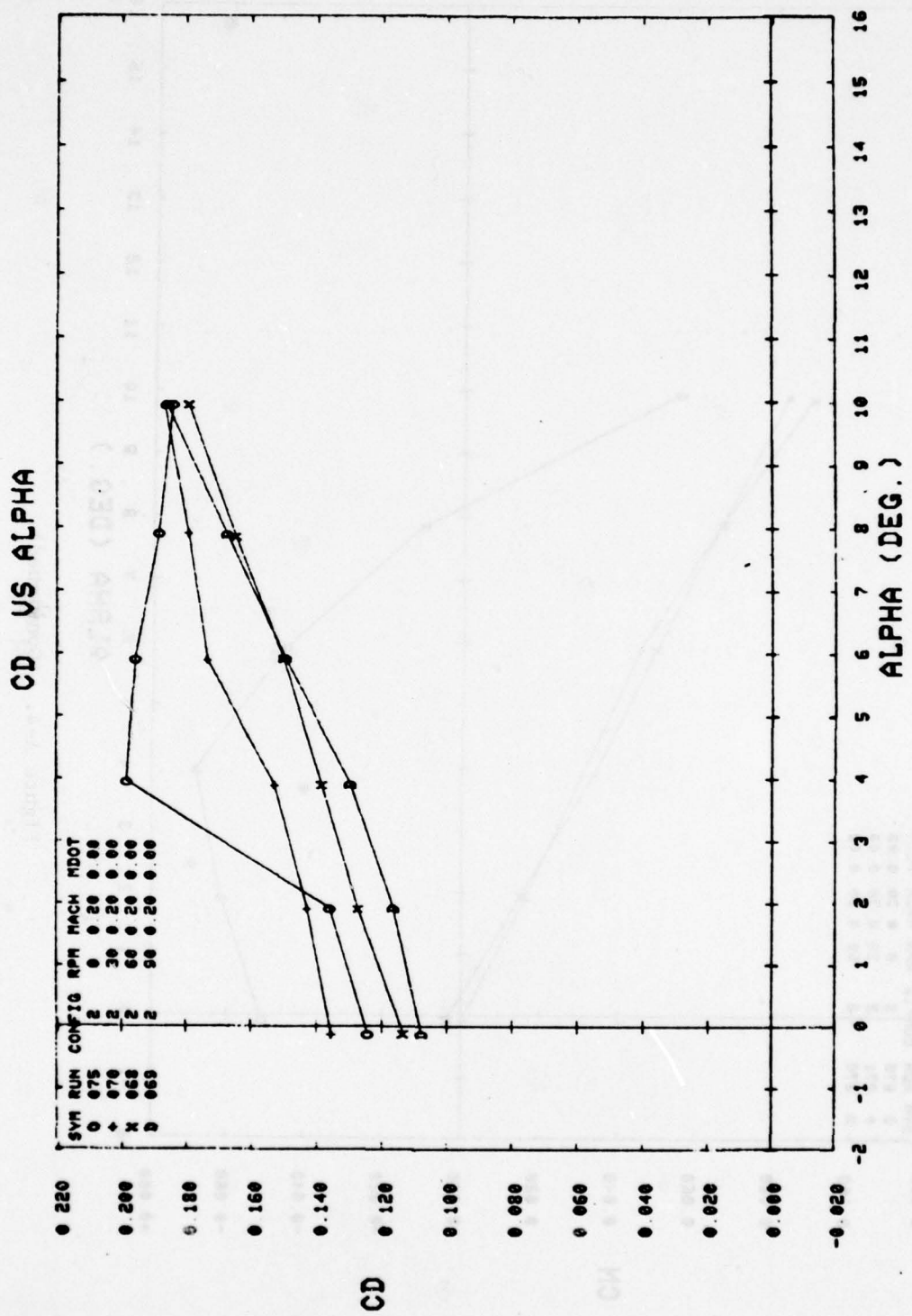


Figure A-4. (Continued).

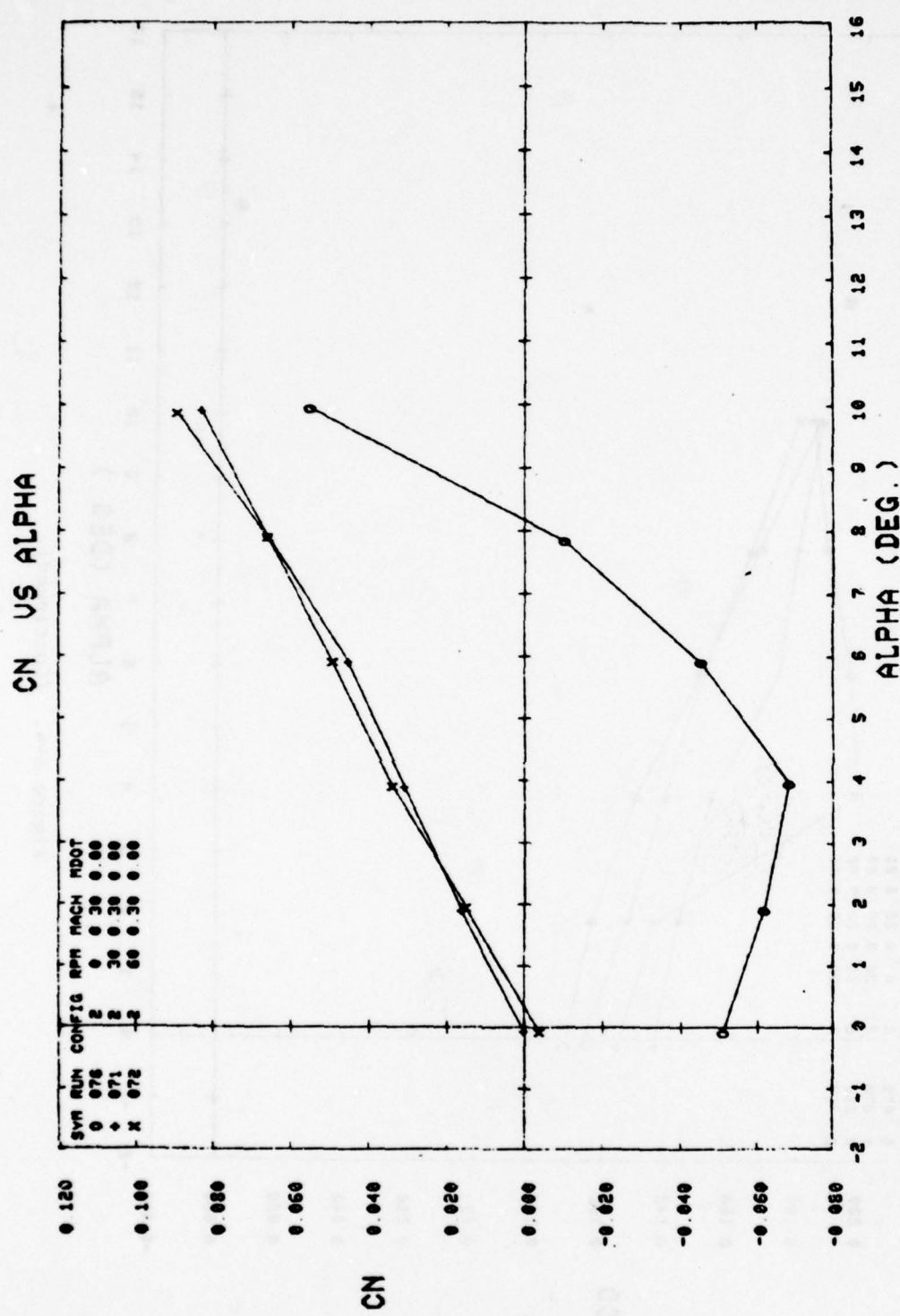


Figure A-4. (Continued).

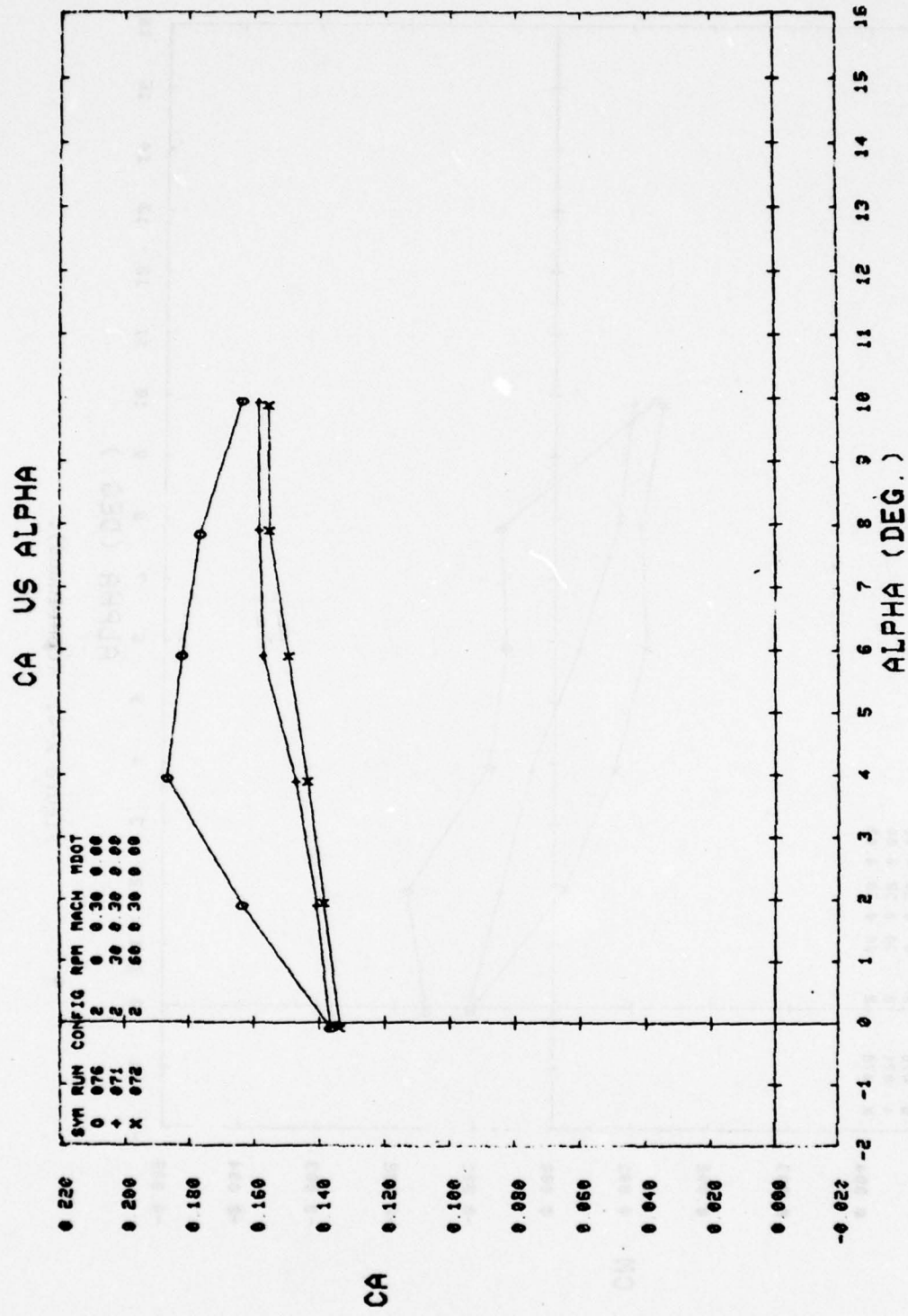


Figure A-4. (Continued).

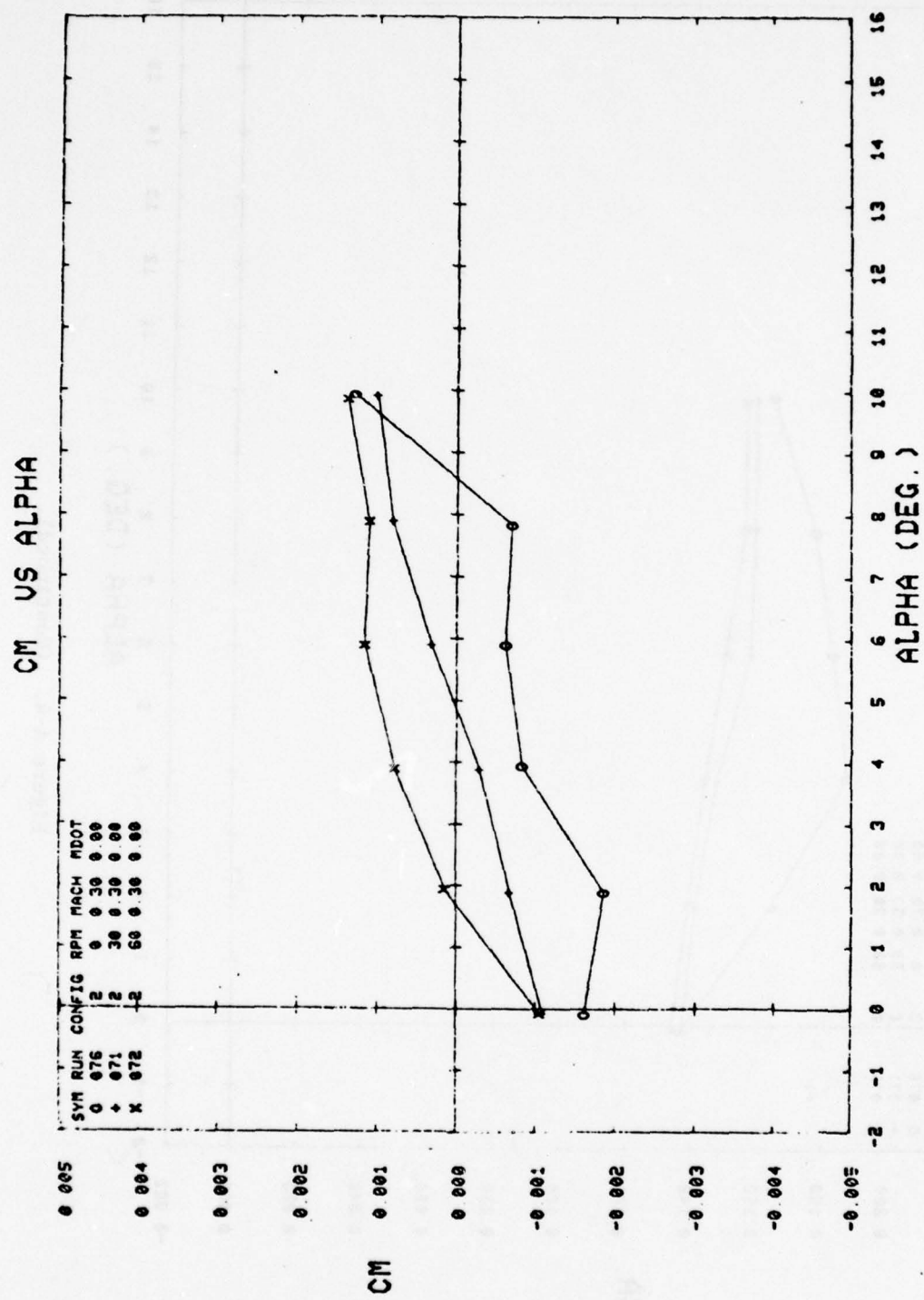


Figure A-4. (Continued).

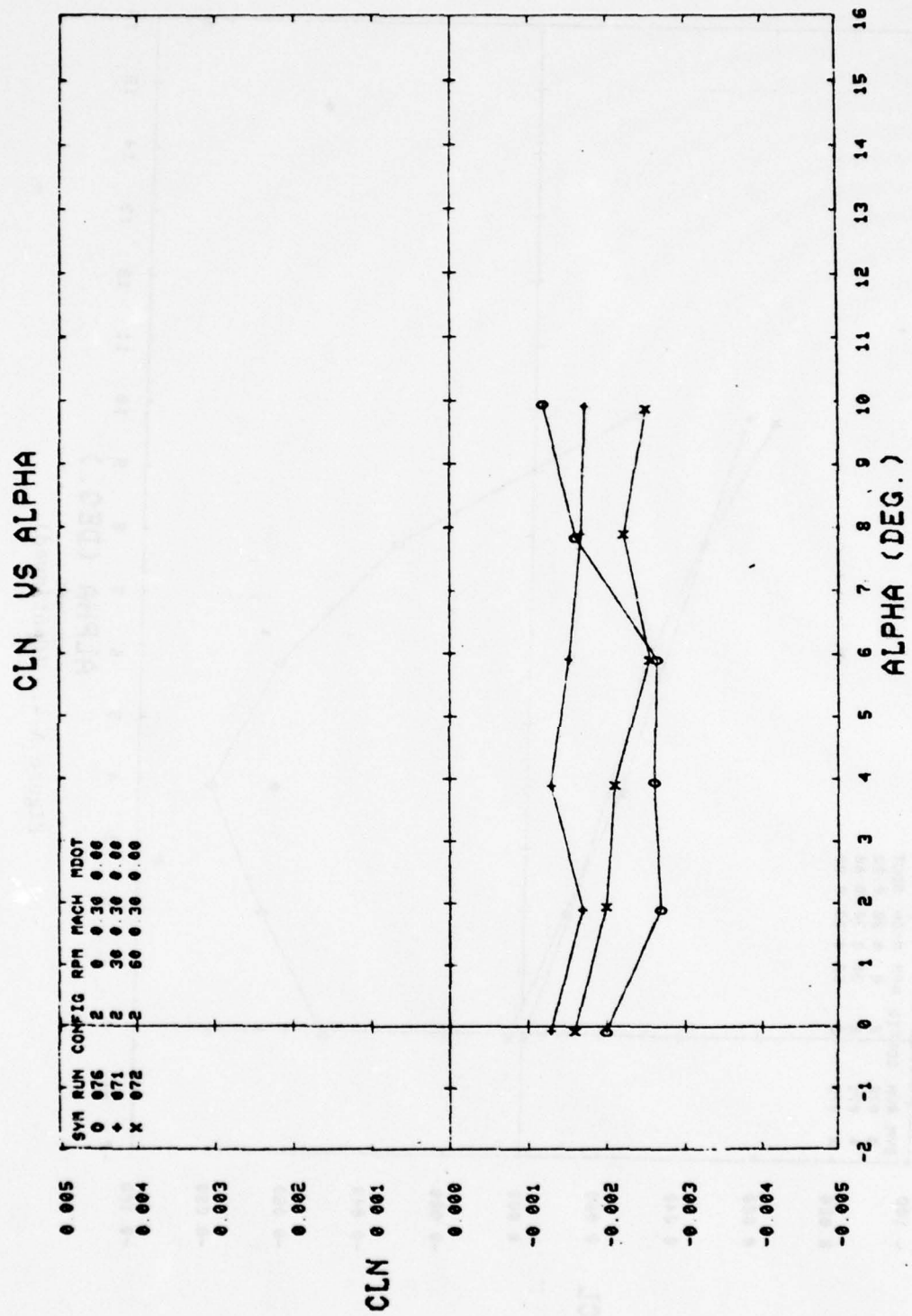


Figure A-4. (Continued).

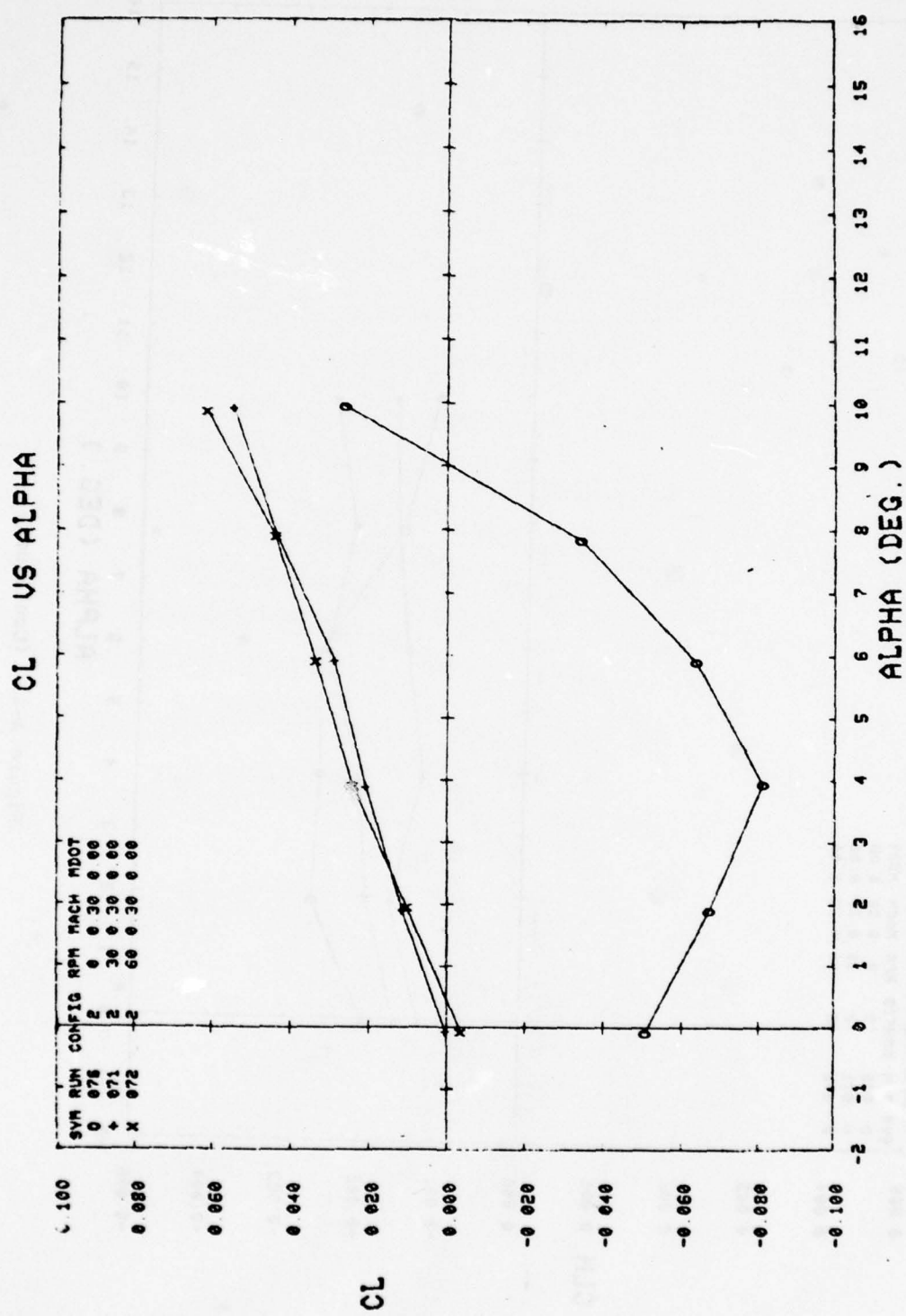


Figure A-4. (Continued).

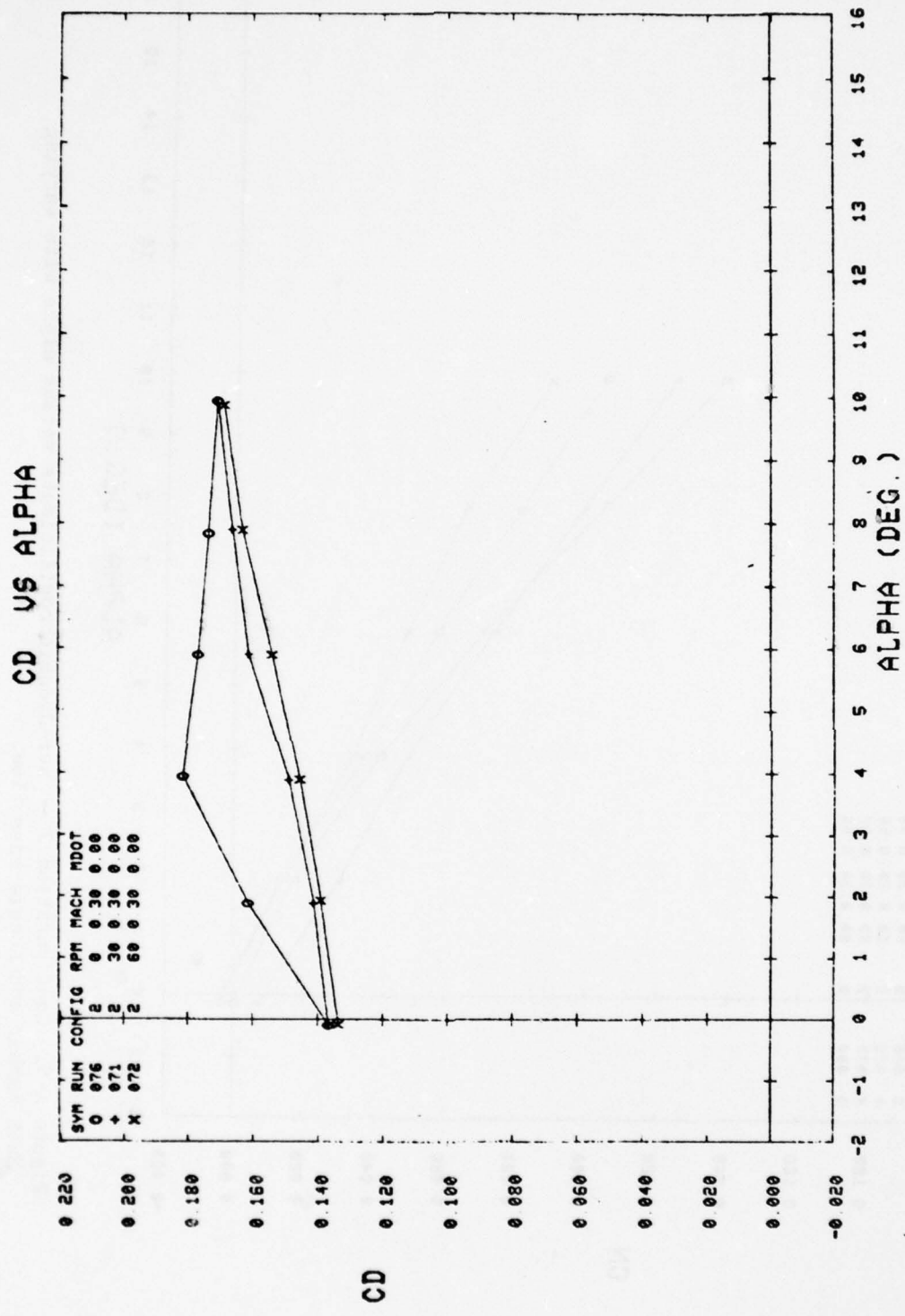


Figure A-4. (Concluded).

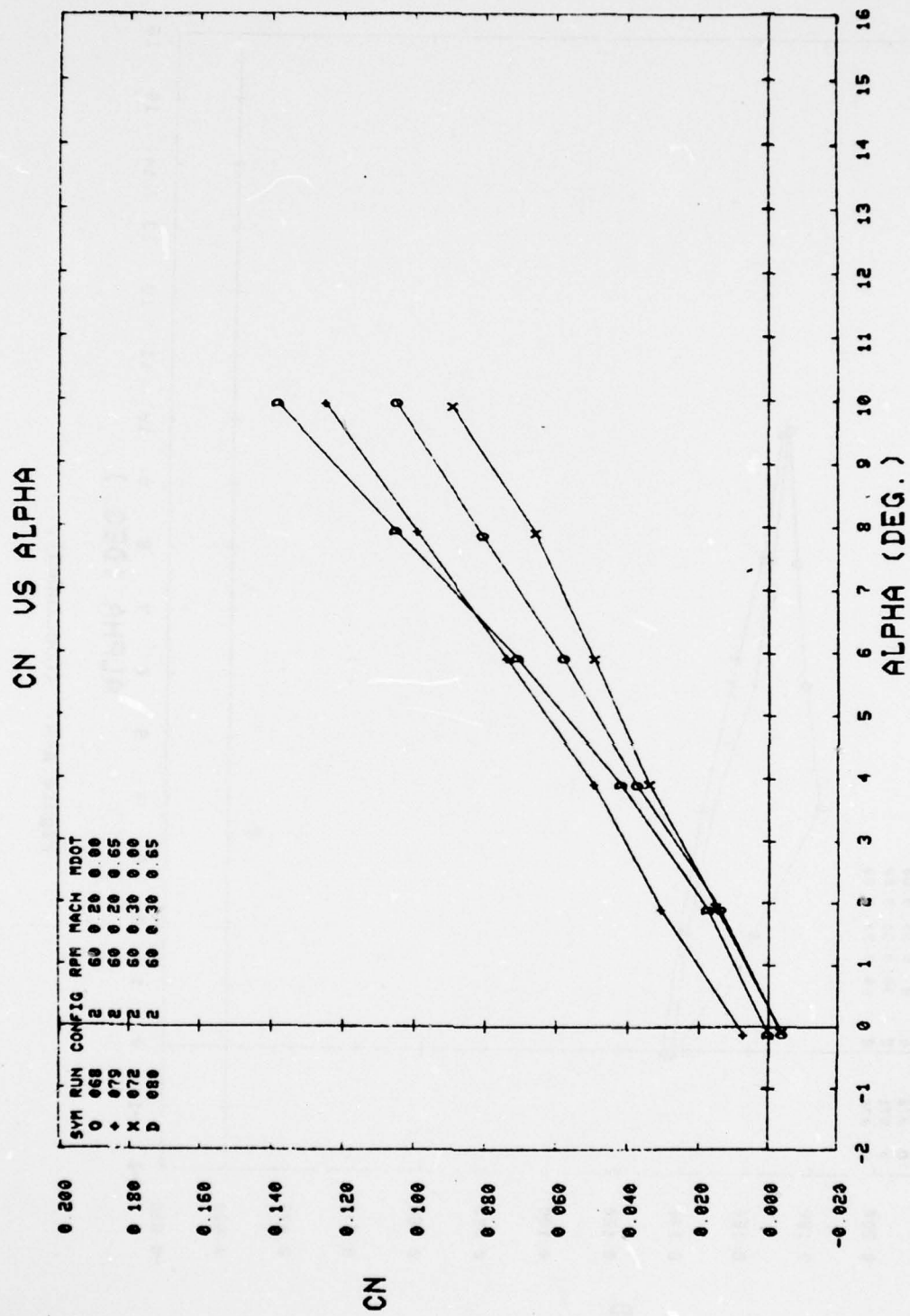


Figure A-5. Configuration 2 — aerodynamic coefficients versus alpha with varying Mach number and nozzle mass flow.

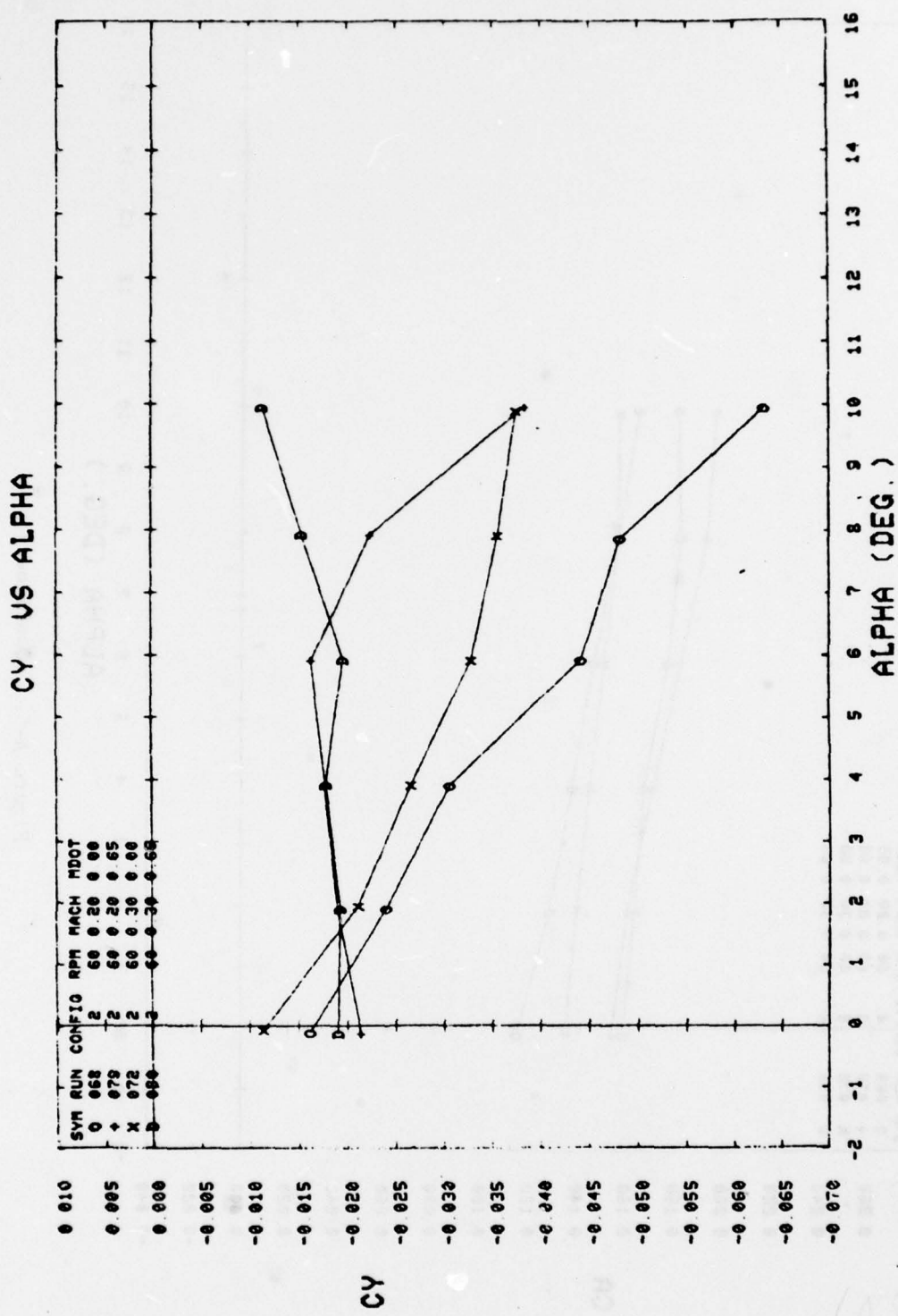


Figure A-5. (Continued).

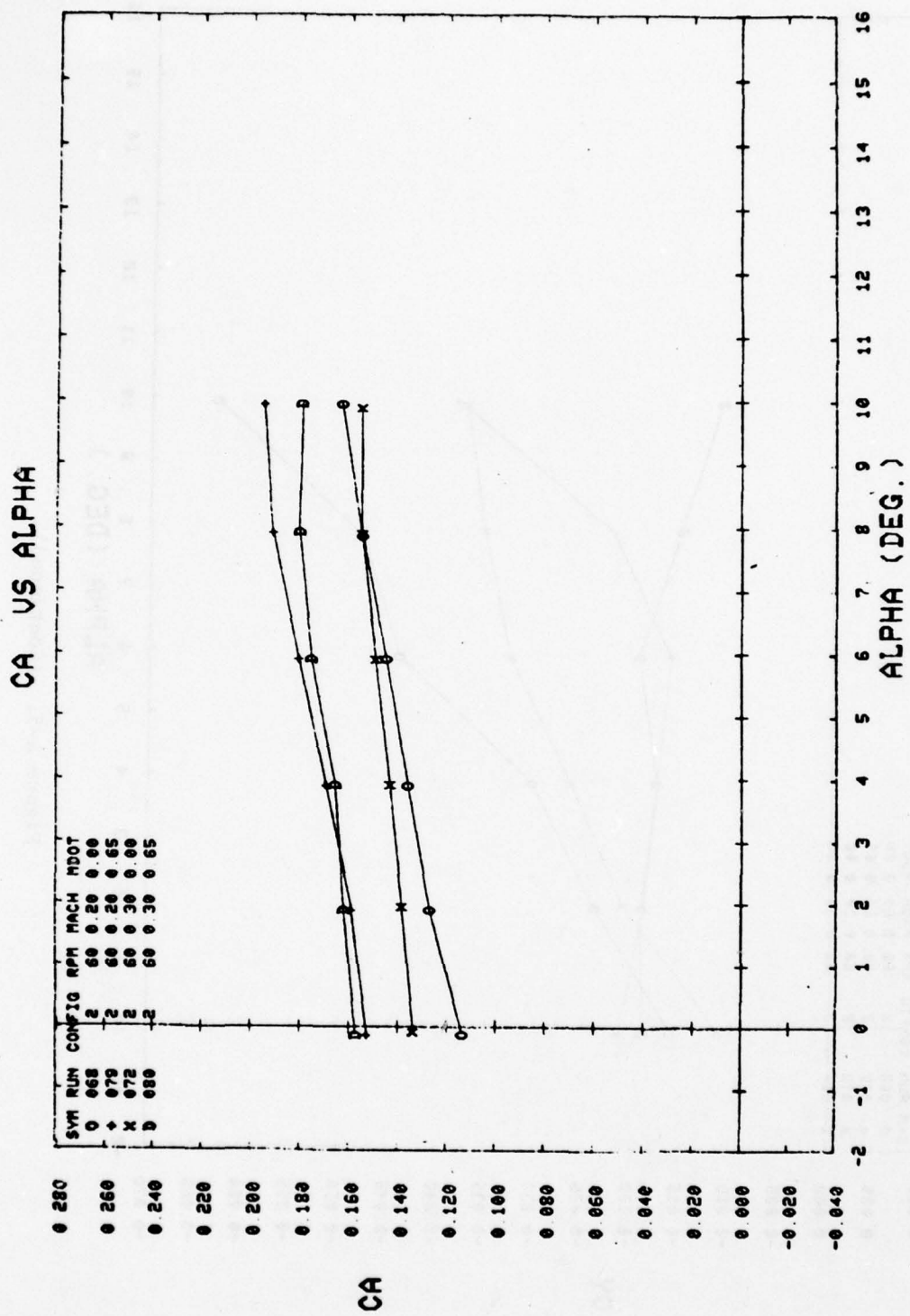


Figure A-5. (Continued).

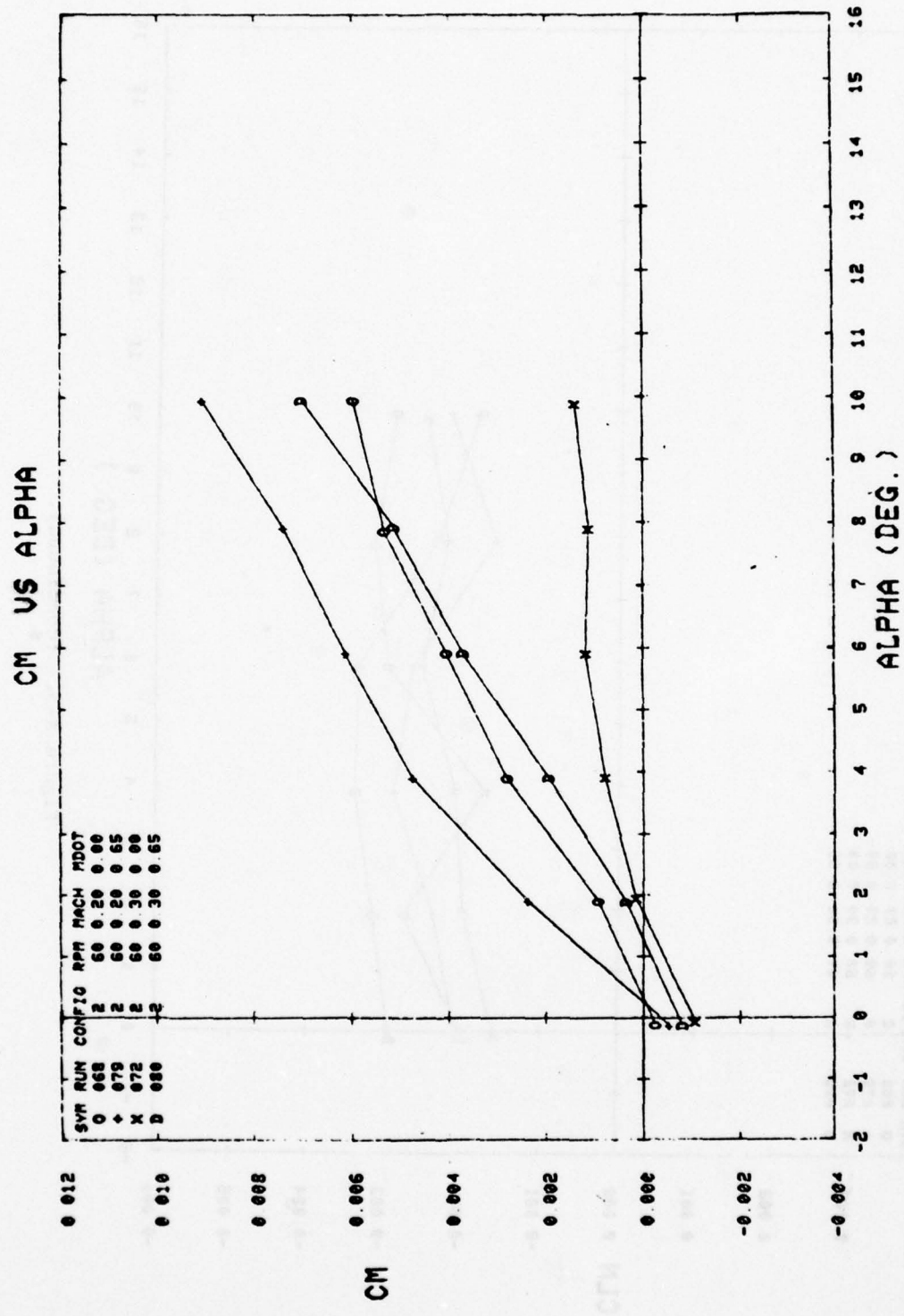


Figure A-5. (Continued).

CLN VS ALPHA

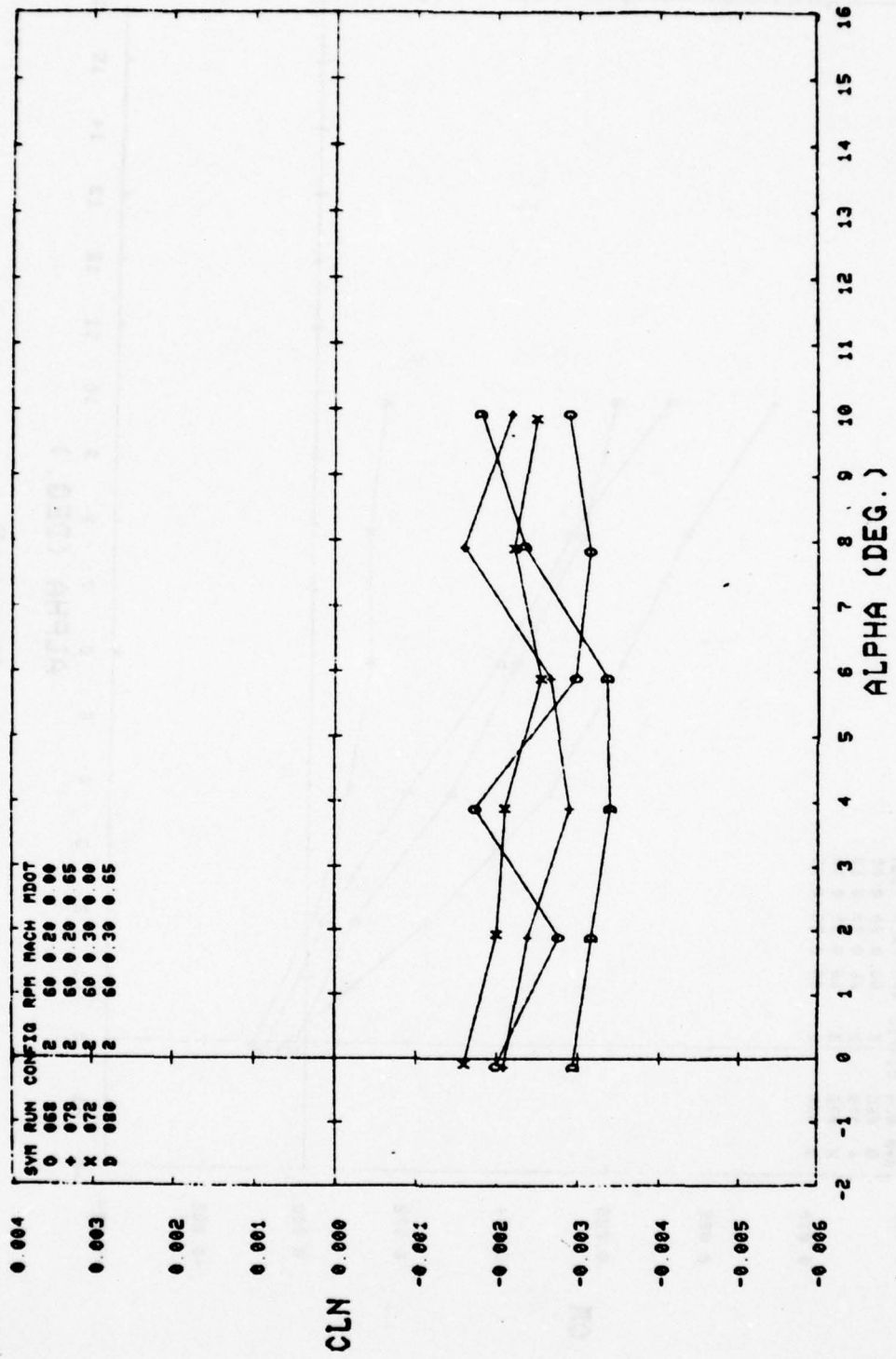


Figure A-5. (Continued).

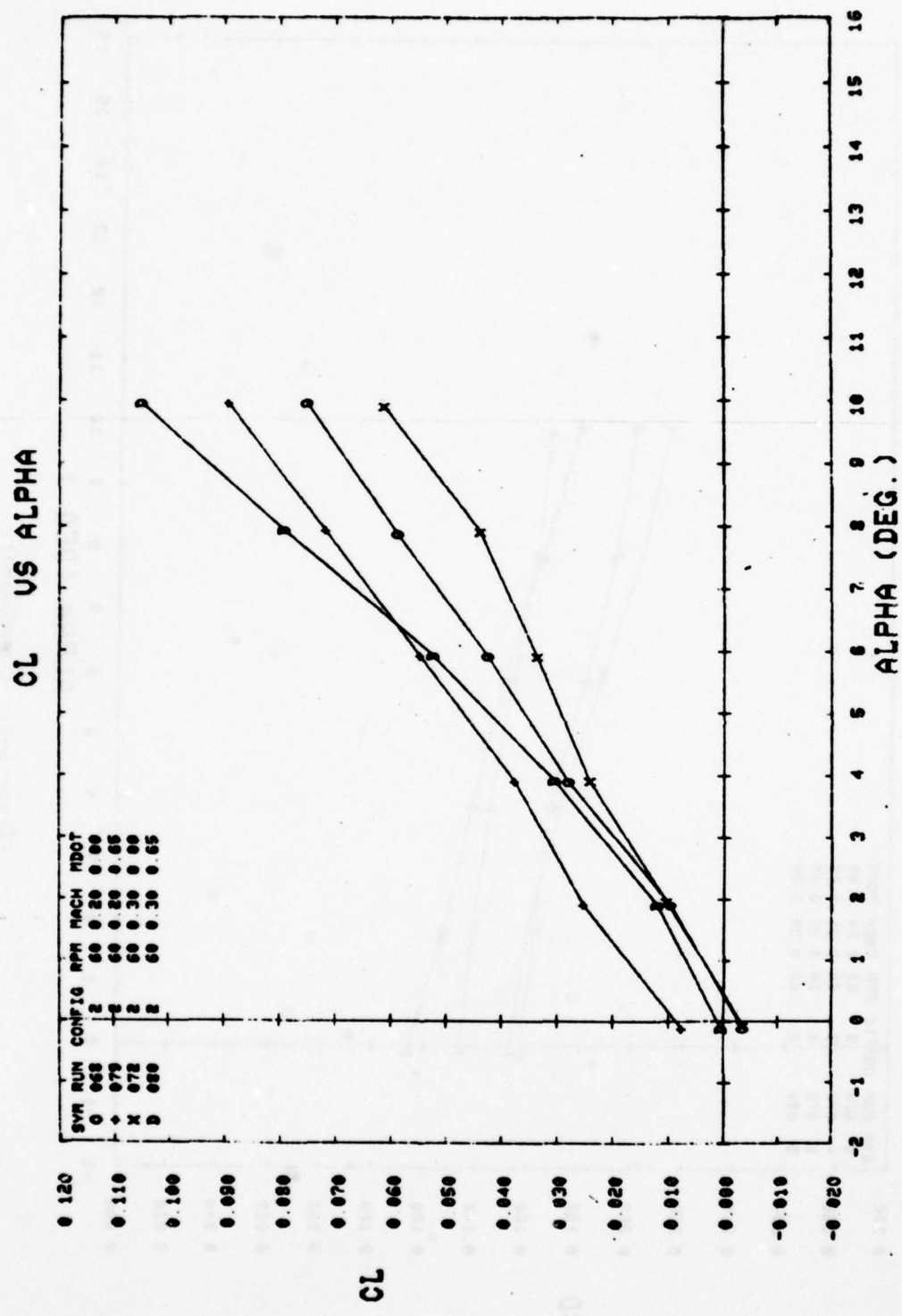


Figure A-5. (Continued).

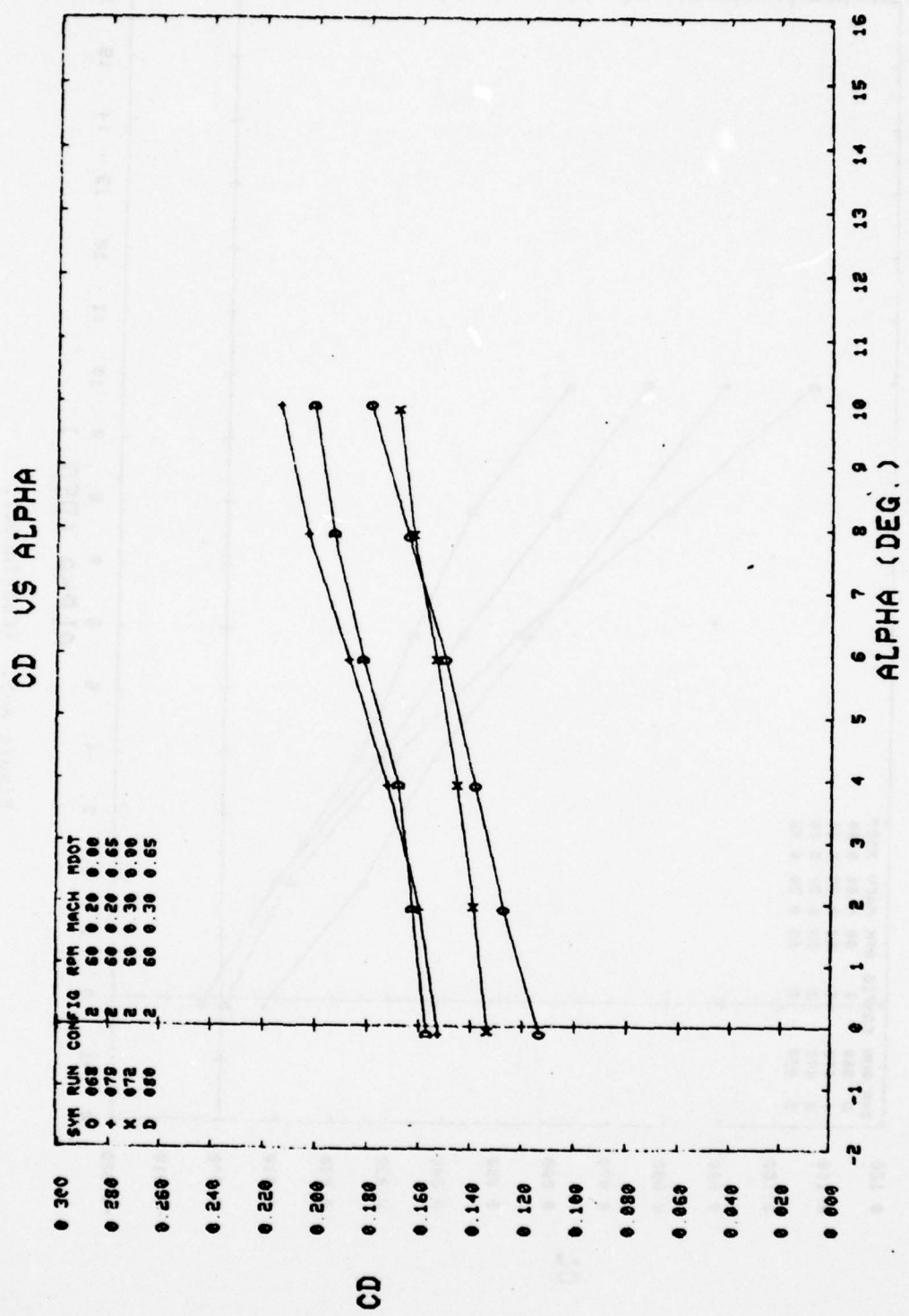


Figure A-5. (Concluded).

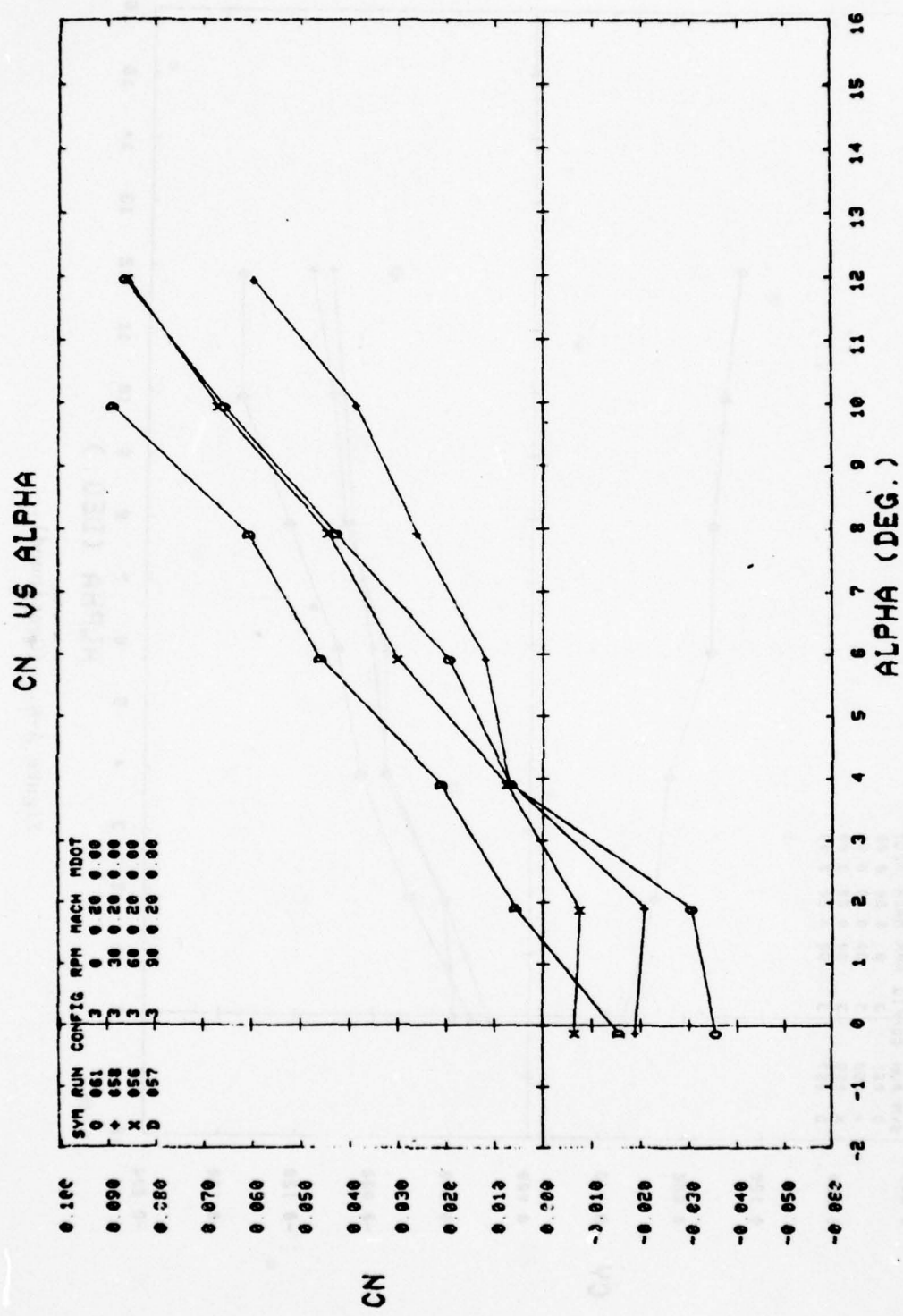


Figure A-6. Configuration 3 — aerodynamic coefficients versus alpha.

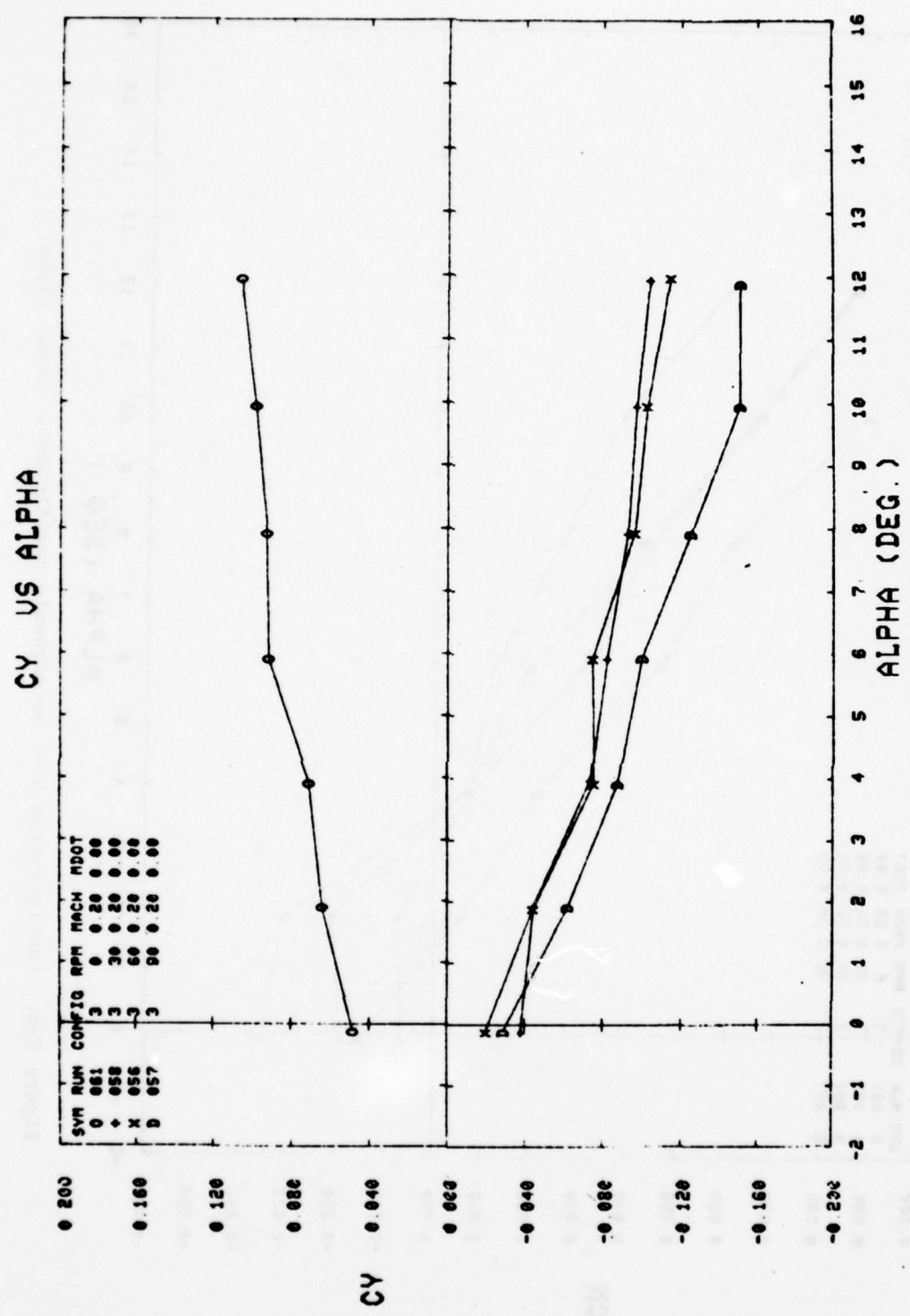


Figure A-6. (Continued).

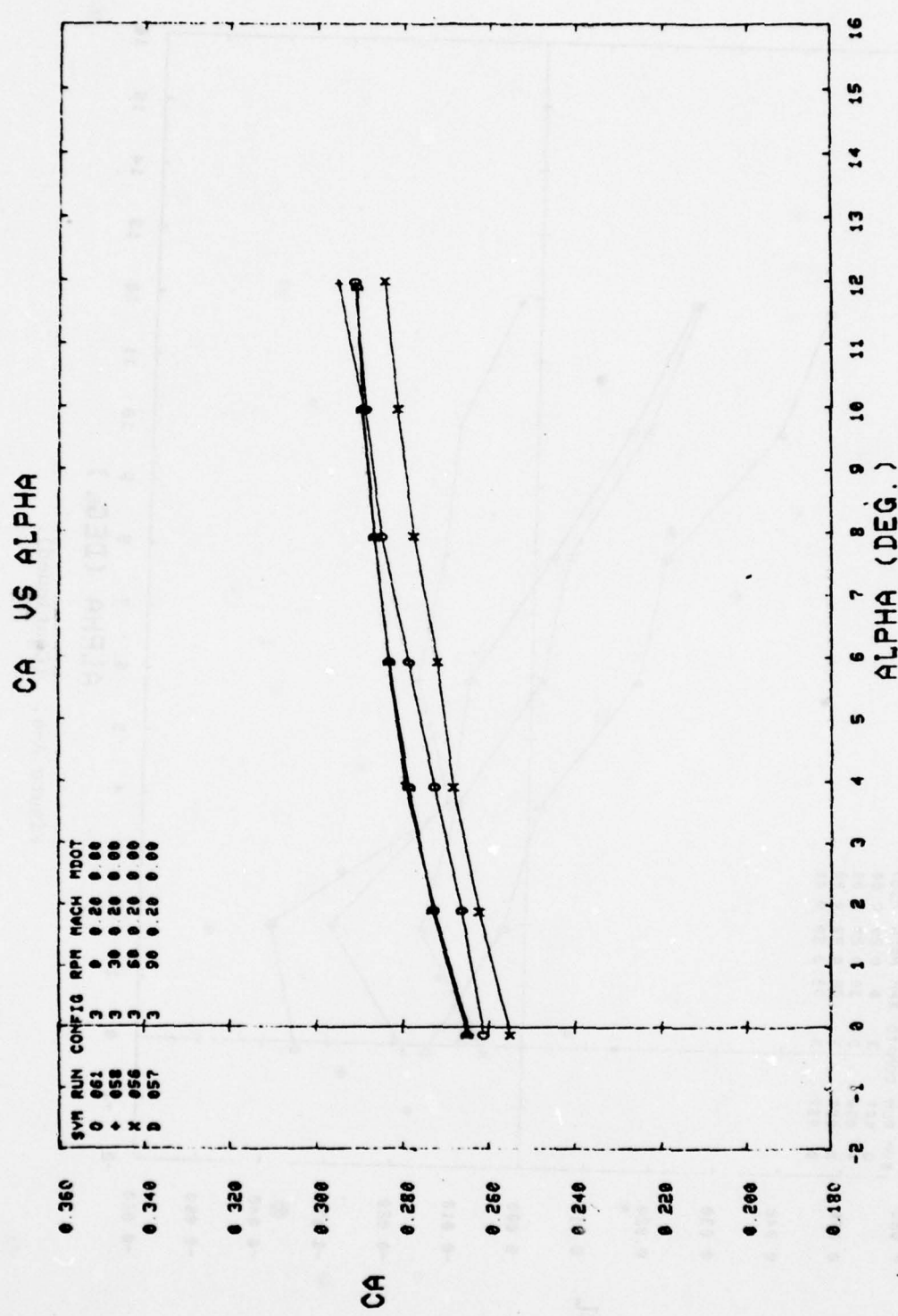


Figure A-6. (Continued).

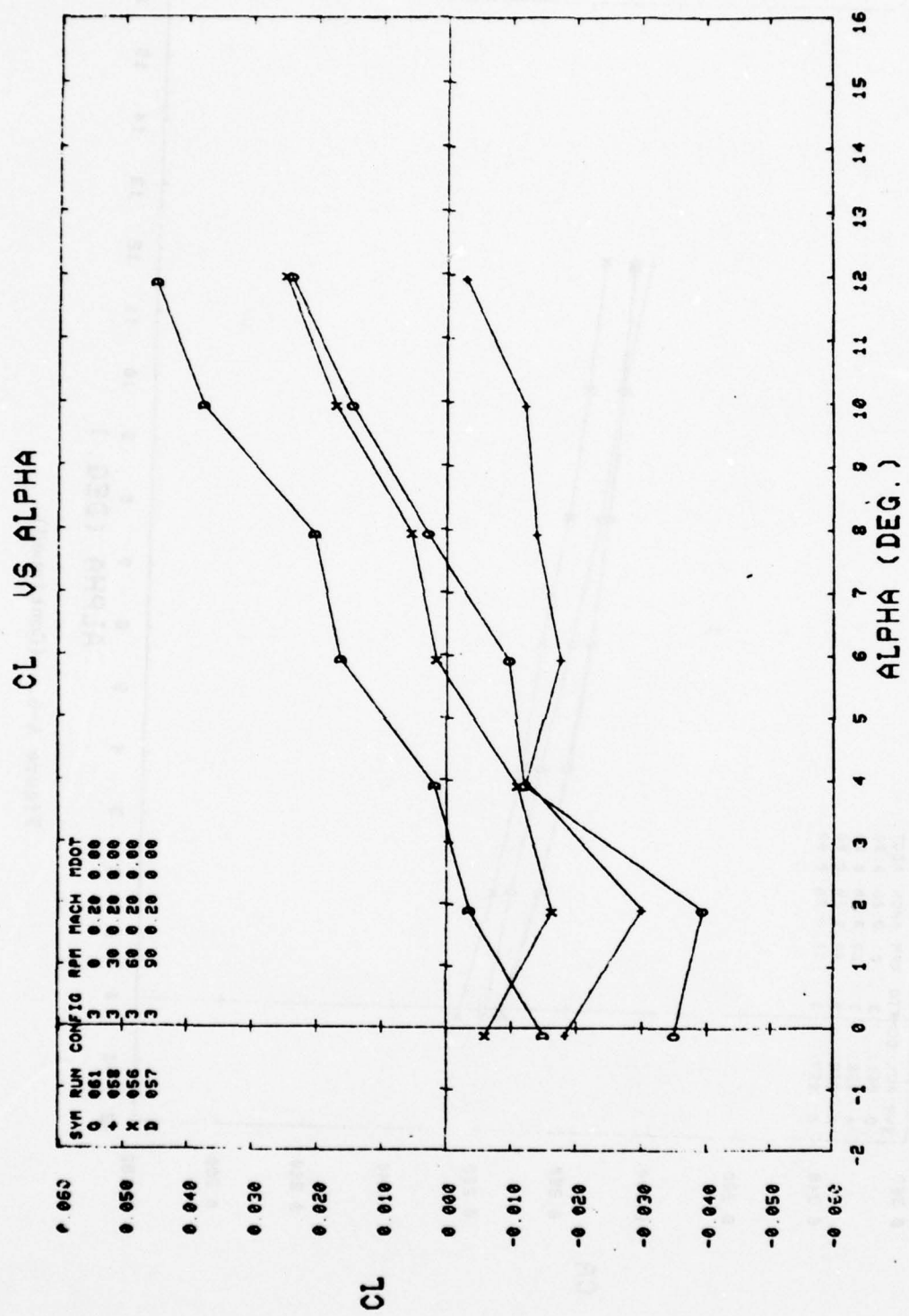


Figure A-6. (Continued).

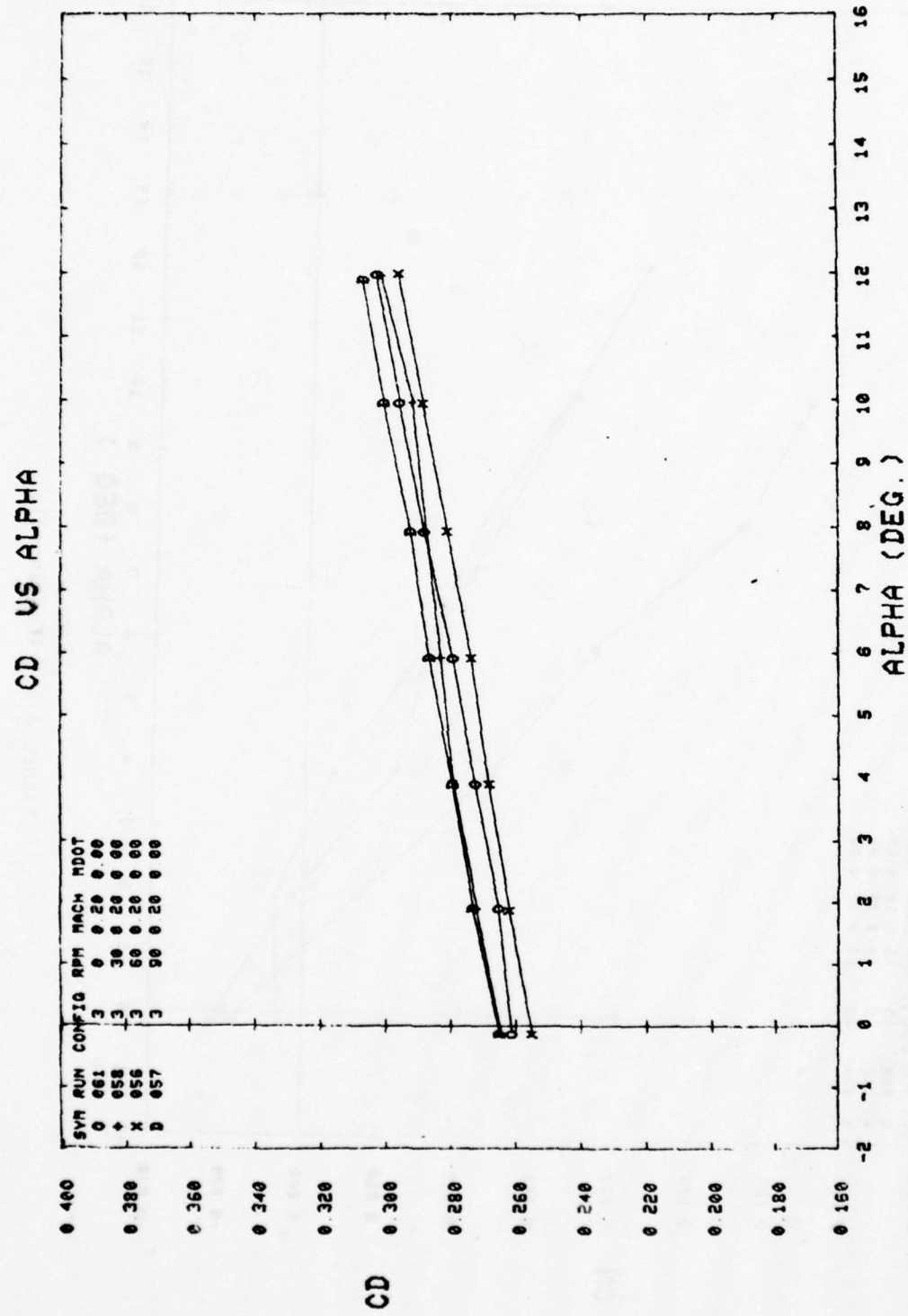


Figure A-6. (Continued).

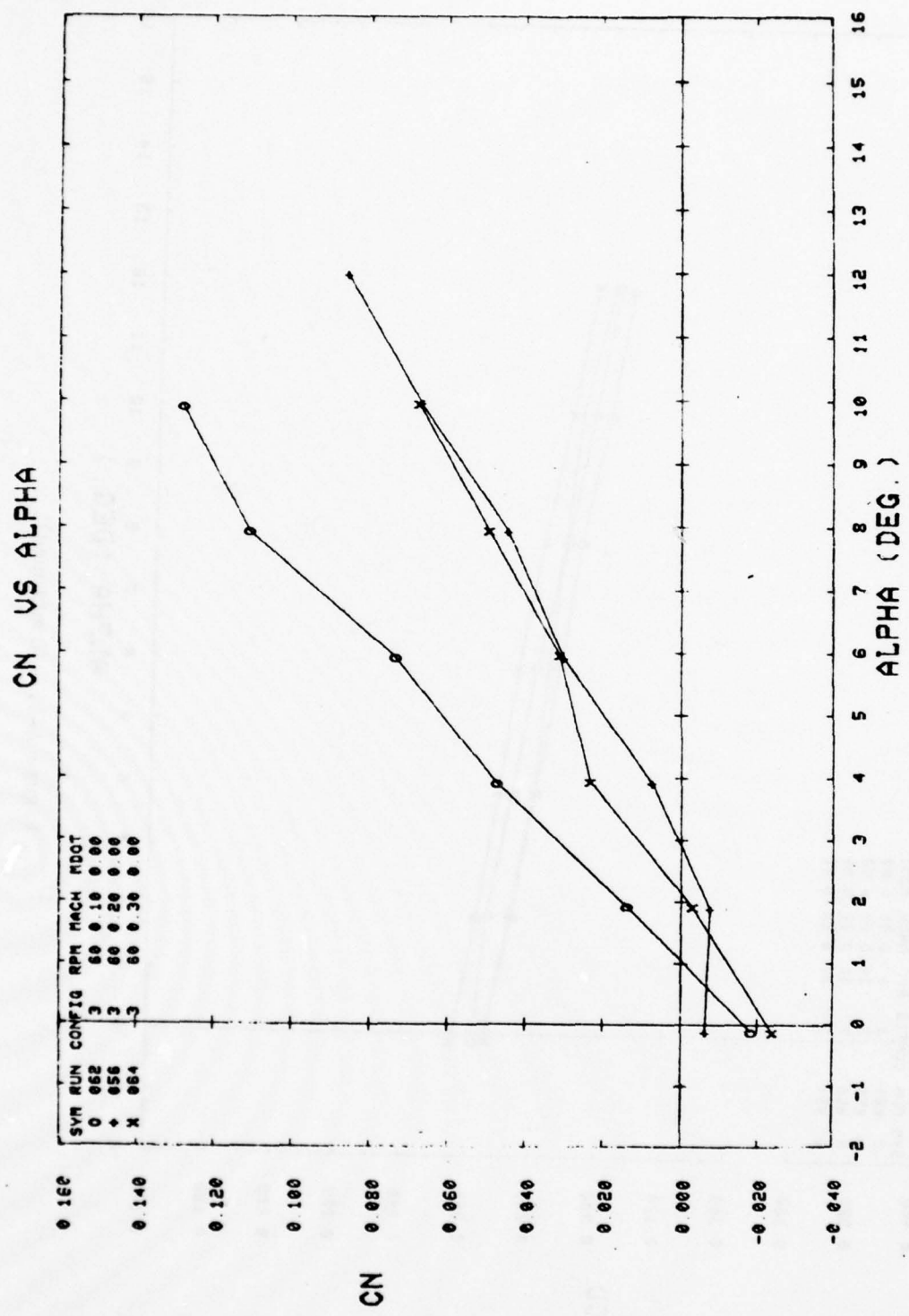


Figure A-6. (Continued).

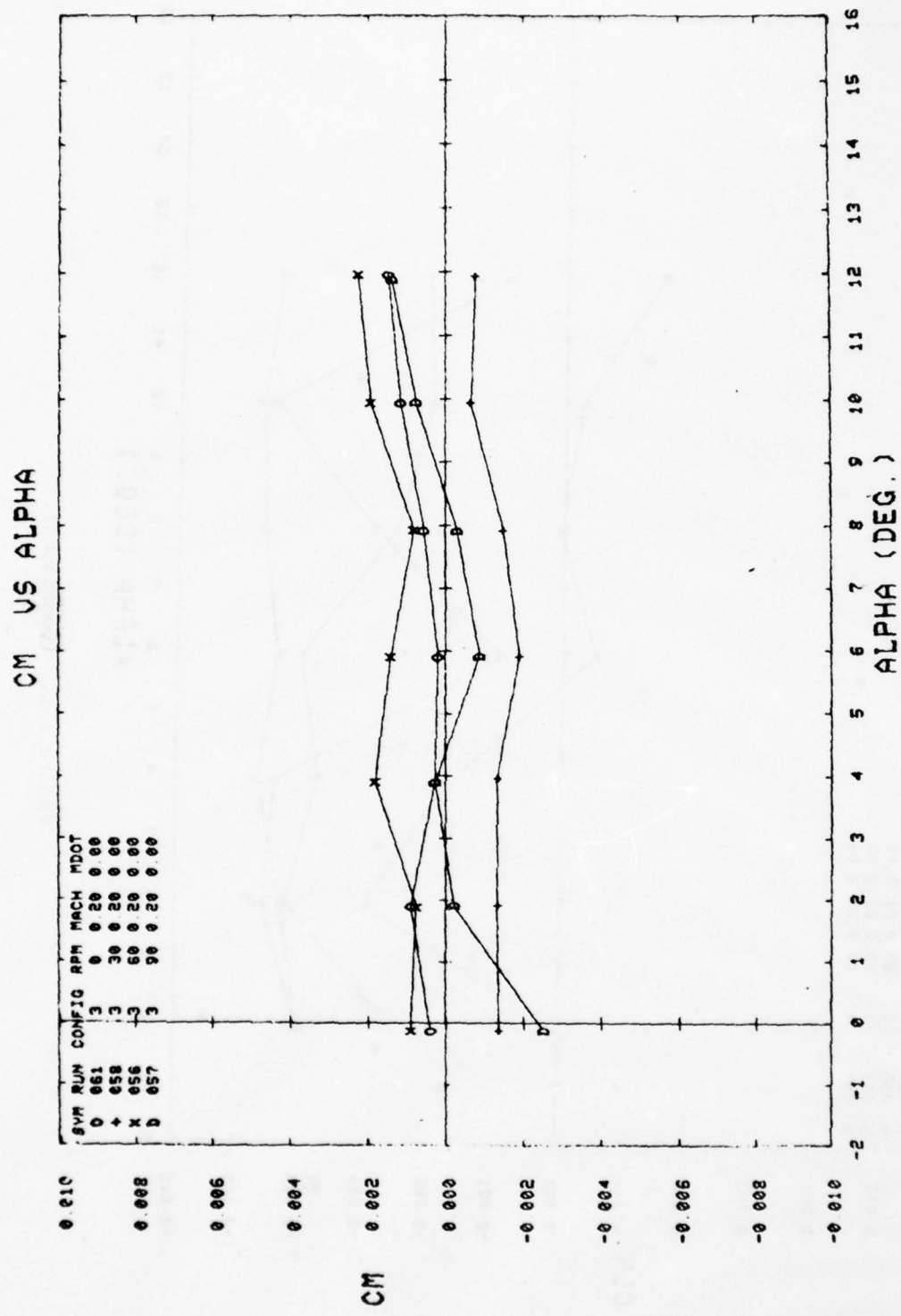


Figure A-6. (Continued).

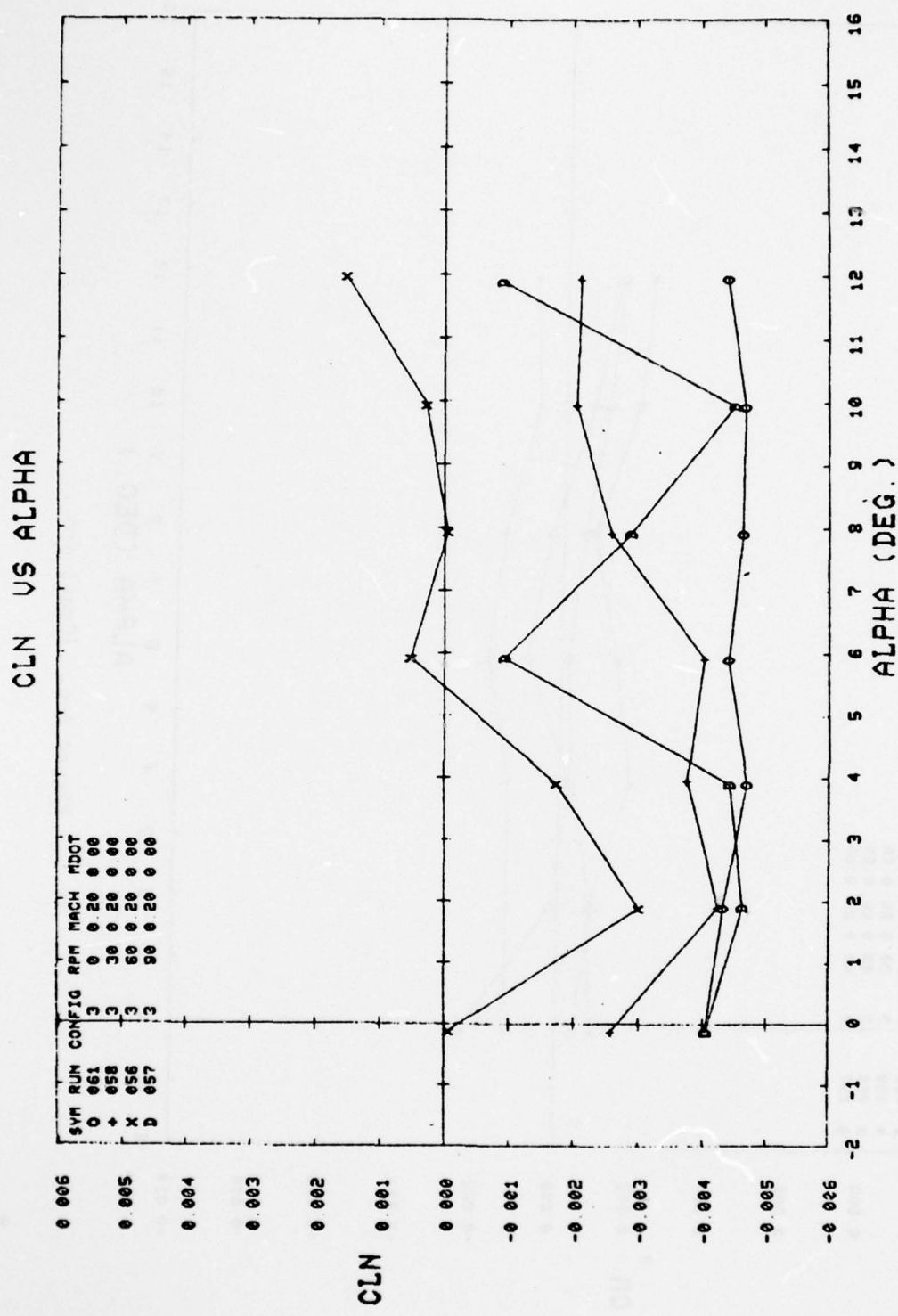


Figure A-6. (Continued).

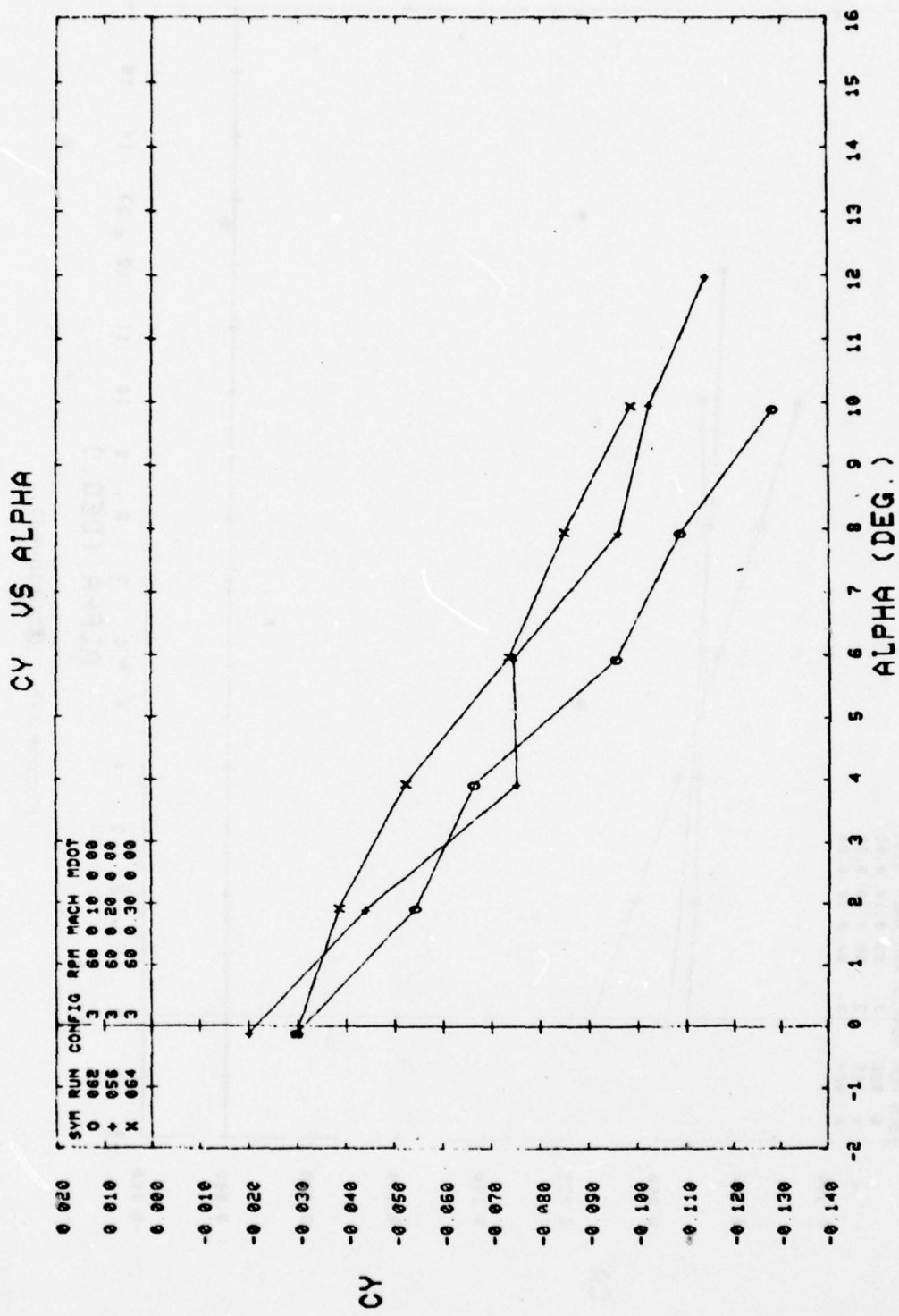


Figure A-6. (Continued).

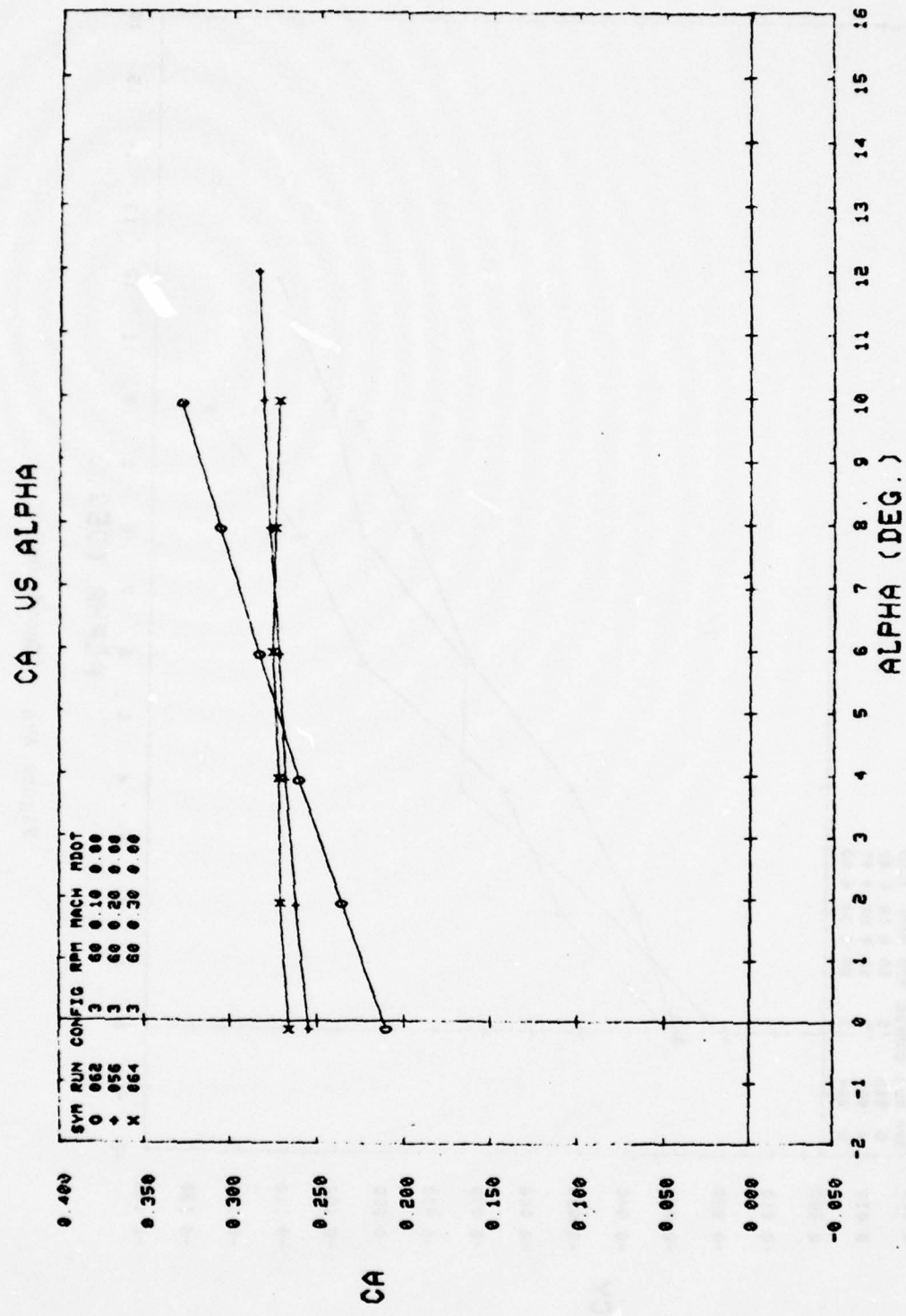


Figure A-6. (Continued).

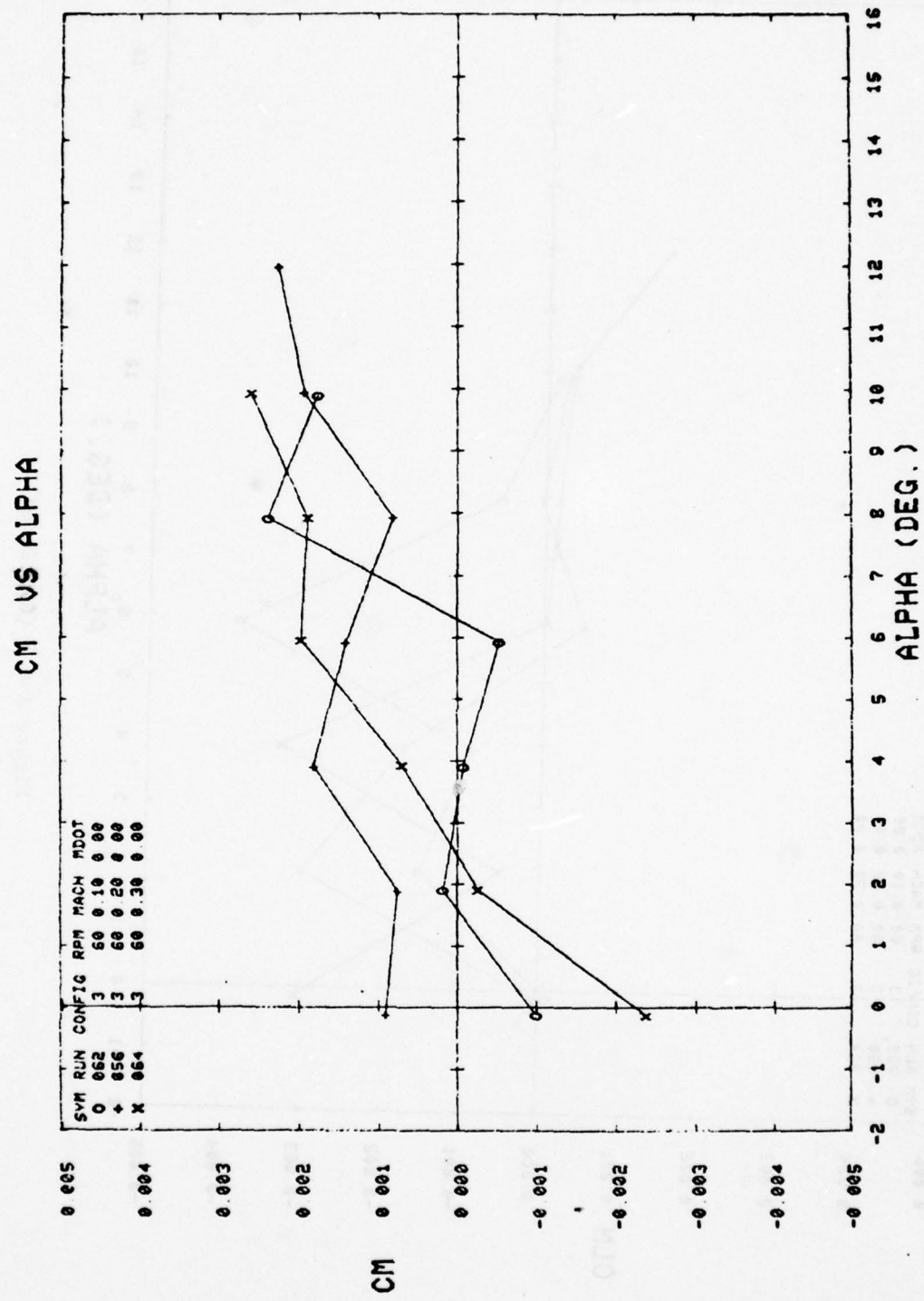


Figure A-6. (Continued).

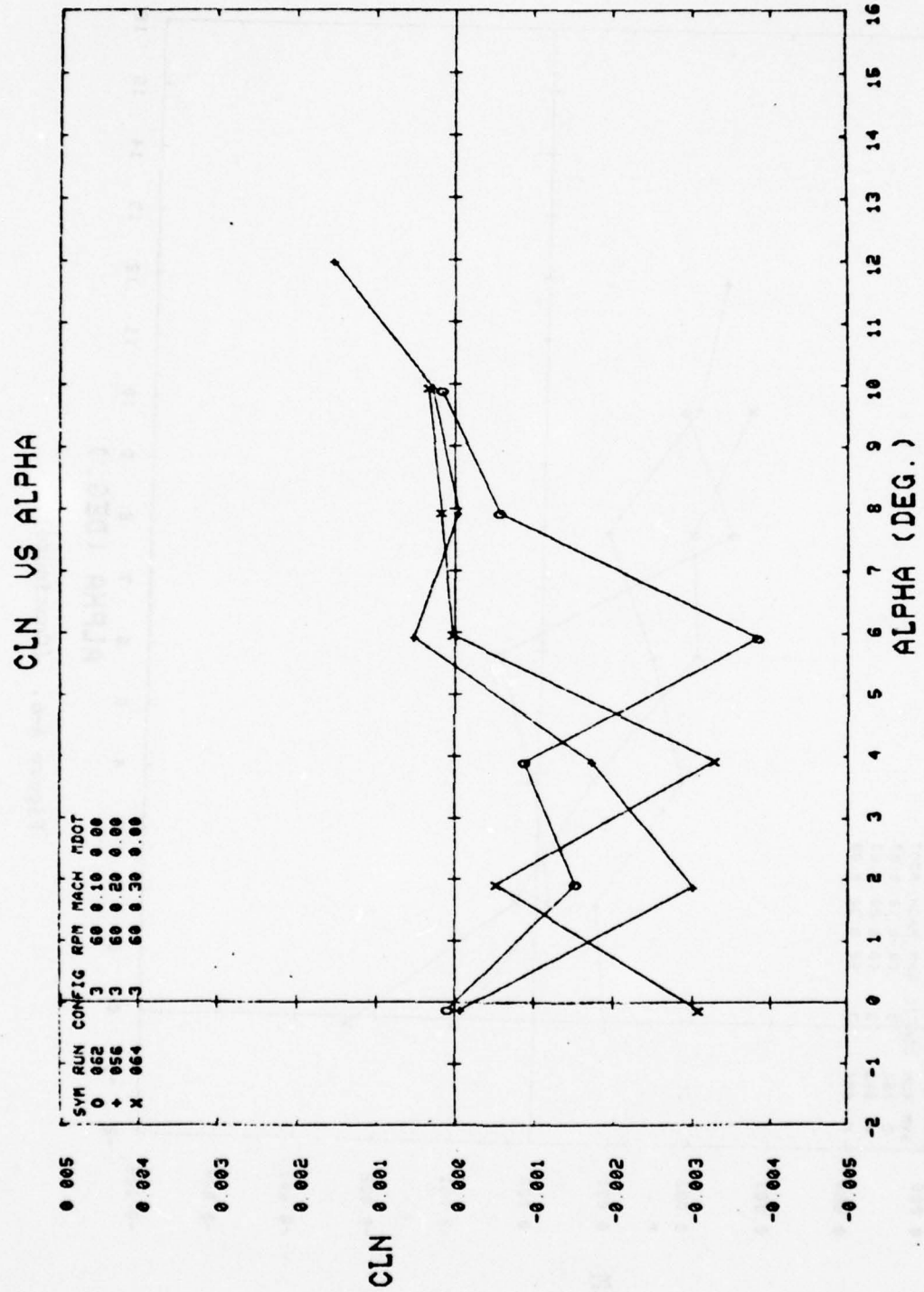


Figure A-6. (Continued).

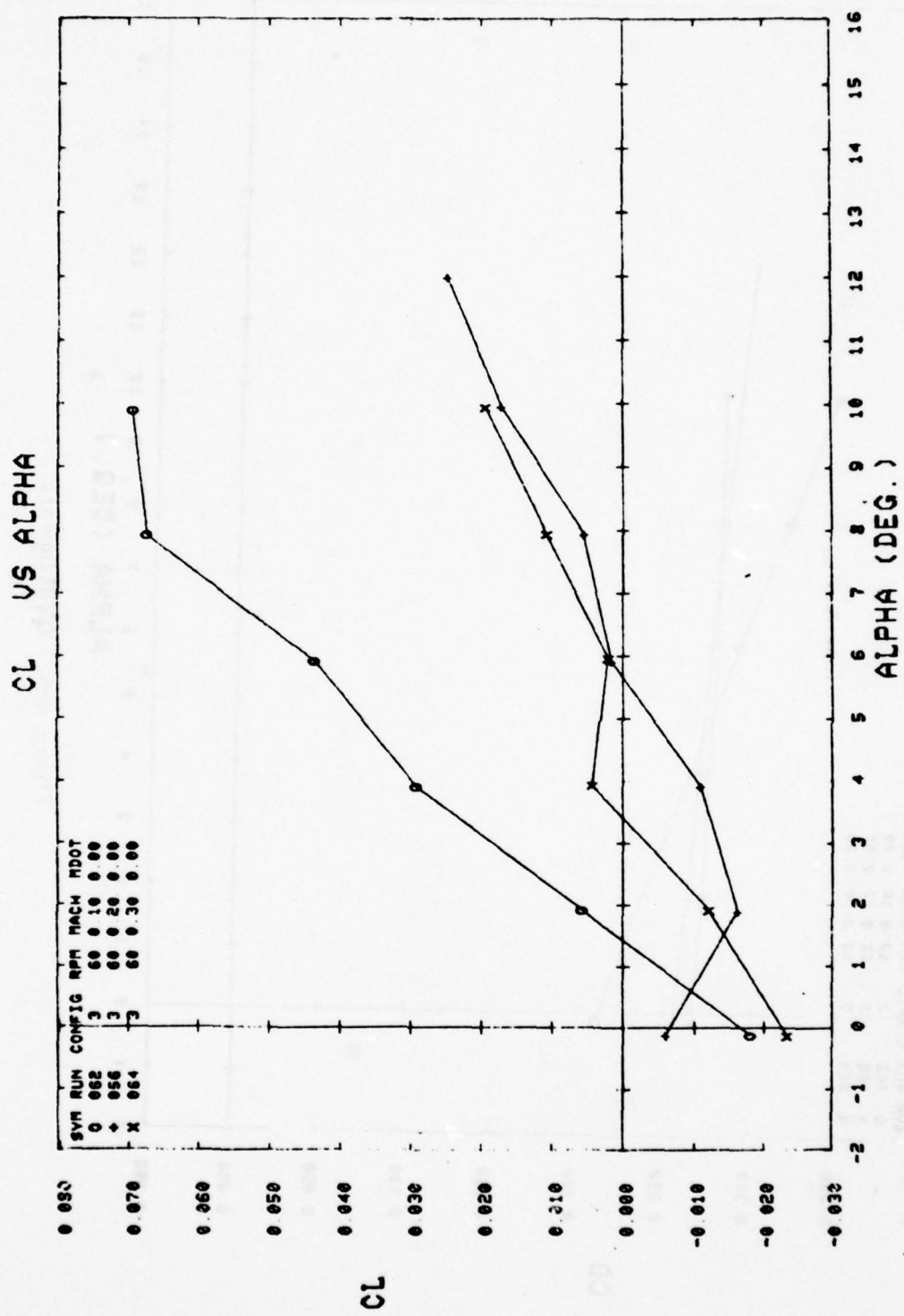


Figure A-6. (Continued).

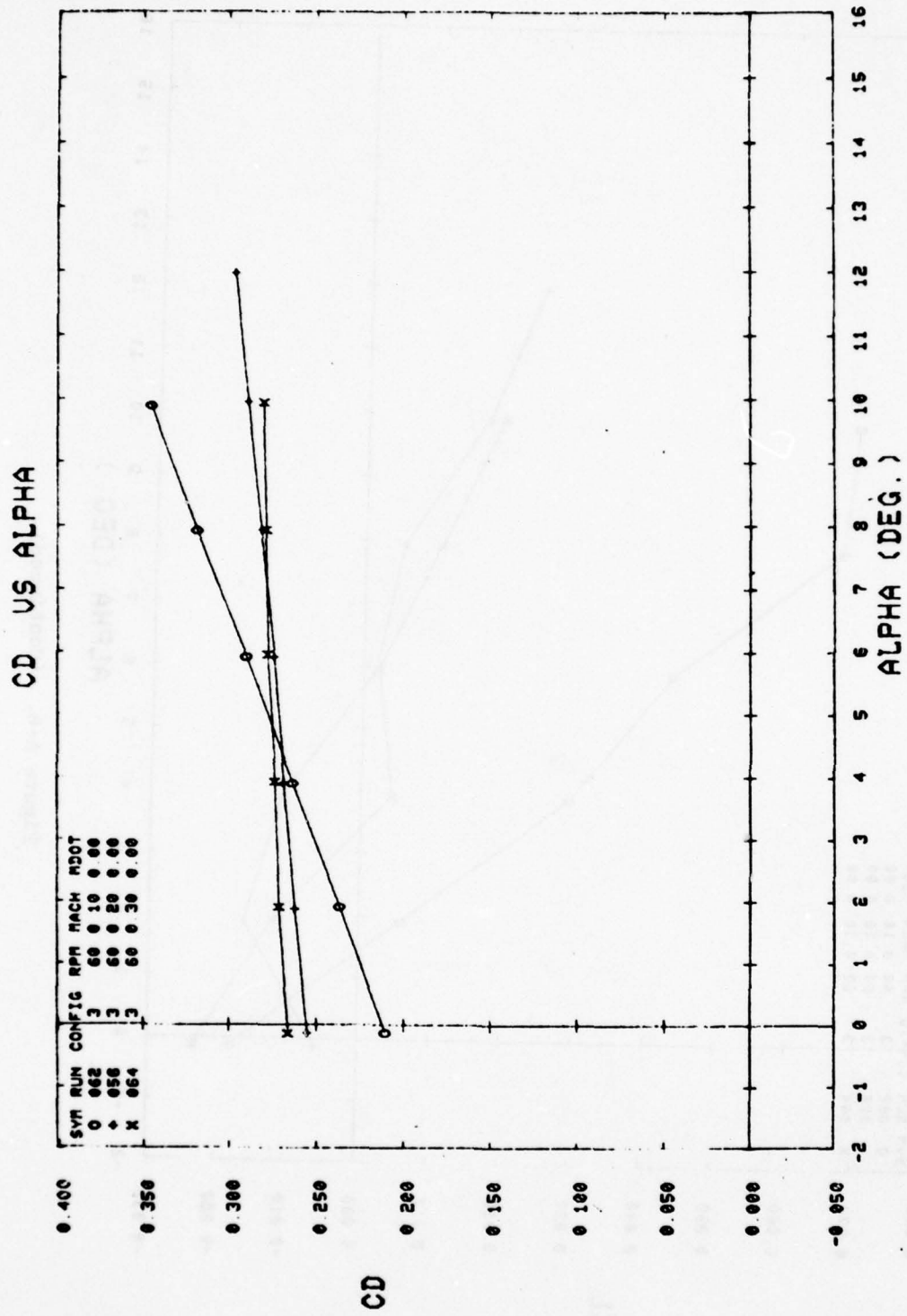


Figure A-6. (Continued).

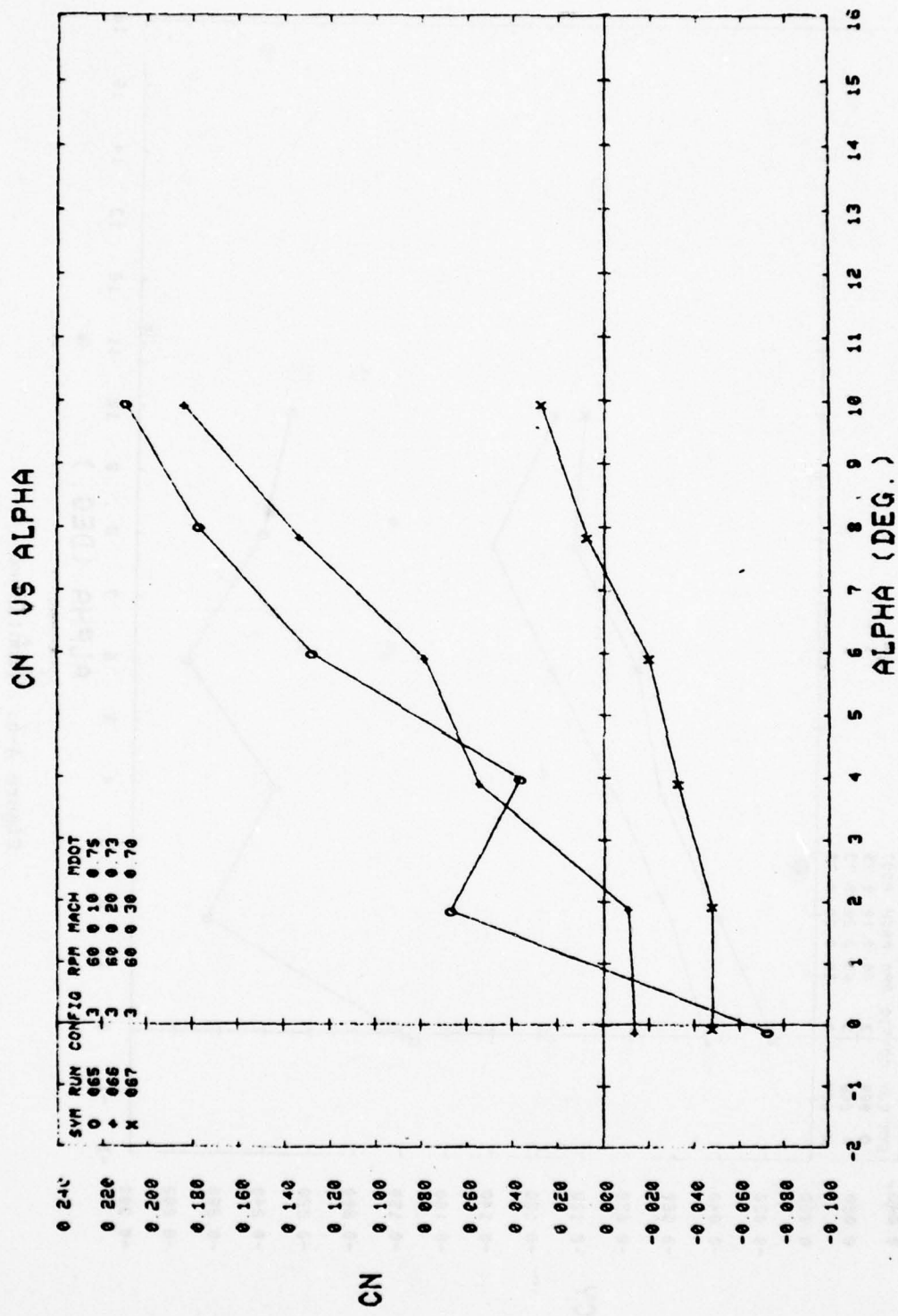


Figure A-6. (Continued).

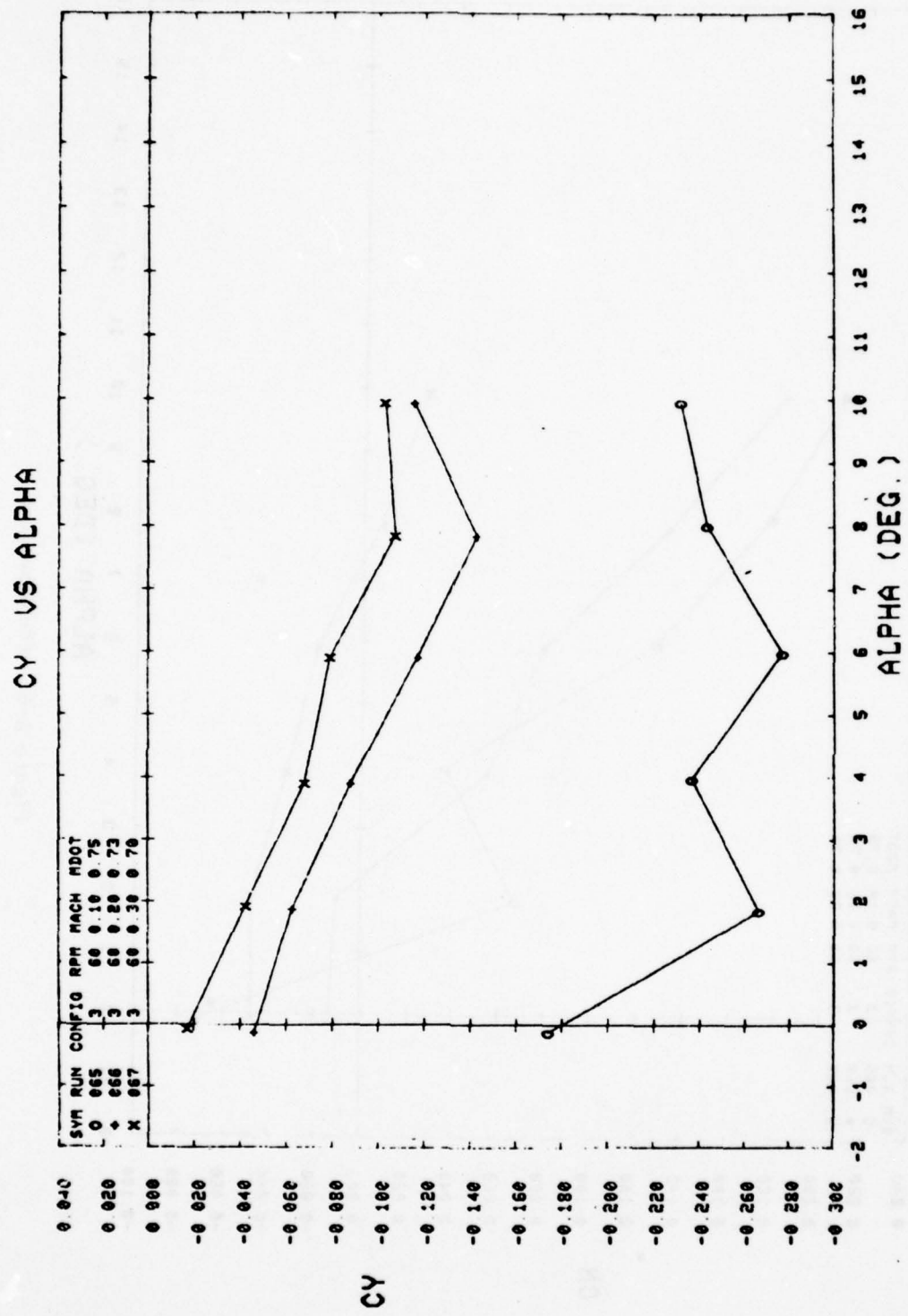


Figure A-6. (Continued).

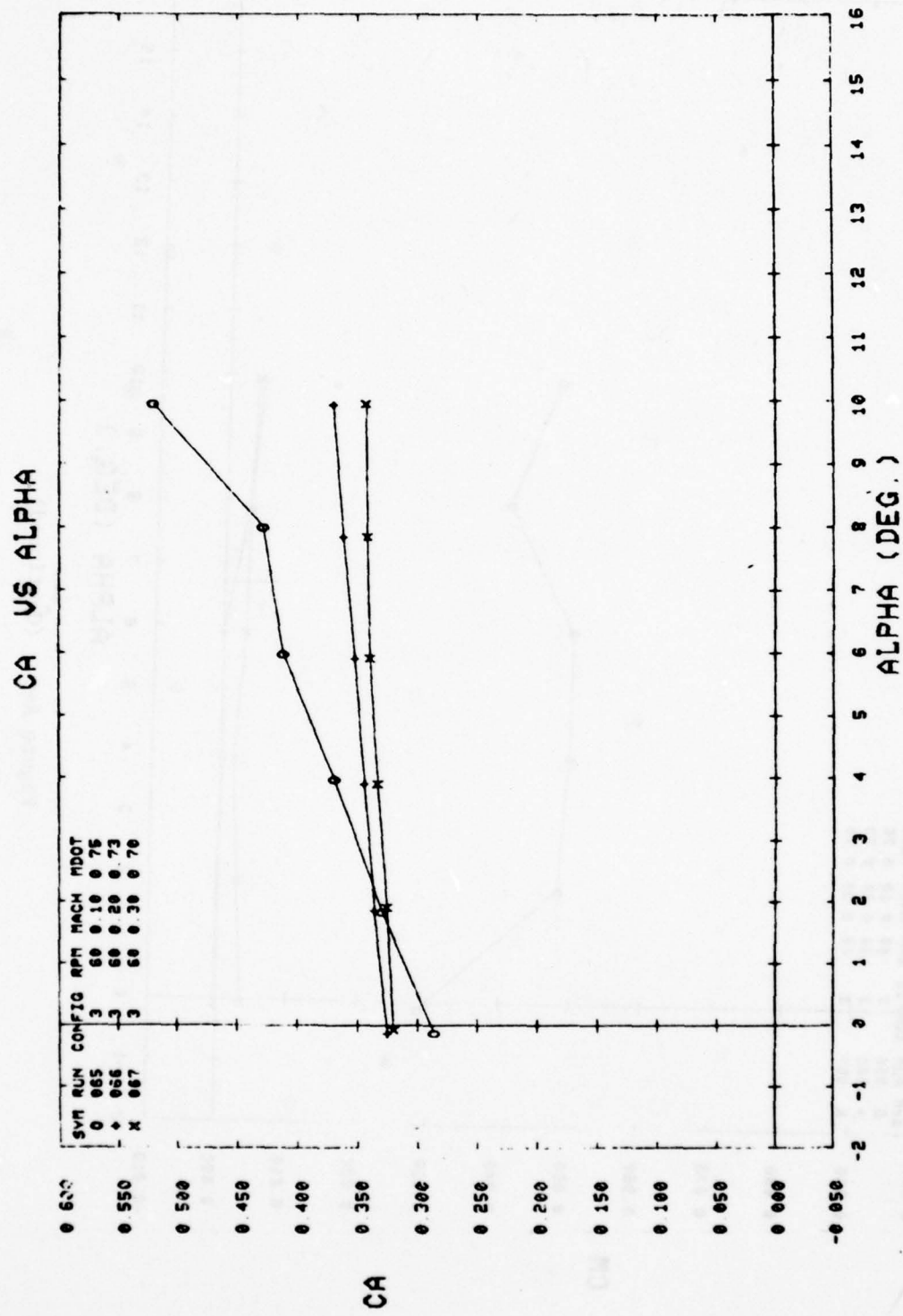


Figure A-6. (Continued).

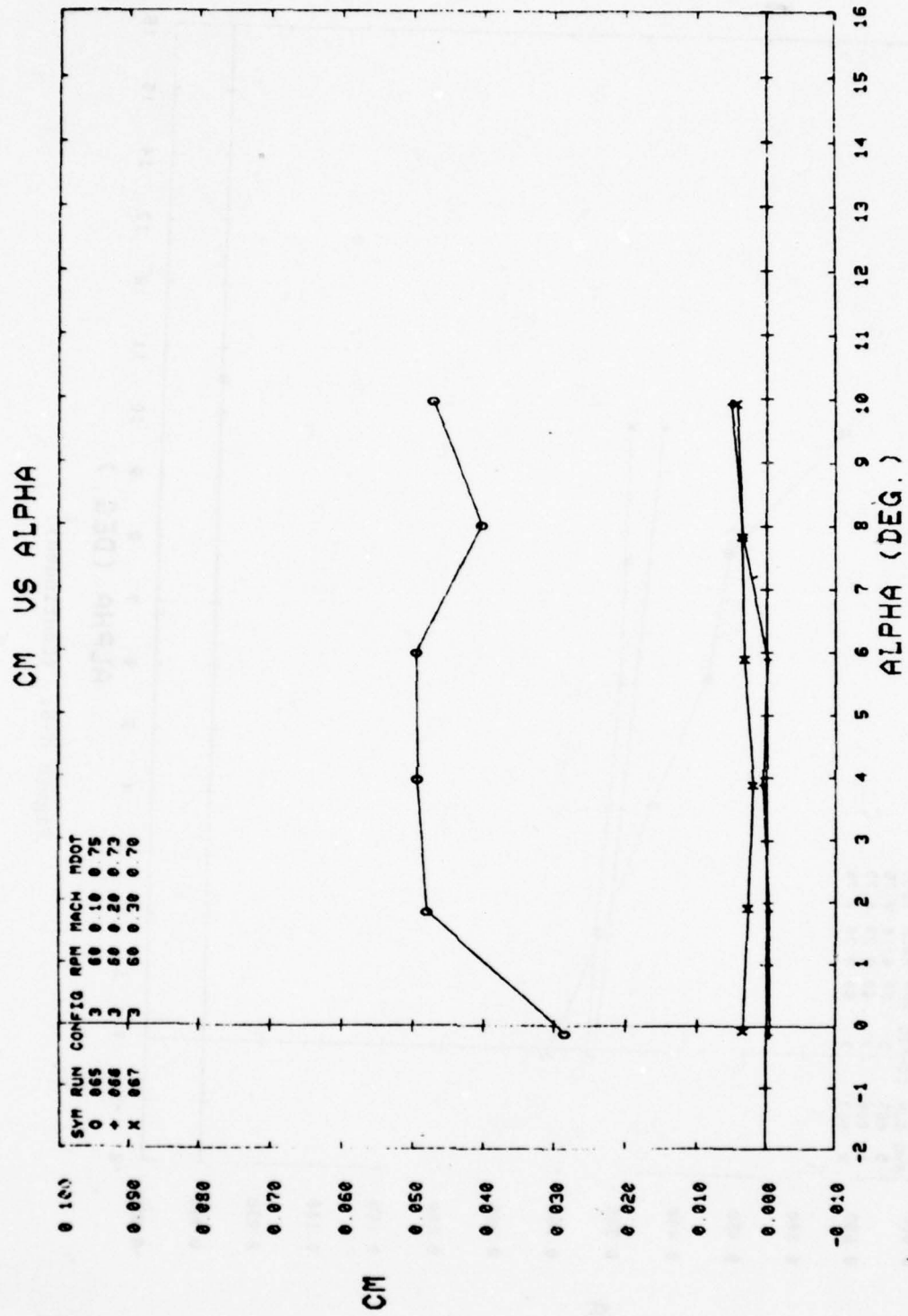


Figure A-6. (Continued).

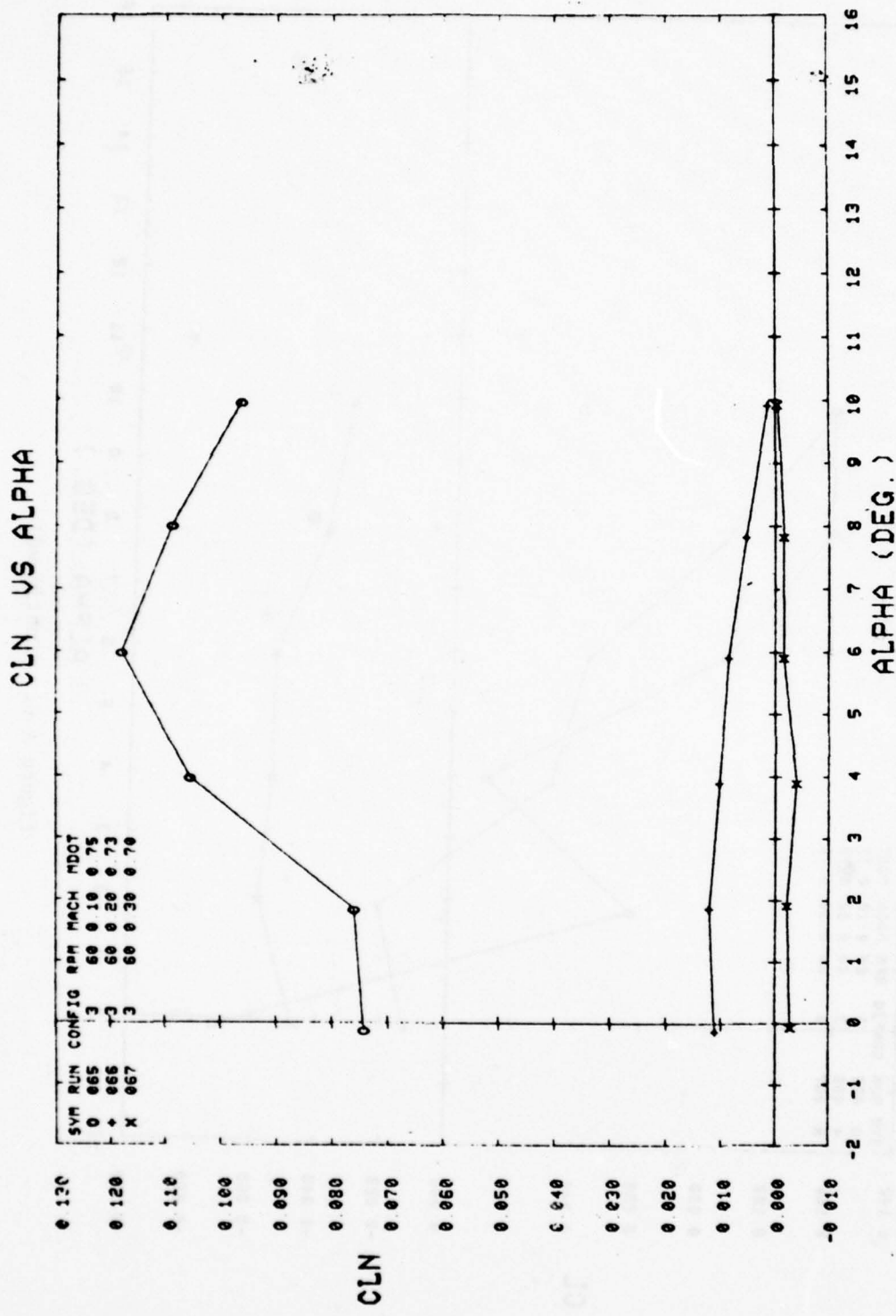


Figure A-6. (Continued).

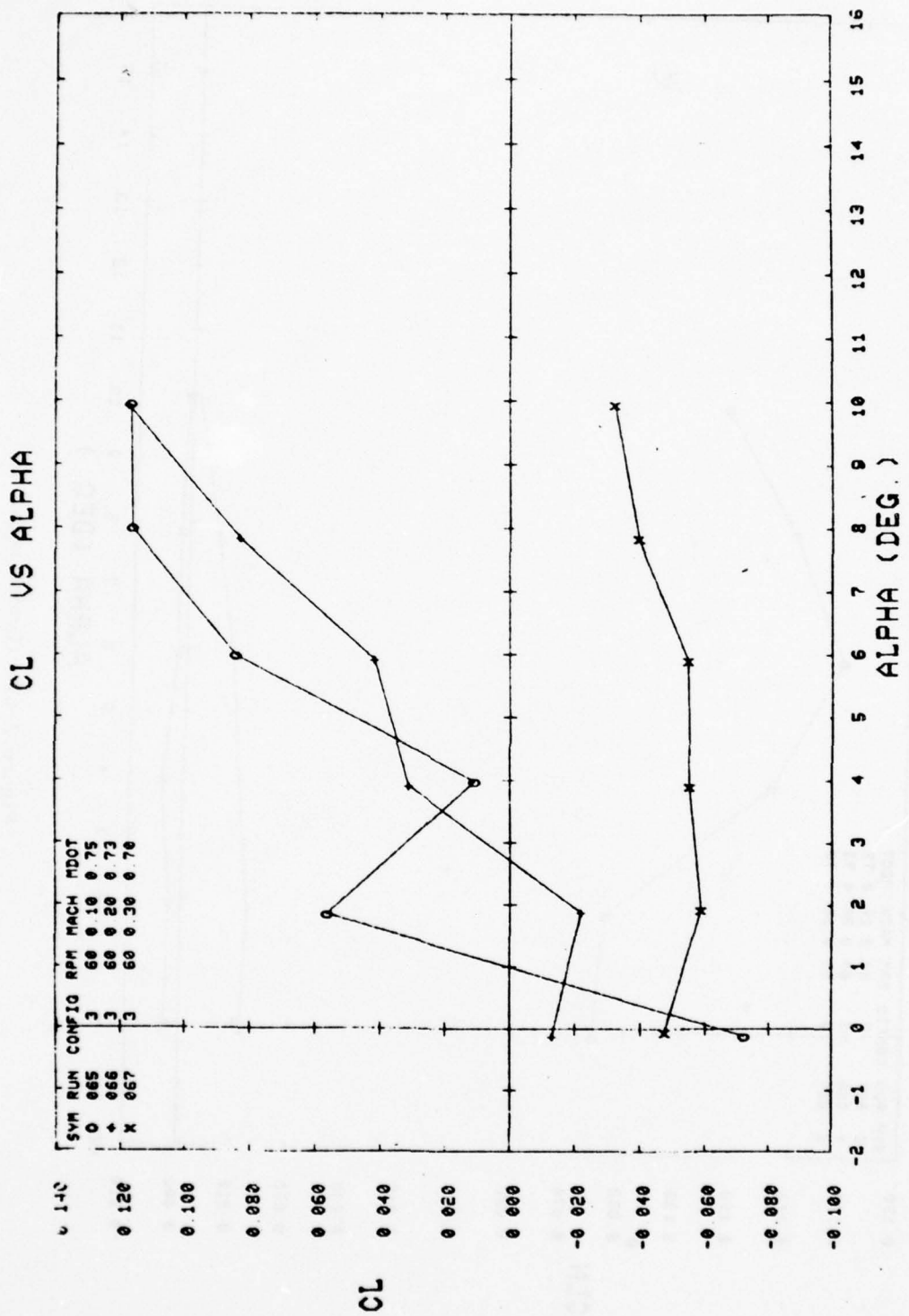


Figure A-6. (Continued).

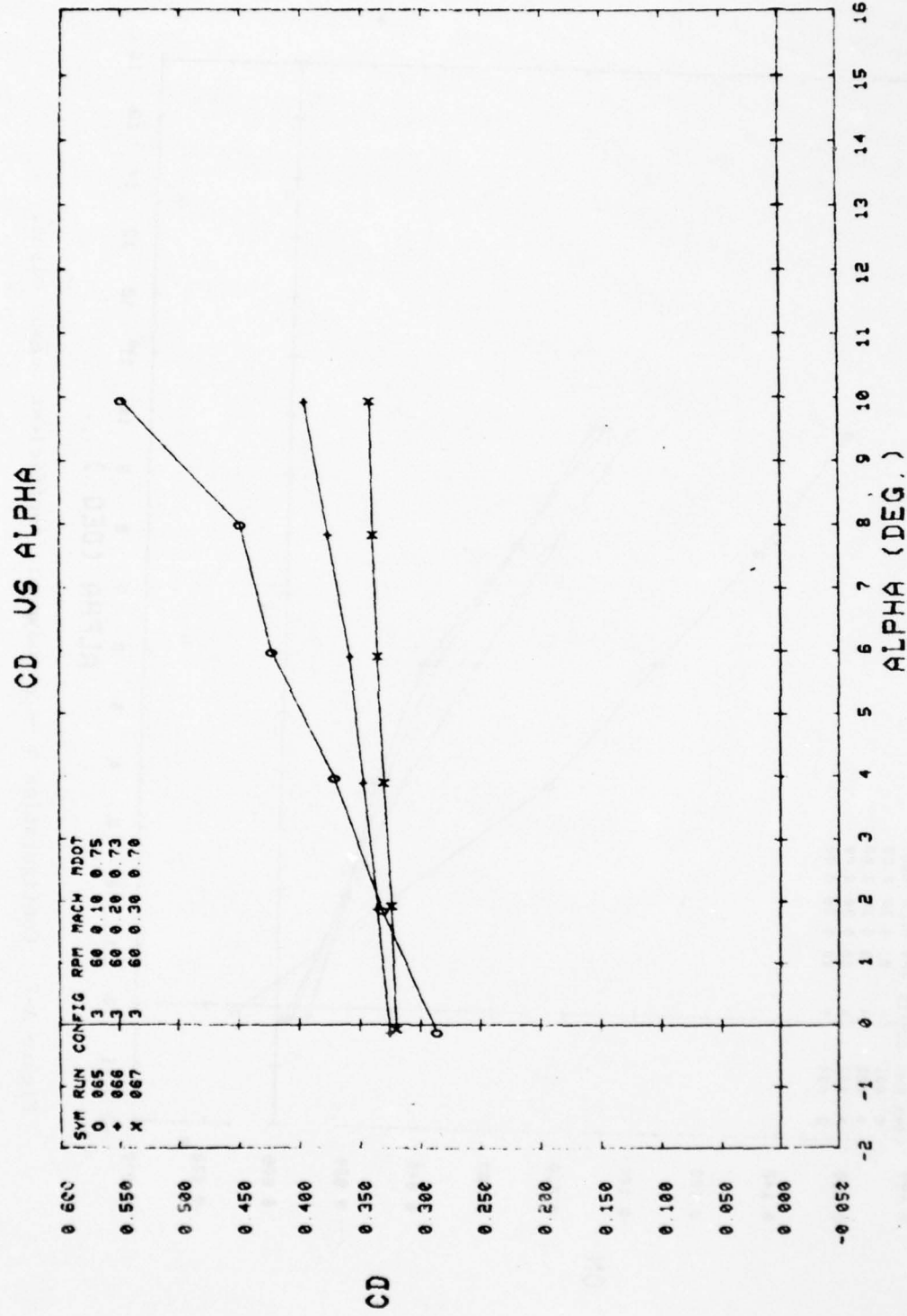


Figure A-6. (Concluded).

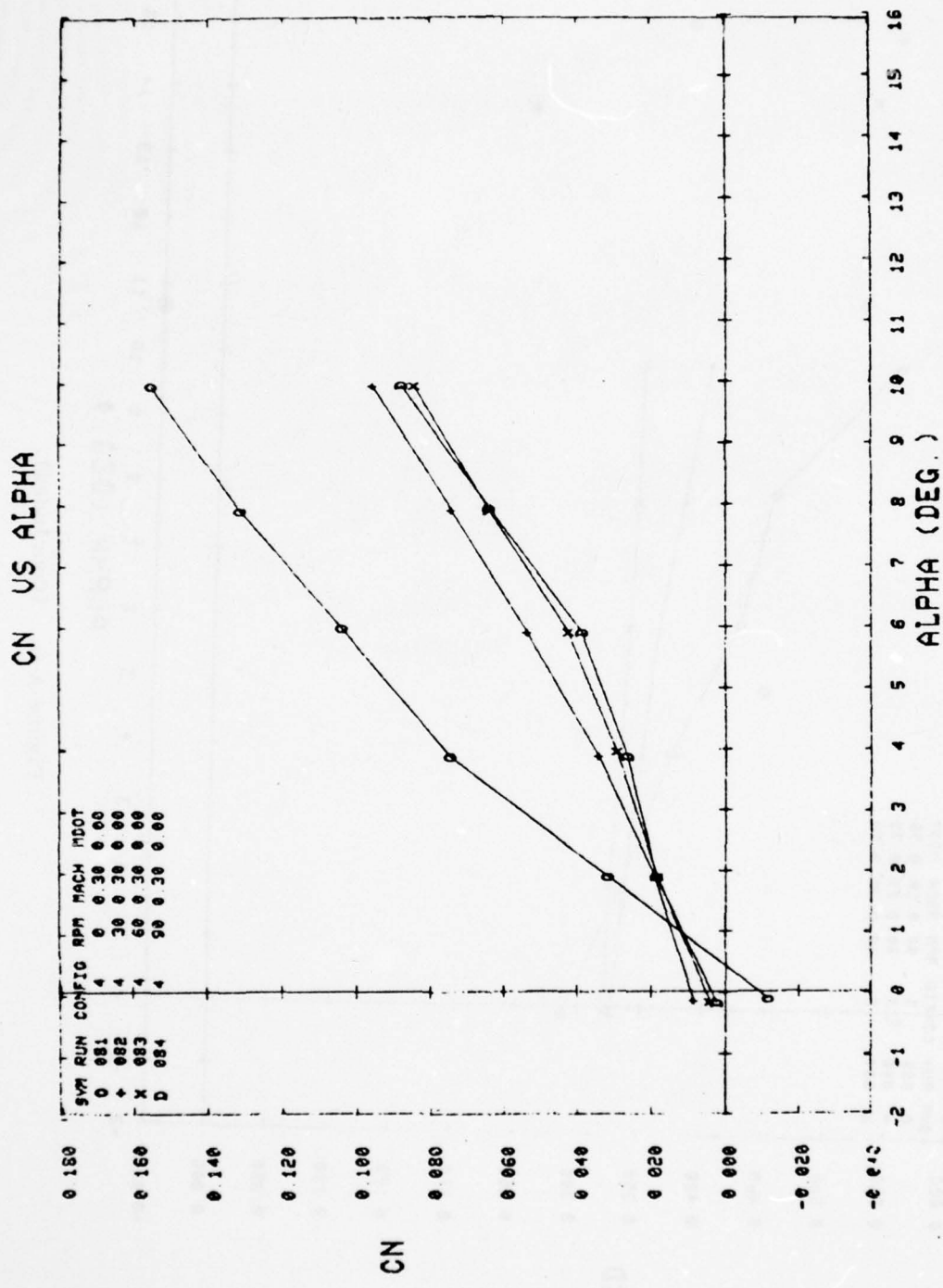


Figure A-7. Configuration 4 — aerodynamic coefficient versus alpha.

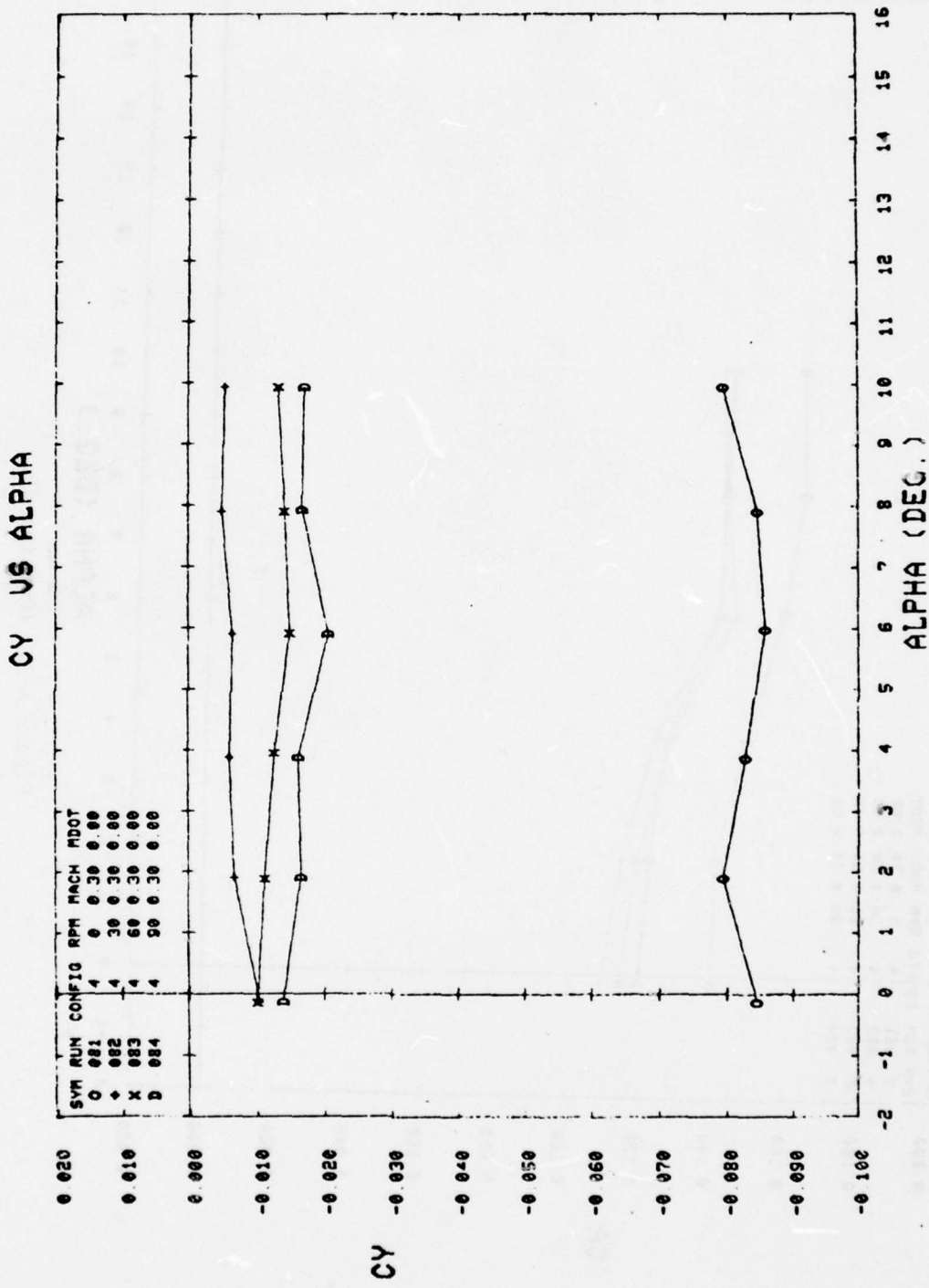


Figure A-7. (Continued).

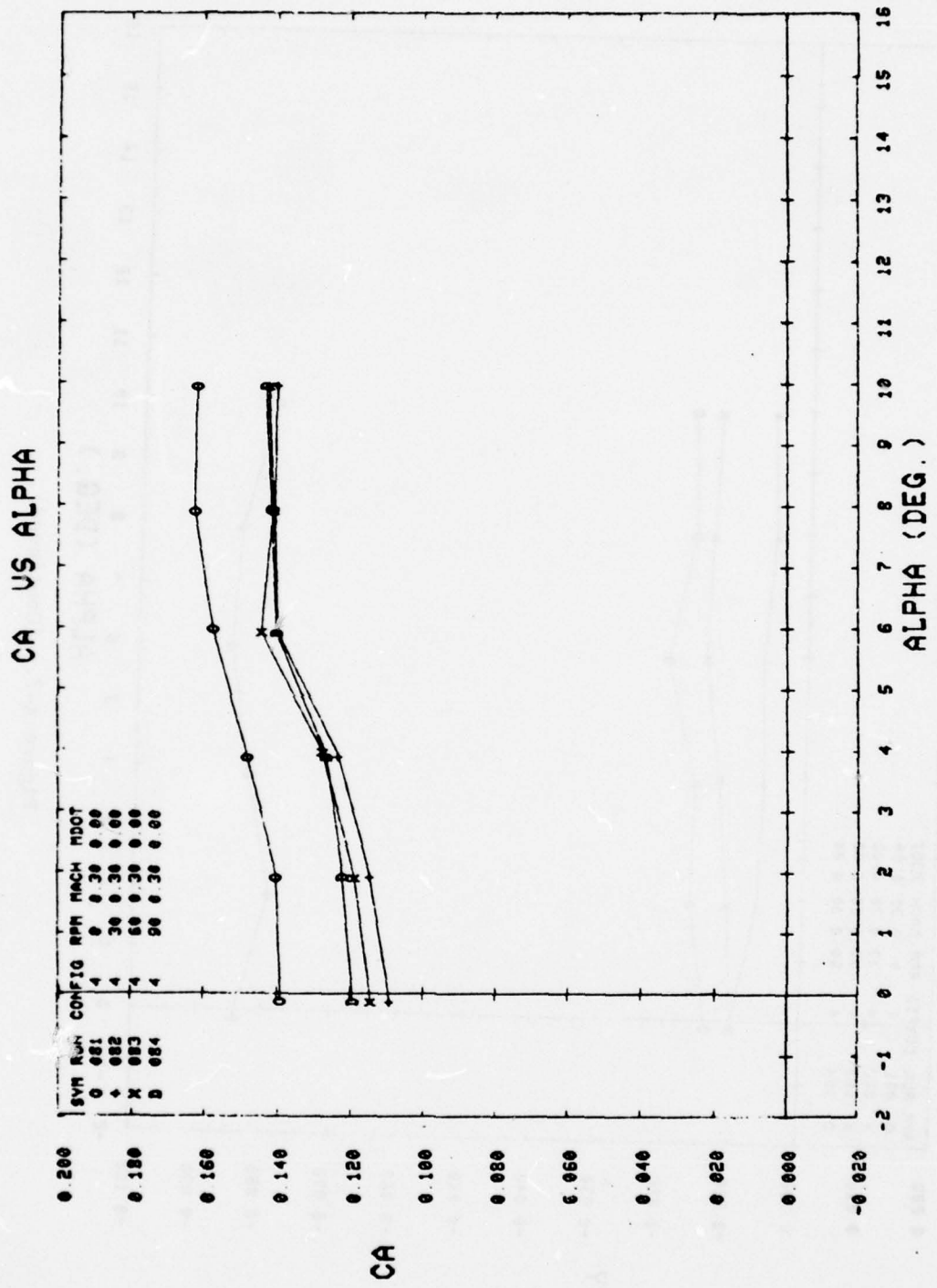


Figure A-7. (Continued).

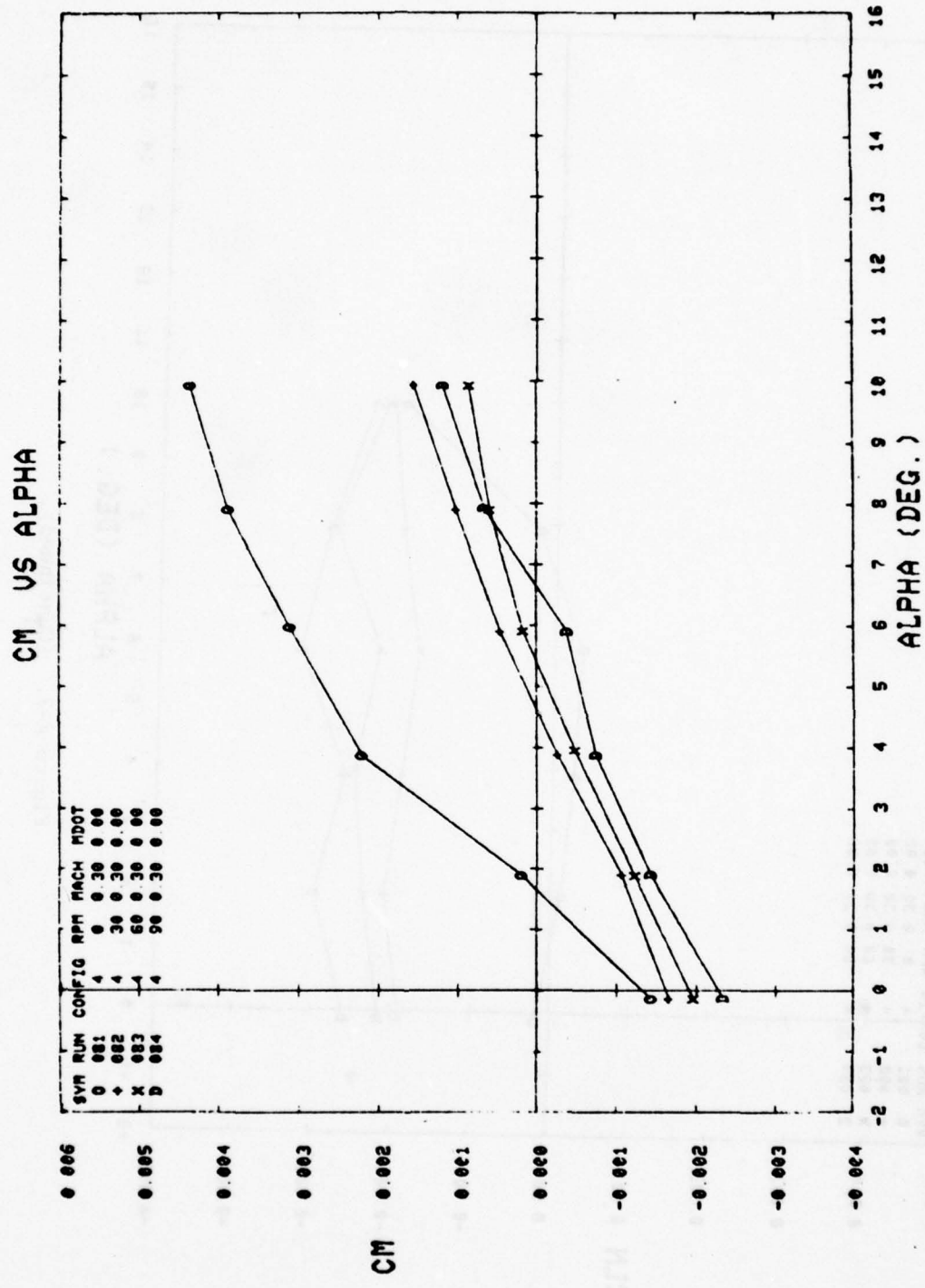


Figure A-7. (Continued).

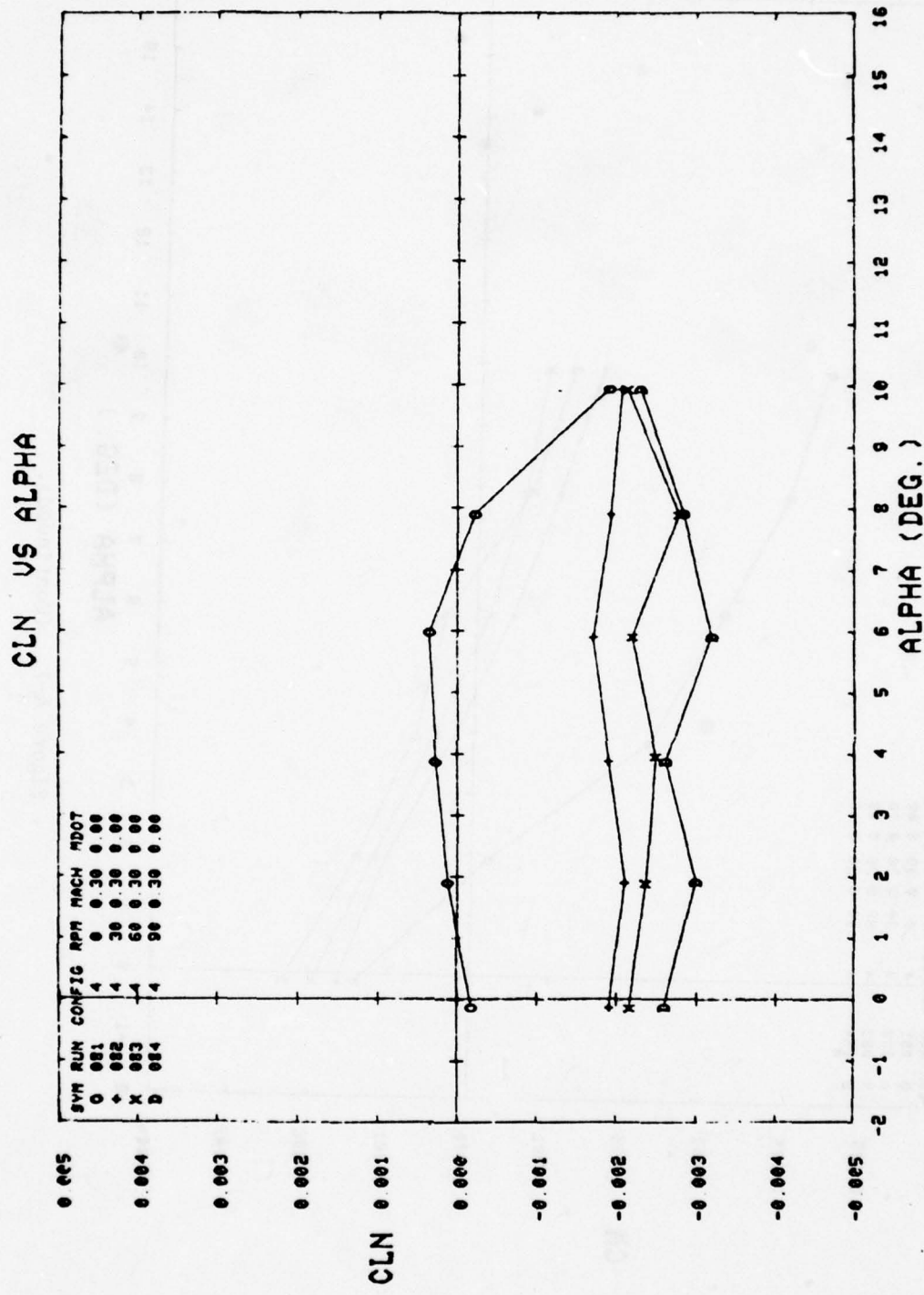


Figure A-7. (Continued).

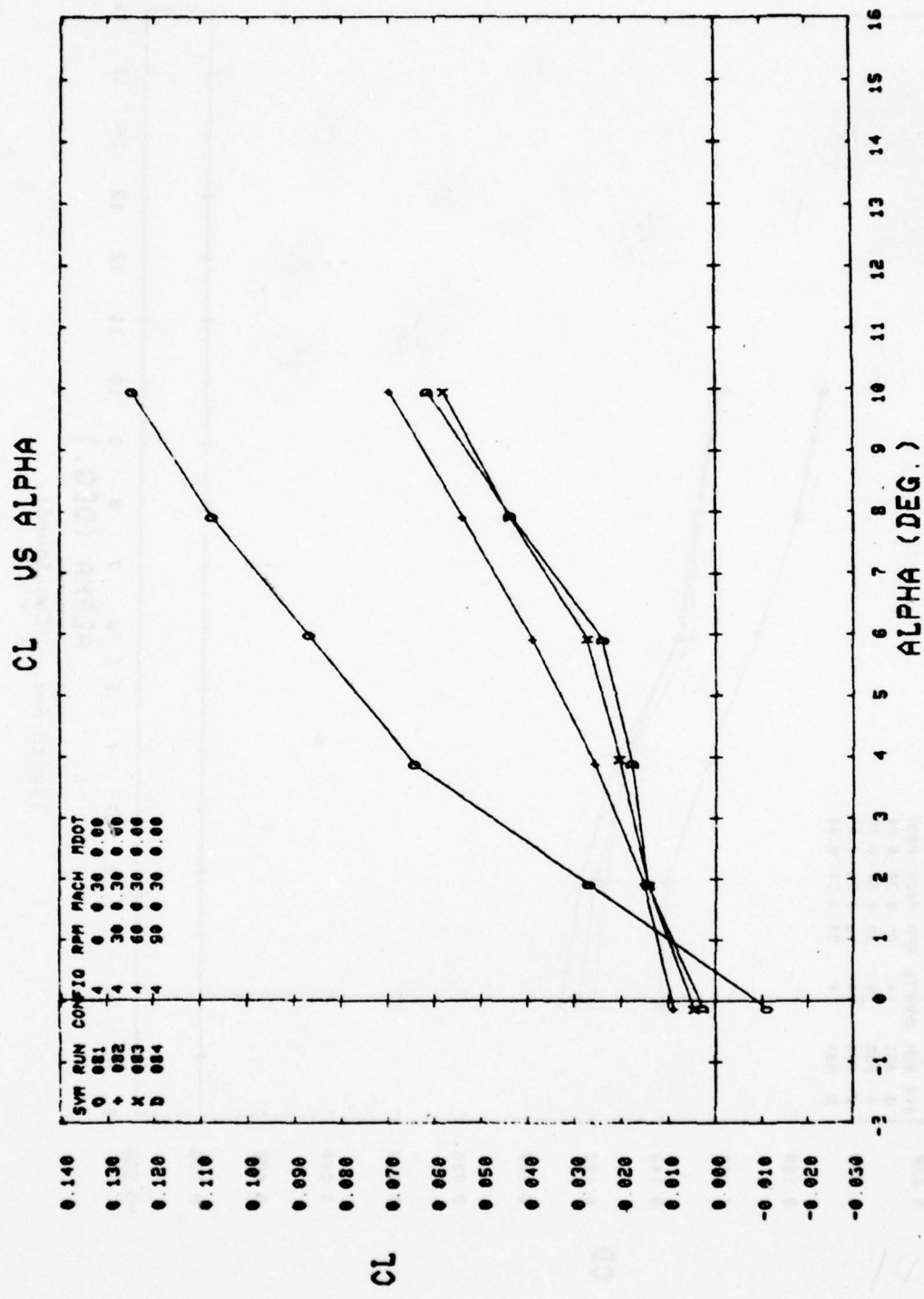


Figure A-7. (Continued).

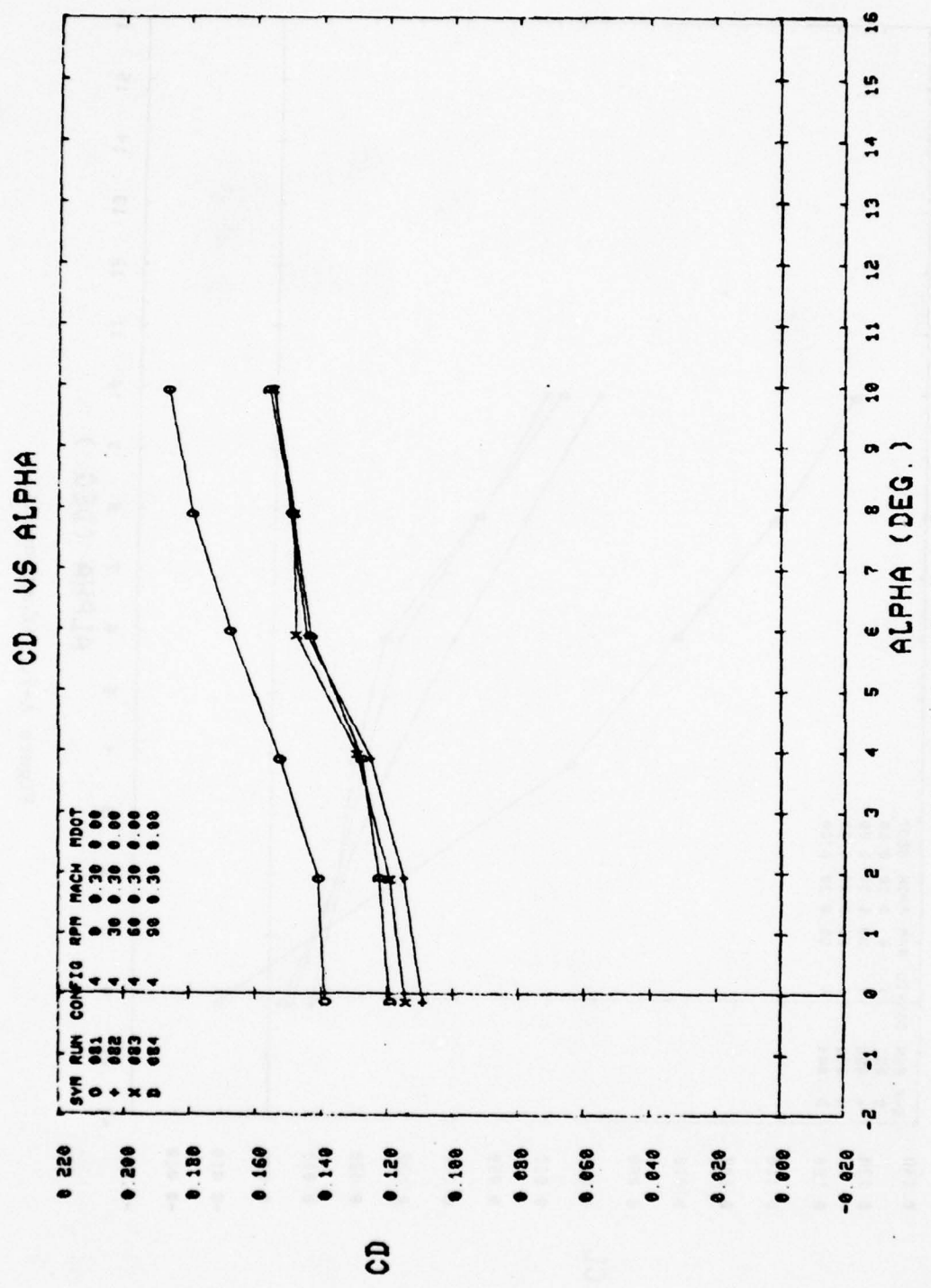


Figure A-7. (Continued).

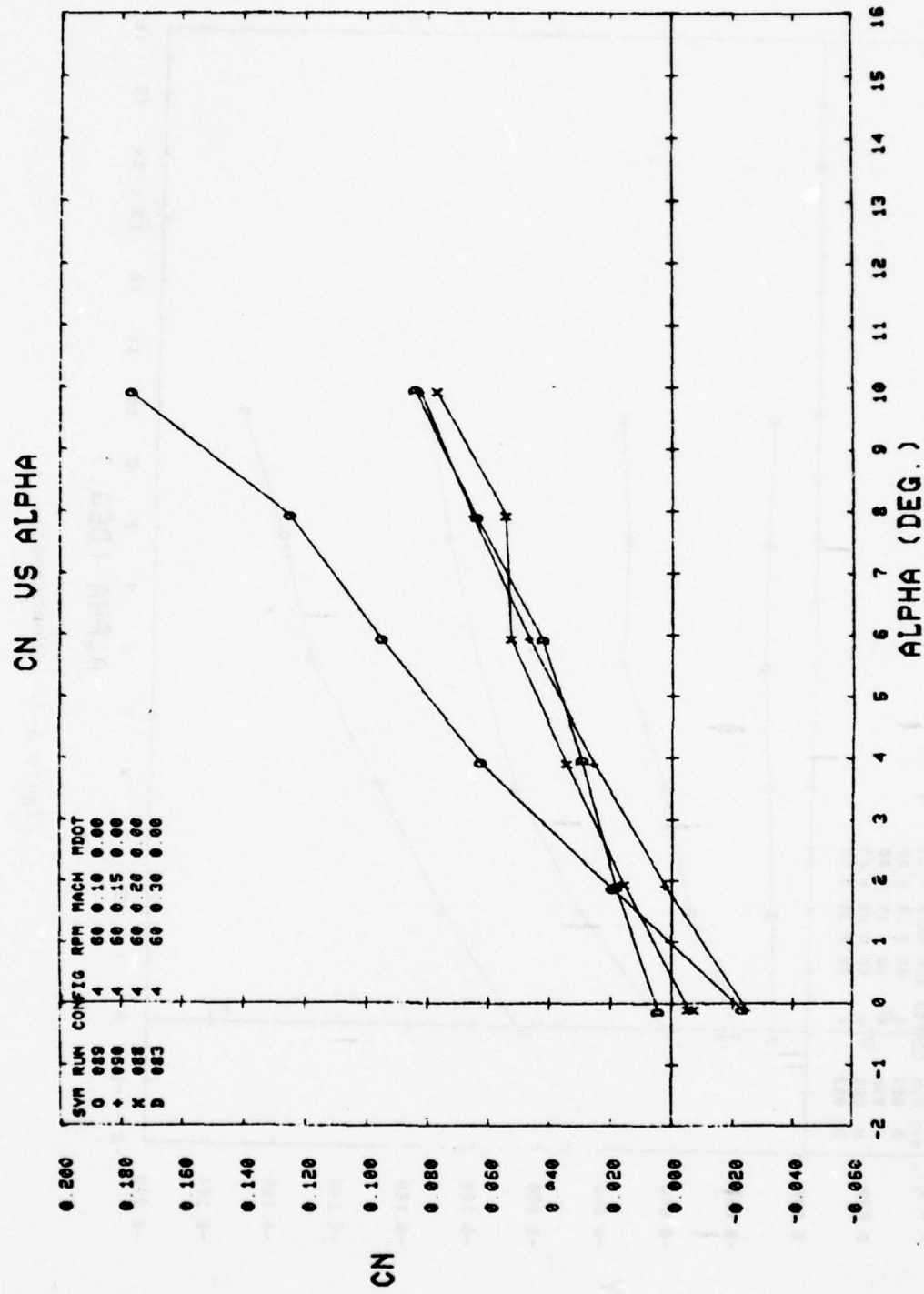


Figure A-7. (Continued).

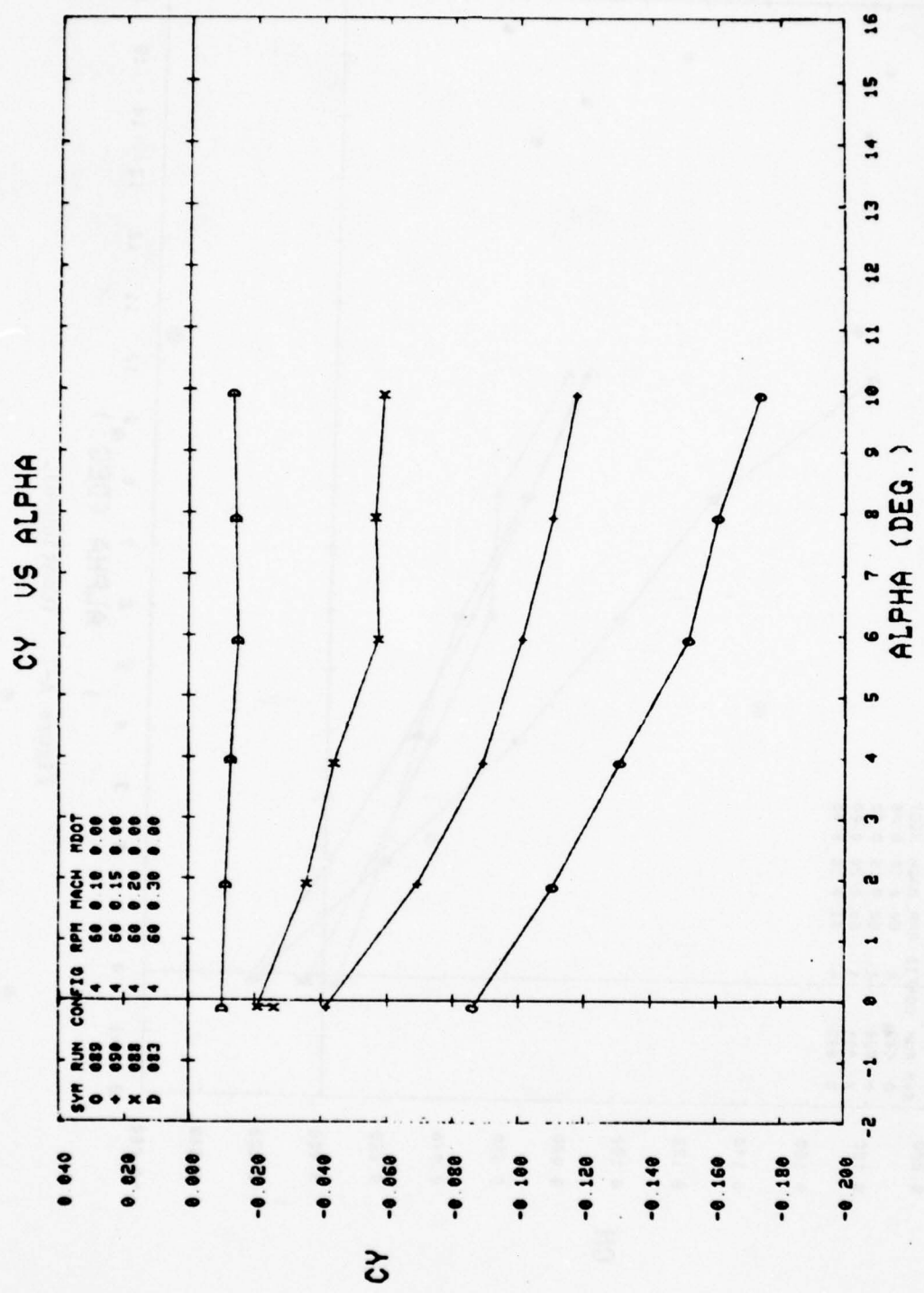


Figure A-7. (Continued).

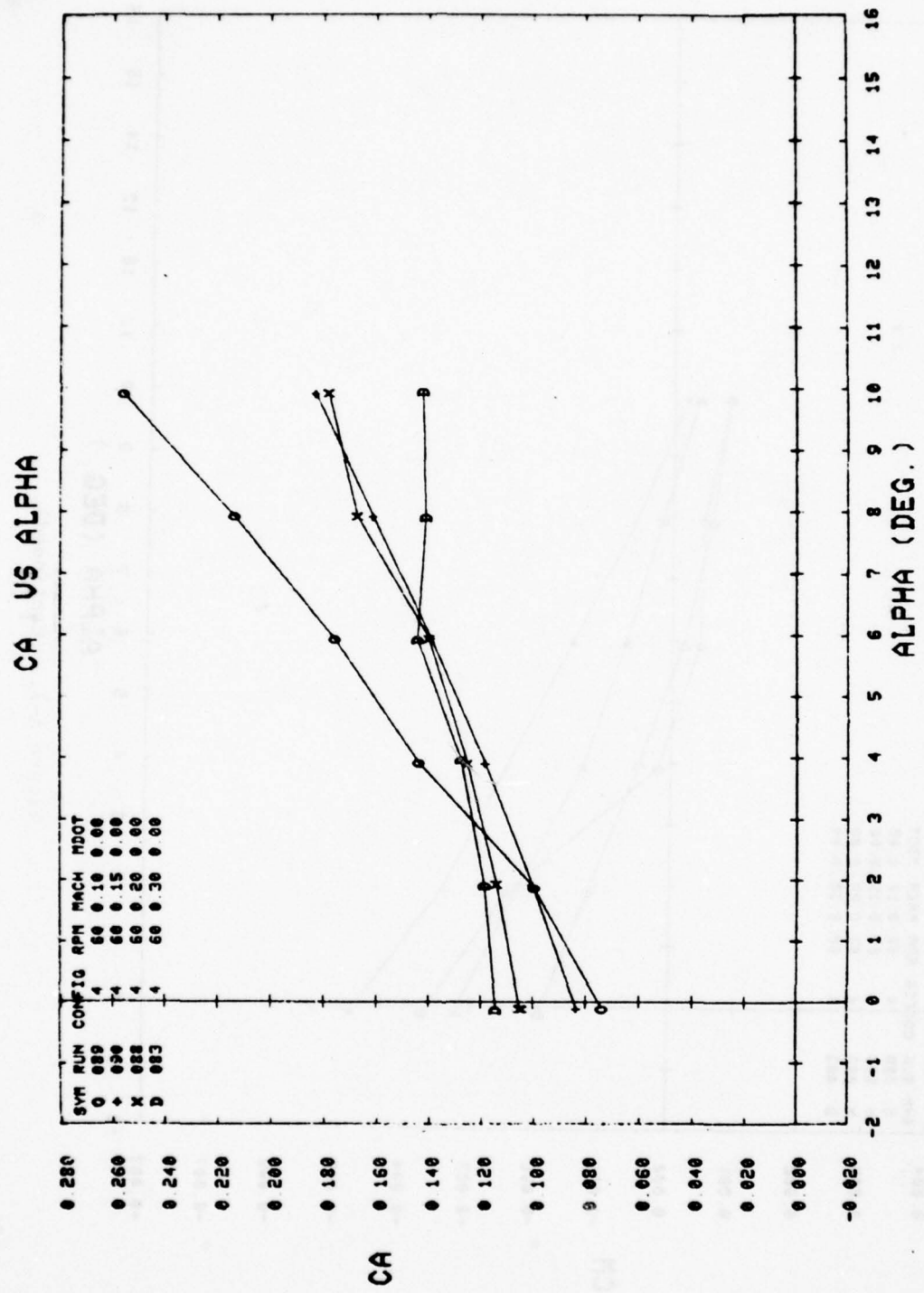


Figure A-7. (Continued).

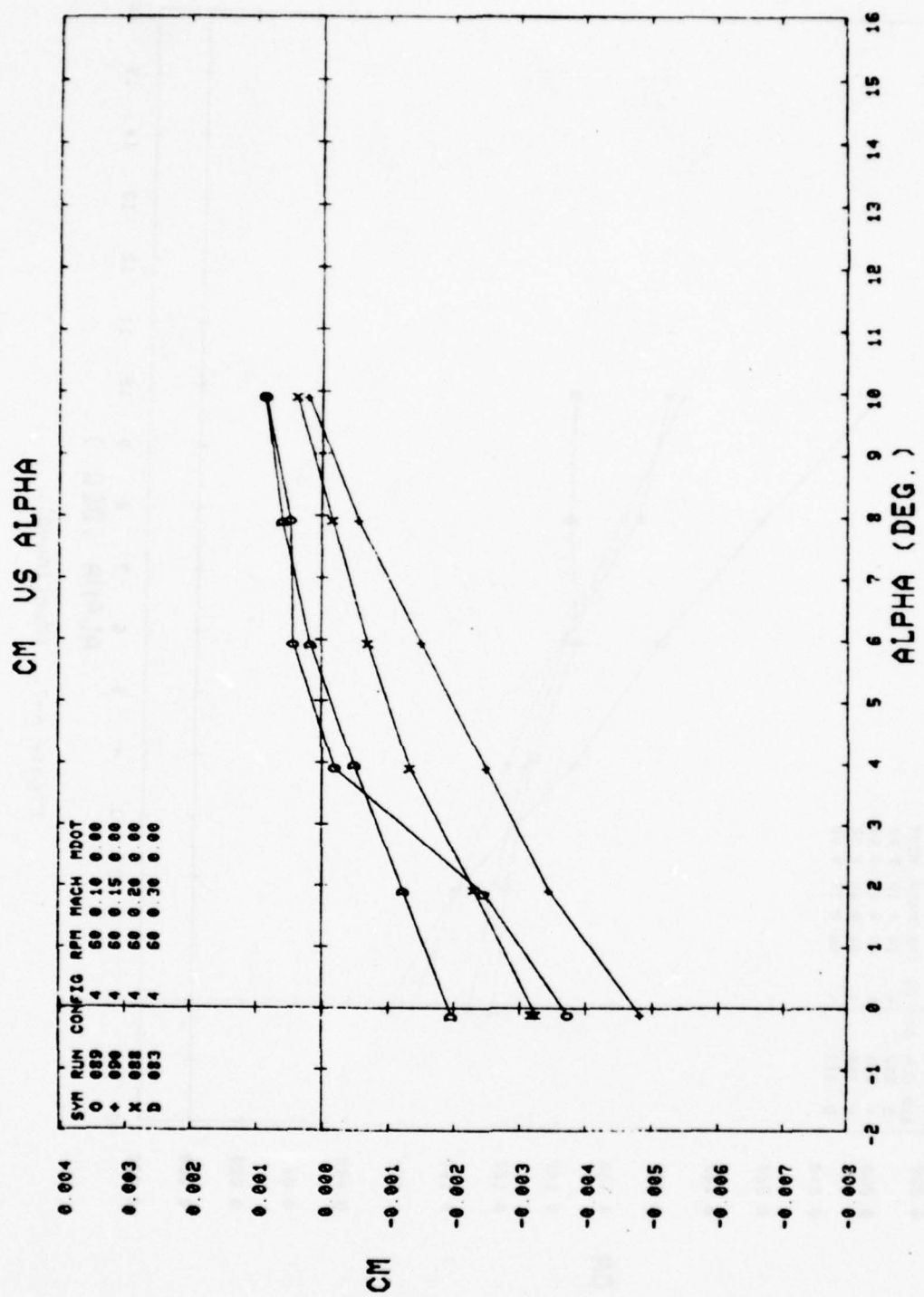


Figure A-7. (Continued).

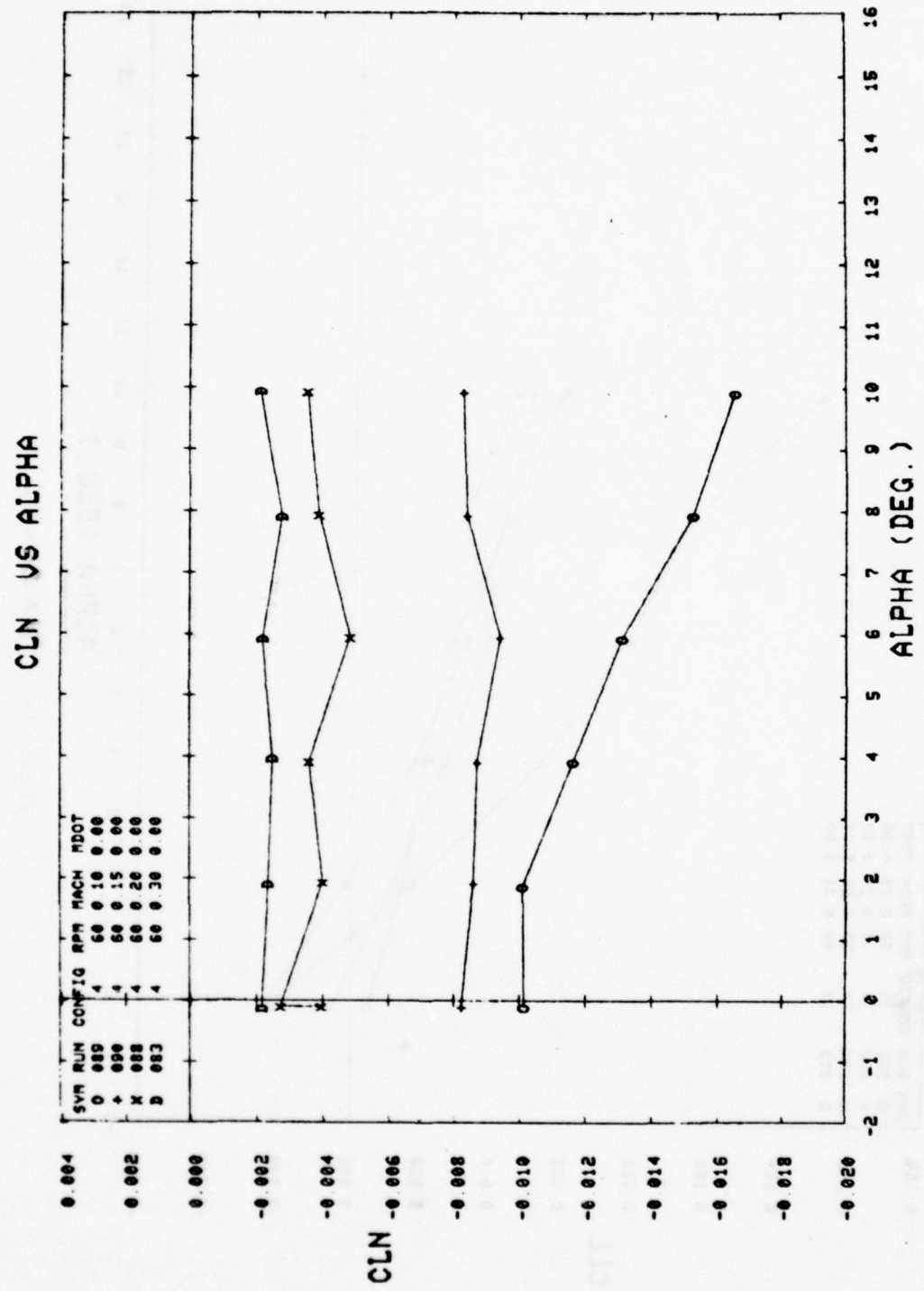


Figure A-7. (Continued).

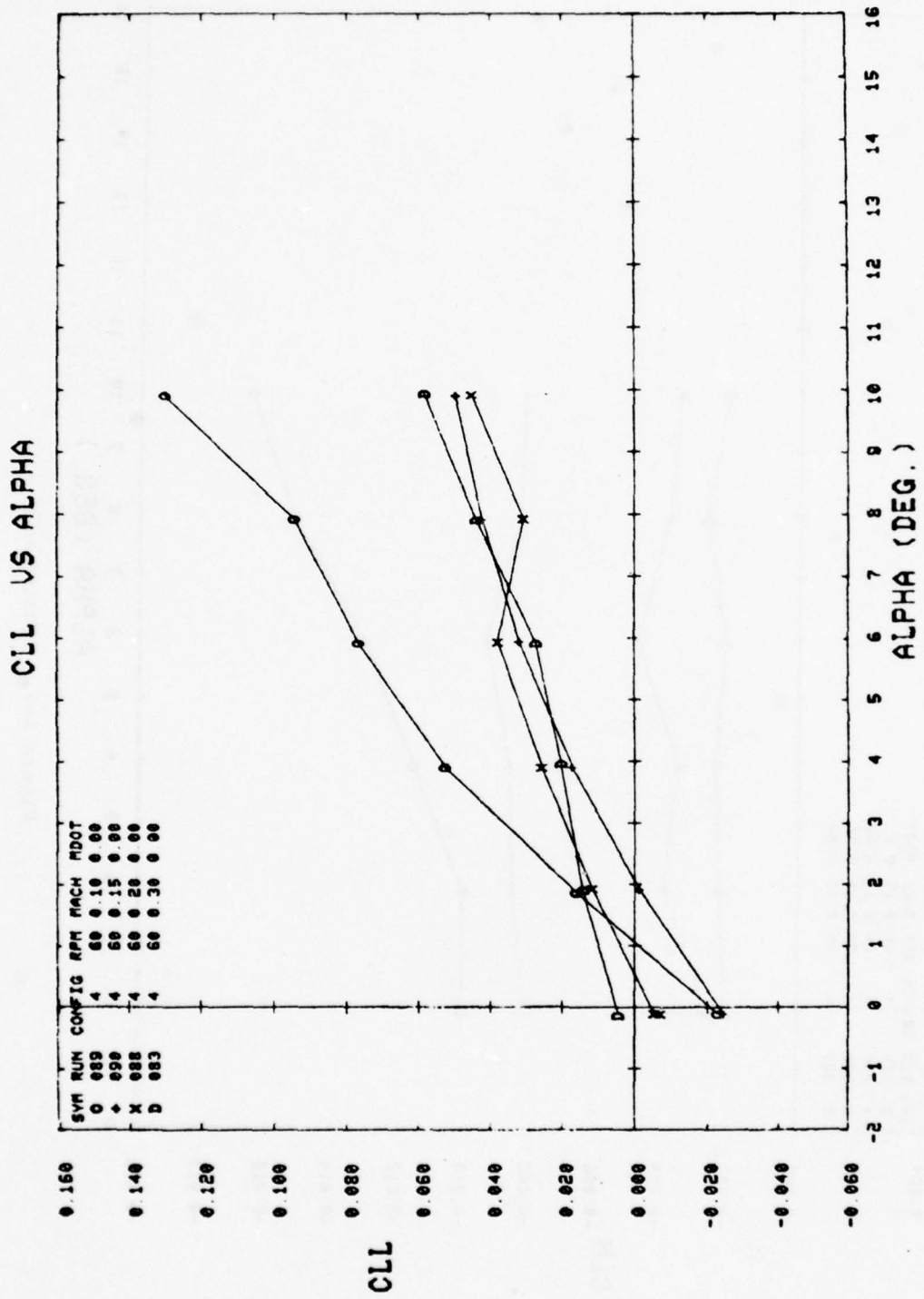


Figure A-7. (Continued).

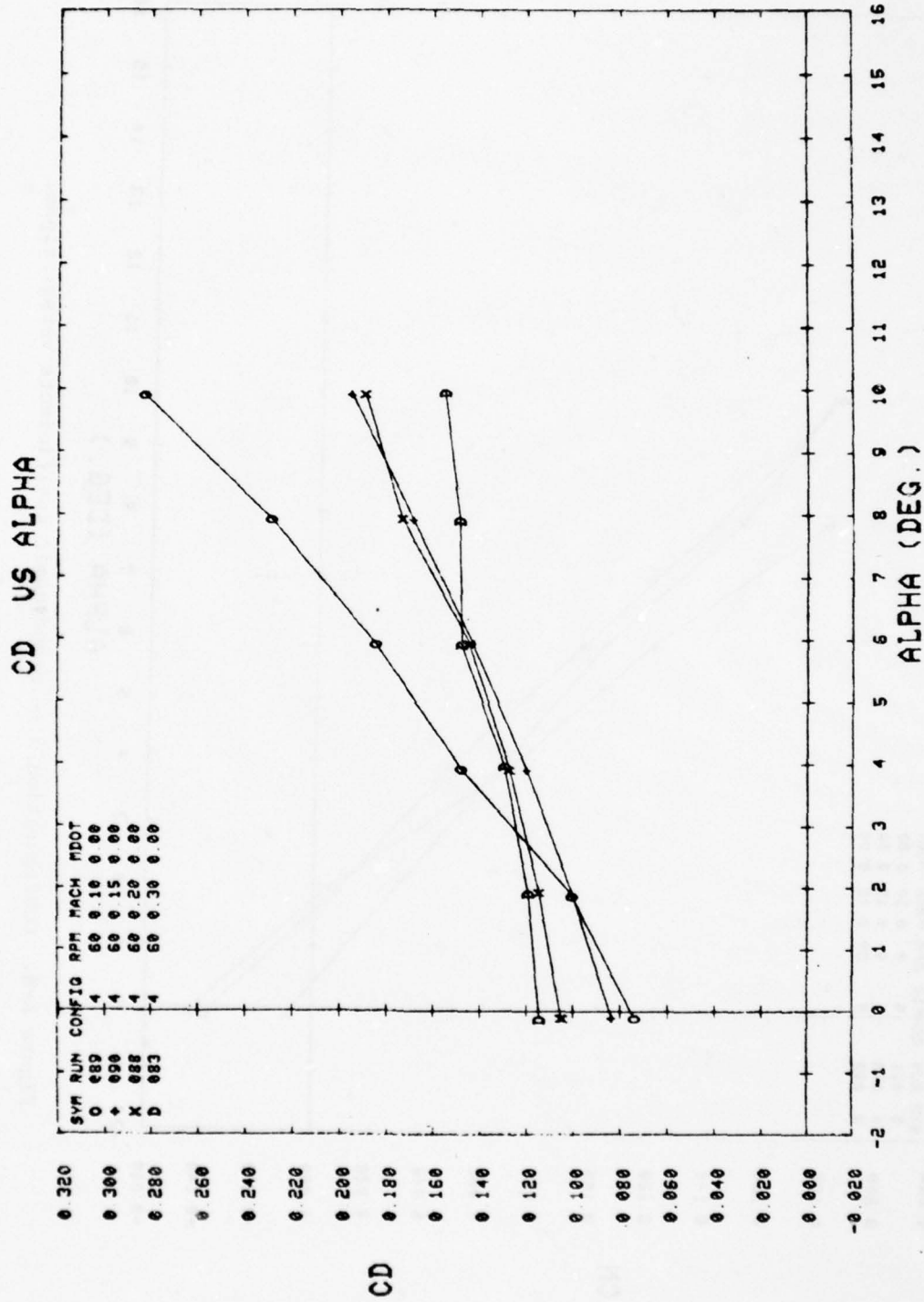


Figure A-7. (Concluded).

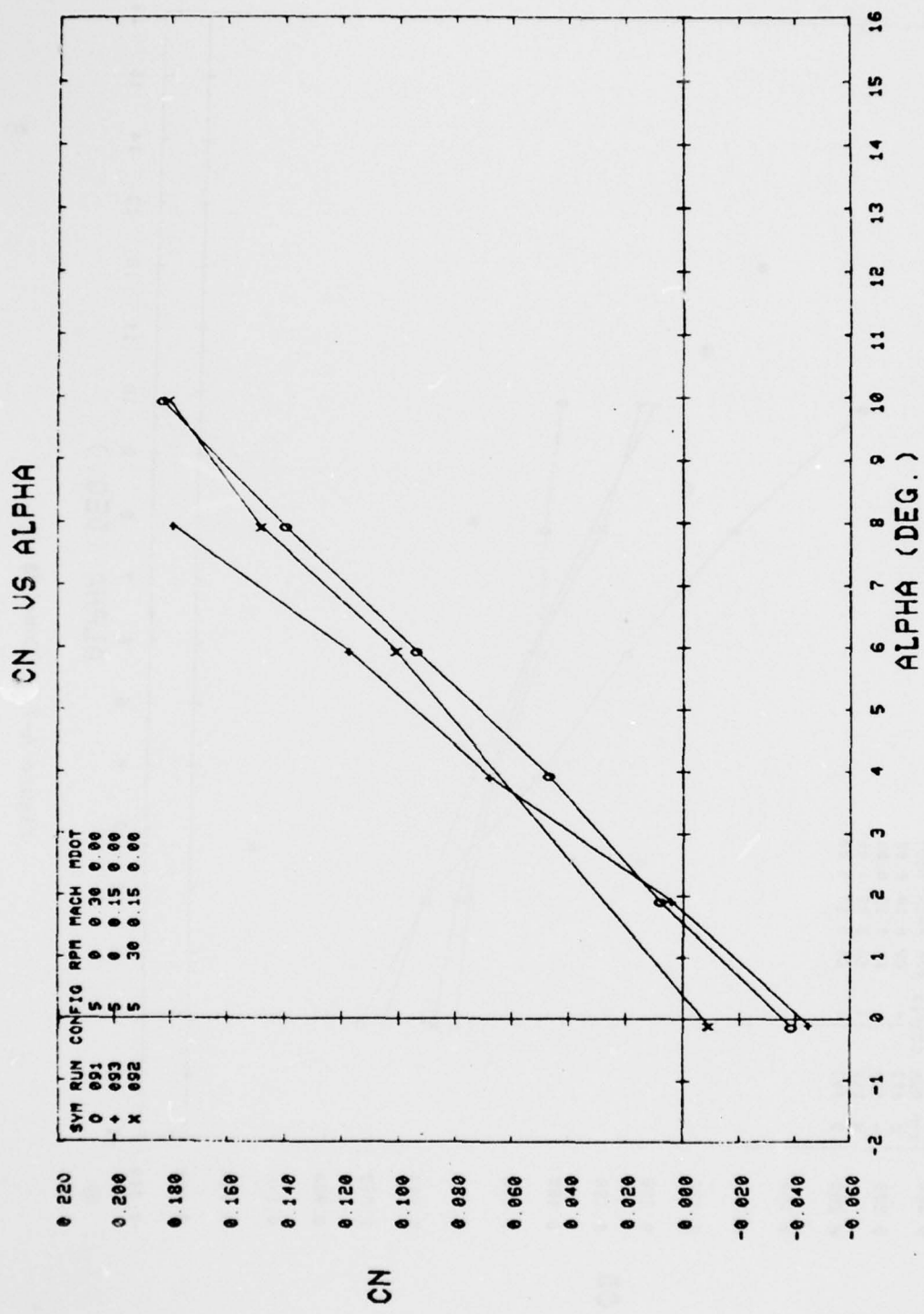


Figure A-8. Configuration 5 — aerodynamic coefficients versus alpha.

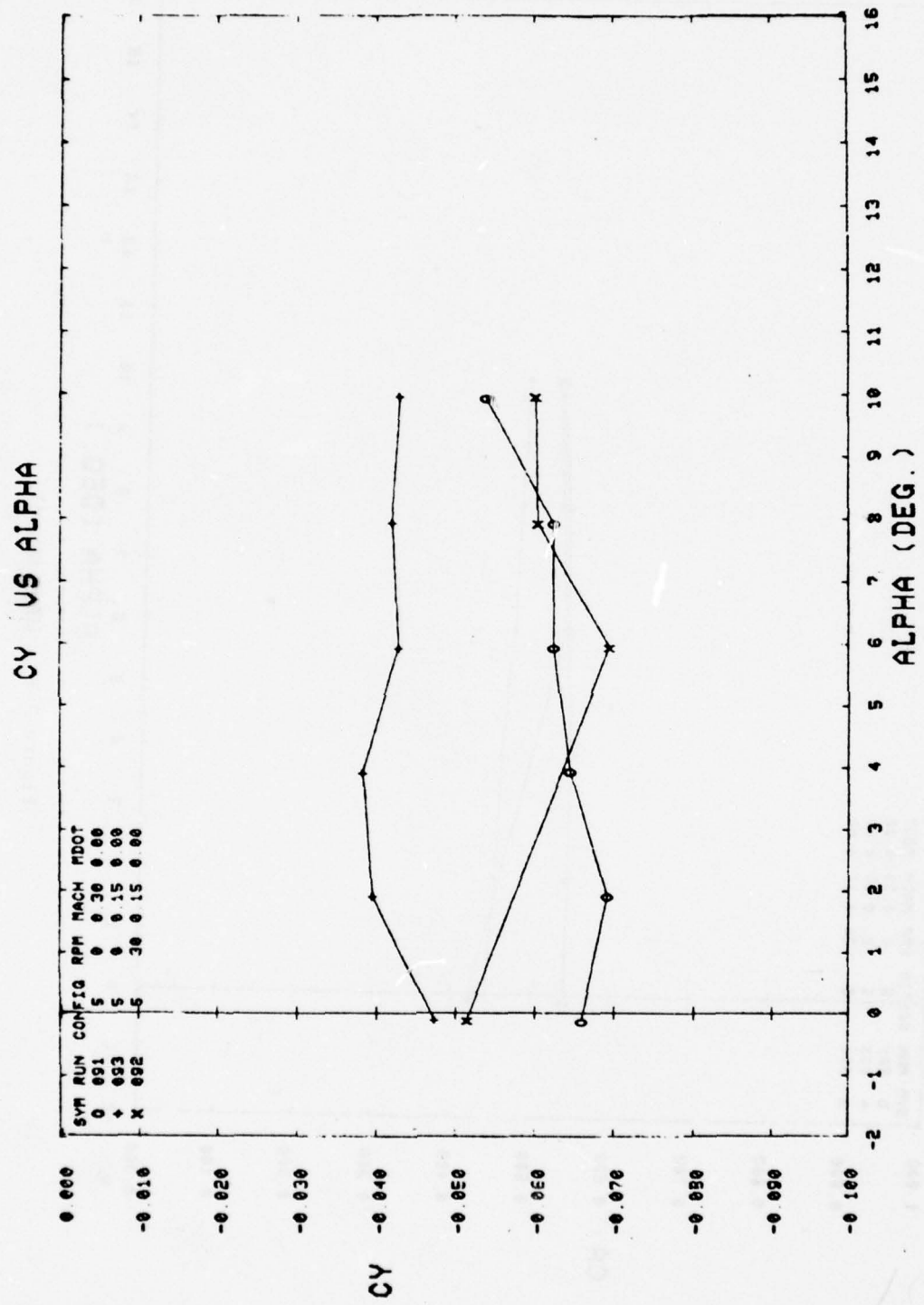


Figure A-8. (Continued).

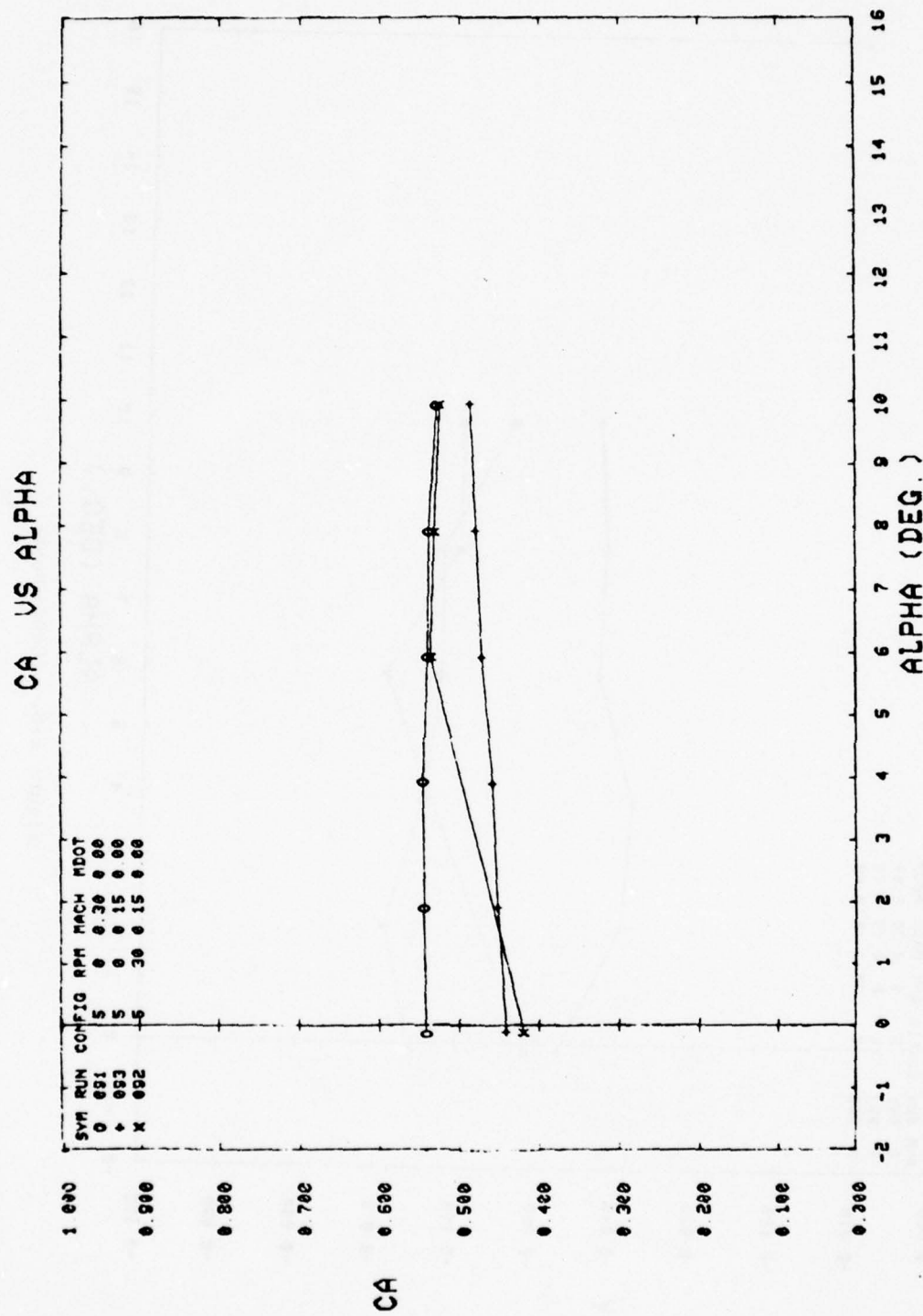


Figure A-8. (Continued).

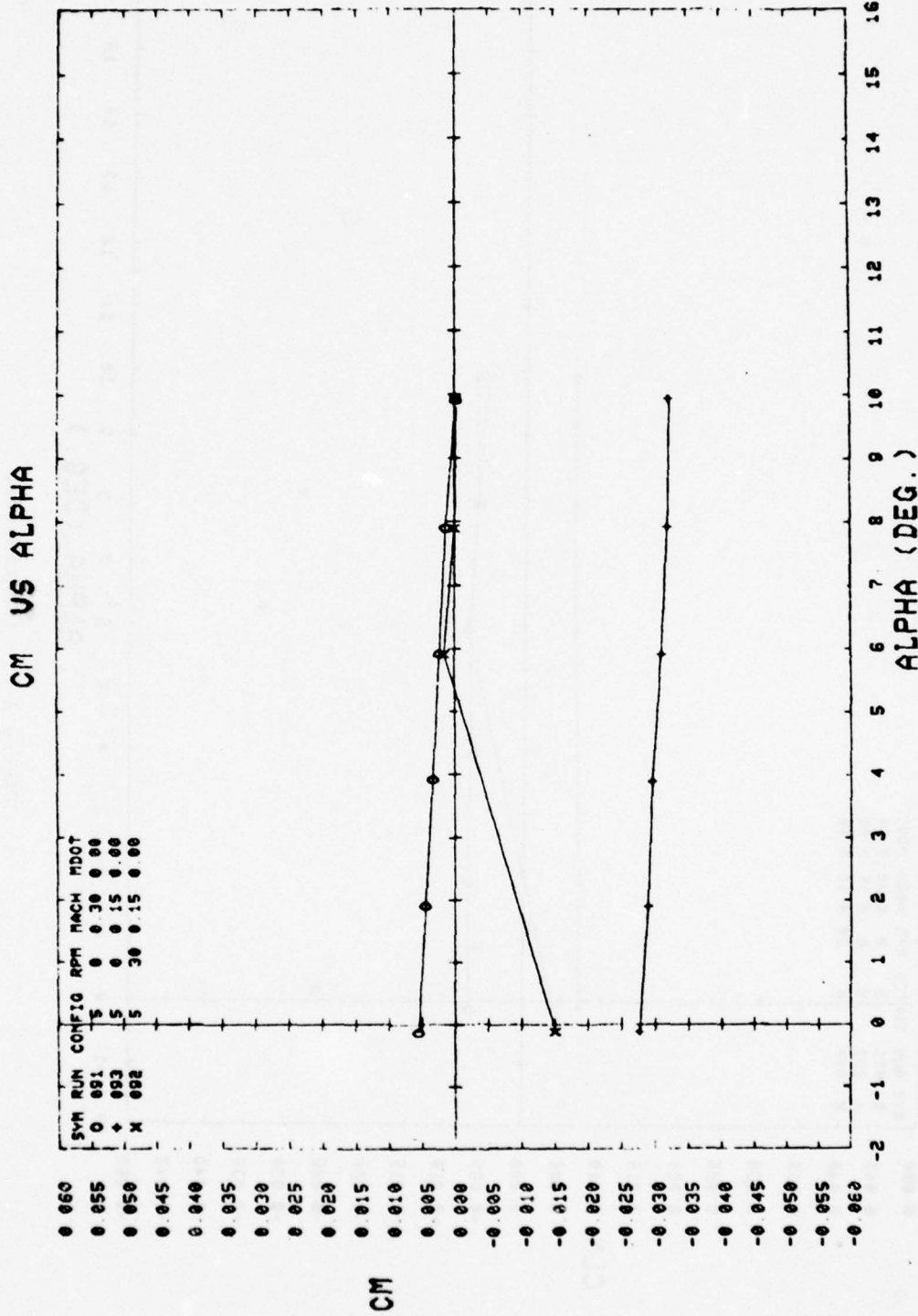


Figure A-8. (Continued).

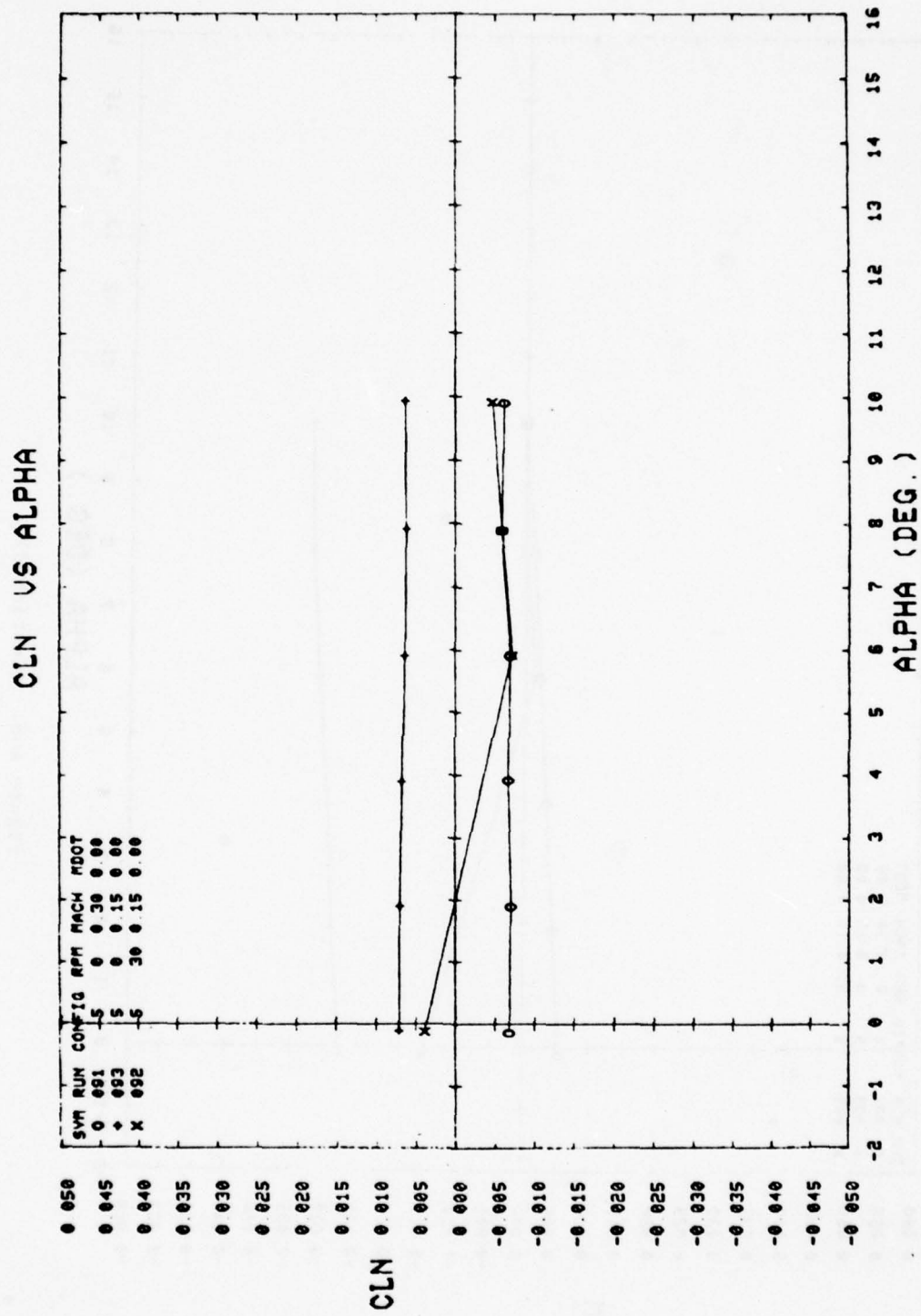


Figure A-8. (Continued).

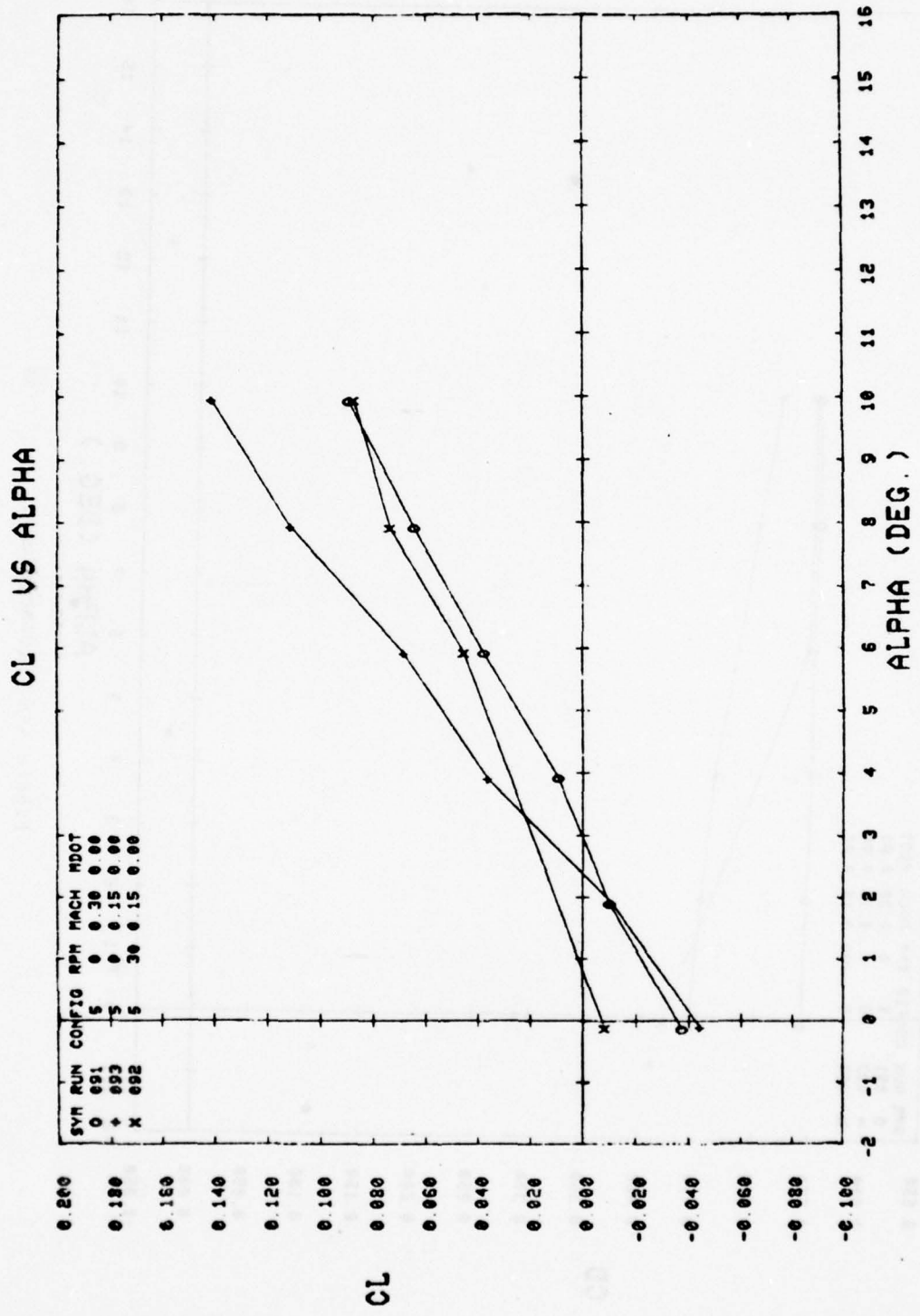


Figure A-8. (Continued).

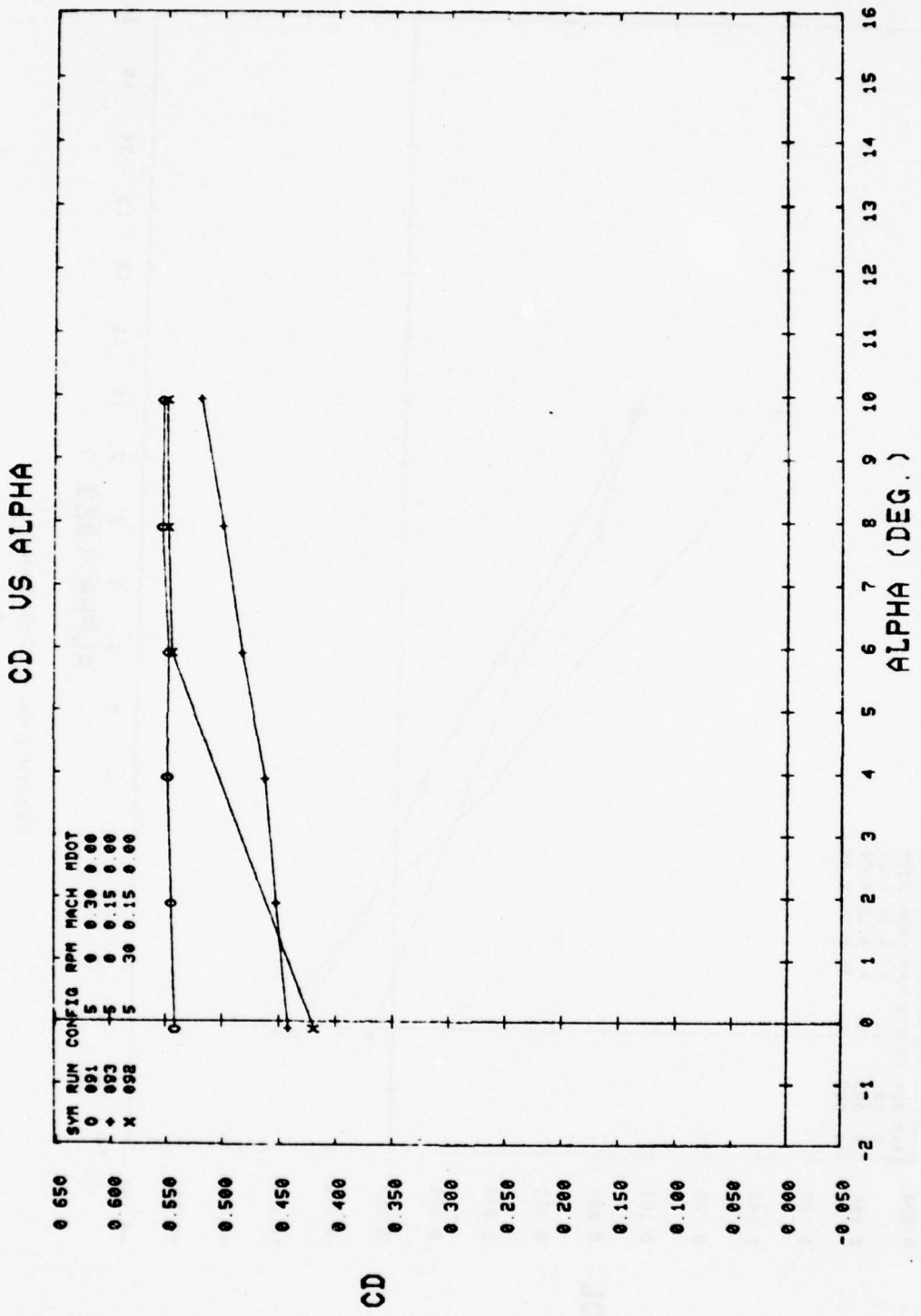


Figure A-8. (Concluded).

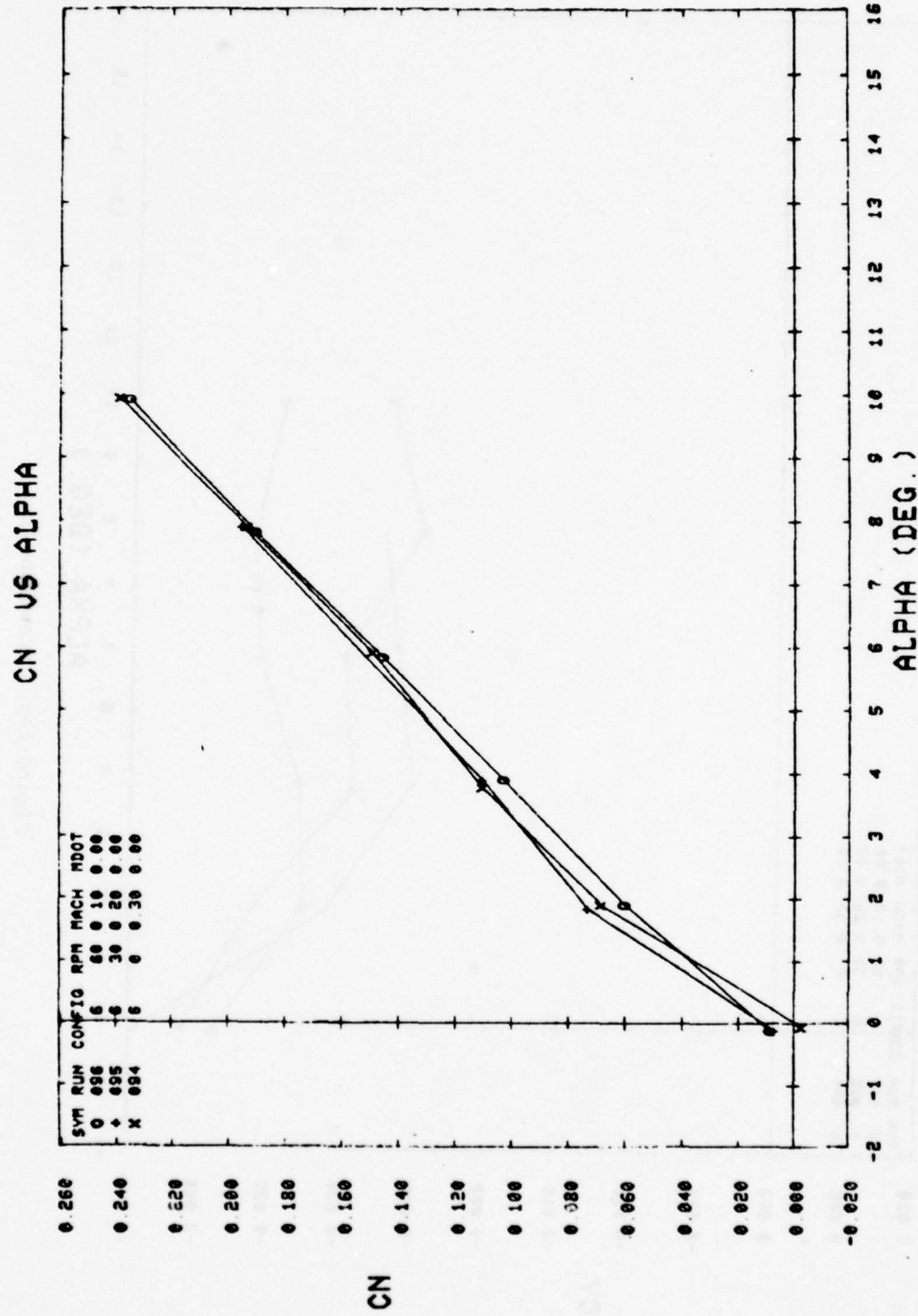


Figure A-9. Configuration 6 — aerodynamic coefficients versus alpha.

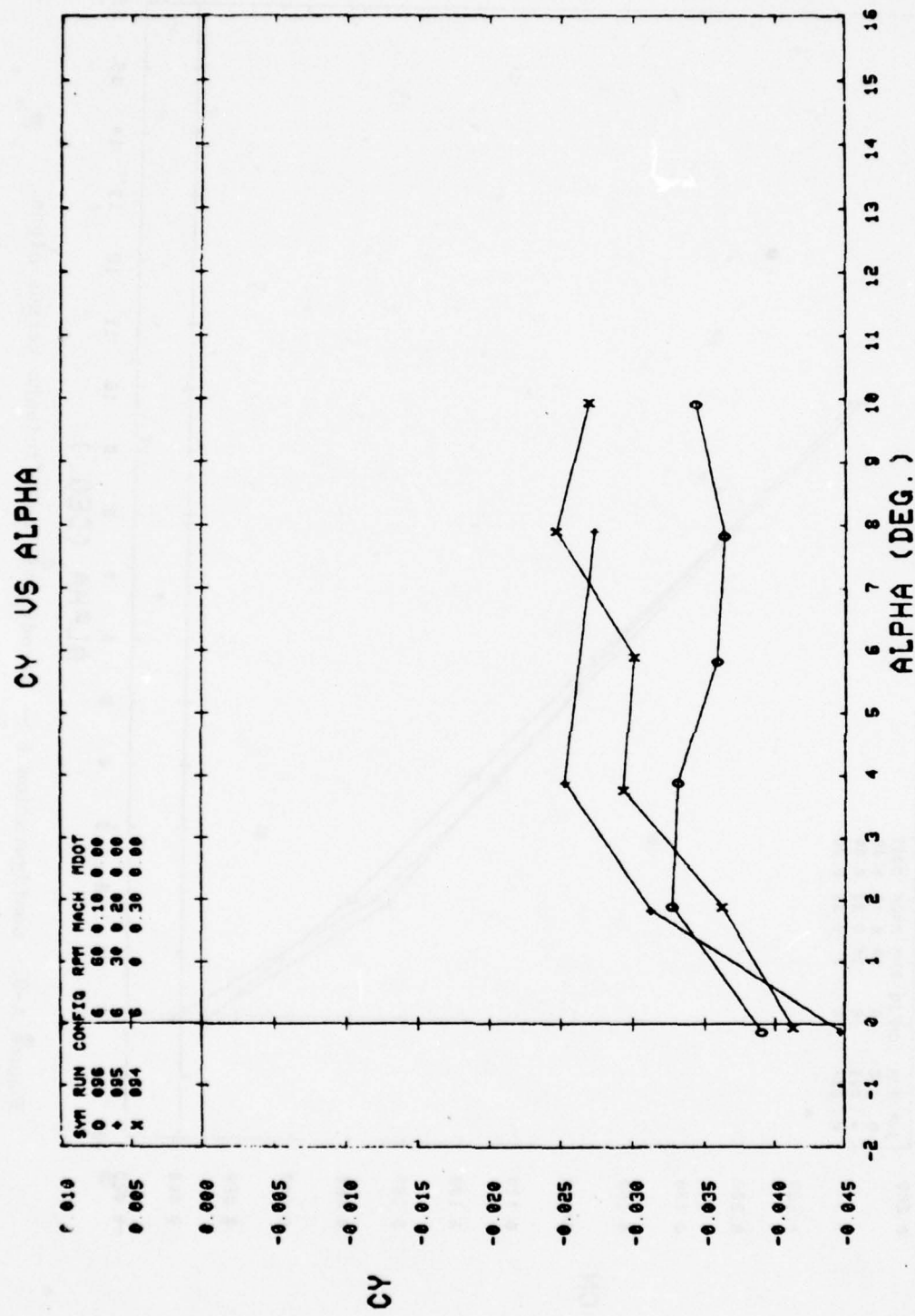


Figure A-9. (Continued).

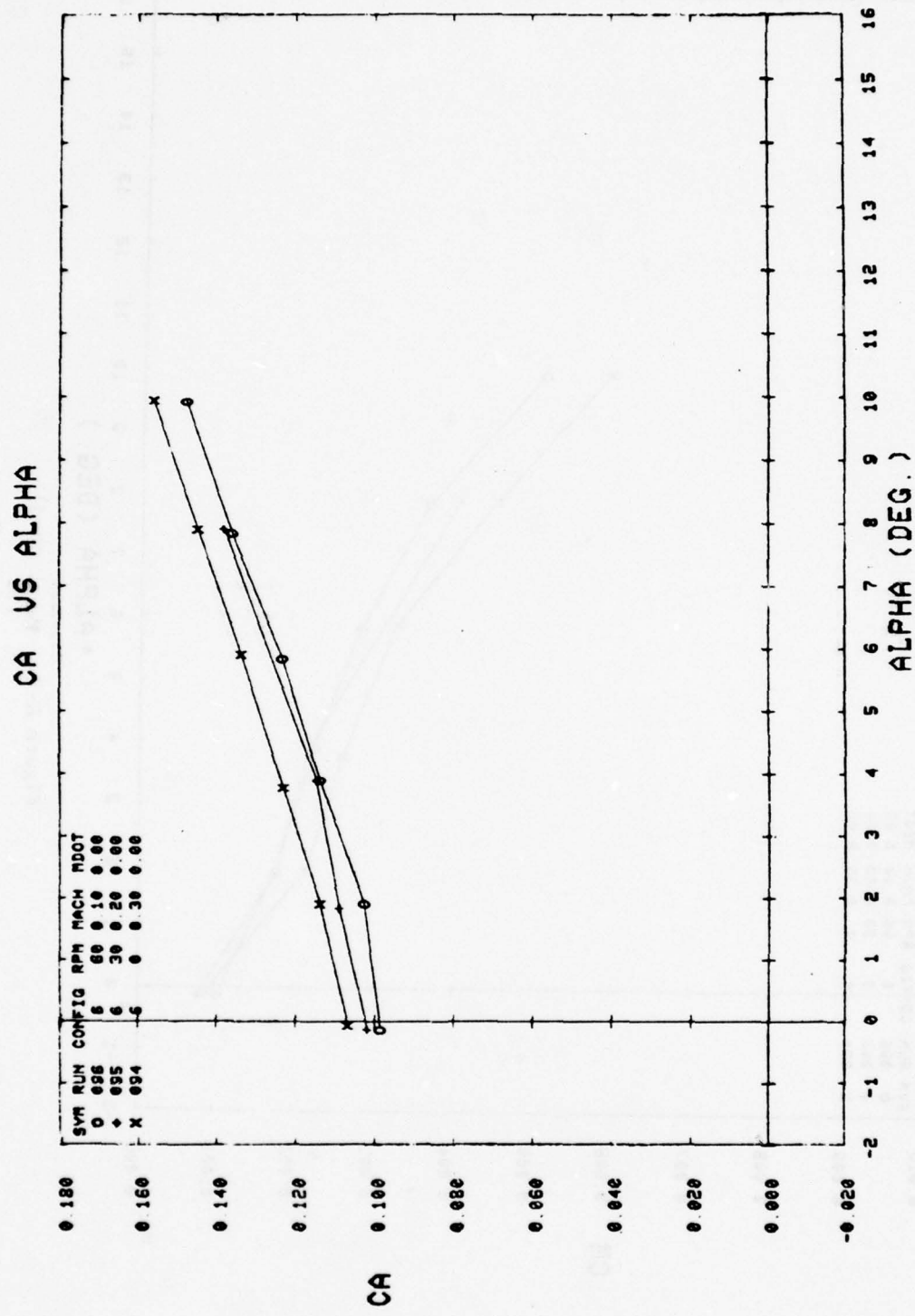


Figure A-9. (Continued).

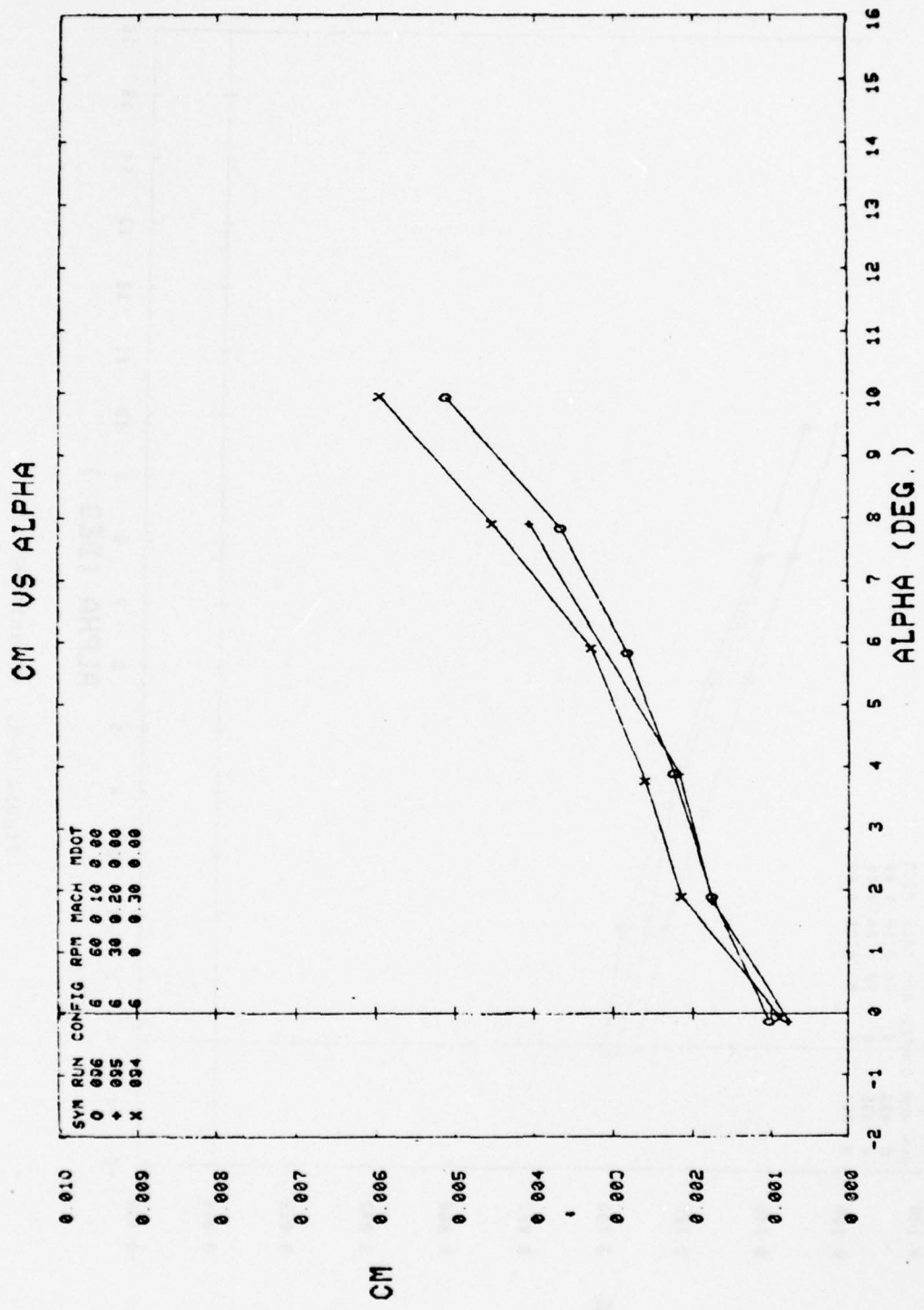


Figure A-9. (Continued).

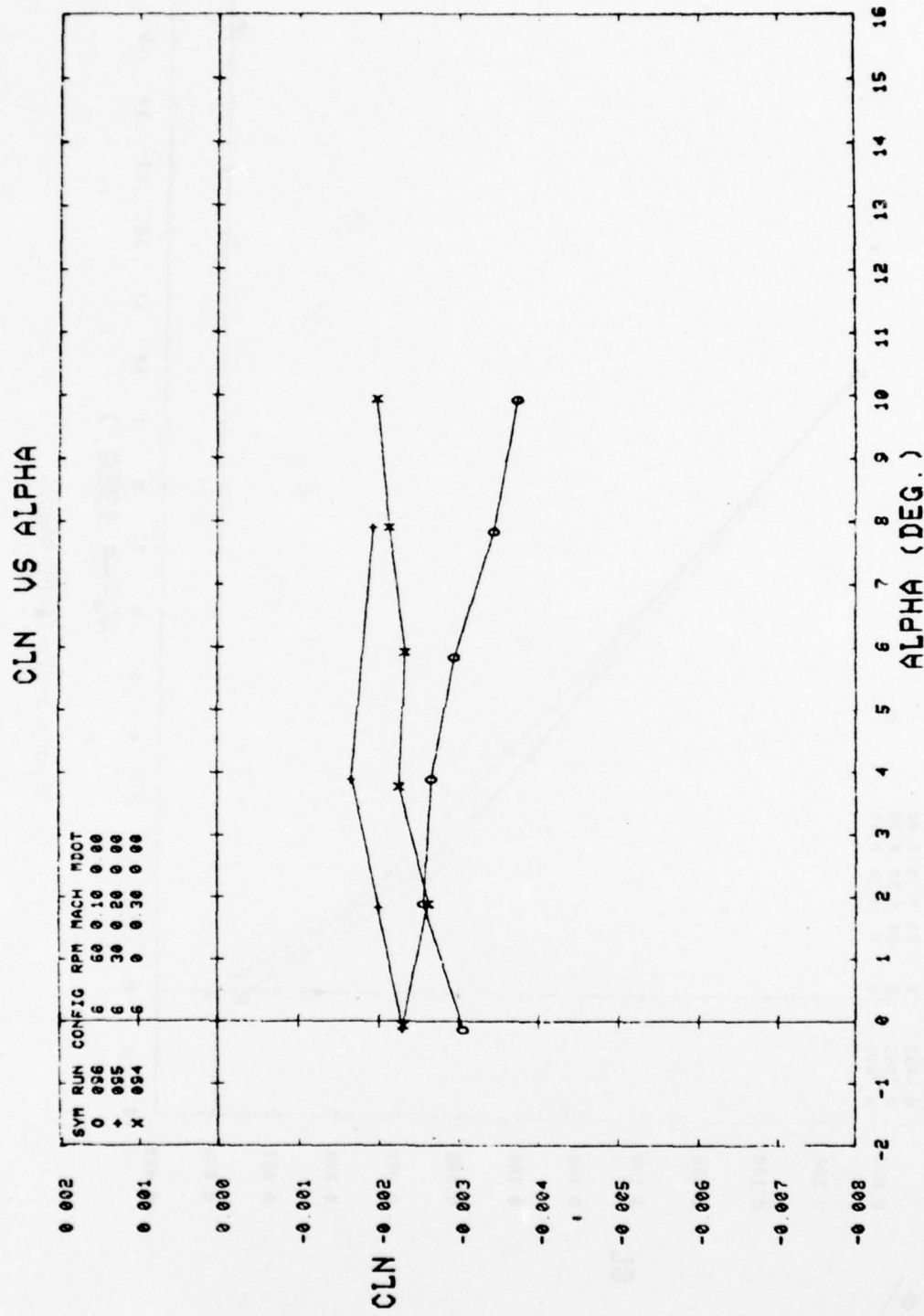


Figure A-9. (Continued).

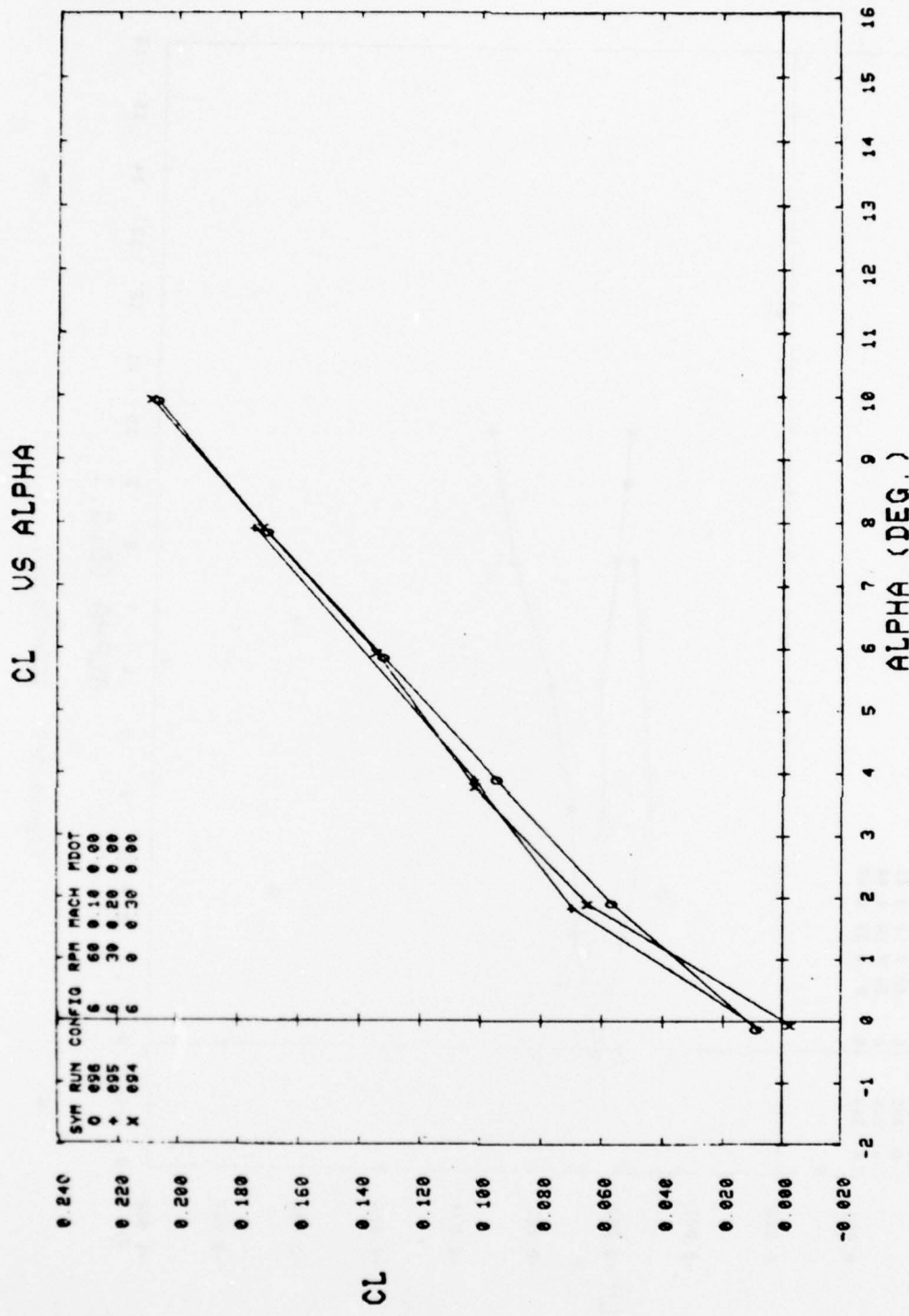


Figure A-9. (Continued).

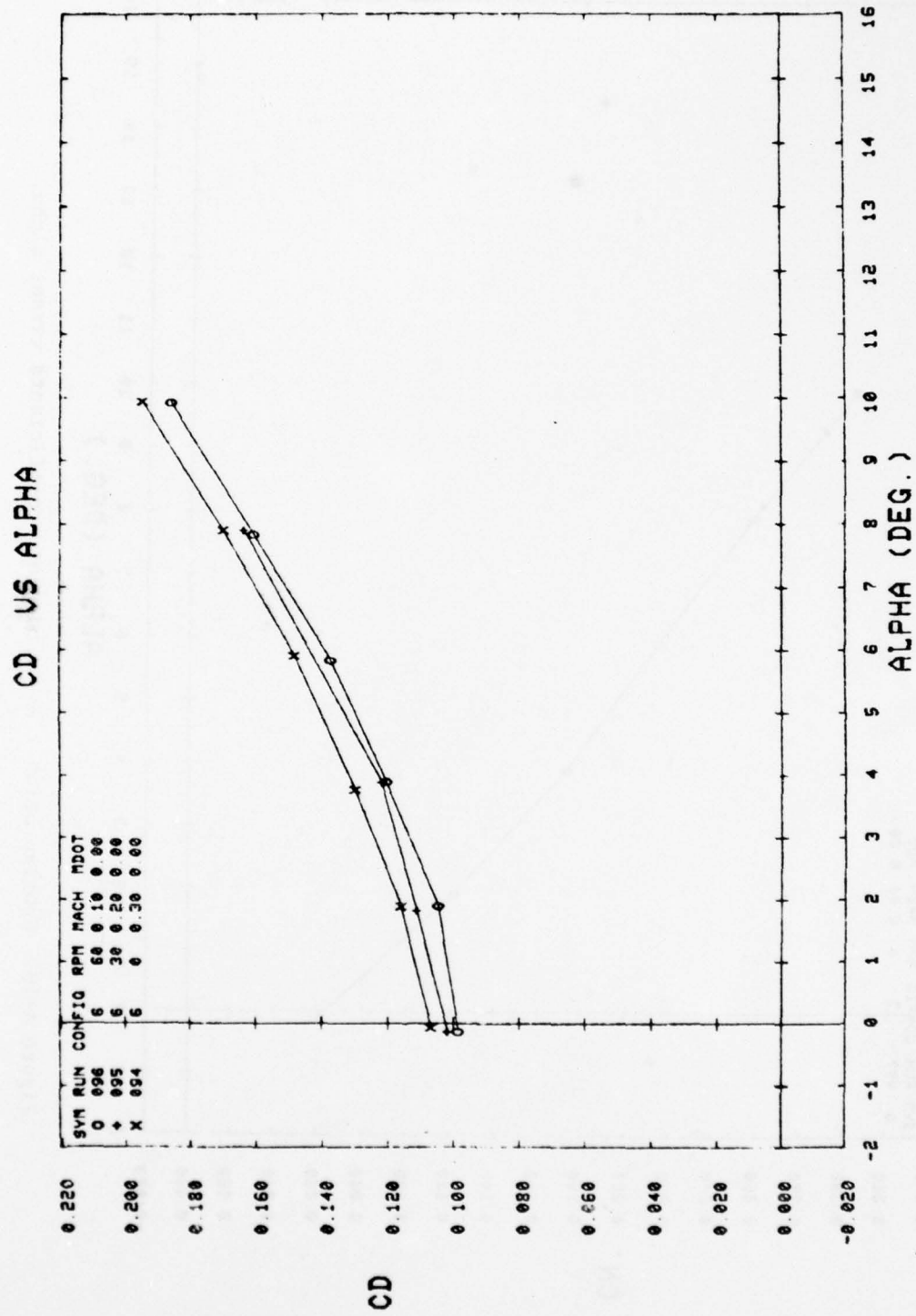


Figure A-9. (Concluded).

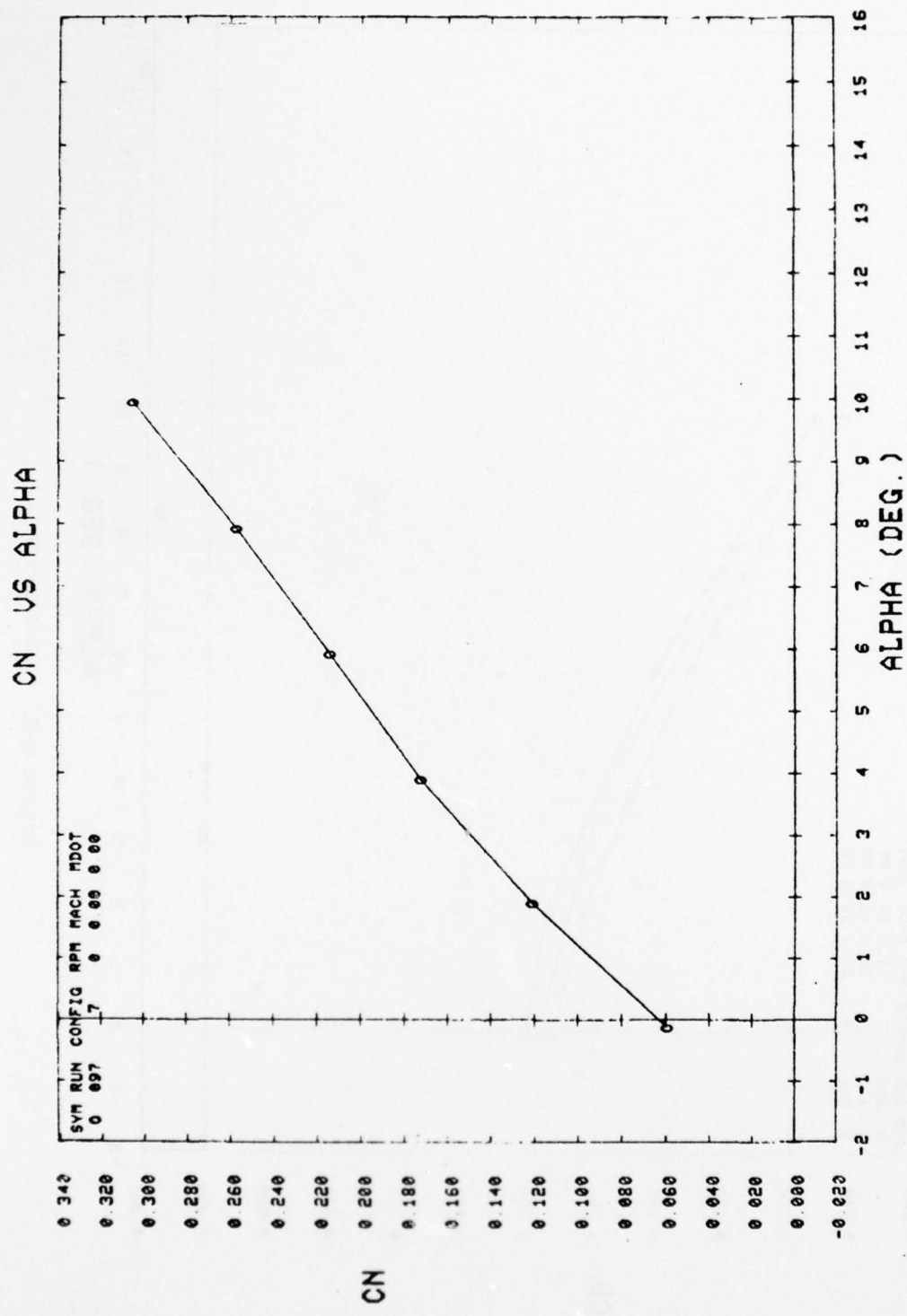


Figure A-10. Configuration 7 — aerodynamic coefficients versus alpha.

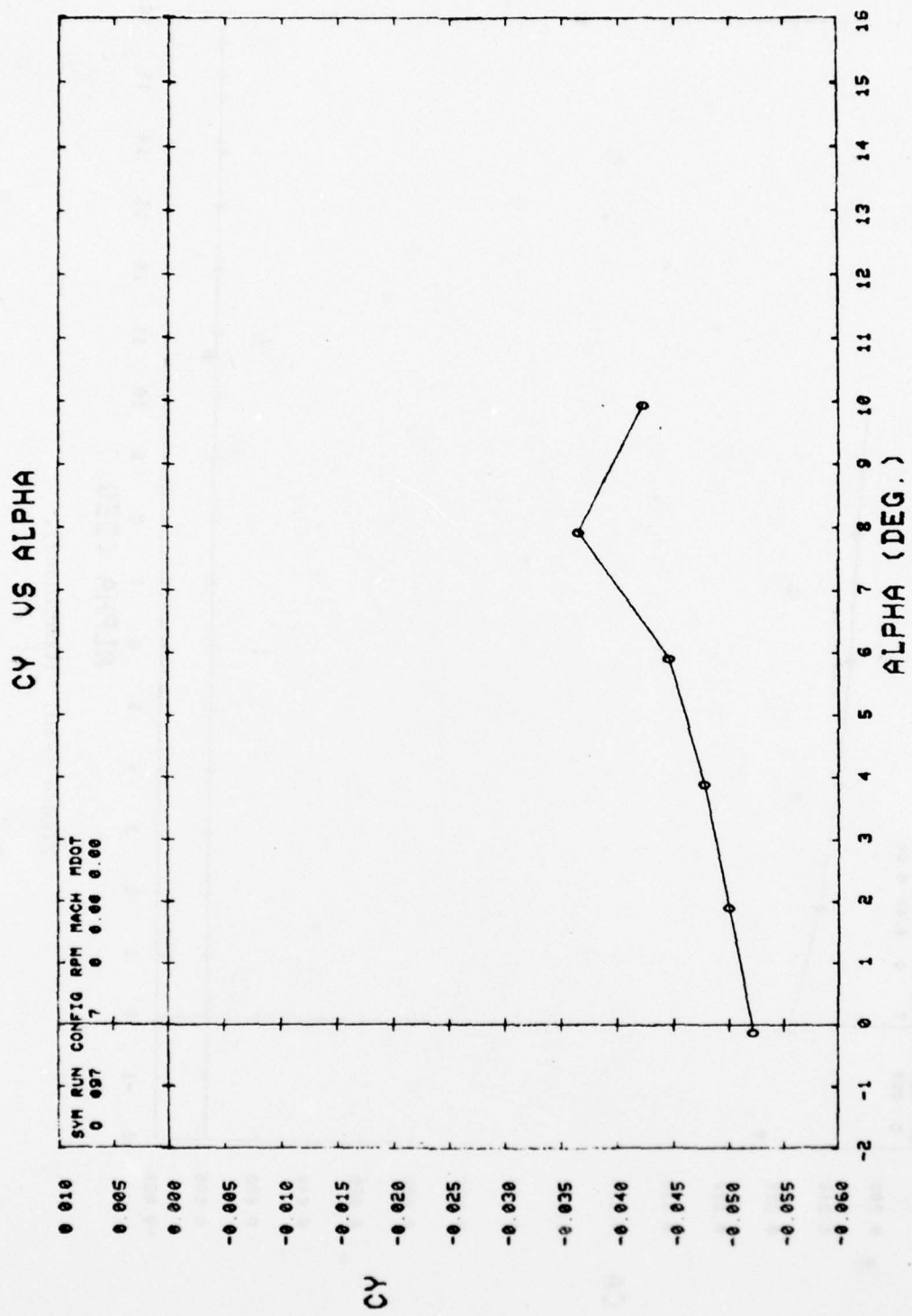


Figure A-10. (Continued).

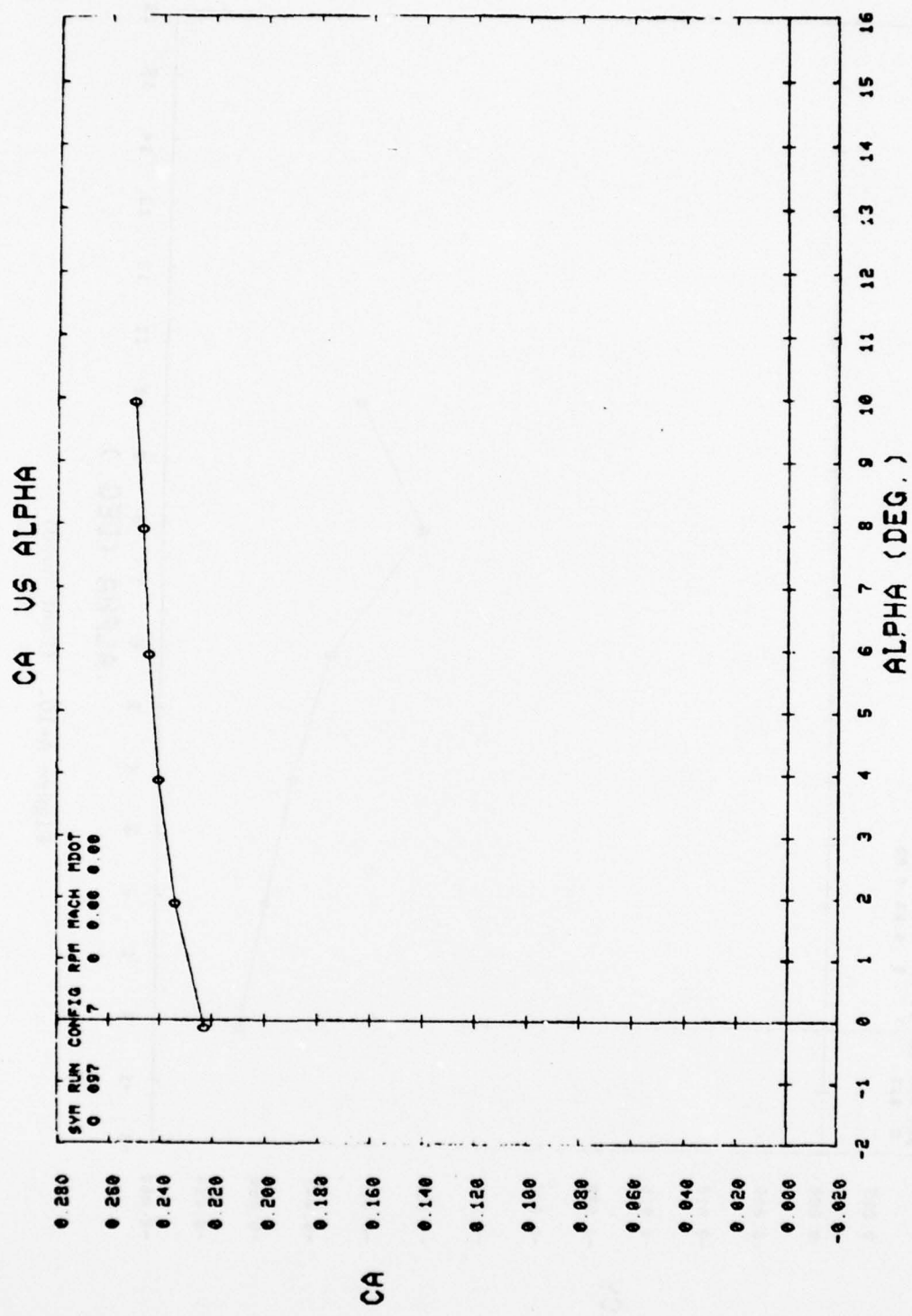


Figure A-10. (Continued).

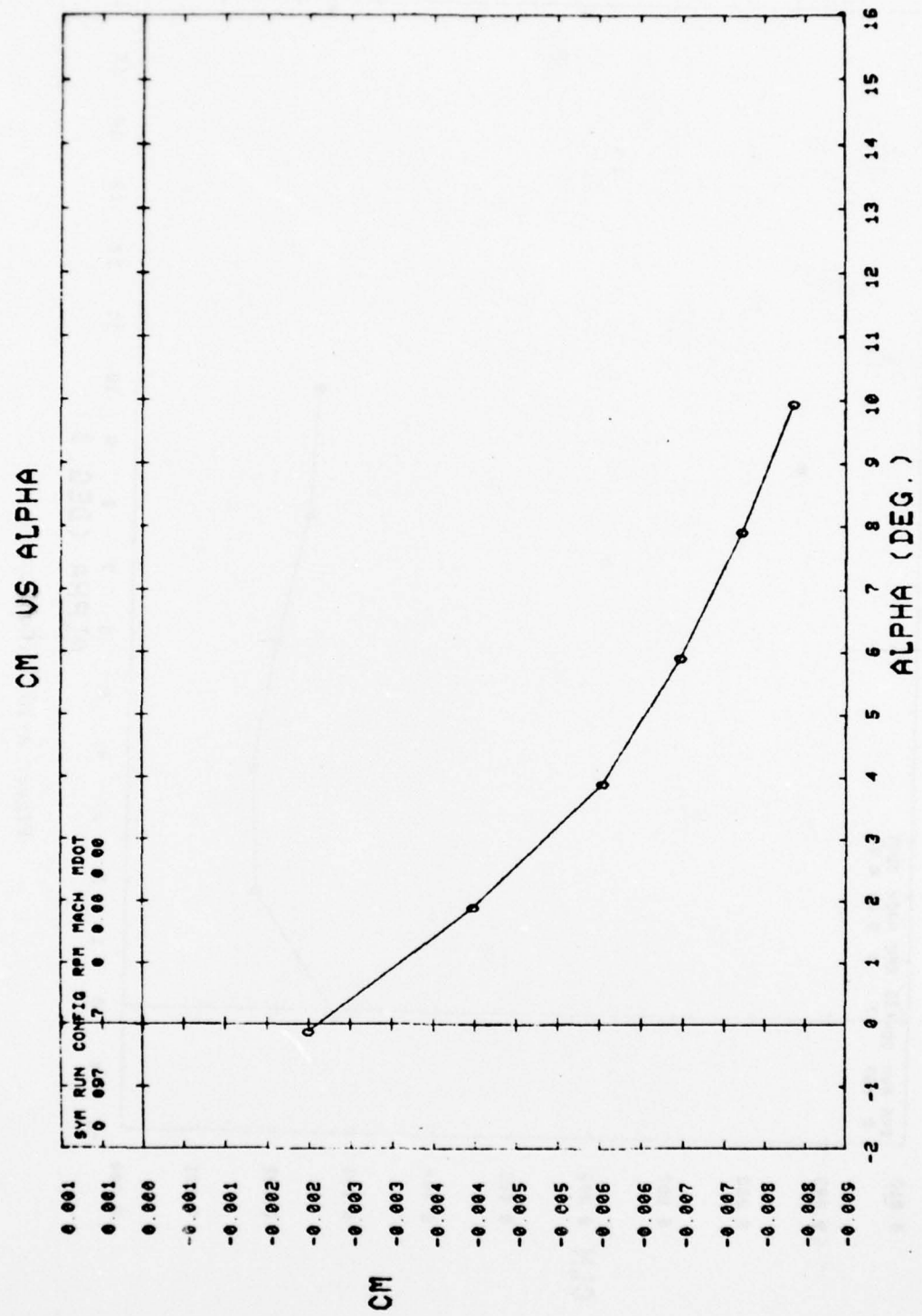


Figure A-10. (Continued).

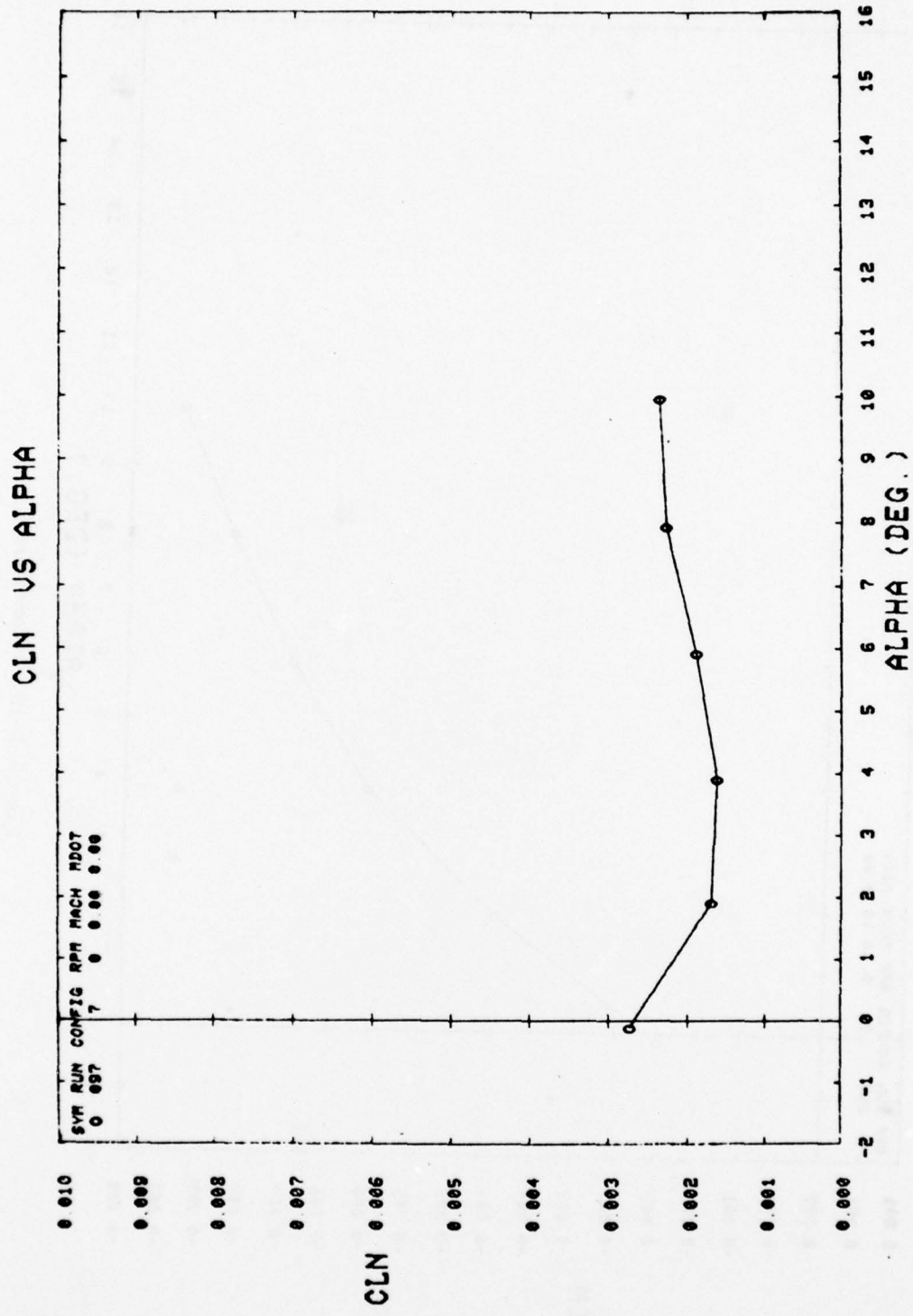


Figure A-10. (Continued).

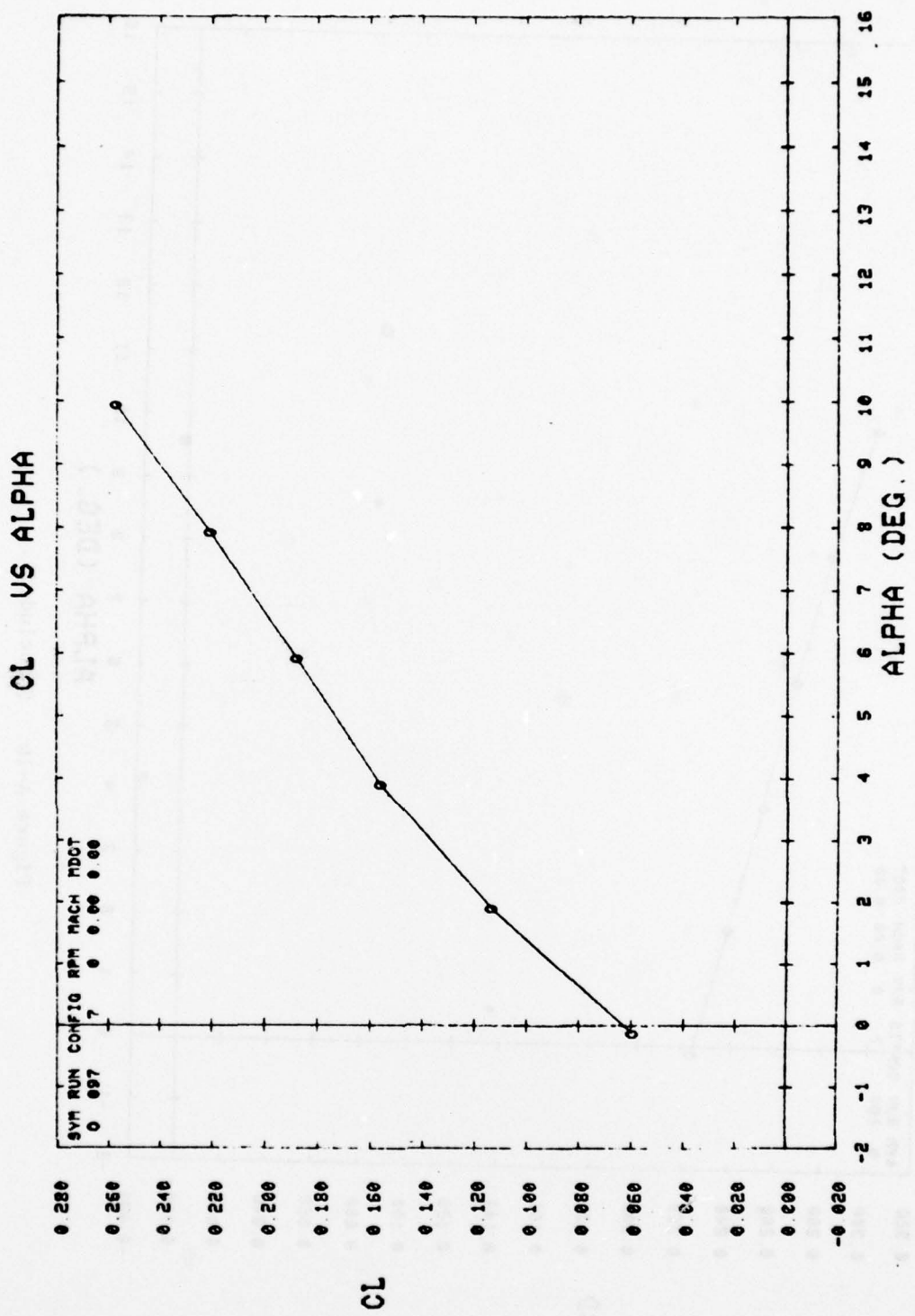


Figure A-10. (Continued).

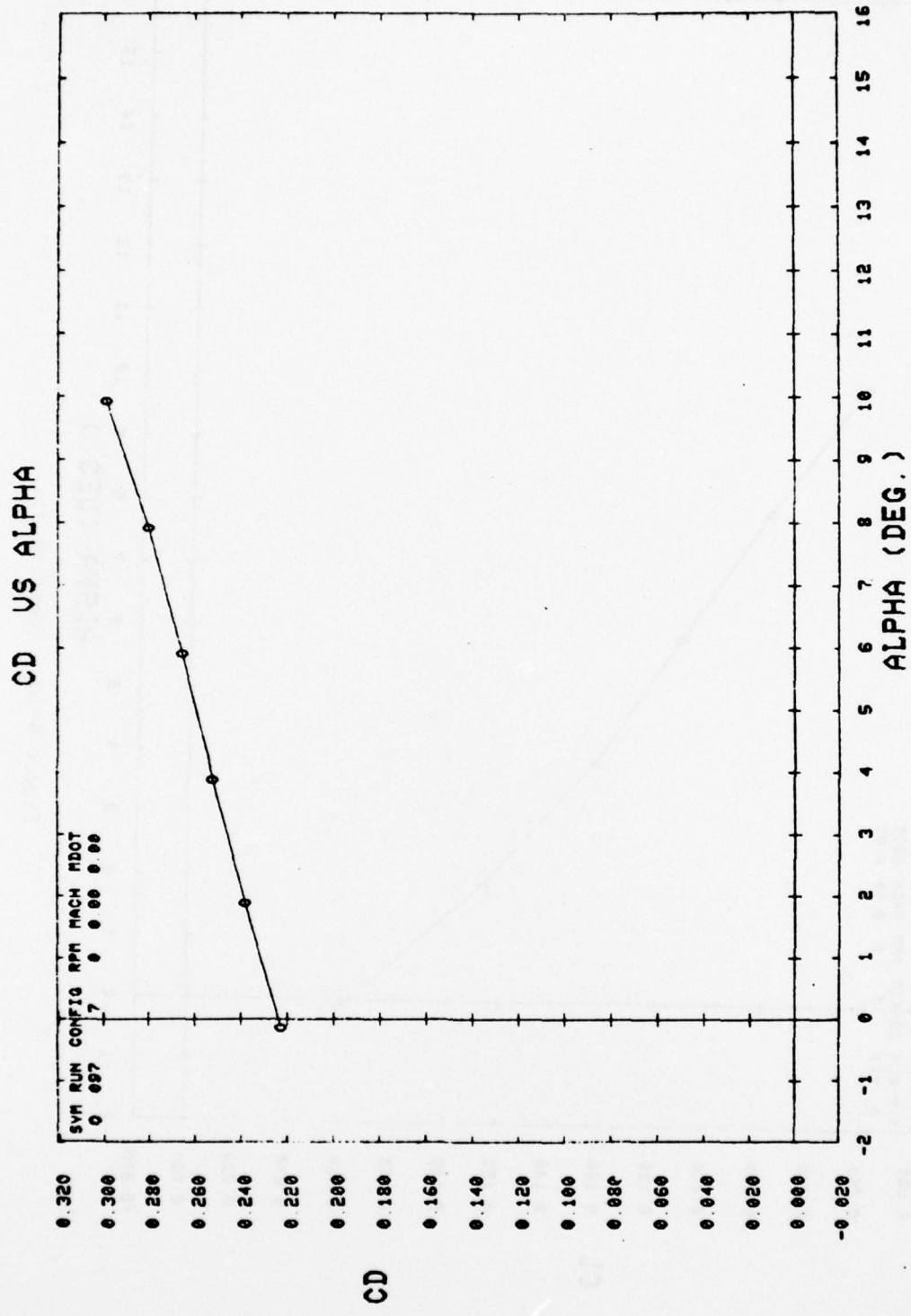


Figure A-10. (Concluded).

**Appendix B. DATA COLLATION SHEETS**

DISC: RDKA25

DATA SET SUMMARY  
TEST FACILITY ARMY TX10 TEST DATE JUNE 78 TEST ID. R A W.

DATA SET	CONFIGURATION	A	M	MDOT	DATA SET POSITION MACH NUMBER							
					1	2	3	4	5	6	7	8
D60001	1	A	0.3	0.0	0	15	30	45	60	90	-15	-60
D60002	1	B	3	0	0	0	0	0	0	0	0	0
D60003	1	B	0.2	0.0	0	0	0	0	0	0	0	0
D60004	1	E	A	0.0	0	0	0	0	0	0	0	0
D60005	1	C	3	0.0	0	0	0	0	0	0	0	0
D60006	1	C	0.3	0	0	0	0	0	0	0	0	0
D60007	1	C	3	0	0	0	0	0	0	0	0	0
D60008	1	D	3	0	0	0	0	0	0	0	0	0
D60009	1	D	3	0	0	0	0	0	0	0	0	0
D60010	1	D	3	0	0	0	0	0	0	0	0	0
D60011	1	D	2	0	0	0	0	0	0	0	0	0
D60012	1	D	1	0	0	0	0	0	0	0	0	0
D60013	1	D	3	0.0	0	0	0	0	0	0	0	0
D60014	1	D	2	0.0	0	0	0	0	0	0	0	0
D60015	1	D	1	0.0	0	0	0	0	0	0	0	0
D60016	1	D	2	0.0	0	0	0	0	0	0	0	0
D60017	1	D	3	0	0	0	0	0	0	0	0	0
D60018	1	D	3	0	0	0	0	0	0	0	0	0
D60019	2	B	3	0.0	0	0	0	0	0	0	0	0
D60020	2	B	2	0.0	0	0	0	0	0	0	0	0
D60021	2	E	A	0.0	0	0	0	0	0	0	0	0
D60022	2	E	0.0	0	0	0	0	0	0	0	0	0
D60023	2	E	0.0	0	0	0	0	0	0	0	0	0
D60024	2	C	3	0.0	0	0	0	0	0	0	0	0
D60025	2	C	2	0.0	0	0	0	0	0	0	0	0

DISC: RDKA25

## DATA SET SUMMARY

TEST FACILITY	TEST DATE	JUNE 78	TEST ID	R A U	DATA SET POSITION / MACH NUMBER								
					1	2	3	4	5	6	7	8	
DATA SET	CONFIGURATION	A	B	M	MDOT	0	.15	.30	.45	.60	.90	-15	-60
D60036	2	C	C	3	0.2	76		71		72		74	
D60037	2	C	C	2	E					79		77	
D60038	2	C	C	3	E					82		78	
D60039	3	D	D	2	0.0	58		57		56		57	
D60040	3	C	C	4	0.0					60		60	
D60041	3	C	C	15	0.0					62		62	
D60042	3	C	C	3	0.0					63		63	
D60043	3	C	C	1	E					64		64	
D60044	3	C	C	2	E					65		65	
D60035	3	C	C	3	E					66		66	
D60036	4	C	C	0.0	81			82		83		84	
D60037	4	C	C	2	0.0	86		87		88		85	
D60038	4	C	C	1	0.0					89		87	
D60039	4	C	C	15	0.0					90		90	
D60040	5	C	C	3	0.0	91							
D60041	5	C	C	15	0.0	93		92					
D60042	6	C	C	3	0.0	94							
D60043	6	C	C	2	0.0	95							
D60044	6	C	C	1	0.0					96			
D60045	7	C	C	0	0.0	97							

SCHEDULES :    A=ALPHA(0-15 DEG) DELTA OF 3 DEG  
                   B=ALPHA(0-15 DEG) DELTA OF 2 DEG  
                   C=ALPHA(0-10 DEG) DELTA OF 2 DEG  
                   D=ALPHA(0-12 DEG) DELTA OF 2 DEG  
                   D=ALPHA(0,8)DEG  
                   A=MACH NO OF .06, .08, .10, .12, .15, .25  
                   B=MACH NO OF .10, .08, .06, .04, .02, .01

**DISTRIBUTION**

	No. of Copies
Defense Documentation Cameron Station Alexandria, VA 22314	12
US Army Materiel Systems Analysis Activity Attn: DRXSY-MP Aberdeen Proving Ground, MD 21005	1
DRSMI-LP, Mr. Voigt	1
DRSMI-T, Dr. Kobler	1
-TBD	3
-TD, Mr. Derrick	20
-TI (Reference Copy)	1
(Record Copy)	1